Manipulating ultracold dysprosium's atomic spin to encode quantum critical, entangled, and topological states of matter

Tanish Satoor

▶ **To cite this version:**

Tanish Satoor. Manipulating ultracold dysprosium's atomic spin to encode quantum critical, entangled, and topological states of matter. Quantum Gases [cond-mat.quant-gas]. PSL Université, 2022. English. NNT : . tel-04064241v1

HAL Id: tel-04064241

https://hal.science/tel-04064241v1

Submitted on 11 Apr 2023 (v1), last revised 28 Oct 2024 (v2)

HAL is a multi-disciplinary open access archive for the deposit and dissemination of scientific research documents, whether they are published or not. The documents may come from teaching and research institutions in France or abroad, or from public or private research centers.

L'archive ouverte pluridisciplinaire **HAL**, est destinée au dépôt et à la diffusion de documents scientifiques de niveau recherche, publiés ou non, émanant des établissements d'enseignement et de recherche français ou étrangers, des laboratoires publics ou privés.

Distributed under a Creative Commons Attribution - NonCommercial - ShareAlike 4.0 International License

PSL
UNIVERSITÉ PARIS

THÈSE DE DOCTORAT
DE L'UNIVERSITÉ PSL

Préparée à École Normale Supérieure

Manipulating ultracold dysprosium's atomic spin to encode quantum critical, entangled, and topological states of matter

Soutenue par
Tanish SATOOR
Le 07 octobre 2022

École doctorale n°564
Physique en Île-de-France

Spécialité
Physique quantique

Composition du jury :

Bruno LABURTHE-TOLRA Université Sorbonne Paris Nord	*Président*
Philipp TREUTLEIN University of Basel	*Rapporteur*
Tommaso ROSCILDE École Normale Supérieure de Lyon	*Rapporteur*
Karyn LE HUR École Polytechnique	*Examinatrice*
Sylvain NASCIMBENE École Normale Supérieure	*Directeur de thèse*

ENS | PSL

Laboratoire Kastler Brossel
Physique quantique et applications

COLLÈGE DE FRANCE
1530

ABSTRACT

This thesis describes three studies using ultracold gases of bosonic dysprosium atoms. We encode quantum states of interest in the large electronic ground state spin $J = 8$ of each atom. Narrow-line optical transitions are used to manipulate these states by creating strong spin-dependent tensor light shifts with negligible heating. Our detection scheme uses arbitrary spin rotations followed by measurement of projection probabilities with single magnetic sublevel resolution.

Firstly, we study a transverse-field Ising model of quantum spin-1/2's with infinite-range interactions. This model shows a paramagnetic to ferromagnetic quantum phase transition in the thermodynamic limit. Our experiment relies on the formal equivalence between the states of a spin $J = 8$ and exchange-symmetric states of $2J = 16$ qubits in the sector of maximum total spin. We probe the thermodynamic and dynamical properties, revealing finite-size quantum critical behaviour around the transition point. We also directly test the fundamental link between symmetry breaking and the appearance of a finite order parameter. This is enabled by access to the collective observable defining the underlying $\mathbb{Z}_2$ symmetry.

Secondly, we partition the electronic spin to reveal entanglement in nonclassical states. By optically coupling the ground level to an excited state $J' = J - 1$, we remove a pair of encoded qubits in a state defined by the light polarisation. We probe the concurrence of qubit pairs extracted from W and squeezed states to quantify their nonclassical character. We directly demonstrate entanglement between the 14- and 2-qubit subsystems via an increase in entropy upon partition. In a complementary set of experiments, we probe the decoherence of a state prepared in the excited level $J' = J + 1$ and interpret spontaneous emission as a loss of a qubit pair in a random state. This allows us to contrast the robustness of nonclassical pairwise correlations of the W state with the fragility of the coherence of a Schrödinger cat state.

Thirdly, we simulate a quantum Hall system by exploiting the electronic ground state spin as a discrete synthetic dimension, and optically coupling it to atomic motion along a second real dimension. This creates an artificial magnetic field, with the two coupled dimensions forming a Hall ribbon with sharp edges along the synthetic axis. We demonstrate that the large number of magnetic sublevels leads to distinct bulk and edge behaviours, and a Hall response characteristic of a non-trivial topology. We perform a preliminary investigation of the entanglement spectrum associated with a partition at the centre of the synthetic dimension, and we explain how future studies could directly implement the corresponding entanglement Hamiltonian. We conclude with a roadmap for extending the techniques presented in this thesis in order to realise many-body topological states.

RÉSUMÉ

Cette thèse porte sur trois études utilisant des gaz ultrafroids d'atomes de dysprosium bosoniques. Nous encodons des états quantiques d'intérêt dans le grand spin électronique $J = 8$ de l'état fondamental de chaque atome. Des transitions optiques étroites sont utilisées pour manipuler ces états en créant de forts décalages lumineux tensoriels dépendant du spin avec un chauffage négligeable. Notre schéma de détection utilise des rotations de spin arbitraires suivies d'une mesure des probabilités de projection de chaque état interne.

Premièrement, nous étudions un modèle d'Ising de spins $1/2$ quantiques soumis à un champ transverse et interagissant à portée infinie. Ce modèle présente une transition de phase quantique du type paramagnétique-ferromagnétique dans la limite thermodynamique. Notre expérience repose sur l'équivalence formelle entre les états d'un spin $J = 8$ et les états symétriques par échange de $2J = 16$ qubits dans le secteur de spin maximal. Nous sondons les propriétés thermodynamiques et dynamiques, révélant un comportement critique quantique de taille finie autour de la transition. Ensuite, nous testons directement le lien fondamental entre la brisure de symétrie et l'apparition d'un paramètre d'ordre fini. Ceci est rendu possible par l'accès à l'observable collectif qui définit la symétrie $\mathbb{Z}_2$ sous-jacente.

Deuxièmement, nous partitionnons le spin électronique pour révéler l'intrication dans les états non-classiques. En couplant optiquement le niveau de base à un état excité $J' = J - 1$, nous extrayons une paire de qubits encodés dans un état défini par la polarisation de la lumière. Nous sondons la concomitance (*concurrence*) des paires de qubits extraites des états W et des états comprimés pour quantifier leur caractère non-classique. Nous démontrons directement l'intrication entre les sous-systèmes à 14 et 2 qubits par une augmentation de l'entropie lors de la partition. Dans un ensemble complémentaire d'expériences, nous sondons la décohérence d'un état préparé dans le niveau excité $J' = J + 1$ et interprétons l'émission spontanée comme la perte d'une paire de qubits dans un état aléatoire. Cela nous permet de contraster la robustesse des corrélations non classiques par paire de l'état W avec la fragilité de la cohérence d'un état chat de Schrödinger.

Troisièmement, nous simulons un système de Hall quantique en exploitant le spin de l'état fondamental électronique comme une dimension synthétique discrète, et en le couplant optiquement au mouvement atomique le long d'une deuxième dimension réelle. Cela crée un champ magnétique artificiel, les deux dimensions couplées formant un ruban de Hall avec des bords nets le long de l'axe synthétique. Nous démontrons que le grand nombre de sous-niveaux magnétiques conduit à des comportements distincts dans le cœur et sur les bords du système, et à une réponse de Hall caractéristique d'une topologie non-triviale. Nous effectuons une étude préliminaire du spectre d'intrication associé à une partition au centre de la dimension synthétique, et nous expliquons comment de futures études pourraient directement implémenter le hamiltonien d'intrication correspondant. Nous concluons avec une feuille de route pour étendre les techniques présentées dans cette thèse afin de réaliser des états topologiques à N corps.

CONTENTS

1 Introduction 11

2 Producing ultracold dysprosium gases 20

2.1 Dysprosium's physical properties . . . 20

2.1.1 Optical trapping . . . 23

2.2 Experimental setup overview . . . 24

2.2.1 A slow jet of atomic dysprosium . . . 24

2.2.2 Magneto-optical trap and transport . . . 25

2.2.3 Evaporative cooling . . . 25

2.2.4 Absorption imaging . . . 29

2.2.5 Magnetic field control . . . 30

2.3 Spin state detection . . . 31

2.4 Spin-dependent light shifts . . . 34

2.4.1 Basic theory . . . 34

2.4.2 Tensor polarisability . . . 35

2.4.3 Examples . . . 38

2.4.4 Dark states . . . 39

2.4.5 Comparision to alkali atoms . . . 40

2.4.6 Experimental implementation . . . 40

2.5 Summary . . . 44

3 Critical behaviour and symmetry breaking in the LMG model 47

3.1 Transverse-field Ising model . . . 48

3.2 The Lipkin-Meshkov-Glick model . . . 50

3.3 Quantum critical behaviour: Finite temperature and size . . . 52

3.4 Mapping the qubit ensemble to a large spin . . . 54

3.5 Experimental implementation . . . 56

3.5.1 Compensating stray magnetic fields . . . 57

3.5.2 Adiabaticity requirements . . . 58

3.6 Ground state properties . . . 59

3.6.1 Mean field theory . . . 61

3.6.2 Beyond the mean-field approach . . . 65

3.6.3 Nonclassicality . . . 67

3.7 Excitations . . . 68

3.7.1 Breathing modes . . . 68

3.7.2 The dipole mode . . . 73

3.7.3 Tunnelling in the ferromagnetic phase . . . 75

3.8 Symmetry breaking . . . 77

3.8.1 In a static field . . . 77
3.8.2 Spontaneous symmetry breaking . . . 79
3.8.3 Interaction-induced symmetry breaking . . . 80
3.9 Perspectives for studying spin models . . . 82
4 Partitioning dysprosium's electronic spin to reveal entanglement 86
4.1 Quantum entanglement . . . 87
4.1.1 Bipartite systems . . . 87
4.1.2 Multipartite systems . . . 90
4.2 Nonclassicality and large-spin systems . . . 92
4.2.1 Preparing nonclassical states . . . 94
4.3 Partitioning dysprosium's electronic spin . . . 96
4.3.1 Qubit mapping formalism . . . 96
4.3.2 Implementing the partition . . . 98
4.4 Nonclassicality of the extracted qubit pair . . . 100
4.4.1 Pair Husimi function . . . 101
4.4.2 Nonclassicality and the link to concurrence . . . 101
4.4.3 Application to the Dicke basis . . . 103
4.4.4 Coherent and W states . . . 105
4.4.5 Squeezed state . . . 107
4.4.6 Schrödinger cat state . . . 108
4.5 Probing entanglement via subsystem entropy . . . 109
4.5.1 W state . . . 110
4.5.2 Schrödinger cat state . . . 111
4.6 Decoherence on qubit loss . . . 114
4.6.1 Robustness of pairwise correlations . . . 115
4.6.2 Fragility of macroscopic coherence . . . 117
4.7 Perspectives . . . 119
4.7.1 Flexible manipulation of entangled states . . . 119
4.7.2 Indistinguishable particle entanglement . . . 121
4.8 Many-body spin physics with dysprosium . . . 121
5 Topology and entanglement spectrum of a synthetic Hall system 126
5.1 Introduction to quantum Hall physics . . . 127
5.2 Synthetic dimension with internal states . . . 131
5.3 Implementing a synthetic Hall ribbon . . . 133
5.4 Ground band properties . . . 135
5.5 Excitations: cyclotron and skipping orbits . . . 136
5.6 Transverse Hall response . . . 137
5.7 A cyclic synthetic dimension: the topological Laughlin pump . . . 139
5.8 The entanglement spectrum and topology . . . 140
5.8.1 Topological entanglement entropy . . . 141
5.8.2 Entanglement spectrum . . . 142

5.8.3 Link to topology in an integer quantum Hall state 143
5.8.4 Link to our synthetic Hall system 148
5.8.5 Towards direct realisation of the entanglement Hamiltonian 151
5.9 Towards many-body topological states 154
A Appendix: Publications 158
A.1 Probing chiral edge dynamics and bulk topology of a synthetic Hall system 158
A.2 Simulating two-dimensional dynamics within a large-size atomic spin . . 178
A.3 Laughlin's topological charge pump in an atomic Hall cylinder 187
A.4 Realization of an atomic quantum Hall system in four dimensions 193
B Résumé étendu en français 200
Bibliography 207

ACKNOWLEDGEMENTS

Cold atoms machines are unwieldy beasts, in need of constant taming and care from a team of experienced hands. At the dysprosium lab at Collège de France, I was lucky to be a member of a scientific family who, in addition to being the highly capable physicists who made this work possible, I found to be kindred spirits with whom it was a pleasure to share every late evening and long meeting over the past four years.

Sylvain is the creative force behind the experiment, and it was always exciting and inspiring to hear his ideas for new projects we could try, whether they came from a flash of inspiration on one of his runs, or after weeks of careful calculations. I am grateful for all his guidance and support, and would particularly like to thank him for his patience and understanding during the (not entirely painless) process of writing this manuscript. I was very fortunate to have Raphael as an effective co-supervisor for the first half of my PhD, and I hope some of his energy, passion for physics, and quasi-perfectionism when constructing an optical setup have rubbed off on me. I would also like to thank Jean, whose keen insights during group meetings and from his lecture courses provided essential fuel to drive our work forwards.

Alex, Thomas, and Vasiliy welcomed me into the group when I arrived as a naive first-year student, explained and re-explained all parts of the setup to me, and showed me how enjoyable working in a cold atoms lab could be, with a bit of music always playing, long discussions on optimal climbing technique, and (bi-)weekly trips to the market for Lebanese food. I spent the most time in the lab with Aurélien, who arrived just a few months after me, and I am grateful to have had such a perceptive, motivated, and ever-cheerful lab partner and friend, especially during the long, dark post-lockdown months. Our discussions on food, art, and the opera went a long way towards making me feel less like a guy who happens to live in Paris, and more like a Parisian. I am also glad to have worked alongside Jean-Baptiste, who, in addition to being a great running partner, both along the Seine and in the mountains, has very quickly progressed from being a new arrival to leading work in the lab. I am happy to leave the experiment in the capable hands of Quentin, Qi, and Nehal, and am excited to see the new directions they take it in.

I would like to extend a big thank you to everyone from our neighbouring experiments, for an inviting atmosphere on the floor, for letting us steal their equipment, for forcing me to eventually learn French, and for all the fun moments and discussions about physics, life, nothing, and everything, shared around a cup of coffee, a bowl of noodles, a beer, or a raclette. A big thank you to Raphaël, Édouard, Brice, Chloé, Guillaume, Franco, Manel, Alexis, Rémy, and to everyone else from the rubidium, ytterbium, and Dy-K teams. I

would also like to thank the other senior researchers on the floor, Jérôme and Alexei, for their help whenever it was needed. Furthermore, I am indebted to the support staff at Collège de France, especially Carmen, and the support staff at LKB and ENS for all their help with administrative and technical matters. I thank the members of the examining jury for their careful reading of this work and their enthusiastic participation at my thesis defence.

Home can be a nebulous concept when your life is spread over three countries, and so I am deeply thankful to all the friends and family who provided a listening ear, a warm place to stay, or just the pleasure of their company, whenever I needed it these past few years. Firstly, I would like to thank my neighbours and friends, specially Charles, Anusree, and Gurugam, at the Maison de l'Inde in Paris, where I could simply walk in to the kitchen after a long day of work and be offered a home-cooked Indian dinner. Secondly, I would like to thank my friends across the Channel; Dan, whose research progress reassured and encouraged me when my own work felt stuck; Lauren and Sophie, who made art with me and kept me sane during the pandemic; Hugh, whose house always feels like home when *home* home in India is too far away; and Dhruva, Adam, and Jess, I am so grateful for you all. Finally, I would like to thank my family in India, and in particular my parents, without whose support I would never have had the courage to leave home to study physics in the first place, whose weekly calls are a constant, and a source of comfort, through thick and thin, and who, when I wasn't able to make it there, brought our home here to me in Paris when I needed it the most. Thank you, thank you all.

For once the disease of reading has laid upon the system it weakens it so that it falls an easy prey to that other scourge which dwells in the inkpot and festers in the quill. The wretch takes to writing.

Virginia Woolf, *Orlando*

1

INTRODUCTION

Quantum physics created a paradigm shift [1] in our understanding of the microscopic world. Amongst the first triumphs of this theory was the precise prediction of the energies of photons, or packets of light, emitted by single atoms. Soon afterwards, quantum physics was successfully applied to systems with a large number of constituents: here, novel collective effects can emerge, which are not a mere sum of the individual constituents' behaviour [2]. Some such effects, like magnetism, have been known since antiquity, while more exotic ones like superconductivity, have only been observed with recent technologies. These collective effects arise through phase transitions, consisting of an emergence of order at the microscopic level, accompanied by the spontaneous breaking of a physical symmetry [3], driven by long-range fluctuations. For example, water molecules collectively 'choose' to crystallise along a specific regular lattice, even though space itself is uniform, and any number of arrangements might be equally favourable. While a true quantum phase transition only occurs in an infinite system at zero temperature, fascinating signatures of the transition, dubbed critical behaviour, are also evident in realistic settings [4].

What is the nature of the long-range correlations driving quantum phase transitions? While a 'shut up and calculate' approach can get one very far in terms of predicting quantum phenomena, physicists have long been plagued and stimulated by the wider implications of quantum mechanics [5] – spooky, unintuitive behaviour with no counterpart in our everyday classical experience. This quantum entanglement, or more generally non-classicality, is not only a philosophical conundrum. It has concrete, detectable physical consequences [6–8]. Creating and manipulating entangled states is relevant for understanding the foundations of quantum physics, as well for developing a new generation of quantum technologies.

The discovery of the quantum Hall effect in 1980 [9] signalled a fundamentally new form of order possible in nature, one that does not fit into the above framework of broken symmetries and critical behaviour [10]. The first experiments observed a physical quantity, called the Hall resistivity, taking universal values completely insensitive to experimental imperfections, to an unprecedented and spectacular degree of precision (one part in ten billion). These measurements were subsequently understood using ideas from a branch of mathematics called topology. Topology concerns itself with the global

structure of surfaces – for example, a football and frisbee are topologically equivalent because they have no holes, but are distinct from a doughnut or coffee mug, which have one hole. In a more abstract sense, topological structure can be assigned to the global arrangement of a system's quantum state, leading to physical properties which depend on only the associated topological invariant ('number of holes'), irrespective of small imperfections. States protected by this topological robustness have promising prospects for quantum computing [11], while certain classes of topological states are fundamental to our understanding of highly correlated quantum systems [12].

In this thesis, I will present experimental studies which traverse and interlink the three themes discussed above: symmetry breaking and critical behaviour near a phase transition, nonclassicality and entanglement, and topological states of matter. This work was performed on a single versatile experimental platform, by encoding the relevant quantum states in the internal degree of freedom (spin) and motion of ultracold dysprosium atoms.

The following chapter-wise introductions aim to give a more substantial taste of things to come, while also providing a convenient reference point to be revisited before reading the respective chapters.

Producing ultracold dysprosium gases

In the 20th century, condensed matter systems such as magnetic materials, superconductors, and liquid helium, were at the forefront of developments in quantum physics. In the last few decades, ultracold atom experiments (and their cousins in the broader field of atomic, molecular, and optical physics) have brought exciting new possibilities to probe the fundamentals of quantum mechanics, understand many-body effects by quantum simulation, and engineer entirely novel systems with no traditional condensed matter counterparts. This is made possible by exquisite control of physical parameters including spatial potentials, interactions, dimensionality, and coupling to the environment – all combined with precise, microscopic detection protocols.

The principles of manipulating atoms' motion and internal states with light were present in early works by Einstein [13] and Kastler [14]. Modern techniques for laser cooling developed rapidly from the mid-1970s onwards following the widespread availability of precisely tunable laser sources. A summary can be found in the 1998 Nobel lectures by Chu, Cohen-Tannoudji, and Phillips [15–17]. These developments culminated in the creation of dilute degenerate ultracold gases, where the size of the quantum wavepacket associated with a single atom i.e. the thermal de Broglie wavelength, is comparable to the spacing between atoms. Depending on the quantum statistics of the atoms involved, such samples form Bose-Einstein condensates (BECs) [18, 19] or degenerate Fermi gases [20]. This was the birth of the field of ultracold atoms in its current incarnation, and several landmark results were attained in the following years. These include the observation of the Mott-insulator to superfluid phase transition [21], the Berezinskii-Kosterlitz-Thouless

transition [22], and the molecular BEC to Bardeen–Cooper–Schrieffer superfluid crossover [23–26] (see refs. [27, 28] for more comprehensive reviews).

The above works were carried out with elements whose inter-atom interactions are given by short-range van der Waals forces. Long-range magnetic dipole-dipole interactions create new possibilities, as first illustrated with chromium BECs with the observation of ferrofluid behaviour [29]. The study of dipolar ultracold gases has accelerated in the last decade, following the cooling of the lanthanide elements dysprosium [30, 31] and erbium [32] to quantum degeneracy. Here, the control of strong long-range interactions and their subtle interplay with short-range interactions has led to the observation of novel droplet [33], and supersolid [34–36] phases (see ref. [37] for a review).

In chapter 2, we will describe our experimental setup for the production of ultracold dysprosium gases. Rather than long-range interactions, the work presented in this thesis exploits another unique feature of dysprosium: its large ground state angular momentum $J = 8$. We explain how we use spin-dependent light shifts associated with narrow-line transitions to create non-linear spin Hamiltonians, with minimal heating effects. Combining this ability with the large internal manifold of $2J + 1 = 17$ states, whose occupation we can detect with single-level resolution, we discuss how our setup acts as a flexible platform to realise the studies described below.

Critical behaviour and symmetry breaking in the Lipkin-Meshkov-Glick model

Phase transitions are ubiquitous in nature, in systems at all energy and length scales, from the quark-gluon plasma in the early universe to liquid helium in laboratory cryostats. Our understanding of phase transitions has historically relied on the non-analytic behaviour of thermodynamic quantities, the spontaneous breaking of symmetry, and fluctuations of the order parameter. These concepts still play a key role in the modern description of phase transitions, which is underpinned by the renormalisation group [38], developed by Fisher, Wilson, and Kadanoff in the 1970s. This theory allows for a unified description of broad classes of systems near a transition in terms of a few universal parameters, independent of the microscopic details of individual systems [4]. In quantum systems, the observed change in behaviour as a control parameter is varied is understood in terms of a true phase transition occurring at a quantum critical point – defined at zero temperature in an infinite system. At finite temperatures, a complex interplay of thermal and quantum fluctuations leads to quantum criticality, where excitations cannot be reduced to an effective theory with weak interactions [39]. In finite systems, the quantum critical point also looms large in the crossover regime, as described quantitatively by universal parameters arising from the theory of finite-size scaling [40].

The distinct properties expected close to a quantum critical point can at times be probed with macroscopic observables, like the slowing of relaxation times. However, revealing specifically quantum properties like many-body quantum entanglement [41], remains challenging. The recent development of highly controlled quantum systems

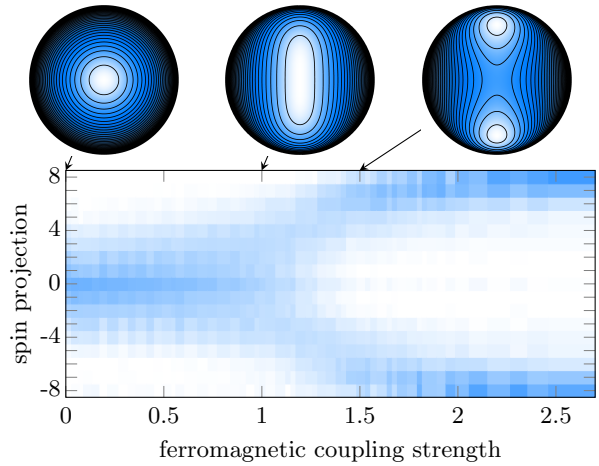

Figure 1.1: Crossover from paramagnetic to ferromagnetic behaviour in the Lipkin-Meshkov-Glick model, as seen in spin projection probabilities along the axis of ferromagnetic interactions. A preview of results from chapter 3.

of mesoscopic size, such as ion crystals [42], optical lattice systems [43], Rydberg atom arrays [44], or interacting photons [45], allows for a microscopic characterization of collective quantum properties [46] such as the full density matrix [45], entanglement entropy [47] or non-local string order [48]. This degree of control could be used to investigate fundamental aspects of quantum phase transitions, such as the link between the breaking of an underlying symmetry and the onset of a non-zero order parameter [3]. This connection cannot be tested in macroscopic systems, where large-size quantum superpositions cannot practically exist and spontaneous symmetry breaking is unavoidable [49].

In chapter 3, we present an experimental study of the Lipkin-Meshkov-Glick model (LMGm), which describes quantum spin-halfs with infinite-range Ising interactions in a transverse field. In the thermodynamic limit, the LMGm exhibits a ferromagnetic phase transition, characterised by spontaneous breaking of a $\mathbb{Z}_2$ symmetry. This model was originally proposed for nuclear systems [50–52], but has found widespread use. For example, the LMGm describes systems undergoing the Dicke superradiance transition [53] (in the zero temperature limit), and two-mode BECs with Josephson-like tunnelling [54, 55]. From a theoretical perspective, the LMGm has been widely investigated due to its mathematical tractability, and its close link, via mean-field theory and finite-size scaling, to the short-range transverse-field Ising model [56].

Our realisation of the LMGm is based on the equivalence between the dysprosium atom's electronic spin $J = 8$ and a set of $N = 2J$ spins-1/2s in an exchange-symmetric state. We simulate the ferromagnetic Ising interactions with a quadratic light shift. Given this encoding of qubits, the moments of the total spin-J give access to few-qubit correlators. We measure the crossover between para- and ferromagnetic behaviours using thermodynamic properties (see fig. 1.1) and the dynamical response. We reveal a regime of quantum critical behaviour and slowed dynamics around the transition point. A spe-

cific asset of our setup is the direct access to the parity observable corresponding to the $\mathbb{Z}_2$ symmetry; this is made possible by single magnetic sublevel resolution which cannot be achieved in macroscopic systems. We investigate the fundamental link between symmetry breaking and the appearance of a finite order parameter. The mesoscopic size of the system affords us a degree of control where we can specifically probe symmetry breaking due to a manually applied perturbation (e.g. to measure the susceptibility), as well as observe spontaneous symmetry breaking from random environmental fluctuations.

Partitioning dysprosium's electronic spin to reveal entanglement

Entanglement has historically been the defining form of strangeness associated with quantum systems. Schrödinger called entanglement "*the* characteristic trait of quantum mechanics, the one that enforces its entire departure from classical lines of thought" [57]. In brief, entanglement allows for situations where the best possible knowledge of a whole (quantum system) does not include the best possible knowledge of its parts (subsystems). Early discussions of entanglement focussed on its relevance for hidden-variable interpretations of quantum mechanics [5, 6]. Today, it is also recognised as a resource in the context of quantum technologies, for tasks like algorithmic computation, communication, cryptography, and teleportation [58].

Entanglement also plays a fundamental role in driving quantum phase transitions [4, 41], in the form of the propagation of correlations over large length scales. Indeed, if the study of the LMG model described above was performed on a system of individually distinguishable qubits, the observed squeezing of a global spin quadrature in the crossover region would imply entanglement between qubits [59]. It is then natural to ask: can any physical meaning be assigned to the 'entanglement of the encoded qubits', and to what extent is it accessible as a resource? This is the line of investigation which drives our second experimental study, presented in chapter 4, where we perform a partition of this ensemble using optical transitions, giving access to entanglement properties.

Let us first clarify that entanglement lies in the more general category of nonclassical behaviour. Nonclassicality can be identified even in cases where subsystems cannot be identified e.g. Fock states in quantum optics. Correlations within indivisible systems can be fundamentally incompatible with a classical description, as demonstrated by the violation of Bell-like inequalities [60]. In dysprosium's ground state spin, if the ensemble of encoded qubits cannot be partitioned, we must restrict ourselves to stating that we can have nonclassical behaviour at the level of the total spin, corresponding to quantum correlations of its internal degrees of freedom.

Before describing our work, it is also helpful to review the kinds of systems used to create and detect entanglement. Minimal entangled systems of qubit pairs, as realised with correlated photons, play a central role in testing the foundations of quantum mechanics [7, 61], through the violation of Bell inequalities [6]. Entanglement can also be engineered in many-particle systems [62], such as an ensemble of interacting atoms [63].

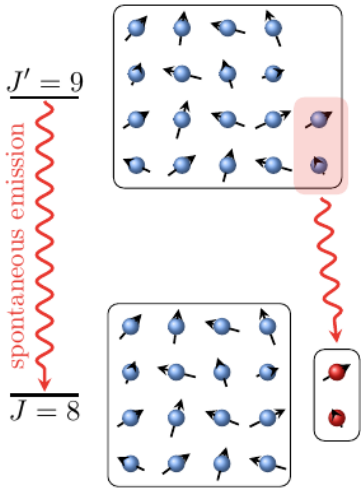

Figure 1.2: A scheme for partitioning the electronic spin of dysprosium by spontaneous emission. A preview of a technique used in chapter 4.

In this case, the atoms are not individually addressable, and quantum correlations are indirectly revealed by measuring global properties, such as a squeezed spin projection quadrature [64–67] or via the quantum enhancement of metrological sensitivity [68–70]. State of the art experiments with photonic systems [71], superconducting qubits [72], trapped ions [73] and Rydberg atom arrays [74] can now produce highly entangled states of tens of individually identifiable qubits, where entanglement is more readily observable.

In our work, we first access entanglement properties by partitioning dysprosium's electronic spin using an optical coupling to an excited state $J' = J - 1$. This removes a pair of qubits in a state defined by the light's polarisation. Starting with the well-known W and squeezed states, we extract the concurrence of qubit pairs, which quantifies their nonclassical character. We also directly demonstrate entanglement between the 14- and 2-qubit subsystems via an increase in entropy upon partition. In a second set of measurements, we probe the decoherence of a state prepared in the excited level $J' = J + 1$ and interpret spontaneous emission as a loss of a qubit pair in a random state (see fig. 1.2). This allows us to contrast the robustness of nonclassical pairwise correlations of the W state with the fragility of the coherence involved in a Schrödinger cat state [75]. These observations are related to the *which path* information carried by the emitted photon's polarisation. Our results can be viewed within the recent debate on nonclassicality and entanglement in systems of indistinguishable constituents [76]. We also discuss prospective experiments involving entangled atoms in spatially separated setups, and more generally discuss many-body spin physics with dysprosium.

Topology and entanglement spectrum of a synthetic Hall system

We now move away from the picture of encoded qubits in the electronic ground state spin. For the realisation of topological systems, we use the $2J + 1$ magnetic sublevels to

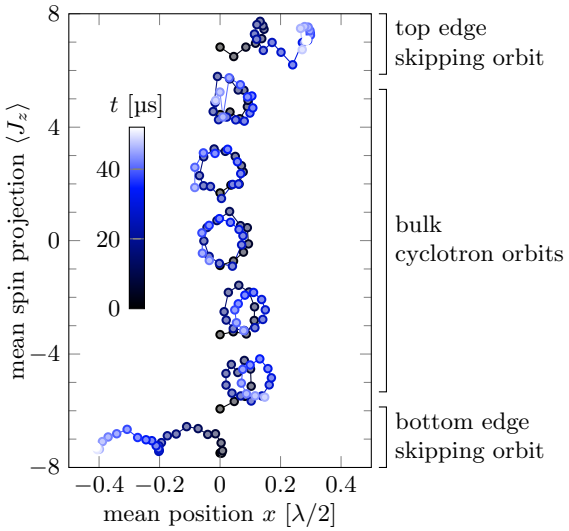

Figure 1.3: Cyclotron and skipping orbits in a synthetic Hall system. A preview of results from chapter 5.

represent a discrete 'position' in a synthetic dimension, as originally proposed in ref. [77]. Motion along neighbouring points in the synthetic dimension is enabled by two-photon laser transitions, which create complex hopping phase factors (cf. the Aharanov-Bohm phase) and a well-defined link to the atom's motion along the photon recoil axis. This motivates an analogy with a charged particle moving in two dimensions in the presence of a perpendicular magnetic field. Thus, we realise a Hall-like system in a ribbon geometry; here, one dimension is along an axis in real space, while the other is a finite synthetic dimension encoded in the spin.

Quantum Hall systems are famous for the extremely robust quantisation of their transverse conductance. In traditional condensed matter systems, impurities and disorder lead to conducting stripes surrounding insulating domains of localised electrons, making comparisons with simple models challenging [78, 79]. The quantised Hall conductance results from the non-trivial topological structuring of the quantum states of an electron band [10]. For an infinite system, this structure is described by the Chern number, a topological invariant taking integer values, which is robust up to a certain degree of disorder [10]. In a real finite-size system, the non-trivial topology leads to gapless edge modes, characterised by unidirectional motion protected from backscattering [79]. These chiral edge modes, together with their generalization to topological insulators, topological superconductors or fractional quantum Hall states [80, 81], lie at the heart of possible applications in spintronics [82] or quantum computing [83].

Initial works using synthetic dimensions of limited sizes were able to measure chiral edge currents [84, 85]. However, the relevance of topological properties requires the notion of a bulk. In chapter 5, we describe the realisation of a synthetic Hall system with distinct bulk and edge properties. In the lowest band, we characterise the dispersionless bulk modes, where motion is inhibited due to a flattened energy band, and chiral edge

states, where the particles are free to move in one direction only. We also study the system's elementary excitations to higher bands, which take the form of cyclotron orbits in the bulk and skipping orbits along the edges (see fig. 1.3). Finally, we measure the Hall drift induced by an external voltage, and characterise the local Hall response of the band using the local Chern marker, which quantifies topological order in real space [86]. Our experiments show that the synthetic dimension is large enough to allow for a meaningful bulk with robust topological properties.

The entanglement properties of many-body states contain key information about topological properties. In particular, the structure of the eigenvalues of a given subsystem's density matrix, known as the entanglement spectrum, gives the many-body excitation spectrum of the chiral edge modes of the overall system [87]. We reinterpret our experimental results from this point of view, revealing a signature of the entanglement spectrum at the single-particle level. We then discuss how the entanglement properties could be probed directly in our system with future experiments, inspired by a recent as-yet-unrealised proposal [88]. We conclude with a perspective on the realisation of many-body topological states with dysprosium.

2

PRODUCING ULTRACOLD DYSPROSIUM GASES

> The rule is, jam to-morrow and jam yesterday –
> but never jam to-day.
>
> Lewis Carroll, *Through the Looking-Glass*

In this chapter, I describe the experimental system used during this thesis – a typical modern ultracold atom experiment, built from 2013 onwards at ENS and Collège de France, Paris. Our dysprosium atoms begin as a vapour at a temperature of 10^3 K. Over a single experimental cycle lasting 20 s, we produce an ultracold quantum gas at 10^{-7} K. The action takes place inside a vacuum chamber, where the low pressures (down to 10^{-10} mbar) provide a high degree of isolation from the environment. We use laser beams sent through windows in the vacuum chamber, and magnetic fields generated by surrounding coils to cool, trap, manipulate, and detect the atoms. The cold and dilute quantum gas we create serves as the starting point for realising the work described in subsequent chapters.

As the fifth-generation PhD student in the group, I was fortunate to have arrived in a lab with a fully operational experimental setup. This chapter begins with an overview of the technical aspects of the setup, which have been described in detail in previous PhD theses and publications [89–94]. I will then devote the bulk of the chapter to describing the techniques underlying the original work carried out during this thesis: the precise and flexible manipulation of the atoms' internal state using spin-dependent light shifts and the subsequent detection of the engineered states.

2.1 DYSPROSIUM'S PHYSICAL PROPERTIES

Dysprosium, from the Greek *dysprositos* meaning 'hard to get', is a lanthanide series rare-earth element with atomic number $Z = 66$. In ambient conditions, it is a silver metallic solid. Dysprosium is notably a highly magnetic element, as we shall see below. This has lead to applications in magnetic data storage, and also for permanent magnets in electric car engines and wind turbines.

Electronic structure & isotopes

Dysprosium's magnetic properties arise from its electronic structure. Like other lanthanides, it has a partially filled $4f$ electron shell in its ground state. The electronic configuration, relative to the nearest noble gas xenon, is

$$[\mathrm{Xe}]4f^{10}6s^2\,,$$

corresponding to four unpaired electrons in the $4f$ shell. The net electronic spin is $S = 2$ which combines with the orbital angular momentum $L = 6$, to give a total electronic ground state angular momentum $J = 8$. So in spectroscopic notation ($^{2S+1}L_J$), the ground state is denoted $^5I_8$. The four unparied electrons lead to a dense forest of excited levels in the optical energy range (cf. the $^2S_{1/2}$ ground state of alkali metal atoms). The strongest relevant transitions (with linewidths $\Gamma \simeq 2\pi \times 30\,\mathrm{MHz}$) form a triplet with excited state momenta $J' = 7, 8, 9$ in the blue part of the spectrum, at wavelengths 405, 419 and 421 nm. These arise from the jj coupling of the valence electron transition $^1S_0 \rightarrow {}^1P_1$ to the $^5I_8$ term, making them analogous to the D1 and D2 lines of alkalis.

Dysprosium has seven stable isotopes, with an average atomic weight of 162.5. The bosonic isotopes all have nuclear spin $I = 0$, such that the total atomic angular momentum remains $F = 8$. Throughout this thesis, we will work with the bosonic isotope ^{162}Dy and denote its total angular momentum as $J = 8$. We prefer ^{162}Dy to ^{164}Dy despite the latter being more naturally abundant (25.3% vs 28.3%), because of the larger background scattering length of ^{162}Dy, which is favourable for evaporative cooling. The first Bose-Einstein condensate (BEC) of dysprosium was produced at Stanford in 2011 [30]. Degenerate quantum gases have also been prepared for the fermionic species ^{161}Dy [95] ($I = 5/2$). Other highly magnetic elements which have been cooled to degeneracy are chromium [96] (in 2005 in Stuttgart), erbium [32] (in 2012 in Innsbruck), and thulium [97] (in 2020 in Moscow). See ref. [37] for a recent review on dipolar quantum gas physics.

Laser cooling

We use two optical transitions for laser cooling, whose properties are summarised in table 2.1. Firstly, we used the $J' = 9$ transition at 421 nm mentioned above. Its large linewidth makes it suitable for applying the strong radiative forces needed to slow down the atomic jet. Note that we also address the atoms using this transition to image them. The second cooling transition is a narrower, red transition with linewidth $\Gamma = 2\pi \times 135\,\mathrm{kHz}$. The low associated Doppler temperature $T_\mathrm{D} = \hbar\Gamma/2k_\mathrm{B} = 3.2\,\mu\mathrm{K}$ allows for its use for a single stage magneto-optical trap (MOT), from which we can efficiently load an optical dipole trap (ODT). We do not describe the principles of laser cooling here – see, for instance, ref. [98].

Wavelength	Linewidth	Doppler temperature	Excited state	
λ [nm]	$\Gamma/2\pi$ [MHz]	T_D [μK]	f shell	valence
421	32.2	774	$4f^{10}\,(^5I_8)$	$6s^2\,(^1P_1)$
626	0.135	3.2	$4f^{10}\,(^5I_8)$	$6s6p\,(^3P_1)$

Table 2.1: Parameters of laser cooling transitions. Data from ref. [99].

Magnetic properties

In the presence of an external magnetic field B (say along z), the degeneracy of the $J = 8$ ground manifold is lifted. The azimuthal angular momentum m remains a good quantum number, with the states acquiring a linear Zeeman shift

$$E = \mu_B g_J B\, m, \text{ or in operator form } H = \mu_B g_J B\, J_z\,.$$

Here, μ_B is the Bohr magneton and $g_J = 1.242$ is the Landé g-factor for the $J = 8$ ground manifold. Note the resulting large magnetic moment of the $m = -8$ ground state, given by $\mu = 9.93 \times \mu_B$. This can be compared to other elements: μ/μ_B equals 1 for ^{87}Rb, 6 for ^{52}Cr, and 6.98 for ^{166}Er.

Interactions

Dysprosium atoms interact with each other via short-range van der Waal's forces and long-range magnetic dipole-dipole interactions.

At low temperatures, the short-range interactions for two ^{162}Dy atoms polarised in $m = -8$ are described by a single parameter, called the s-wave scattering length, denoted a. The effective interaction can be reduced to an isotropic contact pseudo-potential

$$U_{\text{contact}}(r) = \frac{4\pi\hbar^2 a}{m}\delta(r)\frac{\partial}{\partial r}r\,.$$

The prefactor is commonly called the coupling constant $g = 4\pi\hbar^2 a/m$. The background value of a is $126(10)\,a_0$ where a_0 is the Bohr radius. This quantity can be set to any desired value by tuning the external magnetic field close to a Feshbach resonance. The species ^{162}Dy shows nine narrow Feshbach resonances at low fields (0 G to 6 G) [100].

We now consider dipole-dipole interactions for atoms polarised in an external B-field. The interaction potential is given by

$$U_{\text{dd}}(\boldsymbol{r}) = \frac{\mu_0\mu^2}{4\pi}\frac{1-3\cos^2\theta}{r^3}$$

where θ is the relative polar angle between the atoms with respect to the external field. The prefactor can be recast to reveal a length-scale called the dipolar length $a_{\text{dd}} = \mu^2\mu_0 m/12\pi\hbar^2$. We can compare this quantity to a to judge the relative strength

of the long-range term. Indeed, $a_{\mathrm{dd}}/a \sim 1$ for dysprosium, while it is about 10^{-2} for rubidium, justifying the title of dipolar quantum gas in the former case!

2.1.1 *Optical trapping*

We use infrared lasers to create conservative trapping potentials for our atoms. The principle of these *optical dipole traps* (ODTs) is the light-induced coupling of the ground state to the forest of excited energy levels, as we will explain in detail in section 2.4. Here, we restrict ourselves to stating the effect of a monochromatic light field with spatially dependent intensity $I(\boldsymbol{r})$, at the wavelength $\lambda = 1064\,\mathrm{nm}$ used for our ODTs. An attractive potential landscape is created:

$$V(\boldsymbol{r}) = -\frac{1}{2\epsilon_0 c}\mathrm{Re}[\alpha]\; I(\boldsymbol{r})\,,$$

where $\alpha \simeq 184\,\alpha_0$ is a quantity called the polarisability. The unit of atomic polarisability is $\alpha_0 = 4\pi\epsilon_0 a_0^3$.

Our ODT laser beams are, to a good approximation, circular Gaussian beams. A single such beam has an intensity profile

$$I(\boldsymbol{r}) = I_0\left(\frac{w_0}{w(z)}\right)^2 \exp\left(-2\frac{\rho^2}{w(z)^2}\right),$$

where z is the coordinate along the propagation axis, and ρ is the distance from this axis. The deepest part of the trap is on the axis at the focus $z = 0$, where the intensity is I_0 and radius is given by the waist w_0 (typically 30 µm on our setup). The total optical power of the beam is $P = \pi w_0^2 I_0/2$. Away from the focus, the radius increases as

$$w(z) = w_0\sqrt{1 + \left(\frac{z}{z_{\mathrm{R}}}\right)^2},$$

where $z_{\mathrm{R}} = \pi w_0^2/\lambda$ is the Rayleigh range (typically 7 mm).

The magnitude of the potential at the focus corresponds to the trap depth

$$U_0 = \frac{1}{2\epsilon_0 c}\mathrm{Re}[\alpha]\; I_0\,.$$

Near the focus ($z \ll z_{\mathrm{R}}$, $\rho \ll w_0$), such a trap is approximated by a three-dimensional harmonic potential

$$V(\boldsymbol{r}) \approx -U_0 + \frac{m}{2}(\omega_\rho^2\rho^2 + \omega_z^2 z^2), \text{ where } \omega_\rho = \sqrt{\frac{4U_0}{mw_0^2}} \text{ and } \omega_z = \sqrt{\frac{2U_0}{mz_{\mathrm{R}}^2}} \qquad (2.1)$$

are the radial and axial trap frequencies respectively.

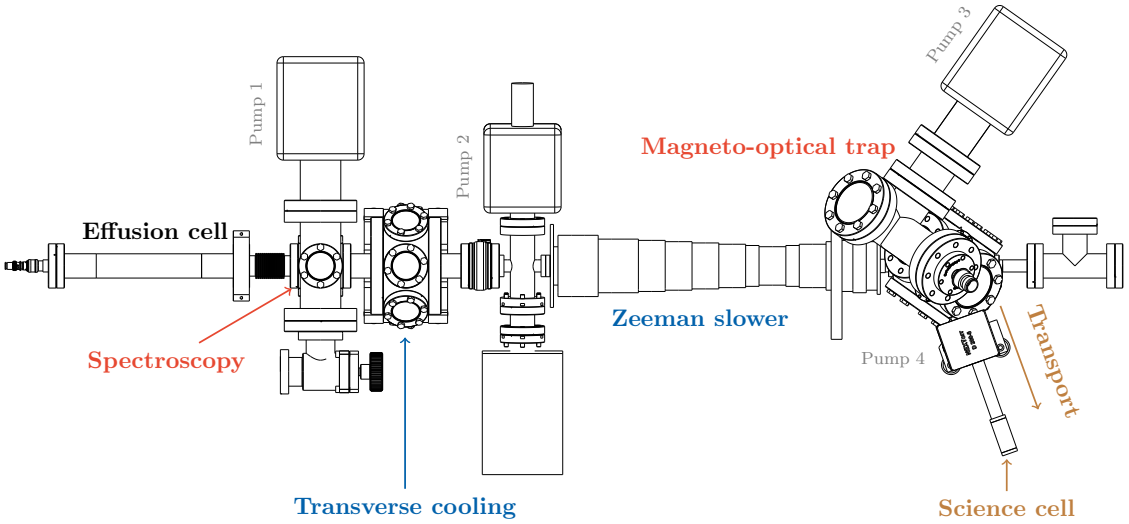

Figure 2.1: Schematic top view of the experimental vacuum chamber. The operations carried out in different sections are described in section 2.2. See fig. 2.2 for a zoom-in on the science cell. For scale, the length of the Zeeman slower is 50 cm.

2.2 EXPERIMENTAL SETUP OVERVIEW

In this section, we briefly describe the stages of the experiment leading to the production of ultracold gases. Figure 2.1 shows a schematic of our experimental system. The design and construction of the experiment have been detailed in refs. [89, 90].

2.2.1 *A slow jet of atomic dysprosium*

The source of our dysprosium atoms is an effusion cell filled with flakes of solid dysprosium. The cell is heated to 1100 °C, where the vapour pressure is sufficient to produce a directed jet of atoms at a velocity of about $500\,\mathrm{m\,s^{-1}}$. The jet's divergence is reduced by a transverse cooling stage located at the cell exit. This 2-D optical molasses, operating on the blue cooling transition at 421 nm, ensures an adequate flux of atoms at the entrance of the Zeeman slower. The Zeeman slower also operates on the blue cooling transition; it uses a spin-flip configuration for the magnetic field over a total length of 50 cm, slowing the atomic get to a velocity of about $8\,\mathrm{m\,s^{-1}}$.

Note that the light at 421 nm is produced with a commercial laser, which is frequency locked to the atomic transition using modulation transfer spectroscopy on a hollow cathode lamp setup. On the other hand, the 626 nm laser is a home-made system based on sum frequency generation with infrared seeds at 1050 nm and 1550 nm in a non-linear PPLN crystal. The frequency lock is more demanding in this case due to the narrow linewidth. It is performed using Lamb dip spectroscopy directly on the atomic jet before the Zeeman slower entrance.

2.2.2 *Magneto-optical trap and transport*

Our magneto-optical trap (MOT) operates on the 626 nm transition and uses a quadrupole B-field gradient along a horizontal axis. During an initial loading stage, 15 seconds in duration, the MOT beams have a high intensity, with saturation parameter $s \sim 50$, and are modulated in frequency; this widens the capture range of atomic velocities. Then, a compression stage follows, where the modulation is turned off and the intensity is ramped down, leading to an increase in density and decrease of temperature, as explained in ref. [93], where a detailed study of our MOT can be found. The balance of radiative and gravitational forces leads to a spin polarisation in the state $|J, m = -J\rangle$. Our MOT typically consists of 10^8 atoms at 15 µK.

The next step consists in transporting the atoms over a distance of 30 cm from the MOT chamber to the science cell. This step has been described in detail in [90]. In short, we turn on a deep optical dipole trap (ODT) at 1070 nm, whose focus initially overlaps with the MOT capture region, allowing for a transfer of the atomic cloud. The optical path of the ODT beam is designed to include a retroreflector mounted on a mechanical translation stage, allowing us to move the focus, and hence the trapped atoms, to the science cell. The total efficiency of the capture from the MOT and the transport steps is 10% (with respect to atom number).

After transport, we use an intermediate Doppler cooling stage. The aim here is to provide a good starting point for subsequent forced evaporative cooling by increasing the atomic collisional rate. A single red-detuned 626 nm beam is used for cooling in this step (see fig. 2.2). The difference in polarisabilities of the ground and excited levels leads to an effective detuning that depends on the polarisation and intensity of the ODT. As explained in ref. [94], we exploit this effect to optimise the cooling effect, resulting in a twofold increase in the collisional rate. Note that the concepts of polarisability and lightshifts will be explained in detail in section 2.4.

The final step before evaporative cooling is the transfer of the cloud into a pair of orthogonal crossed optical dipole traps (cODTs, see fig. 2.2). The cODTs are created with single-mode fibre lasers at $\lambda = 1064$ nm with powers 45 W and 10 W. During the transfer, the focal position of the more powerful laser is rapidly modulated, such that the atoms feel a wider and shallower time-averaged potential – this increases the spatial overlap of the cODTs with the transport ODT and improves the transfer efficiency by a factor of two (see [92] for details). The transport trap is then gradually turned off, preparing us for evaporative cooling in the cODTs.

2.2.3 *Evaporative cooling*

The crossed optical dipole traps together form a three-dimensional trapping potential, given by summing the individual potentials stated in eq. (2.1). We denote the resulting

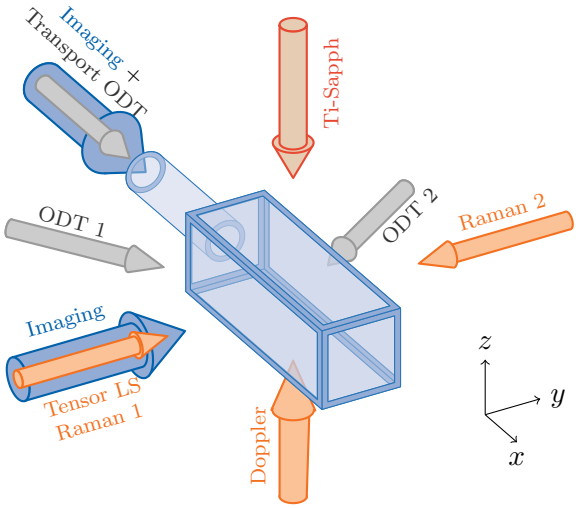

Figure 2.2: Schematic of the glass science cell, with incident laser beams. The atomic cloud arrives from the MOT chamber trapped in the transport optical dipole trap (ODT). It is then cooled by the Doppler cooling beam at wavelength $\lambda = 626\,\text{nm}$, which is incident from the -z direction. This is followed by transfer into the mutually perpendicular crossed ODTs (ODT 1&2, $\lambda = 1064\,\text{nm}$) and evaporative cooling. The spin state is manipulated using the red tensor light shift (LS) beam at 626 nm ($J' = 9$). This beam can also be used in conjunction with an identical counter-propagating beam to induce Raman transitions within the ground manifold ($J = 8$). The Titanium-Sapphire (Ti-Sapph) laser beam from above is also used for tensor lightshifts; it can address transitions with excited state angular momentum $J' = 7, 8, 9$. The spin state can then be detected by either of two absorption imaging beams ($\lambda = 421\,\text{nm}$). Magnetic field control, including production of the Stern-Gerlach gradient to resolve the spin sublevels, relies on magnetic coils surrounding the cell, not shown here. For scale, the outer dimensions of the science cell are $5\,\text{cm} \times 5\,\text{cm} \times 15\,\text{cm}$.

total trap depth U_0, and average trap frequency $\bar{\omega} = (\omega_x \omega_y \omega_z)^{1/3}$. Far from degeneracy, the average energy per particle is that of an ideal gas i.e. $3k_\text{B}T$. The parameter $\eta = U_0/k_\text{B}T$ is on the order of 10, such that the gas is indeed localised at the trap centre, where the potential is harmonic. From a thermodynamic point of view, this system is open, since evaporation is possible: particles with large kinetic energies $\gtrsim U_0$ can escape the central region and be permanently lost, leading to a decrease in the average energy per particle. The principle of forced evaporative cooling is to decrease U_0 over time, such that a fraction of high energy particles, i.e. the tail of the Boltzmann distribution, can escape, leading to a decreasing temperature as the remaining particles rethermalise, as sketched in fig. 2.3. To achieve significant cooling, this process must dominate non-energy selective loss processes, e.g. collisions with background gas, which do not decrease the temperature. A full treatment can be found in standard texts, e.g. ref. [101].

In practice, we wish to implement an evaporation process that increases the degree of quantum degeneracy, as quantified by the phase space density

$$\mathcal{D} = N \left(\frac{\hbar \bar{\omega}}{k_\text{B} T} \right)^3 .$$

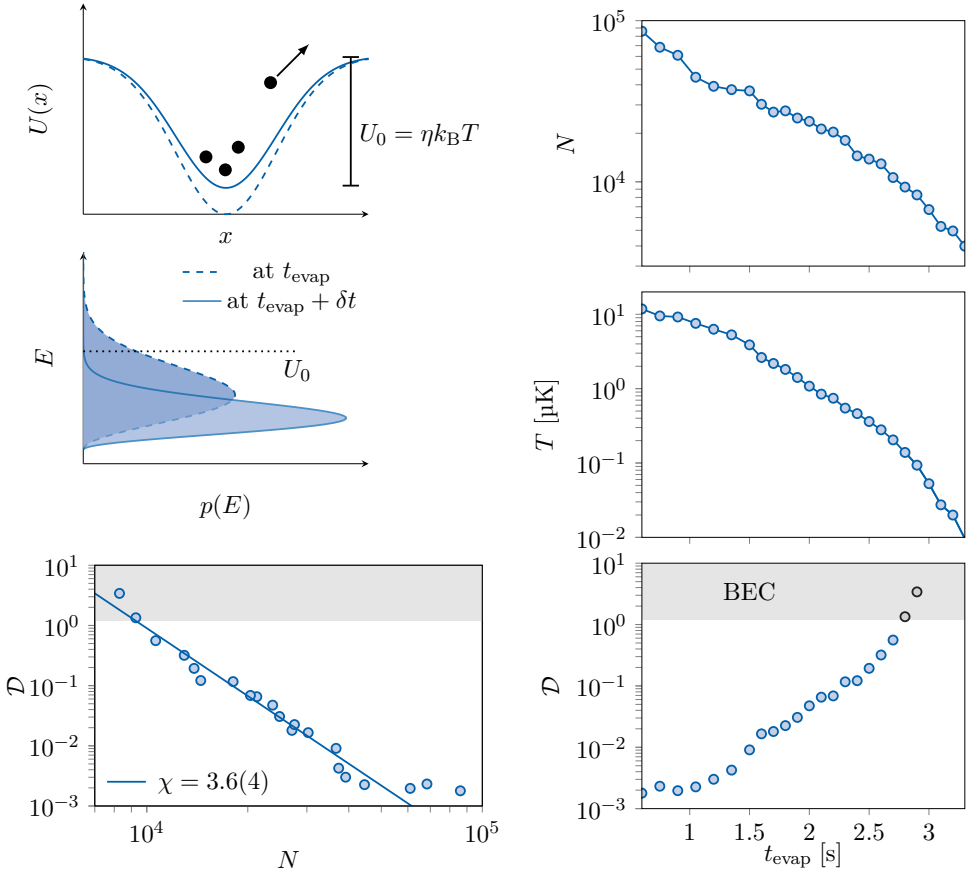

Figure 2.3: Evaporative cooling. *Upper & middle left*: The principle of evaporative cooling, illustrated with a discrete decrease of the trap depth U_0. High energy atoms $E \gtrsim U_0$ can escape from the trap. The remaining atoms rethermalise to a new energy distribution $p(E)$, with a lower energy per particle i.e. a lower temperature. *Right*: The atom number N, temperature T, and phase space density $\mathcal{D}$ during evaporative cooling. The trap depth, not shown here, is ramped down exponentially with time, maintaining $\eta \sim 10$. *Lower left*: The slope of the log-log PSD vs. N plot gives the evaporation efficiency χ. Note that the threshold for condensation is $\mathcal{D} \approx 1.2$.

Ignoring interactions, the critical value for Bose-Einstein condensation is $\mathcal{D} \approx 1.2$. A smooth decrease in U_0 is implemented by exponentially ramping down the cODT powers on the timescale of a few seconds, while roughly maintaining a constant ratio η, and never straying far from thermal equilibrium. It is also important to be left with a detectable number of atoms at the end of the process! In this sense, the efficiency of this cooling process is given by

$$\gamma = -\frac{\mathrm{d}\log\mathcal{D}}{\mathrm{d}\log N}.$$

Another desirable property during evaporation is fast rethermalisation, which is set by the elastic collisional rate

$$\Gamma_{\mathrm{coll}} = \frac{N m \sigma \bar{\omega}^3}{2\pi^2 k_B T}$$

where the collision cross-section is $\sigma = 8\pi a^2$ for bosons at low temperature. In optical traps, the trap opens up over the course of forced evaporation as $\bar{\omega} \propto U_0^{1/2}$. The runaway

Quantity		Typical energy scale $\frac{E}{2\pi\times\hbar}$ [kHz]
Temperature	$k_B T$	10
Trap depth	U_0	100
Trap frequency	$\hbar\bar{\omega}$	0.3
Contact interactions	$\frac{4\pi\hbar^2 a}{m} n$	0.1
Dipolar interactions	$\frac{\mu_0 \mu^2}{8\pi} n$	0.01
Zeeman splitting	$g_J \mu_B B = \hbar\omega_z$	200
Transverse B-field fluctuations	$g_J \mu_B \, \delta B$	0.7
Tensorial light shift coupling	V_0	200
Two-photon recoil	E_{rec}	10

Table 2.2: Relevant experimental energy scales and frequencies. These are evaluated for a cold thermal cloud prepared at the end of evaporative cooling. After turning off the optical dipole traps, this cloud is used as a platform to engineer spin Hamiltonians using spin-dependent light shifts. See text for details and for definitions of the symbols.

regime, where the collisional rate increases with time, cannot be reached with the simple method described here [102] (cf. evaporation with fixed trap frequency in magnetic traps).[1]

Figure 2.3 shows our sample's properties during evaporative cooling. We choose the exponential ramps used to reduce cODT power to optimise phase space density at various intermediate points. The phase space density is calculated from measured atom numbers and temperatures. The temperature is measured using standard time-of-flight expansion. Note that the trap frequencies are calibrated independently by measuring in-trap oscillation frequencies after a quench of ODT power. Throughout this thesis, we will use an ultracold thermal cloud at temperatures of 0.5 µK to 1 µK. The relevant parameters and energy scales for such clouds are summarised in table 2.2.

As indicated in fig. 2.3, our setup is also capable of producing BECs, which were characterised in more detail in ref. [91]. Note that dipolar BECs also pose unique challenges, such as magnetic instabilities, because of the long-range interactions. The work described in this thesis deals with light-induced spin Hamiltonians at the single-atom level. The quantum degeneracy of the gas as a whole does not play a key role. We will return to this topic to give more context at the relevant junctures: we discuss the effect of enhanced inter-atom interaction in the BEC state on the results of chapter 3, give a general perspective on spinor BEC physics with dysprosium at the end of chapter 4, and give an outlook for light-induced artificial gauge fields in our BEC near the end of chapter 5.

[1] Runaway evaporation is possible in optical dipole traps with specialised techniques [103–105].

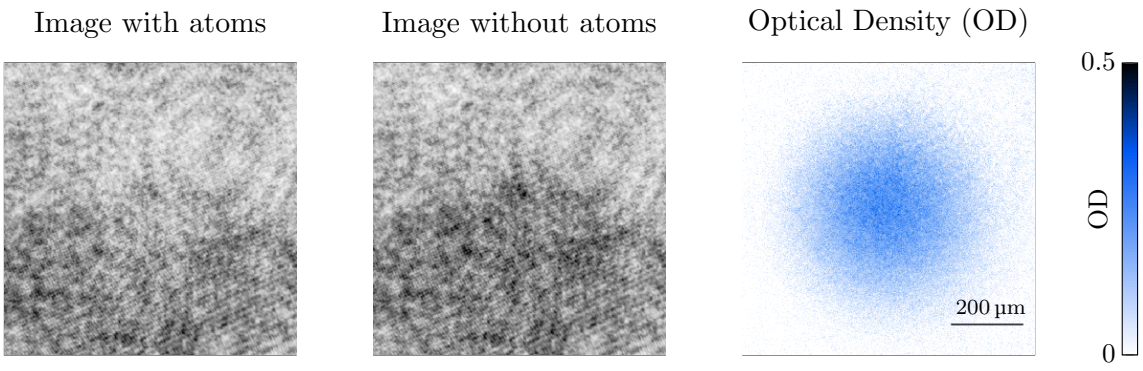

Figure 2.4: Absorption imaging. The density profile of the atomic cloud, integrated along the imaging axis, is proportional to the optical density (OD), as given in eq. (2.2). The OD is calculated as the logarithm of the ratio of the images taken without and with the atoms present in the frame. This example image was taken just after transporting the atomic cloud to the science cell, after a 2.75 ms time-of-flight expansion. In the raw images, darker shades indicate higher intensities.

2.2.4 *Absorption imaging*

We detect the atomic cloud by a standard absorption imaging scheme at the end of every experimental shot. The main imaging axes we use in the science cell are along the two horizontal directions (see fig. 2.2).

Absorption imaging is a destructive measurement process. A collimated beam, resonant with the 421 nm transition, is sent onto the atoms. Following Beer-Lambert's law, the shadow formed due to photon scattering is given by the effective atom-light cross-section σ and the atomic density profile $n(x,y,z)$ integrated along the light propagation axis (say z):

$$I(x,y) = I_0(x,y)\mathrm{e}^{-\sigma\int dz\, n(x,y,z)}$$

The optical system placed after the camera images the atoms onto a digital CCD camera, such that we measure $I(x,y)$ up to imaging efficiencies. A successive image taken after the atoms have fallen out of view measures the reference intensity profile $I_0(x,y)$, such that the integrated density profile can be deduced from the optical density (OD):

$$\mathrm{OD}(x,y) = \log\frac{I_0(x,y)}{I(x,y)} = \sigma\int dz\, n(x,y,z) \tag{2.2}$$

Figure 2.4 shows an example of a measured optical density profile. The typical properties of interest from such an image are the total atom number, the mean in-plane atomic position, the velocity distribution obtained after a long time-of-flight expansion, etc. For a simple two-level system, the resonant cross-section only depends on the wavelength as $\sigma = 3\lambda^2/2\pi$; in our case, the polarisation and spin state of the atomic cloud play a role via Clebsch-Gordan coefficients. Relative cross sections for different $|J,m\rangle$ sublevels can be calibrated by Ramsey interferometry, as we will explain in section 2.3. The absolute atom number will not play a role in the results presented in this thesis.

Nevertheless, we have performed an absolute calibration of the cross section using the critical phase-space density for Bose-Einstein condensation. Finally, certain results need accurate absolute values for atomic displacements, which requires precise calibration of the imaging system's magnification along each axis (at the level of 0.3%). The direction along gravity is simply calibrated using free-fall. For the horizontal direction, we use two-photon Raman transitions, which impart a fixed recoil velocity, to perform the calibration.

2.2.5 *Magnetic field control*

Precise control of magnetic fields in the science cell is essential during the cooling stages as well as for subsequent spin-state manipulation and detection. This is achieved using the following independently controlled coils.

- The static component of the ambient magnetic field, mainly from the Earth's field, is cancelled by three sets of coils in a Helmholtz configuration that encircle the entire experimental table. The produced field is effectively uniform over the entire MOT chamber and science cell setup.

- The shot-to-shot variations of the magnetic field along the vertical axes are reduced by an additional coil controlled by an active compensation system. The primary source of these fluctuations (timescale $\sim 1\,\mathrm{s}$) is the Paris metro line which passes underground in the vicinity of the building. The compensation system reads the z-field value from a probe located near the science cell and generates a corresponding opposing field. This brings down the value of the fluctuations from 2 mG rms to 0.4 mG rms, which is in line with the observed value in the transverse directions, which are unaffected by the metro line.

- The static bias field B we wish to subject the atoms to is generated by another three sets of coils, in this case directly mounted in a cage around the science cell. We precisely calibrate the value of the field using Ramsey interferometry (see section 2.3) and radiofrequency spectroscopy. We usually need a field along the z-axis, although we also use finite transverse tilts of about 5° for certain spin-dependent light shifts, as we shall see later. During Doppler and evaporative cooling stages, the field magnitude is set near 1.4 G, enough for maintaining the spin polarisation in $m = -8$. The gravitational force on the atoms is cancelled by an additional magnetic field gradient. Before applying tensorial light shifts or spin rotations, the bias field is reduced to about 0.1 G and the gravitational compensation is turned off.

- The spin detection protocols explained in the following section use 90° spin rotations. These need to be performed on the microsecond timescale and require a

B-field pulse in a transverse direction. This is produced using coils supplied by a waveform generator + radiofrequency amplifier circuit. The second component for spin detection is a magnetic field gradient. The strong Stern-Gerlach gradient ($\sim 50\,\mathrm{G/cm}$) is produced by a single coil below the science cell, supplied by a circuit designed to produce a large current pulse on a millisecond timescale.

2.3 SPIN STATE DETECTION

In this section, we discuss the conceptual representation and practical detection of states of the ground state electronic angular momentum $J = 8$. Our experiments are carried out in a finite axial field $B_z \sim 100\,\mathrm{mG}$, and hence the eigenstates of J_z, denoted $|J, m\rangle$ (or simply $|m\rangle$), with $-J \leq m \leq J$, form a natural basis (often called the Dicke basis). Remember that the atomic cloud remains polarised in the ground state $|m = -J\rangle$ during evaporative cooling.

A convenient representation of a general state $|\psi\rangle$ within the spin-J manifold is the *Husimi-Q representation*, defined as the overlap with state $|m = J\rangle_{\boldsymbol{n}}$, which is a polarised state along the spatial direction $\boldsymbol{n}$.

$$Q(\boldsymbol{n}) = |\,\langle \psi | J, m = J\rangle_{\boldsymbol{n}}\,|^2 \tag{2.3}$$

This function is usually plotted over a generalised Bloch sphere. We show some examples in fig. 2.5. The state $|m = -8\rangle$ takes the form of a symmetric distribution centred at the south pole, whereas $|m = -4\rangle$ is maximal at the latitude given by the polar angle $\theta = \cos^{-1}(-4/8)$.

We probe spin states by a projective measurement along the z-axis using a Stern-Gerlach technique. A strong magnetic field gradient B' is applied, leading to an m-dependent force $-g_J \mu_B B'\, m$. Each atom is independently projected onto one of the m-states, according to the spin projection probabilities

$$\Pi_m = |\,\langle \psi | J, m\rangle\,|^2 . \tag{2.4}$$

After a time-of-flight expansion long enough to spatially resolve the m-states, we take an absorption image and count the fraction of atoms in each sublevel, leading to a single-shot measurement of the discrete Π_m distribution. See fig. 2.5 for an example of the detection of a state $|m = J\rangle_{\boldsymbol{n}}$ along an equatorial direction. We now have direct access to spin moments such as

$$\langle J_z \rangle = \sum_m m\,\Pi_m \text{ and } \langle J_z^2 \rangle = \sum_m m^2\,\Pi_m .$$

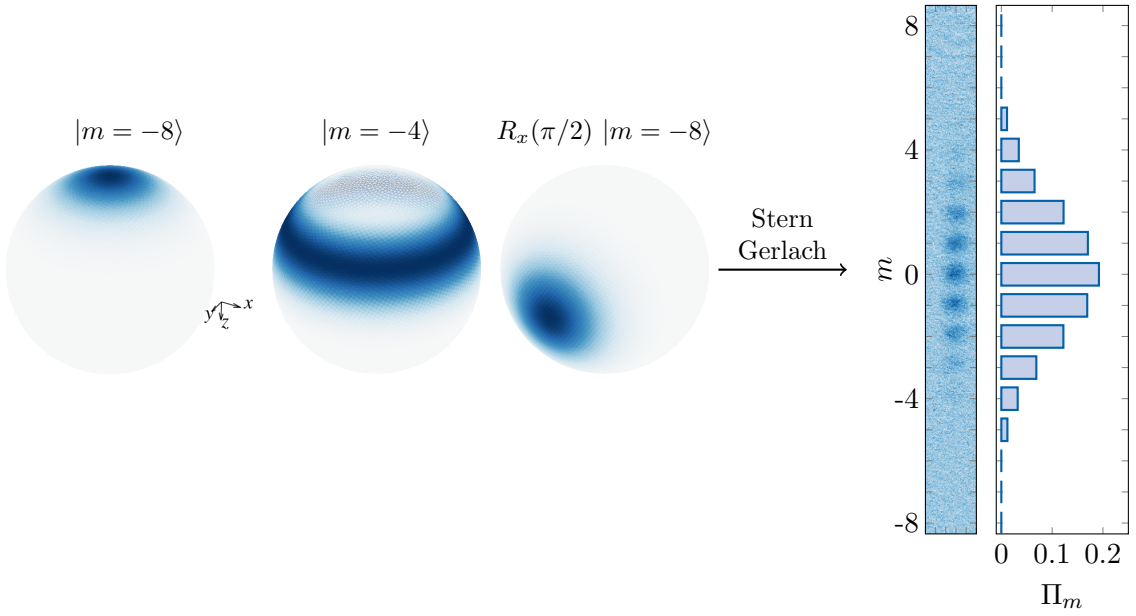

Figure 2.5: Examples of $J = 8$ spin states represented on the Bloch sphere using their Husimi functions. The polarised m-state $|m = -8\rangle$ is a symmetric distribution at the south pole, whereas $|m = -4\rangle$ forms a ring at the latitude given by the polar angle $\theta = \cos^{-1}(-4/8)$. The third state is the state $|m = -8\rangle$ rotated onto the equator – on the right, we show an example of the experimental detection of this state by a projective Stern Gerlach measurement along the z-axis. We show a single shot absorption image, from which we extract the projection probabilities Π_m for each of the $2J + 1$ m-sublevels.

Note that each Π_m is itself effectively a spin moment of order $2J$.[2] As we shall see in the following chapters, this single m-level resolution allows us to probe interesting high-order observables associated with the coherence of the quantum superposition of spin states.

To have complete information on a general spin state $|\psi\rangle$, we need access to the projection probabilities along arbitrary projection axes $\boldsymbol{n}$, denoted $\Pi_m(\boldsymbol{n})$. This requires preceding the above Stern-Gerlach protocol with an operation $\mathcal{R}(\boldsymbol{n})$ that rotates the direction $\boldsymbol{n}$ to the north pole. The first elementary spin rotation at our disposal is an arbitrary azimuthal rotation $R_z(\phi)$, corresponding to a simple waiting period of time $t = \phi/\omega_z$, where $\omega_z = g_J \mu_B B/\hbar$ is the Larmor frequency set by the axial field. The second elementary spin operation we consider is a $\pi/2$ rotation around the y-axis $R_y(\pi/2)$. This is produced by a strong B-field pulse along the y-axis, over a timescale of about 5 µs. In practice, the axial field is not negligible compared the pulse amplitude, such that the '$\pi/2$-pulse' is effectively a composite rotation $R'_y(\pi/2) = R_z(\phi_a)R_y(\pi/2)R_z(\phi_b)$, where

[2] In fact, the projection probability Π_m is the expectation value of the following operator, which is of order $2J$ in J_z:

$$\prod_{m' \neq m} \frac{J_z - m'}{m - m'} .$$

We cannot directly implement such operators with the techniques discussed in this chapter, but the Stern-Gerlach detection scheme gives us access to Π_m.

$\phi_{a,b}$ are constants that we calibrate independently. These two spin operations can be combined as follows to perform the general rotation we need

$$\mathcal{R}(\boldsymbol{n}) = R'_y(\pi/2)R_z(\phi_2)R'_y(\pi/2)R_z(\phi_1)\,,$$

where $\phi_{1,2}$ depend on the spherical angles θ, ϕ along the projection axes $\boldsymbol{n}$ as

$$\theta = \phi_2 + \pi + \phi_a + \phi_b \text{ and } \phi = -(\phi_1 + \pi/2 + \phi_b)$$

Ramsey interferometry

We now present a Ramsey interferometry experiment as a simple illustration of the spin detection and rotation techniques explained above. Starting in the ground level $|m = -8\rangle$, we apply a sequence of rotations $R'_y(\pi/2)R_z(\phi)R'_y(\pi/2)$. We measure the projection probabilities Π_m as a function of the rotation angle ϕ, as shown in fig. 2.6. Note that each slice at a given waiting time t corresponds to a measured probability distribution Π_m, averaged over a handful of realisations. This type of presentation of data will reappear extensively throughout this thesis. As for the familiar Ramsey experiment in a two-level system, we see that the final state varies smoothly from the south ($\Pi_{-8} \sim 1$) to the north pole ($\Pi_8 \sim 1$) on the Bloch sphere. The frequency of this oscillation is simply the Larmor frequency ω_z, thus providing a convenient calibration of the total magnetic field. The coherence time of this oscillation is limited by magnetic field fluctuations and is typically around 200 µs. A posteriori rescaling of the acquired phase ϕ for each data point, using the field fluctuations recorded independently on a magnetic field probe near the science cell, can increase the effective coherence time by a factor of 1.5.

We can also use this experiment to calibrate the relative m-dependent imaging efficiencies. These arise from the optical cross-section for each m-state with respect to the $J' = 9$ excited level addressed by our imaging beam at 421 nm. This depends on Clebsch-Gordan coefficients and the chosen polarisation for the imaging beams. In short, we use the assumption that the total atom number is independent of ϕ, and rescale the raw Π_m values to reflect this. The rescaling coefficients can then be applied to any spin measurements taken with the same imaging setup (see refs. [89, 91] for more details). Starting in $|-8\rangle$ and using only spin rotations, our experiments would be limited to the family of maximally polarised states $|m = J\rangle_{\boldsymbol{n}}$. Leaving this manifold of states requires creating non-linear spin couplings, which we achieve with spin-dependent light shifts.

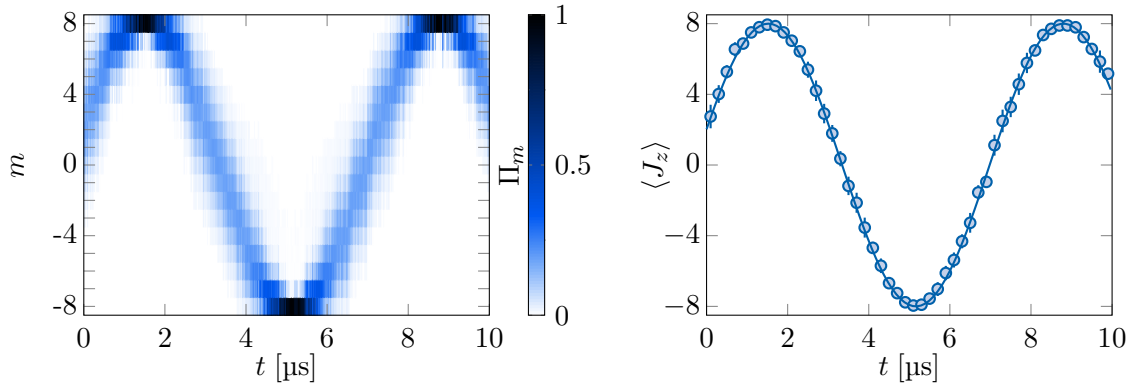

Figure 2.6: Ramsey interferometry Left: Spin projection probabilities Π_m measured during a Ramsey experiment. Starting with all atoms polarised in $|J, m = -8\rangle$, we perform a $\pi/2$-pulse, wait for duration t, and then perform a second $\pi/2$-pulse. The state is not exactly $|m = 8\rangle$ at $t = 0$ because our $\pi/2$-pulses are not perfect – they include azimuthal rotations (see text). Right: The frequency of the oscillation of the average magnetisation $\langle J_z \rangle = \sum_m m\,\Pi_m$ gives the Larmor frequency $\omega_z = 2\pi \times 137.7(4)$ kHz, corresponding to an axial magnetic field $B = 79.3(2)$ mG.

2.4 SPIN-DEPENDENT LIGHT SHIFTS

2.4.1 *Basic theory*

We first consider a two-level atom in the presence of a laser light field at frequency ω:

$$\boldsymbol{E} = \frac{1}{2} E \mathrm{e}^{-\mathrm{i}\omega t}\, \boldsymbol{\epsilon} + \text{c.c.}$$

Here, $\boldsymbol{\epsilon}$ is a complex polarisation vector, and E is the magnitude of the electric field related to the light intensity via $I = \epsilon_0 c E^2/2$. At lowest order, the atom-light interaction hamiltonian V is given by the electric dipole term

$$V = -\boldsymbol{d} \cdot \boldsymbol{E}$$

where $\boldsymbol{d}$ is the electric dipole operator. A resonant frequency ω_0 is associated with optical transition ground level $|g\rangle$ and excited level $|e\rangle$. We work far from the resonance in a dressed state formalism, such that V describes an energy displacement or *light shift* of the ground state. Using second-order perturbation theory, and hereafter using the rotating wave approximation (RWA), to discard a term at $\mathrm{O}(\omega + \omega_0)^{-1}$, we get

$$V = \frac{1}{4} |E|^2 |\, \langle e | \boldsymbol{d} \cdot \boldsymbol{\epsilon} | g \rangle \,|^2 \frac{1}{\Delta + \mathrm{i}\Gamma/2},$$

where we have introduced the detuning $\Delta = \omega - \omega_0$ and the linewidth of the excited level, Γ.

The real and imaginary parts of the above expression have distinct physical consequences. Consider the dependence on the laser frequency ω: the imaginary part has

a Lorentzian shape centred at the resonance $\Delta = 0$. It represents the rate of incoherent scattering of photons

$$\Gamma_{\text{scatt}} = \text{Im}\,[\alpha(\omega)]\frac{E^2}{2\hbar}\,.$$

The frequency dependence of V is represented by a quantity called the *polarisability*, denoted α. In contrast, the real part represents a conservative light potential, with negative (resp. positive) energy shifts for red (resp. blue) detuning. which is defined by the familiar expression

$$V = -\text{Re}\,[\alpha(\omega)]\frac{E^2}{4} = -\text{Re}\,[\alpha(\omega)]\frac{I}{2\epsilon_0 c} \tag{2.5}$$

Hence, a spatially varying laser field $I(r)$ generates a corresponding potential landscape $V(r)$ – this is the principle of optical dipole traps, as introduced in section 2.1.1.

2.4.2 *Tensor polarisability*

The simple treatment presented above is not sufficient in case the ground and excited optical levels themselves have an internal structure. In this case, the polarisability is, in general, a tensor: in addition to a simple global shift of the ground state, proportional to the laser intensity, the atom-light interaction also couples states within the ground manifold. In this section, we state certain key results and explain the practical consequences for our subsequent experiments – more detailed explanations can be found in refs. [106, 107]. We give results for a ground manifold of total electronic spin J, with no hyperfine structure. The total light shift operator V then acts on a Hilbert space of dimension $2J+1$, spanned by the states $|J, m\rangle$. The light shift can be decomposed into scalar, vector and tensor components:

$$\begin{aligned} V &= -\frac{E^2}{4}(\mathcal{V}_s + \mathcal{V}_v + \mathcal{V}_t) \\ \mathcal{V}_s &= \alpha_s\,\mathbb{I} && (2.6) \\ \mathcal{V}_v &= -\mathrm{i}\alpha_v\,\frac{(\boldsymbol{\epsilon}^* \times \boldsymbol{\epsilon})\cdot \boldsymbol{J}}{2J} && (2.7) \\ \mathcal{V}_t &= \alpha_t\,\frac{3[(\boldsymbol{\epsilon}^*\cdot\boldsymbol{J})(\boldsymbol{\epsilon}\cdot\boldsymbol{J}) + (\boldsymbol{\epsilon}\cdot\boldsymbol{J})(\boldsymbol{\epsilon}^*\cdot\boldsymbol{J})] - 2\boldsymbol{J}^2}{2J(2J-1)} && (2.8) \end{aligned}$$

Note that $\boldsymbol{J}$ is a vector whose components are the spin operators J_i, such that the inner product with a polarisation vector is given by $\boldsymbol{\epsilon}\cdot\boldsymbol{J} = \epsilon_x J_x + \epsilon_y J_y + \epsilon_z J_z$. We see that the scalar term corresponds to the simple light shift from the previous section, whereas the vector and tensor terms produce spin-dependent Hamiltonians of the type J_i and $J_i J_j$ respectively.

The frequency-dependent polarisability components are determined by the strength of the coupling to the excited level manifold J'. They are given by:

$$\begin{aligned}\alpha_s &= \sqrt{\frac{1}{3(2J+1)}}\mathcal{A}^{(0)} \\ \alpha_v &= -\sqrt{\frac{2J}{(J+1)(2J+1)}}\mathcal{A}^{(1)} \\ \alpha_t &= -\sqrt{\frac{2J(2J-1)}{3(2J+1)(2J+3)}}\mathcal{A}^{(2)},\end{aligned}$$

where the frequency dependence is encoded in the coefficients $\mathcal{A}^{(K)}$, given by:

$$\begin{aligned}\mathcal{A}^{(K)} = 3\pi\epsilon_0 c^3 \frac{\Gamma}{\omega_0^3}\mathrm{Re}\left[\frac{1}{\omega_0-\omega+\mathrm{i}\Gamma/2}+\frac{(-1)^K}{\omega_0+\omega+\mathrm{i}\Gamma/2}\right] \\ \times(-1)^{J+J'+K+1}(2J'+1)\sqrt{2K+1}\begin{Bmatrix}1 & K & 1\\ J & J' & J\end{Bmatrix}.\end{aligned} \tag{2.9}$$

Here, the curly braces denote the Wigner-6j symbol, and Γ refers to the linewidth of the single excited level J' for which this formula applies. Note that the prefactor in the above expression can be written as

$$\frac{3\pi\epsilon_0 c^3\Gamma}{\omega_0^3} = \frac{d^2}{\hbar} = \frac{4\hbar\Omega_R^2}{E^2}, \tag{2.10}$$

where d is the reduced dipole matrix element $|\langle J||\boldsymbol{d}||J'\rangle|$ and Ω_R is the Rabi frequency.

To get the total values of the polarisability components $(\alpha_s, \alpha_v, \alpha_t)$ at a given frequency, we must use the above results and sum the contributions from all the excited levels. Figure 2.7 shows the values of the three components over a wide range of wavelengths. For our dipole traps at 1064 nm, there are no transitions nearby – in this case, the main contribution is from the blue transitions near 400 nm, leading to a dominant 'background' scalar polarisability of $\alpha_s \simeq 184\,\alpha_0$ [108, 109].[3] The vector and tensor terms are two orders of magnitude smaller. Note that the imaginary components of polarisability (obtained by instead taking the imaginary part of the complex term in eq. (2.9)) are a further five orders of magnitude smaller [110].

In practice, we are most interested in the spin-dependent light shifts at a frequency where a single transition dominates and in the regime where $\Gamma \ll \Delta \ll \omega_0$. Then, the above formulae for the light shift operator can be condensed into a friendlier form:

[3] Remember that in Hartee atomic units, the unit of polarisability is $\alpha_0 = E_h/(ea_0) = 4\pi\epsilon_0 a_0^3$.

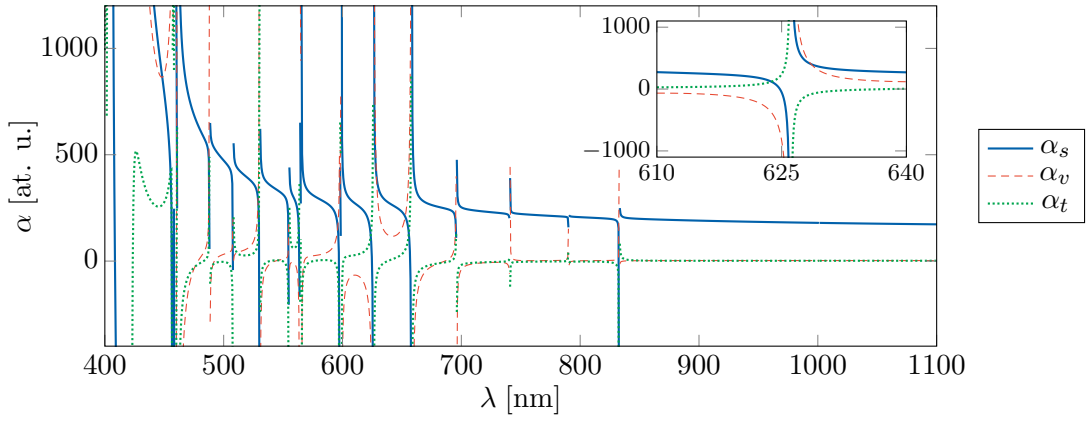

Figure 2.7: The scalar, vector and tensor polarisabilities as a function of wavelength. The inset shows a zoomed view around the 626 nm transition. The calculations are performed using a limited set of transitions [111], with the additional inclusion of transitions accessible by our Ti-Sapph laser in the range 695–1005 nm.

J'	α_0 (scalar)	α_1 (vector)	α_2 (tensor)
$J-1$	$5/17$	$-15/17$	$-5/17$
J	$1/3$	$-1/9$	$5/9$
$J+1$	$19/51$	$152/153$	$-40/153$

Table 2.3: Dimensionless coefficients for light shift calculations, given here for $J = 8$ (see text for details).

$$V = V_0 \left(\alpha_0 \mathbb{I} - i\alpha_1 \frac{(\boldsymbol{\epsilon}^* \times \boldsymbol{\epsilon}) \cdot \boldsymbol{J}}{2J} + \alpha_2 \frac{3[(\boldsymbol{\epsilon}^* \cdot \boldsymbol{J})(\boldsymbol{\epsilon} \cdot \boldsymbol{J}) + (\boldsymbol{\epsilon} \cdot \boldsymbol{J})(\boldsymbol{\epsilon}^* \cdot \boldsymbol{J})] - 2\boldsymbol{J}^2}{2J(2J-1)} \right) \tag{2.11}$$

$$\text{with } V_0 = \frac{3\pi c^2 \Gamma}{2\omega_0^3} \frac{I}{\Delta}. \tag{2.12}$$

The values of the dimensionless coefficients α_i depend on the excited level electronic spin J', and they are listed in table 2.3. Note that these coefficients are of the same order of magnitude for the scalar, vector, and tensor terms. The background effect of all other transitions appears mainly as a scalar polarisability, which does not play a role in the spin Hamiltonians that we realise.

The general idea will be to choose a detuning to the target transition of $\Delta \sim 10^5\,\Gamma$. This allows us to reach atom-light couplings in the range $V \sim h \times 0.1\,\text{GHz}$ to 1 GHz for reasonable laser intensities with negligible photon scattering. In the following chapters, we will use laser beams close to narrow-line transitions to create tensor light shifts and hence manipulate the atomic spin state. We now aim to illustrate the physical consequences of eq. (2.11) with some examples that are directly applicable to our experimental protocols.

2.4.3 *Examples*

Example I: $J' = 9$ transition at 626 nm
Consider a beam blue-detuned beam near this transition ($\Gamma = 2\pi \times 135\,\text{kHz}$) and linearly polarised along x i.e. $\boldsymbol{\epsilon} = \hat{\boldsymbol{x}}$. The scalar polarisability creates a repulsive potential. The beam is focussed on the atoms, with a waist ($\sim 50\,\mu\text{m}$) much larger than the spatial extent of the cloud ($\sim 5\,\mu\text{m}$). In addition, the experimental timescales are much shorter than the oscillation period in this trap. So we can consider a uniform, static light field over the atomic cloud. The vector light shift vanishes since the cross product $\boldsymbol{\epsilon}^* \times \boldsymbol{\epsilon}$ in eq. (2.11) is zero. Hence, only the tensor term is relevant for light-induced spin dynamics. Since $\boldsymbol{J} \cdot \boldsymbol{\epsilon} = J_x$ in eq. (2.11), the tensor light shift is proportional to J_x^2 (up to an additive constant). Rearranging the prefactors in the tensor term, we can write the spin Hamiltonian in the simple form

$$H = V_0 \frac{-J_x^2}{(J+1)(2J+1)} \tag{2.13}$$

Such a spin coupling will be used to implement the LMG model in chapter 3, and to prepare non-classical states via one-axis twisting dynamics in chapter 4 (albeit with a different optical transition in the latter case).

Example II: $J' = 7$ transition at 696 nm
We now consider a beam blue-detuned to this narrow transition ($\Gamma = 2\pi \times 15\,\text{kHz}$), with a σ_- circular polarisation i.e. $\boldsymbol{\epsilon} = (\hat{\boldsymbol{x}} - \mathrm{i}\hat{\boldsymbol{y}})/\sqrt{2}$. This time, the vector term contributes a term proportional to J_z, since $\boldsymbol{\epsilon}^* \times \boldsymbol{\epsilon} = \hat{\boldsymbol{z}}$. The tensor term is proportional to J_z^2 (up to an additive constant), since

$$(\boldsymbol{\epsilon}^* \cdot J)(\boldsymbol{\epsilon} \cdot J) = (J_x + \mathrm{i}J_y)(J_x - \mathrm{i}J_y) = -J_z^2 + \text{const.}$$

Again, the spin Hamiltonian takes a simple form

$$H = V_0 \frac{(J_z + J)(J_z + J - 1)}{2J(2J-1)}$$

Note that, in contrast to the previous example, this spin Hamiltonian commutes with J_z and hence will not induce spin dynamics for an atom initially in the state $|m = -8\rangle$. Additionally, we have not dropped any additive constants in this formula, such that the light shifts from this transition indeed vanish when $\langle H \rangle = 0$ – we will return to this point shortly. The results presented in this section so far are in fact valid to lowest order in the ratio Ω_R/Δ, where Ω_R is the Rabi frequency defined in eq. (2.10). Higher order terms must be determined as follows. We work in a basis diagonal with respect to the light shift operator – here, it is simply the eigenstates of J_z i.e. the states $|m\rangle$. Using eq. (2.11) (and ignoring the factor V_0), we can calculate a dimensionless light shift matrix element

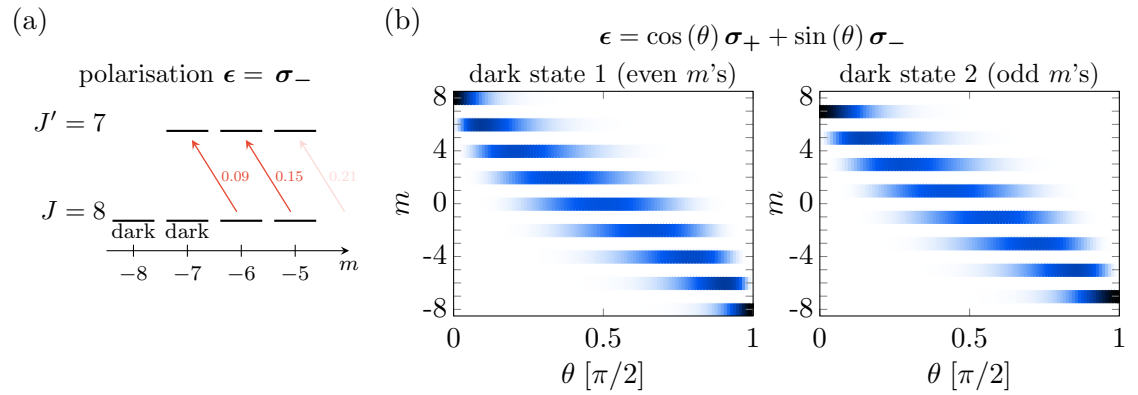

Figure 2.8: Dark states for a transition to an excited level $J' = 7$ from the ground level $J = 8$. (a) An example for circularly polarised light $\epsilon = \sigma_-$. The states $m = -7$ and -8 in the ground manifold are not coupled to the excited level i.e. they are dark. In red, we show the (approximate) Clebsch-Gordan coefficients for some other m-states. (b) More generally, the pair of dark states vary with the polarisation. Here, we show the dark states' spin projection probabilities as the polarisation is smoothly varied from σ_+ to σ_- as a function of the parameter θ. The dark states form the null space of the light-atom coupling operator for this transition; we choose to plot them in a basis decomposed on even and odd m-sublevels.

Q_m for each of these states. We now assign each state its own effective Rabi coupling $\Omega_{R,m} = \sqrt{Q_m}\Omega_R$. Then, the diagonal elements of the light shift operator are given by

$$V_m = \hbar\left(\sqrt{\left(\Omega_{R,m}^2 + \frac{\Delta^2}{4}\right)} - \frac{\Delta}{2}\right). \tag{2.14}$$

It is simple to check that we recover the previous expressions when $\Delta \gg \Omega_R$, which gives $V_m \simeq \hbar\Omega_R^2/\Delta \times Q_m$. The Q_m factors will play an important role in chapter 4, where we interpret them in terms of the state of the encoded qubits.

2.4.4 *Dark states*

Dark states are defined as those having a vanishing expectation value with respect to the atom-light interaction Hamiltonian V. Here, we consider them for a single optical transition. First, consider the case of an excited level $J' = J - 1$: stepping out of the dressed-state picture for a moment, we see that V couples a Hilbert space of dimension $2J + 1 = 17$ to one with dimension $2J' + 1 = 15$. So there must be a two-dimensional dark subspace in the ground manifold.[4] For the case of circular polarisation σ_-, it is clear that the dark states must be $m = -7$ and -8, as illustrated in fig. 2.8a. In general, these states vary smoothly with the laser polarisation, as we show fig. 2.8b. Continuing this reasoning, there are no dark states for excited levels with $J' = J + 1$. The case $J' = J$ is ambiguous – in our case (and generally for whole number values of J), the

[4] This follows from the rank-nullity theorem in linear algebra.

properties of the Clebsch-Gordan coefficients ensure that one dark state exists for any polarisation [112].

The inherent protection of dark states from decoherence by spontaneous emission has led to applications in subrecoil laser cooling [112], electromagnetically induced transparency [113], and stimulated Raman adiabatic passage [114]. Recently, their potential for realising long-lived many-body topological states has also generated significant interest [115]. We will discuss such a possibility for our experimental setup in chapter 5. Below, in section 2.4.6, we use a dark state to precisely calibrate the polarisation of a laser beam used to generate light shifts. Dark states will also play an important conceptual role in our results in chapter 4.

2.4.5 *Comparision to alkali atoms*

We conclude the theoretical discussion of light shifts by comparing dysprosium to alkali elements, which are not well-suited for creating the spin Hamiltonians described here. For alkalis, the picture of a single, isolated transition considered above is complicated by relatively narrowly split fine and hyperfine structure terms, leading to unfavourable scaling of the strength of the vector and tensor light shift terms relative to the photon scattering rate [116]. This advantage of lanthanide atoms also carries forward to the Raman coupling scheme we use to produce synthetic gauge fields. Another key advantage, resulting from the complex electronic structure, is the presence of narrow-line transitions at energies far from the dominant blue transitions (cf. the lack of such transitions away from the D1-D2 manifold of alkalis). This allows for strong couplings without heating, an important factor for the creation of levels well-separated compared to thermal and interaction energy scales, e.g. for topological Bloch bands [117].

2.4.6 *Experimental implementation*

We now describe the laser and optical setups for the creation of spin-dependent light shifts. We will mainly discuss a tunable Titanium:Sapphire (Ti-Sapph) laser system which was implemented for this purpose during the course of this thesis. We use a commercial Ti-Sapph laser[5] consisting of a 15 W pump laser at 532 nm, followed by a laser cavity containing the Ti-Sapph crystal, and a remotely controlled birefringent filter for wavelength tuning over a range from 695 nm to 1005 nm. The nominal laser power varies over 2–5 W within this range.

There are several transitions accessible using this laser system, which are shown in fig. 2.9. The transition at 741 nm has already been studied by the Stanford group and used for a narrow-line MOT [30, 99]. The transition at 1001 nm has been measured to have a ultra-narrow width at the level of a Hertz [118]. The other accessible transitions

[5] M Squared SolsTiS

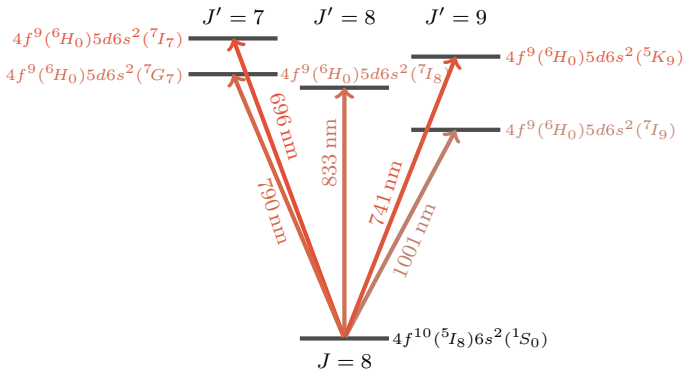

Figure 2.9: Optical transitions accessible using the Ti-Sapph laser.

have kHz-level linewidths. We will mainly use the 696 nm line here and in chapter 4; we also mention some results with the 833 nm line towards the end of this section.

The optical path for the Ti-Sapph laser beam is as follows: at the laser output, a small amount of light is sent to a wavelength meter, while the rest can be divided between two equivalent optical paths, each with an AOM (for power control), and coupled to an optical fibre going to a second setup nearer the science cell. The two paths are set up for easy switching between a pair of wavelengths, which could, in the future, be aligned along different optical paths towards the atoms; here, we will only consider a single final path arriving at the atoms from the $+z$ direction, which is shown in fig. 2.2.[6] The optical elements placed just before the science cell are indicated in fig. 2.10. The beam is focussed onto the atomic cloud with a waist of about 50 µm. The elements for precise control of the polarisation are explained in detail below.

We also briefly mention the separate laser system for light shifts at 626 nm, which is outside the range of the Ti-Sapph. This homemade laser is identical to the main red laser used for the MOT (but it does not require a frequency lock due to the large detuning used). As shown in fig. 2.2, this system produces two counter-propagating beams along the $\pm y$ directions, with similar beam characteristics as those for the Ti-Sapph. While only one beam is needed to produce a simple quadratic light shift (chapter 3), both are used when engineering two-photon couplings between m-sublevels (chapter 5).

Polarisation control

Example I: Linear polarisation

The precise control of polarisation is crucial for the spin-dependent Hamiltonians we wish to implement. Consider the example we introduced in the previous section: a Hamiltonian $H = V_0 J_x^2$ produced by the linearly polarised 626 nm beam $\epsilon = \hat{x}$ propagating along the y-axis. A key feature of the dynamics induced by this Hamiltonian, starting in the

[6] In fact, the beam is aligned with a tilt of 5° with respect to the z-axis to prevent alignment of retroreflection from the walls of the glass cell on the atomic cloud; our glass cell has no anti-reflection coating. The magnetic field is also tilted in the same manner, such that the quantisation axis is still along the incident beam.

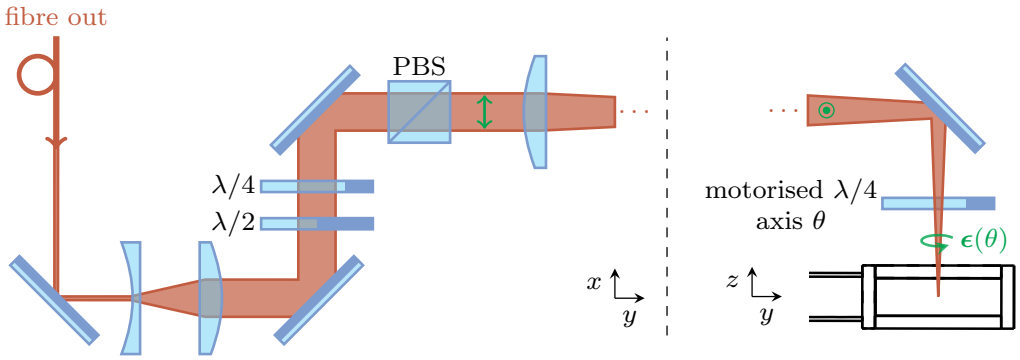

Figure 2.10: Optical path of the Ti-Sapph laser beam onto the atoms. A polarising beam splitter (PBS) placed before the final focussing lens ensures that the polarisation is linear and parallel to the surface of the last out-of-plane mirror. This guarantees that the polarisation is unchanged until the final motorised quarter-wave plate. The adjustable orientation θ of the waveplate's fast-axis creates a polarisation vector $\boldsymbol{\epsilon}(\theta)$, and hence a light shift $V(\boldsymbol{\epsilon})$ on the atomic cloud, located at the focus in the science cell. The polarisation is precisely and smoothly tunable between circular σ_-, linear along x, and circular σ_+.

state $|m-8\rangle$, is the fact that only even-m states are populated.[7] If a small component of circular polarisation is introduced, it creates a vector lightshift proportional to J_y, which couples even- and odd-m states. To achieve a clean linear polarisation, we place a polarising beam splitter (PBS) just after the final focussing lens, before the beam enters the glass cell. We expect small imperfections from at least four sources: the convergence of beam through the PBS, the finite extinction ratio of the PBS ($\sim$ 1000 : 1 for transmission), any shift in polarisation induced by the quartz walls of cell itself, and optical defects like astigmatism. We find that these effects are negligible in the spin dynamics we observe, where the dominant source of defects are Zeeman couplings from transverse magnetic field fluctuations, which also introduce terms proportional to J_y (and indeed also J_x).

Example II: Tunable circular polarisation

This case is more involved – we implement a circular polarisation smoothly tunable (e.g. on consecutive experimental shots) between σ_- and σ_+ for the vertical 696 nm Ti-Sapph beam. As explained at the end of section 2.4.2, σ_- light leads to a lightshift proportional to $(J_z+8)(J_z+7)$. Crucially, this cancels exactly for the dark ground states $|m=-7\rangle$ and $|m=-8\rangle$. This property will play a key role in chapter 4. The polarisation vector is parametrised by an angle θ

$$\boldsymbol{\epsilon} = \left(\cos^2\Theta + \mathrm{i}\sin^2\Theta\right)\hat{\boldsymbol{x}} + \sin\Theta\cos\Theta(\mathrm{i}-1)\hat{\boldsymbol{y}}\,, \text{ where } \Theta = \theta + \pi/4\,. \tag{2.15}$$

The pair of polarisation dependent dark states vary smoothly with θ, reaching $m = 7, 8$ for σ_+ polarised light (at $\theta = 0$).[8] The polarisation state given in the equation above is

[7] This corresponds to the conservation of the parity $\langle P_z\rangle$, which will be introduced in chapter 3.

[8] The intermediate case $\theta = \pi/4$ gives linear polarisation along x, with the pair of dark states being $|m=\pm 8\rangle_{\hat{\boldsymbol{x}}}$.

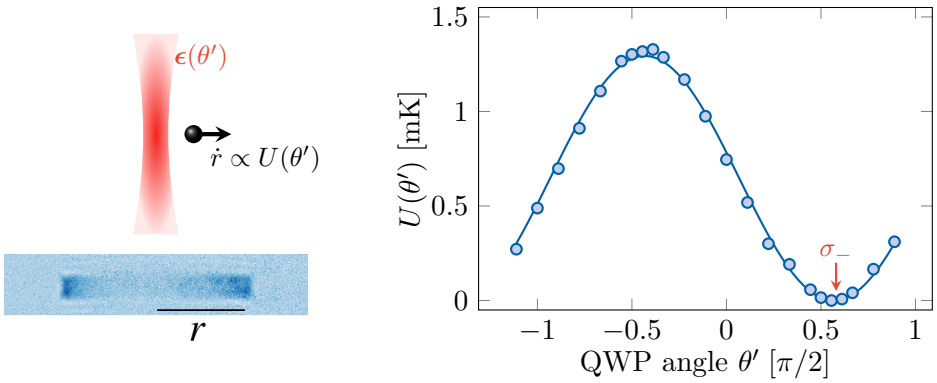

Figure 2.11: Calibration of tunable circular polarisation at wavelength $\lambda = 696\,\text{nm}$. Top left: Measurement protocol. A linearly polarised blue-detuned vertical laser beam is sent through a quarter-waveplate oriented at an angle θ' and acquires a polarisation state ϵ. The beam is then focussed onto the atomic cloud (internal state $m = -8$). The atoms are repelled, and far from the laser they acquire a constant velocity $\dot{r}$, such that the kinetic energy $m\dot{r}^2/2$ gives the polarisation-dependent potential energy at the focus, denoted $U(\theta')$. Bottom left: We image the 'exploded' cloud in the horizontal plane, and extract a radius r from the integrated disk profile. This is repeated for several expansion times to extract the velocity. Right: The measured trap depths (discs) and the fitted variation with respect to the waveplate orientation (solid curve). The fitting parameters are a global factor to account for the laser intensity and the offset of θ' from the angle θ defined in eq. (2.15). The point of vanishing tensorial light shift ($\theta = 0$) corresponds to a circular polarisation σ_-. Note that although the light shift from the $\lambda = 696\,\text{nm}$ transition vanishes at $\theta = 0$, the background polarisability creates an attractive potential, which we do not resolve on the energy scale of this measurement.

created when linearly polarised light along x is incident on a quarter-wave plate (QWP) whose fast axis is oriented at $\Theta = \theta + \pi/4$ with respect to the incident electric field. This is the situation we implement on our setup, where the last optical elements on the beam path are a PBS followed by a QWP, as shown in fig. 2.10. The QWP is mounted on a remotely controlled motorised rotating mount[9], allowing for precise shot-to-shot tuning of the polarisation. As shown in fig. 2.11, the polarisation is calibrated by measuring the repulsive potential felt by the $m = -8$ state as a function of the QWP orientation – the minima corresponding to σ_- polarised light. We also verify that the spin state does not evolve for circular polarisation. The purity of the σ_- polarisation we prepare will be validated more quantitatively in chapter 4 by our direct measurements of the lightshifts of the $m = -8, -7$ states, which are consistent with zero at a precision of one part in 10^4.

We also conducted tests on polarisation-dependent dark states for the $J' = 8$ transition at 833 nm. Here, there is only a single dark state instead of the degenerate pair we have for the $J' = 7$ transition. For a linear-x polarisation, the dark state is $|m = 0\rangle_{n=\hat{x}}$. In our preliminary investigations, we aimed to adiabatically prepare this state by starting in our usual ground state $|m = -8\rangle$ and ramping up the laser power, with promising initial results.

[9] Newport 8410 closed loop Picomotor piezo rotation mount

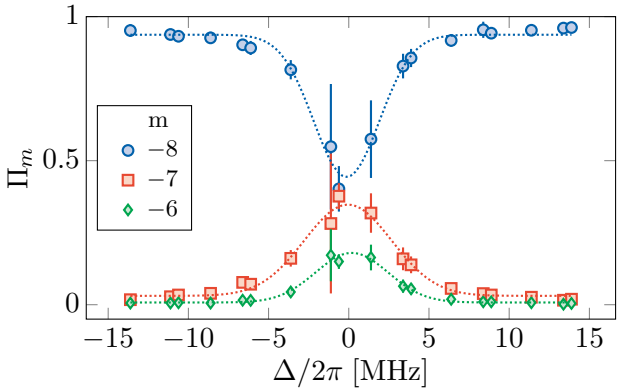

Figure 2.12: Precise frequency control of the Ti-Sapph laser near the $\lambda = 696\,\text{nm}$ transition. We induce weak spin dynamics using a pulse of fixed duration and intensity (see text), and measure the resulting spin projection probabilities Π_m as a function of the detuning Δ. The detuning is scanned by varying the lock setpoint. The absolute resonant frequency measured is $\omega_0 = 2\pi \times 430.735\,818\,\text{THz}$ and the fitted width, limited by the resolution of wavelength meter, is $2\pi \times 2.3\,\text{MHz}$.

Detuning control

The frequency of the Ti-Sapph laser is monitored with a commercial wavelength-meter[10]. For tensor light shifts at 696 nm realised in this thesis, we typically use detunings of 0.1 GHz to 10 GHz. To stabilise against frequency drifts on the timescale of seconds, we lock the laser directly to the interferometer of the wavelength meter, where the correction is fed back to a laser cavity mirror piezo. A good test of this lock is the determination of the location of the resonance. We pulse x-linear polarised light on the atomic cloud in $m = -8$, inducing spin dynamics. We choose a very low intensity, such that the $m = -7, -6$ states are perturbatively populated, resulting in the resonance feature shown in fig. 2.12. The frequency lock is stable enough to resolve the resonance down to a width of 2 MHz; we also observe long-term drifts on the order of a few megahertz per day. We conclude by noting that the polarisation and detuning control could also be used in studies exploiting polarisation-dependent tune-out wavelengths (where the total light shift, summing contributions from all transitions, vanishes) or polarisation-dependent magic wavelengths (where the ground and excited state polarisabilities are equal).

2.5 SUMMARY

We have now introduced all the ingredients needed to understand our experiment as a simulator of light-induced spin-dependent Hamiltonians. We again draw the reader's attention to the energy scales listed in table 2.2. We see that thermodynamic and many-body effects play a secondary or negligible role to the energy scale of tensorial lightshifts and the Zeeman splitting (each around $h \times 200\,\text{kHz}$). These terms will form the basis of

[10] Highfinesse WS6-200

the Ising-like spin model studied in chapter 3, and will be used to generate non-classical spin states in chapter 4. Finally, we will use a pair of Raman laser beams in chapter 5, which in addition to creating spin-dependent light shifts, resonantly couple neighbouring m-sublevels, which naturally introduces the two-photon recoil as a relevant energy scale for the atoms' motion. Throughout, we can understand the physics in terms of the spin and motional states at the single-atom level, and consider the atomic ensemble as a convenient averaging mechanism. Deviations from this picture will be addressed as needed, both to clarify the interpretation of our results, and where they provide interesting future avenues for many-body studies. These future projects will need to be complemented by technical developments, which are currently in various stages of planning: the group plans to characterise spin-dependent contact interactions, install a microscope objective to image many-body ground states in artificial gauge fields, and install magnetic shielding to allow experiments at low fields, where interaction effects are dominant.

3

CRITICAL BEHAVIOUR AND SYMMETRY BREAKING IN THE LMG MODEL

> Waiter, bring me a cup of coffee
> without cream. ...
> I'm sorry, sir, we have no cream,
> can it be without milk?
>
> Ernst Lubitsch, *Ninotchka*

In this chapter, I describe an experimental study of the Lipkin-Meshkov-Glick model (LMGm) of quantum spin 1/2s with infinite-range interactions in a transverse magnetic field. This model exhibits a continuous paramagnetic to ferromagnetic phase transition in the thermodynamic limit.

The work presented in this chapter has been published in the following article [119]:
Probing quantum criticality and symmetry breaking at the microscopic level
V. Makhalov*, T. Satoor*, A. Evrard, T. Chalopin, R. Lopes, S. Nascimbene
Physical Review Letters 123 (12), 120601 (2019)
* These authors contributed equally

This chapter is structured as follows: I begin by introducing basic concepts relating to quantum phase transitions in section 3.1, using the transverse-field Ising model. This is followed by a description of the LMG model in section 3.2, and a discussion on quantum critical behaviour in section 3.3. Section 3.4 explains the formalism by which our system realises the LMGm, while section 3.5 explains its experimental implementation. Our measurements of ground state properties are presented in section 3.6, which also includes theoretical treatments of the LMGm via the mean-field approach and an expansion around the critical point. We investigate excitations in the LMGm in section 3.7, followed by a study of symmetry breaking in section 3.8. Finally, section 3.9 discusses perspectives for future studies building on the results of this chapter.

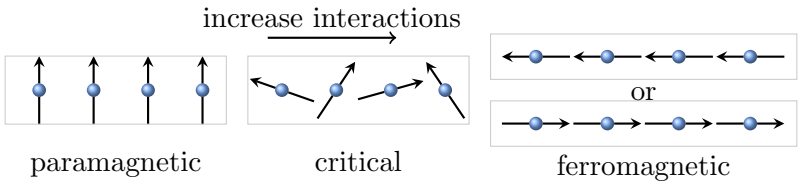

Figure 3.1: Phase transition in the transverse-field Ising model, as the interaction strength λ/ω_z is increased.

3.1 TRANSVERSE-FIELD ISING MODEL

The transverse-field Ising model describes quantum spin 1/2s on a lattice with nearest-neighbour interactions in the presence of an external transverse field. It is one of the most widely used models to study quantum phase transitions [120], and we discuss it qualitatively here to introduce some basic concepts and allow comparisons to the LMG model. The discussion below broadly follows ref. [4], where a rigorous treatment can be found.

The 1-D transverse Ising model is described by the Hamiltonian

$$H = -\hbar\lambda \sum_{\{i,j\}} \sigma_{ix}\sigma_{jx} + \frac{\hbar\omega_z}{2}\sum_i \sigma_{iz} \tag{3.1}$$

where $\{i,j\}$ denotes a sum over nearest neighbours, and individual spins are represented by the Pauli matrices

$$\sigma_x = \begin{pmatrix} 0 & 1 \\ 1 & 0 \end{pmatrix},\ \sigma_y = \begin{pmatrix} 0 & -\mathrm{i} \\ \mathrm{i} & 0 \end{pmatrix},\ \sigma_z = \begin{pmatrix} 1 & 0 \\ 0 & -1 \end{pmatrix},$$

which satisfy the commutation relations $[\sigma_u, \sigma_v] = 2\mathrm{i}\varepsilon_{uvw}\,\sigma_w$.

Here, λ is the strength of the interactions along the x-axis for spins on neighbouring sites. We restrict ourselves to the ferromagnetic case $\lambda > 0$, where co-alignment is favoured. In addition, the second term represents the tendency of spins to align along an externally applied magnetic field along z of magnitude $\omega_z > 0$. This tends to disrupt the magnetic order created by spin-spin interactions.

Let us first consider an infinite system at zero temperature. The nature of the ground state is determined by the relative strength of the two terms in eq. (3.1), as illustrated in fig. 3.1. At $\lambda/\omega_z = 0$, the ground state is paramagnetic, taking the form

$$|0\rangle = \prod_i |{\downarrow}\rangle\,,$$

where $|{\downarrow}\rangle$ is the eigenstate of σ_z polarised along $-z$. In this state, the x-projections of the spins are completely uncorrelated, i.e. two-spin correlator vanishes, with $\langle 0|\sigma_{ix}\sigma_{jx}|0\rangle = 0$, and they are also unpolarised in this direction, as given by the magnetisation, $\langle 0|\sigma_{ix}|0\rangle =$

0. Introducing weak interactions $\lambda \ll \omega_z$ creates local correlations over a scale defined by the correlation length ξ, such that

$$\langle 0|\sigma_{ix}\sigma_{jx}|0\rangle \sim \mathrm{e}^{-|i-j|/\xi}.$$

In the opposite limit, $\lambda/\omega_z \to \infty$, the interactions dominate and we can identify two degenerate ferromagnetic ground states

$$|0\rangle_+ = \prod_i |{\rightarrow}\rangle \text{ and } |0\rangle_- = \prod_i |{\leftarrow}\rangle\,,$$

where $|{\rightarrow}\rangle$ and $|{\leftarrow}\rangle$ are the eigenstates of σ_x polarised along $\pm x$ respectively. These states are mapped to each other by the global $\mathbb{Z}_2$ symmetry generated by the operator $\prod_i |\sigma_z\rangle$, which performs the rotation

$$\sigma_x \to -\sigma_x\,,\ \sigma_y \to -\sigma_y \text{ and } \sigma_z \to \sigma_z\,, \tag{3.2}$$

under which the Hamiltonian is invariant. However, an infinite system always 'chooses' one of the two ground states in the ferromagnetic phase, upon being nudged infinitesimally by the environment. This leads to the appearance of a finite magnetisation $\langle\sigma_{ix}\rangle = \pm 1$ at every site, which acts as the *order parameter*. Crucially, there is also a *spontaneous breaking of the symmetry* of the Hamiltonian, since neither ground state shares the original $\mathbb{Z}_2$ symmetry. In this sense, the order parameter can be seen as an additional quantity needed to fully specify the state of a system having undergone spontaneous symmetry breaking [49].

The ferromagnetic ordering also implies long-range correlations, as reflected in the behaviour of the ferromagnetic correlator

$$\langle\sigma_{ix}\sigma_{jx}\rangle = 1 \text{ for } |i-j| \to \infty\,.$$

We see that the nature of correlations is fundamentally different to that of the paramagnetic case; in fact, it can be shown that a smooth change between the two limits is not possible as we vary λ/ω_z. This change instead occurs via a *second-order phase transition* at a critical coupling $\lambda = \omega_z$, where the lowest excitation gap δ vanishes. Near the transition, the system's physical properties are described by universal critical exponents, shared by numerous models said to be in the same *universality class*. In our Ising model example, the vanishing gap is given by

$$\delta = |1 - \lambda/\omega_z|^{z\nu}$$

with critical exponents $z\nu = 1$. Note that ν is the critical exponent describing the corresponding divergence of the correlation length $\xi \sim |1-\lambda/\omega_z|^{-\nu}$. A universality class is not defined by the microscopic structure of the models, but rather by global properties like the associated symmetries, the lattice's dimensionality, and the number

of degrees of freedom of the order parameter. The prediction of this universal critical behaviour has wide-ranging consequences [121], and has been a major triumph of the scaling theories of critical phenomena and the renormalisation group, developed by Fisher, Wilson, and Kadanoff in the 1970s.

Due to the simplicity of the transverse-field Ising model, these scaling exponents can be obtained exactly using a Jordan-Wigner transform of the spin operators to spinless fermions [122] (though no exact solution exists in 2-D). In fact, our quantum Hamiltonian eq. (3.1) shares a universality class with the 2-D classical Ising model. In cases where such simplifications are not possible, a common first attempt to gain physical insight into the transition is the *mean-field approximation*. Here, each spin site is assigned a non-interacting Hamiltonian in the presence of a 'mean field' created by the rest of the system. This technique ignores quantum fluctuations and can give incorrect critical exponents, particularly in lower spatial dimensions. This is the case for the 1-D transverse-field Ising model, where we find $(z\nu)_{\mathrm{MF}} = 1/2$. As it turns out, this is the correct critical exponent for the LMG model! We will explain in the coming pages how the LMG model can be viewed as the mean-field limit of this transverse-field Ising chain.

3.2 THE LIPKIN-MESHKOV-GLICK MODEL

The remainder of this chapter is dedicated to the study of a version of the transverse-field Ising model with infinite-range interactions, given by the Hamiltonian

$$H = -\frac{\hbar\lambda}{4(N-1)} \sum_{1\leq i\neq j\leq N} \sigma_{ix}\sigma_{jx} + \frac{\hbar\omega_z}{2} \sum_{1\leq i\leq N} \sigma_{iz}. \tag{3.3}$$

This model shows a second-order phase transition at $\lambda = \omega_z$ in the thermodynamic limit. The terms have the same physical meaning as for the Ising Hamiltonian eq. (3.1), the main difference being that we now have infinite-range ferromagnetic interactions. The prefactor $(N-1)^{-1}$ ensures that the energy per spin is extensive. We also maintain the $\mathbb{Z}_2$ symmetry of the Ising chain (see eq. (3.2)). We note that the LMGm is often considered with an additional interaction term $\lambda_y \sigma_{iy}\sigma_{jy}$ along the y-direction. We set this term to zero, and briefly return to it at the conclusion of the chapter to elucidate the resulting possibilities. The model's infinite range interactions imply that notions of length-scales and dimensionality are no longer relevant, which may seem like a fatal blow to its physical applicability. However, it has found a wide range of uses, starting with its original formulation for interacting nucleons undergoing a shape change transition by Lipkin, Meshkov, and Glick [50–52].

The mathematical treatments used in this chapter reflect the wide range of systems where the LMGm applies (see fig. 3.2). Firstly, the form shown in eq. (3.3) has strong links to other infinitely-coordinated models. The most famous of these is the Dicke model [123], which describes N qubits interacting with a single light mode. This model was predicted to show a second-order quantum phase transition to a superradiant phase when the

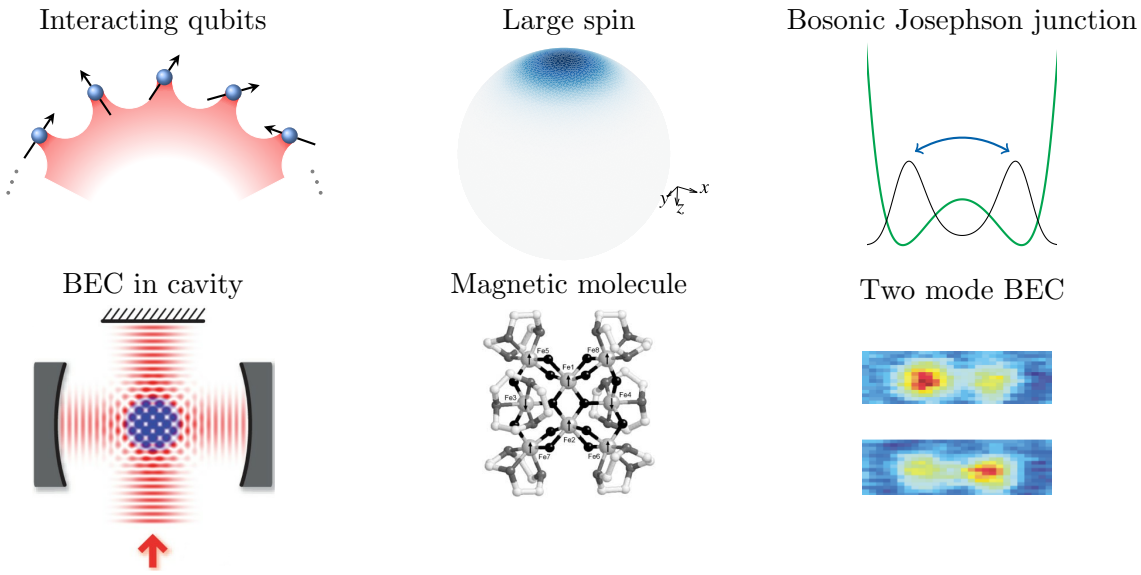

Figure 3.2: Three possible formulations of the LMG model and examples of their corresponding experimental realisations. The lower panels are adapted from works showing the Dicke model for a BEC in a cavity with a transverse pump (Baumann et al. [124]), a magnetic Fe8 molecular complex (Gatteschi and Sessoli [128]) with ground state spin $S = 10$, and a BEC tunnelling in a double well potential (Albiez et al. [54]).

atom-light coupling is comparable to the qubit splitting; this has since been confirmed with a BEC coupled to an optical cavity [124]. After tracing out the photonic degrees of freedom, the effective inter-qubit interactions are infinite-ranged. In the limit of zero temperature and to lowest order in the spin-light coupling, the Hamiltonian eq. (3.3) is recovered, and it can be separately checked that these systems share a universality class [53]. We also note that infinitely coordinated qubit systems can be realised with single-mode spinor BECs [125], arrays of trapped ions [126], and using light-mediated atom-atom interactions [127].

Secondly, the LMGm can describe the tunnelling of interacting bosons between degenerate modes [129–131], as realised with two mode BECs in a double-well potential [54, 55]. At a fixed atom number N, the Josephson oscillations of the atom number difference $N\langle\sigma_{ix}\rangle$ between the wells are well described by the Hamiltonian 3.3. Here, the z-field maps to tunnel coupling between wells and λ maps to the strength of two-body contact interactions. Interestingly, the broken-symmetry ferromagnetic states correspond to self-trapping of the BEC [129] – we will show dynamics between such states with measurements of macroscopic tunnelling in section 3.7.3.

Thirdly, the 'large spin' picture we develop in the following section restates the LMGm in terms of a single spin $J = N/2$ under a quadratic coupling proportional to J_x^2. This picture applies to large spin single-molecule magnets [128], most famously Mn_{12}-acetate, where the non-linear coupling arises from the anisotropic arrangement of ions. The coherent manipulation of Rydberg atoms' spins can also produce this

type of physics [132]. Finally, our experiments with ultracold dysprosium atoms also fall into this third category. We use a single dysprosium atom with ground state spin $J = 8$ to study the LMGm for $N = 16$ qubits. In our case, the effective ferromagnetic interactions are produced by a tensor light shift, creating a term proportional to J_x^2 in the spin Hamiltonian.

We conclude this section by pointing out that the LMGm is in a position of prime importance due to its mathematical tractability; in particular, the model is integrable [133, 134], and conservation laws mean that the relevant Hilbert space dimension scales linearly with the number of spins N (as explained in section 3.4). This is a crucial factor given the scarcity of quantum critical systems with exact solutions, as evidenced by the rich body of theoretical work surrounding the model, which we cite throughout this text.

3.3 QUANTUM CRITICAL BEHAVIOUR: FINITE TEMPERATURE AND SIZE

So far, we have spoken of the qualitative change in the nature of the ground state across the phase transition, but $\lambda = \lambda_c$ itself i.e. the *quantum critical point* (QCP), is of central importance. At the QCP, the ground state is an entangled superposition of an exponentially large number of fluctuating states [4]. This QCP, and the associated quantum phase transition, only occur at $T = 0$ in the thermodynamic limit. However, the theoretical framework of quantum phase transitions still underpins the description of realistic systems of a finite temperature and size. Indeed, a QCP acts like a singularity on the phase diagram, strongly affecting thermodynamic properties and dynamics in its vicinity (see fig. 3.3). At finite temperatures, this leads to the regime of quantum criticality, where the energy gap $\hbar\Delta$ is less than the thermal energy scale $k_B T$, and there is an intricate interplay of quantum and thermal fluctuations, which cannot be described by an effective theory with weak interactions. We do not delve deeper into this fascinating subject and instead refer the interested reader to refs. [39, 135].

We now turn to systems of finite size, which also strongly feel the effect of the underlying quantum critical point. We shall see that our experiments are effectively at near-zero temperatures for the spin degrees of freedom. So when we speak of *critical behaviour* from here on, it refers to signatures of the QCP visible in the crossover regime for our finite-size system – which we will be evident in our results.

Let us briefly return to our Ising chain with nearest-neighbour interactions, now imposing a finite chain length L. Deep in the paramagnetic phase where $\xi \ll L$, the system's bulk behaves identically to the infinite chain. The effect of the system's finite size is felt upon approaching the transition, when $\xi \sim L$. In this region, the non-analytic behaviour of physical quantities in the thermodynamic limit is smoothed out over a finite range of coupling strengths around the transition[1] (see fig. 3.3). This phenomenon is described quantitatively by the theory of finite-size scaling, introduced in

[1] It is also possible to define a shift of the phase transition point, with this shift also scaling inversely with N. For convenience, we maintain the convention $(\lambda/\omega_z)_c = 1$ throughout the text, even for our finite system.

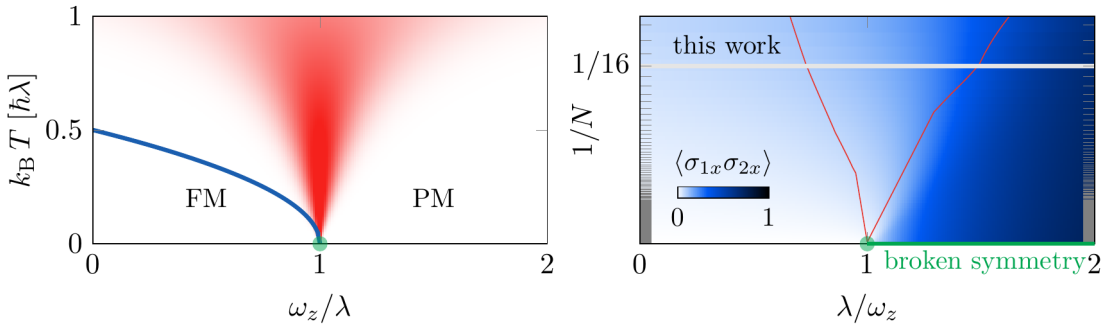

Figure 3.3: Effect of a quantum critical point (QCP) at $T = 0$, $N \to \infty$ on systems at finite temperature T (left panel) and finite system size N (right panel). The QCP is indicated as a green disk at $\lambda = \omega_c$. The strongly interacting regime persists at finite temperature in the quantum critical 'fan' (red), where quantum and thermal fluctuations compete. The QCP extends to a line of phase transitions (blue) driven by thermal fluctuations. Our experiments are effectively at $T \to 0$ (see text). Note that the x-axis is inverted with respect to the convention used elsewhere. In finite systems, the non-analytic behaviour associated with the QCP is smoothed over a critical crossover region, and the true ground state does not show broken symmetry. The red curves enclose the zone where the ferromagnetic correlator deviates significantly from its value in the thermodynamic limit. Our experiments simulate a system with $N = 16$ spins.

1972 by Fisher and Barber [40]. In short, finite-size scaling asserts that a thermodynamic quantity A, which disappears as $A \sim (\lambda - \lambda_c)^a$ in the thermodynamic limit, is given by $A_{\lambda=\lambda_c} \sim L^{-a/\nu}$ for a finite system. Here, ν is the critical exponent giving the divergence of the correlation length $\xi \sim (\lambda - \lambda_c)^{-\nu}$. Note that the upper critical dimension d_c is another particularly important quantity: it gives the number of dimensions above which a mean-field approach is valid, and it is often difficult to determine theoretically.

Let us now return to infinitely coordinated systems. Although the correlation length is not defined here, the theory of finite size scaling has nevertheless been extended to this case [56, 136], with scaling relations of the type $A_{\lambda=\lambda_c} \sim N^{a_{\mathrm{MF}}/\nu^*}$ where a_{MF} is the mean-field scaling exponent. It turns out that the relation $\nu^* = \nu_{\mathrm{MF}}\, d_c$ holds for a large family of models [136]. Here, ν_{MF} and d_c are the mean-field critical exponent and the upper critical dimension in the corresponding short-range model. In this way, the finite size behaviour of infinitely coordinated models can provide crucial information about analogous short-range models.

For the LMGm in particular, certain finite size scaling exponents have been calculated explicitly [137, 138]. For example, the excitation gap Δ, which is strictly zero at the critical point in the thermodynamic limit, behaves as $\Delta \sim N^{-1/3}$ in the finite LMGm, which we will compare to our results in section 3.7.3.

3.4 MAPPING THE QUBIT ENSEMBLE TO A LARGE SPIN

Here, we explain the formalism of the large-spin picture, which underpins our experimental realisation of the LMGm. Let us begin by recasting the spin operators from the Hamiltonian 3.3 as follows:

$$J_\alpha = \frac{1}{2}\sum_i^N \sigma_{i\alpha} \text{ , for } \alpha = x, y, z\,. \tag{3.4}$$

After a few lines of algebra, this allows us to write our Hamiltonian as

$$H = -\frac{\hbar\lambda}{N-1}J_x^2 + \hbar\omega_z J_z\,, \tag{3.5}$$

up to a constant term, which we discard. We see that this Hamiltonian conserves the total spin and parity, since

$$\left[H, \boldsymbol{J}^2\right] = [H, P_z] = 0\,,$$

where

$$P_z = \prod_{i=1}^N \sigma_{i,z} \tag{3.6}$$

is the parity operator directly corresponding to the $\mathbb{Z}_2$ symmetry. These symmetries allow us to identify subset Hilbert spaces with independent dynamics, within our overall Hilbert space of N-qubit states. Firstly, we have the spin sectors of defined total spin $J = N/2 - n$ where $n = 0, 1, 2, \ldots$, down to $J = 0$ or $1/2$. The manifolds with even (odd) n consist purely of states symmetric (anti-symmetric) under an exchange of any qubit pair. Each spin sector can be conveniently represented in the Dicke basis $|J, m\rangle$, where the integer $-J \leq m \leq +J$ is the spin projection along the z-axis. This situation is summarised in fig. 3.4, where we also indicate the parity of these basis states.

It is easy to check that the ground state in the limits $\lambda/\omega_z = 0$ and $\lambda/\omega_z \gg 1$ belongs to the $J = N/2$ manifold, and so this must be the case throughout the phase diagram. Moreover, the lowest excited states also have $J = N/2$, as can be seen in fig. 3.5. This can be explained by a scaling argument: $\langle H\rangle$ is extensive in N, so the gap between the overall ground state (from the $J = N/2$ manifold) and the lowest-energy state of the $J = N/2 - 1$ manifold must be a constant of order $\hbar\omega_z$. In contrast, the gaps within the $J = N/2$ manifold can be arbitrarily small, and they indeed vanish at the critical point in the thermodynamic limit, as we will see in section 3.6.1. Moreover, the conservation of $\langle \boldsymbol{J}^2\rangle$ implies that after starting in the ground band, any phase transition dynamics cannot involve states with $J < N/2$. Finally, a brief word on states which have no exchange symmetry i.e. physical states accessible only by N distinguishable qubits: these states simply add degeneracies to excited states outside the $J = N/2$ manifold [139] and do

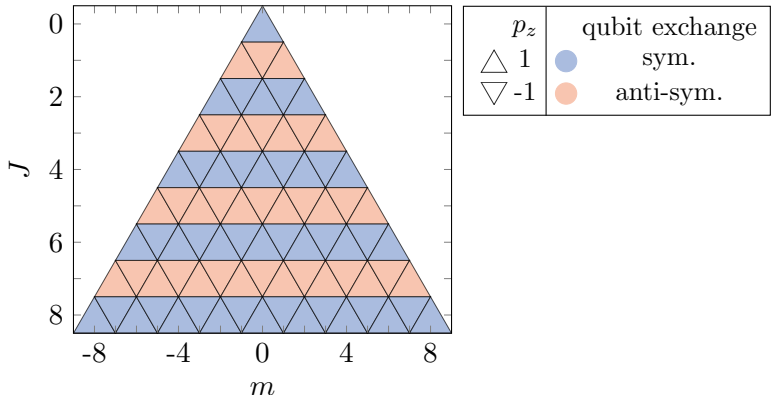

Figure 3.4: Hilbert space for $N = 16$ qubits, when represented as in the Dicke basis for a composite spin of magnitude $J = 0, 1, 2 \ldots, N/2$. Each state is represented by a triangle; the symmetry under the exchange of qubits, and the expectation value p_z for the parity operator is indicated (see legend). Our experiments are carried out in the maximal spin sector $J = N/2$, of dimension $N + 1$. Note that if states which have no exchange symmetry are included, the Hilbert space is of dimension 2^N (these states are not shown here).

not complicate this discussion. Considered together, the preceding facts justify using the electronic ground state spin $J = 8$ of a single ^{162}Dy atom, which can only explore the maximal spin sector, to simulate the phase transition and low-energy dynamics in the LMGm for $N = 16$ qubits. The restriction to the maximal spin sector is also imposed by symmetrisation of the wavefunction in spinor BEC realisations of the LMGm [125].

We note that we have dramatically reduced the dimension of Hilbert space considered from 2^N to $N + 1$. Additionally, the definition eq. (3.4) and the exchange symmetry of qubits means that one- and two-qubit observables can now be expressed in terms of experimentally accessible moments of the spin J,

$$\langle \sigma_{i\alpha} \rangle = \frac{\langle J_\alpha \rangle}{N} \tag{3.7}$$

$$\langle \sigma_{i\alpha} \sigma_{j\alpha} \rangle = \frac{4\langle J_\alpha^2 \rangle - N}{N(N-1)} \qquad \text{for } \alpha = x, y, z\,. \tag{3.8}$$

We can further divide the $|J = 8, m\rangle$ Dicke basis into even and odd parity sectors, respectively corresponding to eigenvalues $+1$, -1 of P_z. Equivalently, P_z counts if there are an even or odd number of qubits pointing up. A unique feature of our system is that the symmetry is directly accessible from measurements of the spin projection probabilities Π_m using the relation

$$p_z \equiv \langle P_z \rangle = \sum_{m=-J}^{J} (-1)^m \Pi_m\,, \tag{3.9}$$

along with the single m-state resolved detection of our experimental setup. We also note that eigenstates of P_z satisfy

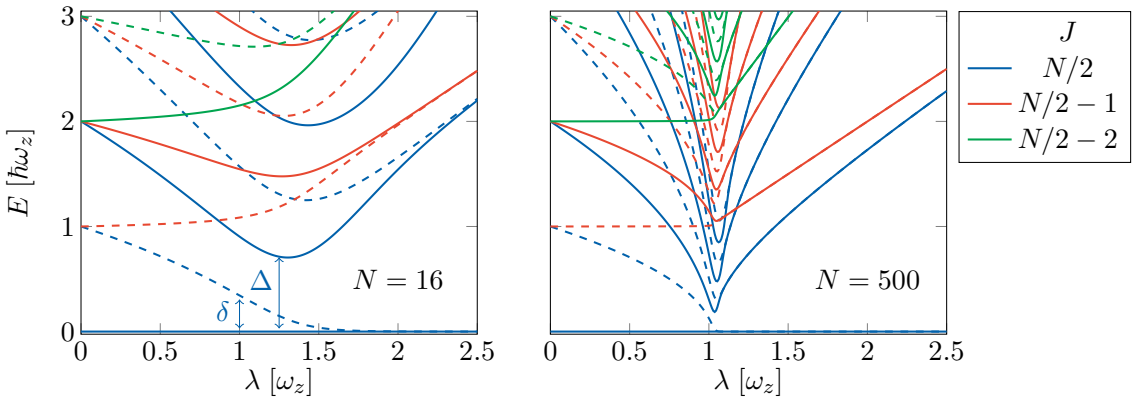

Figure 3.5: Full spectrum of the N-qubit LMGm, for $N = 16$ (our experiment) and $N = 500$, showing the sharpening of phase transition features at $\lambda/\omega_z = 1$ on approaching the thermodynamic limit. Red, blue, and green curves represent states in the three largest total spin J sectors. Even (odd) parity states are denoted with solid (dashed) lines. All energies are plotted with respect to the ground state, which is in the $J = N/2$ sector, with even parity. Note that this plot only explicitly shows states either symmetric or anti-symmetric under qubit exchange. The remaining states, leading to the full 2^N Hilbert space dimension, simply add degeneracies in the sectors with $J < N/2$. The parity gap (δ) and the dynamical gap (Δ) are defined from the ground level to the first excited state of odd and even parity respectively.

$$\langle J_\alpha \rangle = \langle J_z J_\alpha \rangle = \langle J_\alpha J_z \rangle = 0 \text{ for } \alpha = x, y$$

In the remainder of the chapter, we will freely switch between the large-spin and interacting qubit formulations of the LMGm. Since our qubits are in fact virtual, or encoded, particular care must be taken when speaking of properties like entanglement, as we will explain in section 3.6.3.

3.5 EXPERIMENTAL IMPLEMENTATION

Our measurements are performed on ultracold samples of $N_{at} = 1.3(3) \cdot 10^5$ atoms, initially held in an optical dipole trap at a temperature $T \simeq 1.1(1)\,\mu K$. The atomic spin is initially polarised in $|m = -J\rangle$, under a magnetic field $\boldsymbol{B} = B\hat{z}$ with $B = 114(1)\,mG$, corresponding to a Larmor frequency $\omega_z = 2\pi \times 198(2)\,kHz$. This field creates the Zeeman splitting corresponding to the external field term in the LMGm, and indeed our initial state naturally corresponds to the LMGm ground state at $\lambda = 0$, where all qubits are anti-aligned with the field. To simulate ferromagnetic interactions, we apply a laser beam close to the 626 nm optical transition (excited level $J' = 9$), focussed on the atomic cloud (with a waist of 50 µm). The laser is far-detuned on the blue side of the transition by $2\pi \times 21\,GHz$. The beam is linearly polarised along the x direction, resulting in a quadratic Zeeman light shift proportional to $-J_x^2$, as explained previously in section 2.4. The coupling strength λ, proportional to the beam's power, is controlled dynamically

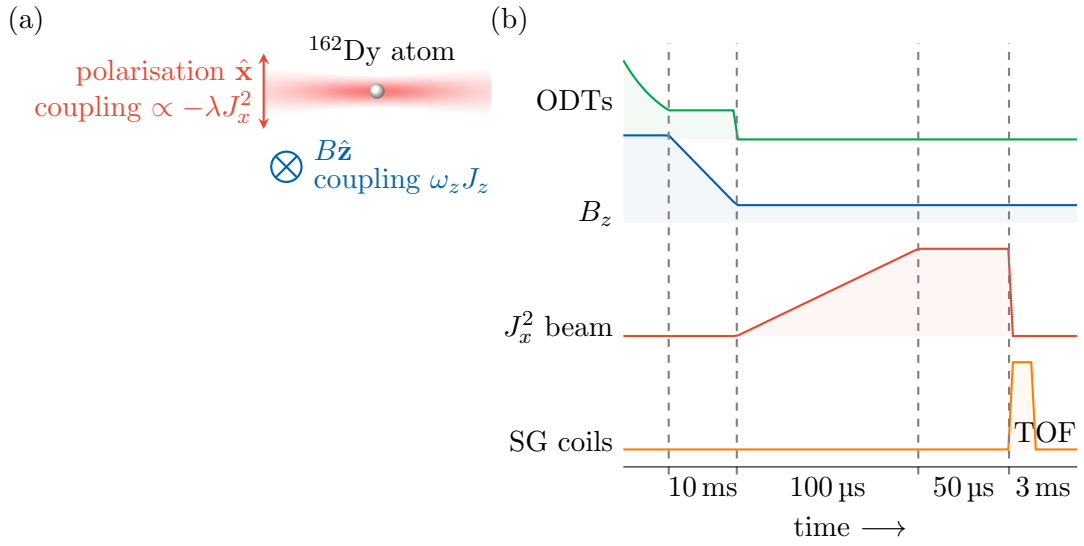

Figure 3.6: (a) Scheme of the experiment, based on laser-induced non-linear dynamics of the electronic spin of dysprosium atoms (quadratic light shift $\propto -\lambda J_x^2$), in the presence of a magnetic field inducing a Zeeman coupling $\omega_z J_z$. (b) Typical experimental sequence. After the end of evaporative cooling in the optical dipole traps (ODTs), the z-magnetic field is ramped down to $B \sim 100\,\mathrm{mG}$. Then, the ODTs are turned off and the 626 nm J_x^2 coupling is ramped up, to realise the LMGm at a particular interaction strength. Then, a further step like a quench of the J_x^2 beam power might be carried out, depending on the aim of the measurement (here, we just show a holding period). The non-linear coupling is applied on the typical timescale of a few hundred microseconds. Then, a Stern-Gerlach (SG) magnetic gradient is pulsed, followed by a time-of-flight (TOF) expansion and absorption imaging of the $2J+1 = 17$ atomic clouds to measure spin projection probabilities.

using the RF power sent to an AOM. Figure 3.6 gives an overview of our experimental scheme.

The Zeeman energy scale $\hbar\omega_z \sim k_\mathrm{B} \times 9\,\mu\mathrm{K}$ is much larger than the kinetic temperature of the gas, which also has an interparticle collision rate on the order of one per 10 ms (negligible on our experimental timescales). Hence, each atom's spin degrees of freedom are isolated, and our experiments study the LMGm in an isolated system at an effective $T \simeq 0$. Combined with the fact that the light and B-fields are uniform over the sample, one can conclude that a single experimental run corresponds to $N_\mathrm{at} \sim 10^5$ realisations of an identical experiment, over which we average in our detection scheme. We will revisit the prospect of probing interaction and finite-temperature effects towards the end of the chapter.

3.5.1 *Compensating stray magnetic fields*

While trying to engineer the Hamiltonian of eq. (3.5) on our setup, we are naturally susceptible to introducing unwanted terms proportional to $\omega_x J_x$ and $\omega_y J_y$; these terms break the Hamiltonian's $\mathbb{Z}_2$ symmetry. They appear when stray magnetic fields in the

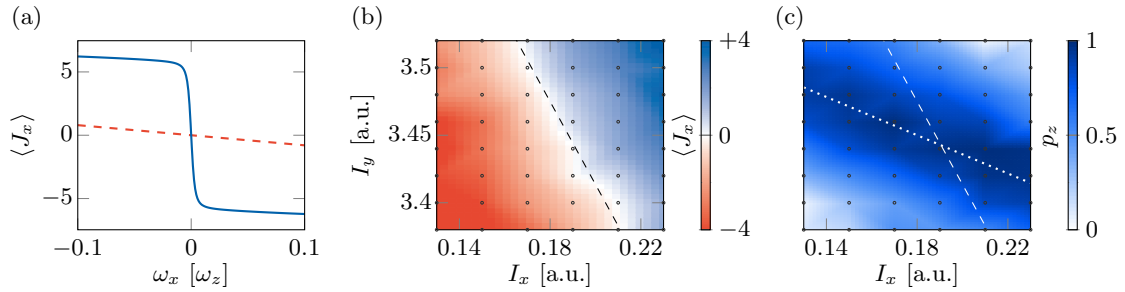

Figure 3.7: Stray magnetic field compensation (a) Expected magnetisation along x-direction $\langle J_x \rangle$ of the ground state of the LMGm at $\lambda/\omega_z = 0$ (dashed red line) and in the ferromagnetic case $\lambda/\omega_z = 2$ (solid blue line). We use the ferromagnetic state for the subsequent calibration. (b) Measured magnetisation as a function of current set-points (I_x, I_y) in compensation coils. The colour is interpolated from measurements (black circles). The dashed line is the contour of fitted $\langle J_x \rangle = 0$. (c) Measured parity p_z as a function of currents in compensation coils. The colour is interpolated from actual data points (black circles). The dotted line is the curve of fitted maximal p_z, while the dashed line from (b) is also shown. For our experiments, we set the compensation currents to the intersection of the two fitted lines. Note that directions x, y of B-fields created by the coils are not the same as those defined by the LMG Hamiltonian.

x-y plane are not cancelled.[2] The simplest method to set the offset of the x and y fields to zero is to set $\lambda = 0$, and measure the spin projection probabilities along the z-axis. Fields along the x or y directions would slightly tilt the coherent states and give non-zero projection probabilities $\Pi_{m=-7}$, $\Pi_{m=-6} \ldots$, which we can aim to minimise.

However, we exploit the enhanced sensitivity of the ferromagnetic ground state for a more clever calibration, illustrated in fig. 3.7. A $\omega_x J_x$ perturbation polarises the total spin along either of $\pm x$ and drastically reduces the mean parity. In practice, we measure p_z and $\langle J_x \rangle$ versus applied fields, fit lines of $p_z = 1$ and $m_x = 0$ and work at their intersection point. These contours do not coincide as expected from theory, which could be caused by a slight miscalibration of the Ramsey waiting time used to measure $\langle J_x \rangle$. Such field adjustment needs to be repeated roughly every twelve hours to take into account global field offsets from neighbouring experiments or the Paris metro system. We will reconsider such perturbations to the LMGm in our final set of experiments where we study parity breaking.

3.5.2 *Adiabaticity requirements*

We aim to adiabatically prepare the ground state in both the paramagnetic and ferromagnetic regimes. This requires caution, because of the expected minimum near $\lambda/\omega_z = 1$ in the dynamical gap Δ to the first excited state of even parity (see fig. 3.5). In order to choose an appropriate ramp speed, we simulate the system dynamics by solving the Schrödinger equation numerically with a light coupling increasing at constant speed $\dot{\lambda}$, as performed in our experiments. As shown in fig. 3.8 we find that the calculated

[2] Our active B-field compensation system (see section 2.2.5) only minimises shot-to-shot fluctuations along the z-axis.

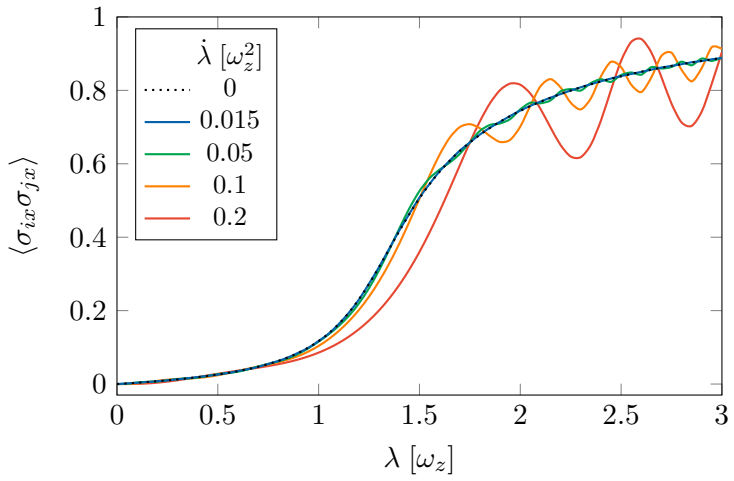

Figure 3.8: Simulation of adiabatic state preparation. Ferromagnetic correlator $\langle \sigma_{ix}\sigma_{jx}\rangle$ as a function of the coupling λ calculated in the state reached after a linear ramp of the from zero to λ, for different ramp speeds $\dot{\lambda}$.

two-qubit ferromagnetic correlator $\langle \sigma_{ix}\sigma_{jx}\rangle$ significantly deviates from the ground state value for ramp speeds $\dot{\lambda} \gtrsim 0.05\,\omega_z^2$. We decided to use the ramp speed $\dot{\lambda} = 0.015\,\omega_z^2$, for which the correlator is practically indistinguishable from the ground-state value, and the ramp can be considered adiabatic. This corresponds to ramping to $\lambda/\omega_z = 1$ in 54 µs. The magnetic field compensation discussed in the previous section also plays a role in adiabaticity since it minimises mixing with the odd-parity excited levels.

3.6 GROUND STATE PROPERTIES

In this section, we investigate the properties of the LMGm's ground state. Figure 3.9 shows the measured spin projection probabilities $\Pi_m(\boldsymbol{n})$ along the $\boldsymbol{n} = \hat{\boldsymbol{x}}$ and $\hat{\boldsymbol{z}}$ directions. In the paramagnetic limit $\lambda/\omega_z = 0$, we start with a coherent state along the z-axis $|-J\rangle_z$, which has a symmetric Gaussian distribution in the m_x sublevels around $m_x = 0$. This distribution broadens as we approach $\lambda/\omega_z = 1$. For $\lambda/\omega_z \gtrsim 2$, it becomes a clear bifurcation between states polarised along $\pm x$. We deliberately show single shot data in fig. 3.9a to highlight that each run of the experiment produces the bifurcated distribution, and it is not an average of several fully polarised states. Hence, the standard Ising-type order parameter $\langle \sigma_{1x}\rangle = \langle J_x\rangle / J$ remains close to zero in our system. However, a single shot is effectively averaged over all atoms, so the $\Pi_m(\hat{\boldsymbol{x}})$ data alone cannot rule out a situation with half of the atoms in each symmetry broken state – which could occur if spin domains form in the cloud.

A direct measurement of the $\mathbb{Z}_2$ symmetry comes to our rescue here, as we see that only even sublevels remain populated in the measured $\Pi_m(\hat{\boldsymbol{z}})$ distribution, and indeed the mean parity $p_z \equiv \langle P_z\rangle$ remains close to one for all values of interaction strengths. The small decrease for large interactions is explained by shot-to-shot field B_x fluctuations

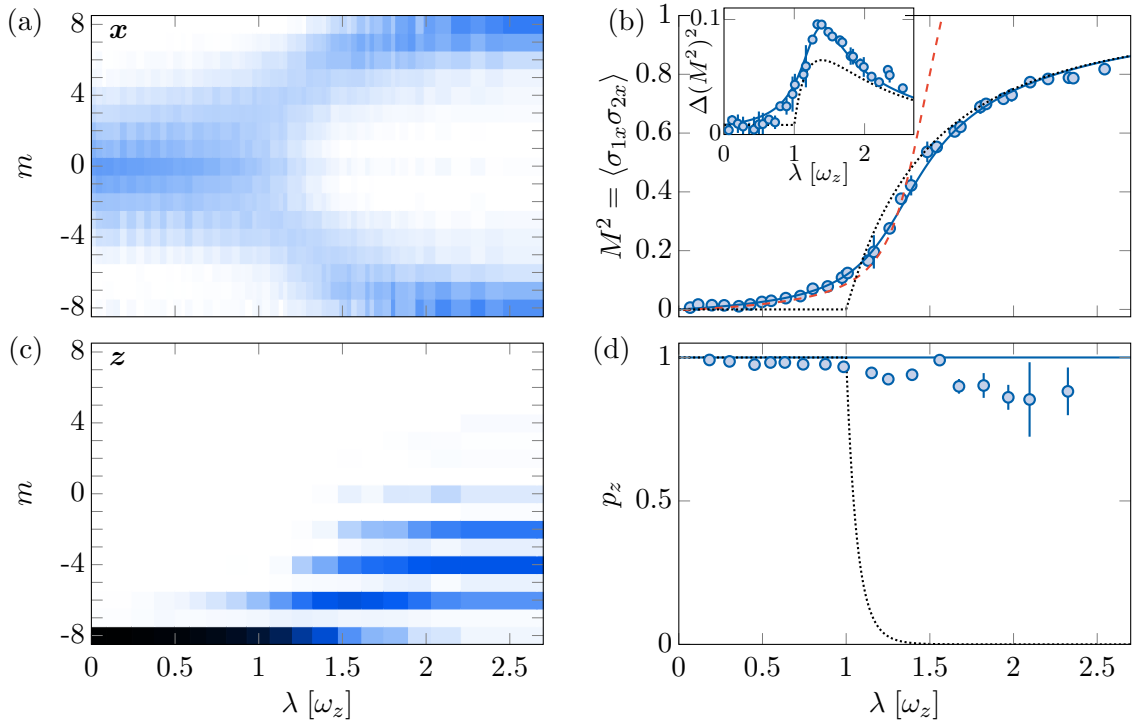

Figure 3.9: Ground state properties from the x- and z-projection probabilities. (a,c) Measured projection probabilities $\Pi_m(\boldsymbol{n})$ for $\boldsymbol{n} = \hat{\boldsymbol{x}}$ and $\hat{\boldsymbol{z}}$ respectively as a function of the interaction strength λ. Evolution of the (b) spin pair correlator $\langle \sigma_{1x}\sigma_{2x} \rangle$, (b, inset) its fluctuations, and (d) the mean parity p_z. The solid blue (dotted black, dashed red) lines correspond to the LMGm (mean-field approximation, critical Hamiltonian, respectively). No averaging is performed in (a). In other panels, all data is averaged over about five independent measurements. In all figures, error bars represent the 1-σ statistical uncertainty. The colour scale for the spin projection probabilities used throughout is the same as fig. 2.6.

of rms width $\sigma_B = 0.4\,\mathrm{mG}$. These fluctuations couple the even ground state in the ferromagnetic phase to its nearly degenerate odd counterpart. This mechanism would cause true symmetry breaking ($p_z \to 0$) in a macroscopic system. In this sense, our $N = 16$ system could be qualified as not truly macroscopic, or alternately, the fluctuations are too well under control to see spontaneous symmetry breaking! A more quantitative discussion will follow with the measurements of susceptibility in section 3.8.

Setting symmetry breaking aside, magnetic ordering along the x-direction is probed by the two-spin correlator $\langle \sigma_{1x}\sigma_{2x} \rangle$, which is a standard effective magnetisation used for the LMGm [56]. We remind the reader that this quantity is linearly related to $\langle J_x^2 \rangle$ via eq. (3.7). We see that in fig. 3.9c that the correlator increases smoothly with interaction strength, characteristic of a para- to ferromagnetic crossover in a finite system. We also measure an increase in fluctuations of this effective magnetisation (see fig. 3.9c, inset) which is a generic feature of continuous phase transitions [140]. To concretely link our measurements to the underlying quantum critical point, we now take a brief detour to present two theoretical treatments: the mean-field approximation and a series expansion of the Hamiltonian around the critical point.

3.6.1 *Mean field theory*

The mean-field approximation consists in creating an effective single-particle Hamiltonian for each qubit. To this end, a mean field $\boldsymbol{B}_{\text{eff}}$ is constructed, representing the average interaction effect felt by a qubit due to the rest of the system, neglecting quantum fluctuations in the process. Conveniently, the mean-field approach gives exact results for the LMGm's thermodynamic quantities and critical exponents [56]. This can be understood as the extension for the case of spin models with finite range interactions: there, mean-field theory only works for spatial dimension d greater than d_c (the upper critical dimension); this occurs when the coordination number becomes large enough, and quantum fluctuations become less relevant. Hence, the maximal coordination number $N-1$ means that the LMGm in the thermodynamic limit can be seen as a mean-field version of the 1-D Ising model of section 3.1.

We first rearrange our Hamiltonian eq. (3.3) to the form

$$H = \frac{\hbar}{2}\sum_{i=1}^{N}\left[-\lambda\left(\frac{1}{N-1}\sum_{j\neq i}\frac{\sigma_{jx}}{2}\right)\sigma_{ix} + \omega_z\sigma_{iz}\right].$$

The i^{th} spin is thus subjected to an external z-field, and an x-field proportional to the mean spin projection along x of all other spins. We can now make the mean-field approximation

$$\begin{aligned}\sigma_{ix}\sigma_{jx} &\to \langle\sigma_{jx}\rangle\sigma_{ix} + \langle\sigma_{ix}\rangle\sigma_{jx} - \langle\sigma_{ix}\rangle\langle\sigma_{jx}\rangle,\\ &= \langle\sigma_{ix}\rangle\sigma_{ix} + \langle\sigma_{ix}\rangle\sigma_{jx} - \langle\sigma_{ix}\rangle^2,\end{aligned} \tag{3.10}$$

where we have used the exchange symmetry of the ground state to set $\langle\sigma_{jx}\rangle = \langle\sigma_{ix}\rangle$ for all i, j. This substitution leads to the mean-field Hamiltonian, which is a simple sum of single-spin Hamiltonians

$$H_{\text{mf}} = \frac{\hbar}{2}\sum_{i=1}^{N}\left(-\lambda\langle\sigma_{ix}\rangle\sigma_{ix} + \omega_z\sigma_{iz}\right), \tag{3.11}$$

up to a constant energy shift. Now each qubit is merely subjected to a field $\boldsymbol{B}_{\text{eff}} = -\lambda\langle\sigma_{ix}\rangle\hat{\boldsymbol{x}} + \omega_z\hat{\boldsymbol{z}}$, and must be anti-aligned with respect to it. This gives a self-consistency relation for the x-magnetisation

$$\langle\sigma_{ix}\rangle = \frac{\lambda\langle\sigma_{ix}\rangle}{\sqrt{(\lambda\langle\sigma_{ix}\rangle)^2 + \omega_z^2}},$$

whose solution is

$$\langle \sigma_{ix} \rangle = 0 \qquad \text{for } \lambda \leq \omega_z, \tag{3.12}$$

$$= \pm\sqrt{1 - \left(\frac{\omega_z}{\lambda}\right)^2} \qquad \text{for } \lambda > \omega_z. \tag{3.13}$$

We note the non-analyticity at the quantum critical point, and can also read off the critical exponent $\beta = 1/2$ associated with the order parameter's appearance at the transition. From the approximation eq. (3.10), it is also clear that our correlator $\langle \sigma_{ix}\sigma_{jx} \rangle$ is simply equal to $\langle \sigma_{ix} \rangle^2$ within mean-field theory.

The condition of anti-alignment with $\boldsymbol{B}_{\text{eff}}$ also gives the z-magnetisation

$$\langle \sigma_{iz} \rangle = -1 \qquad \text{for } \lambda \leq \omega_z,$$

$$= -\omega_z/\lambda \qquad \text{for } \lambda > \omega_z.$$

and hence the mean-field expectation value of the parity

$$p_z = \langle \prod_{i=1}^{2J} \sigma_{i,z} \rangle = \langle \sigma_{i,z} \rangle^{2J}$$

$$\implies p_z = (-1)^{2J} \qquad \text{for } \lambda \leq \omega_z, \tag{3.14}$$

$$= (-\omega_z/\lambda)^{2J} \qquad \text{for } \lambda > \omega_z\,, \tag{3.15}$$

which rapidly decays to zero after crossing the transition.

Dynamical properties The mean-field approach can also be used to calculate the excitation dynamics of the system – we will compare these with our measurements in section 3.7. We are interested in the gaps to the first excited level of odd and even parities, which we denote δ and Δ respectively (see fig. 3.5a).

We first focus on the odd gap δ. Consider the coupled equations of motion for the spin components σ_x and σ_y of a spin-1/2 (we drop the subscript i for clarity):

$$\dot{\sigma_x} = \frac{\mathrm{i}}{\hbar}\left[H, \sigma_x\right] = -\omega_z \sigma_y$$

$$\dot{\sigma_y} = \frac{\mathrm{i}}{\hbar}\left[H, \sigma_y\right] = \frac{\lambda N}{N-1}(\sigma_x\sigma_z + \sigma_z\sigma_x) + \omega_z\sigma_x\,,$$

where we have applied the standard commutation relations. Considering these equations as describing the dynamics of a semiclassical spin-1/2, we can set them to be equal to $\mathrm{i}\delta\sigma_x$ and $\mathrm{i}\delta\sigma_y$ respectively. The excitation frequency δ can then be evaluated by the random phase approximation [136], which consists in replacing σ_z with its mean-field expectation value, leading to

$$\frac{\delta}{\omega_z} = \sqrt{1 - \frac{\lambda}{\omega_z}} \qquad \text{for } \lambda \leq \omega_z, \tag{3.16}$$

$$= 0 \qquad \text{for } \lambda > \omega_z. \tag{3.17}$$

We see that the odd gap vanishes at the transition point in the mean-field approximation. From the square-root decay on the paramagnetic side of the transition, we can infer the product of critical exponents $\nu z = 1/2$.

Semiclassical variational technique

The familiar mean-field approach presented above is equivalent to a variational technique with coherent collective spin states; this method provides an intuitive picture of the transition and allows us to extract the remaining energy gaps in the thermodynamic limit.

We consider coherent states of the collective spin J, pointing along a direction $\boldsymbol{n}$ given by spherical angles θ, ϕ. In terms of the underlying qubits, this is a product state of the form

$$|\theta, \phi\rangle = \bigotimes_{i=1}^{2J} \left(\cos(\theta/2) e^{-i\phi/2} |\uparrow\rangle_i + \sin(\theta/2) e^{i\phi/2} |\downarrow\rangle_i \right) .$$

The fluctuations in average magnetisation in a direction $\boldsymbol{m} \perp \boldsymbol{n}$ have a relative magnitude $\Delta J_{\boldsymbol{m}}/J = (2J)^{-1/2}$. Then, in the large J limit, the spin behaves like a classical vector

$$\boldsymbol{J} = J(\sin\theta\cos\phi, \sin\theta\sin\phi, \cos\theta), \tag{3.18}$$

Substituting this in the Hamiltonian 3.5 gives the variational energy

$$\langle H \rangle = \hbar J \left(\frac{-\lambda}{2} \sin^2\theta \cos^2\phi + \omega_z \cos\theta \right),$$

where we have already applied $2J - 1 \simeq 2J$ for convenience. Minimising $\langle H \rangle$ gives the ground state

$$|\theta = \pi\rangle \quad \text{for } \lambda \leq \omega_z,$$
$$|\theta = \cos^{-1}(-\omega_z/\lambda), \phi = 0 \text{ or } \pi\rangle \quad \text{for } \lambda > \omega_z.$$

It is easy to check that we recover the mean-field magnetisation of eq. (3.12) from this solution. The emergence of a pair of symmetry-broken degenerate states (in the x-z plane) at the transition is apparent in the semiclassical energy landscapes plotted in fig. 3.10 for different values of the coupling. In fact, the plotted energy contours are the classical orbits of the spin vector in the variational potential. Note the flatness of the potential at the cusp of the double well in the ferromagnetic phase. This corresponds to

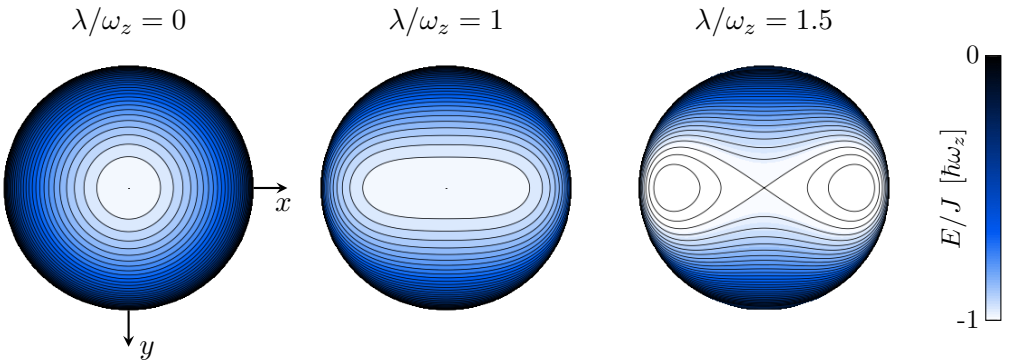

Figure 3.10: Semiclassical energy landscape for $\lambda/\omega_z = 0, 1, 1.5$ for coherent states of the total spin J, parametrised by spherical angles (θ, ϕ). We show a view of the spin-J Bloch sphere, looking down at the south pole. We see the emergence of two degenerate minima in the x-z plane for $\lambda/\omega_z > 1$, corresponding to a broken-symmetry ferromagnetic state.

the divergence of the LMGm's density of states in the thermodynamic limit, which is associated with an excited-state phase transition [141].

Dynamical properties We can calculate the associated excitation frequencies by expanding around the minima to recover harmonic oscillator potentials in terms of the conjugated variables $J_z = J\cos\theta$ and ϕ. This leads to the following results: in the paramagnetic phase, we recover the result eq. (3.16) for the odd gap δ. The lowest order expansion becomes exact in the thermodynamic limit. So when $\lambda \leq \omega_z$ the even gap is given by $\Delta = 2\delta$. In the ferromagnetic phase, Δ is the first excitation energy away from the doubly degenerate ground manifold; we obtain it using an expansion around either double well minimum, giving the value in the second equation below.

$$\frac{\Delta}{\omega_z} = 2\sqrt{1 - \frac{\lambda}{\omega_z}} \qquad \text{for } \lambda \leq \omega_z, \tag{3.19}$$

$$= \sqrt{\left(\frac{\lambda}{\omega_z}\right)^2 - 1} \qquad \text{for } \lambda > \omega_z, \tag{3.20}$$

In summary, we have calculated several ground state and dynamical properties of interest within the framework of mean-field theory. Comparing these to our results in fig. 3.9, we see that the mean-field theory accurately describes the ferromagnetic correlations deep in the para- or ferromagnetic regimes, where the system behaves like the bulk of an infinite system. As expected, mean-field theory fails to capture the behaviour around the quantum critical point, as well as the lack of true symmetry breaking in our system.

3.6.2 *Beyond the mean-field approach*

We will now improve on the mean-field approach by considering the first-order quantum correction to the above calculations. We apply a Holstein-Primakoff transformation [142] to express the spin operators in terms of bosonic creation and annihilation operators $a^\dagger$ and a, as

$$\begin{aligned} J_z &= -J + a^\dagger a, \\ J_+ &= \sqrt{2J} a^\dagger \sqrt{1 - a^\dagger a/(2J)}, \\ J_- &= \sqrt{2J} \sqrt{1 - a^\dagger a/(2J)}\, a. \end{aligned}$$

Remember that in our notation, J is a scalar, while J_z, $J_\pm$ are quantum operators. The standard approach is to substitute these expressions into the Hamiltonian and apply the approximation $\langle a^\dagger a \rangle \ll J$ i.e. we assume the state is not too far from a classical coherent state. This is a valid approximation in the paramagnetic regime and close to the critical point on the ferromagnetic side. We do not reproduce these rather long calculations here (see, for example ref. [138]). A more convenient (but ultimately equivalent) approach is to define effective position and momentum operators X and P, via

$$\begin{aligned} a &= (J^{1/6} X + \mathrm{i} J^{-1/6} P)/\sqrt{2}, \\ \text{and } a^\dagger &= (J^{1/6} X - \mathrm{i} J^{-1/6} P)/\sqrt{2}, \end{aligned}$$

such that $[X, P] = \mathrm{i}$. The exponent $1/6$ has been chosen such that the Hamiltonian now takes the elegant form

$$\begin{aligned} H = &- J - 1/2 && (3.21) \\ &+ \frac{1}{J^{1/3}} \left(\frac{1}{2} P^2 + \frac{1}{8} X^4 - \frac{\epsilon}{2} X^2 \right) && (3.22) \\ &+ \mathcal{O}(1/J^{2/3}), && (3.23) \end{aligned}$$

where we define $\epsilon = J^{2/3}(\lambda/\omega_z - 1)$. We now see this low-energy Hamiltonian is dominated in the limit $J \gg 1$ by the physics of a particle in a quadratic plus quartic type potential, with a double well structure appearing when crossing $\epsilon = 0$, as in the textbook Landau picture of a second-order phase transition [3]. At lowest order, the position and momentum operators are simply given by $X = J^{-2/3} J_x$ and $P = -J^{-1/3} J_y$. As plotted in fig. 3.9, the low energy Hamiltonian 3.22 sufficiently accounts for the measured deviations of the ferromagnetic correlator with respect to the thermodynamic limit around $\lambda = \omega_z$. In this sense, our 16 qubit system can be considered to be mesoscopic, since a first-order correction captures the measured finite-size effects.

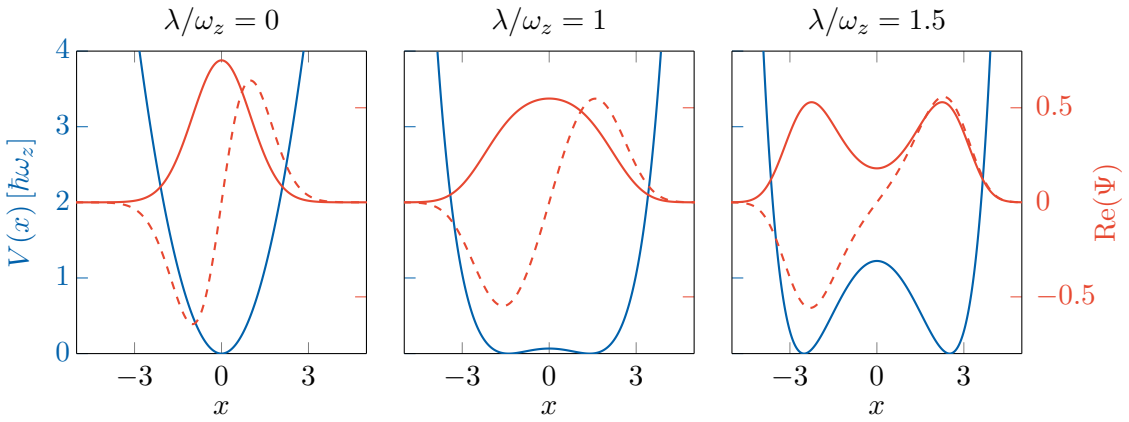

Figure 3.11: Equivalent 1-D potential $V(x)$ (blue curve) for the LMGm, for three values of the interaction strength λ/ω_z. The potentials are offset to set their minima to zero. See the text for the explicit expression for $V(x)$. The real part of the ground state and first-excited wavefunctions (calculated numerically) for a single particle in this potential $\mathrm{Re}(\Psi)$ are plotted with solid and dashed red curves respectively.

Exact mapping to double-well potentials

We briefly state here an interesting theoretical result whereby the exact spectrum of our Hamiltonian can be recovered from the stationary states of a single quantum particle in a cleverly chosen one-dimensional potential. This concept is already hinted at by the critical Hamiltonian eq. (3.22). Ulyanov and Zaslavskii [143] proved that the spectrum of our large-spin LMGm Hamiltonian corresponds to the first $2J+1$ eigenvalues in

$$\left(-(J-1/2)^{-1}\frac{d^2}{dx^2} + V(x)\right)\Psi = E\Psi,$$
$$\text{with the potential } V(x) = \frac{(2J-1)\omega_z}{\lambda}\sinh^2\tilde{x} - (J+1/2)\cosh\tilde{x}\,, \qquad (3.24)$$
$$\text{where } \tilde{x} = x\sqrt{\frac{\omega_z}{\lambda}}$$

Note that $1/J$ plays the role of $\hbar$ here such that classical dynamics are recovered in the $J \to \infty$ limit. Figure 3.11 shows the shape of this potential and its two lowest-lying states. In the ferromagnetic regime, we see the two nearly degenerate states of opposite parity separated by the gap δ which have the rough form $(|\mathrm{L}\rangle \pm |\mathrm{R}\rangle)/\sqrt{2}$, where $|\mathrm{L}\rangle$ and $|\mathrm{R}\rangle$ are states localised to the left and right wells respectively. This result has a fundamental link to the theoretically important class of quasi-exactly solvable quantum models [144], which have partial algebraic solutions. Such an equivalent potential can also be recovered from a Majorana polynomial representation of the LMGm's eigenstates [145, 146].

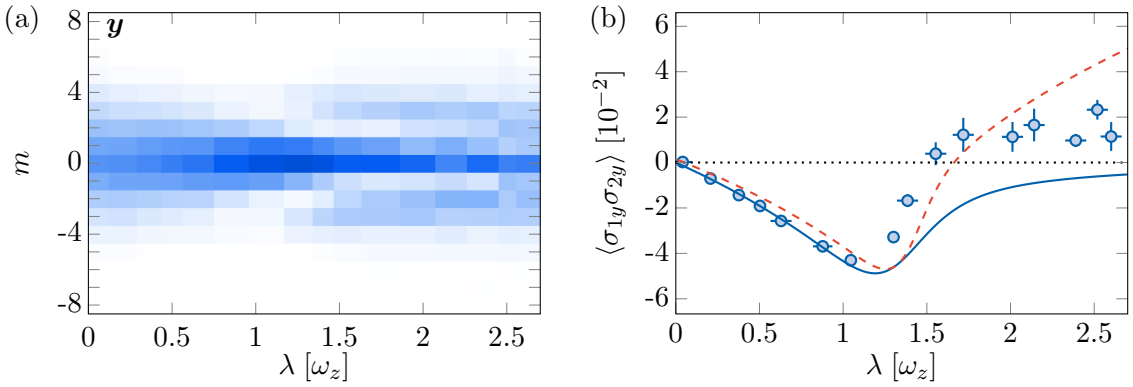

Figure 3.12: Nonclassicality and squeezing from the y-projection probabilities. (a) Measured projection probabilities $\Pi_m(\hat{\boldsymbol{y}})$ as a function of the interaction strength λ. (b) Evolution of the two-qubit correlator $\langle\sigma_{1y}\sigma_{2y}\rangle$. The solid blue, dotted black, and dashed red lines correspond to the $J = 8$ LMGm, mean-field approach, and critical Hamiltonian expansion respectively.

3.6.3 *Nonclassicality*

Measurements of the ground state presented so far, projected along x- and z-oriented measurement axes, gave us access to magnetic correlations and symmetry breaking (or the lack thereof). What then can the y direction tell us? We start with a Gaussian coherent state at $\lambda = 0$ ($\Delta J_x \Delta J_y = J/2$), and see an increase of the correlator $\langle\sigma_{ix}\sigma_{jx}\rangle$ i.e. an increase in the variance ΔJ_x^2. It follows that there can be a squeezing along the conjugated y-direction near the critical point (cf. one-axis twisting dynamics $H = -\chi J_x^2$ at short times). A squeezing is visually apparent in our measurements of the spin projection probabilities $\Pi_m(y)$ as we approach $\lambda/\omega_z = 1$ from the paramagnetic side, shown in fig. 3.12a. We also plot the resulting correlator $\langle\sigma_{1y}\sigma_{2y}\rangle$ which assumes negative values in a broad range of interaction strengths. In the ferromagnetic phase, the measured correlator significantly exceeds the expected values, which we attribute to shot-to-shot variations of the spin rotation parameters used for measurement along y, caused by magnetic field fluctuations.

In terms of the simulated qubits, separable states which are symmetric upon exchange must satisfy $\langle\sigma_{1\boldsymbol{n}}\sigma_{2\boldsymbol{n}}\rangle = \langle\sigma_{1\boldsymbol{n}}\rangle^2$ for all directions $\boldsymbol{n}$, and thus can only exhibit positive correlators [147, 148]. Therefore, the measured correlator corresponds to an entangled state of the simulated qubits, illustrating the fundamental role of quantum entanglement in driving the phase transition [4, 41]. We also see in fig. 3.12b that the mean-field calculation completely fails to capture this entanglement, which does in fact exist even in the thermodynamic limit [53]. The negative correlator appears at the level of the full first quantum correction at order $1/J$ [138], explaining the qualitative agreement of data with the critical hamiltonian expansion. From a theoretical point of view, the LMGm is a goldmine for the study of entanglement near the critical point [149–155]; measures such as the entanglement entropy and the concurrence can be studied along with their universal scaling, and exact calculations are possible in some cases.

Despite the above discussion, our system cannot be called entangled, since we cannot partition the qubit ensemble and access few-qubit observables. In other words, there is no way to speak of two entangled subsystems A and B within a single atomic spin J. This type of partition will be the main subject of the next chapter, where we also introduce criteria to demonstrate entanglement more pedagogically. For now, we restrict ourselves to stating that we have nonclassical behaviour at the level of the large spin, corresponding to quantum correlations of its internal degrees of freedom.

3.7 EXCITATIONS

We now extend our study to the dynamics of the system, by measuring the energy gaps of low-lying excitations. Consider the coherent evolution of an excited state of our system ψ, prepared at a coupling λ_f, where we are interested in measuring the frequency gap $\Delta_j^k \equiv \omega_k - \omega_j$ between the j$^{\text{th}}$ and k$^{\text{th}}$ excited levels:

$$\psi(t) = A_0 \left|0\right\rangle + \sum_{j=1}^{N} A_j \mathrm{e}^{-\mathrm{i}\omega_j t} \left|j\right\rangle ,$$

where the A_j's are complex amplitudes. The expectation value of an observable O evolves as:

$$\langle O\rangle(t) = \sum_{j=0}^{N} |A_j|^2 O_{jj} + \sum_{0\leq j<k\leq N} 2\mathrm{Re}(A_j^* A_k \mathrm{e}^{-\mathrm{i}\Delta_j^k t} O_{jk}) ,$$

where O_{jk} are matrix elements. There is an oscillating component at frequency Δ_j^k with amplitude $A_{j,k} = 2|A_j A_k O_{jk}|$ (assuming no other energy difference happens to coincide here). Hence, to optimise the signal, we should aim to prepare an initial excited state with maximal $|A_j A_k|$, and choose an observable with a large overlap $|O_{jk}|$.

3.7.1 *Breathing modes*

Due to the $\mathbb{Z}_2$ parity symmetry of the LMGm, the eigenstates can be divided into decoupled sectors of even and odd parity. We first focus on excitations to the even sector, which conserve the symmetry of the ground state. In a general LMGm system of N real qubits, the even gaps define the natural dynamics of the system in the paramagnetic phase. The energy scale, on the order of $\hbar\omega_z$, is set by the z-magnetic field, which in practice dominates symmetry-breaking environmental couplings of the type $\hbar\omega_{x,i}\sigma_{x,i}$. The lowest even gap, which we call the dynamical gap, Δ_0^2 (simply denoted Δ elsewhere in the chapter), is of particular interest. For instance, it is the dominant excited mode for a weak modulation of the interaction strength, since such an excitation cannot change the total spin J or the parity P_z. When the first odd gap (Δ_0^1 or δ) closes in the ferromagnetic phase, Δ_0^2 represents the fundamental excitation away from the manifold of the two broken-

symmetry states. Note that for system sizes $N \gtrsim 8$, Δ_0^2 is the lowest even excitation near $\lambda = 1$, across all total spin sectors (cf. fig. 3.5).

In the equivalent 1-D potential picture, symmetry-preserving excitations cannot change the mean position of the wavefunction; they correspond to breathing modes with oscillating width. Hence, $\langle \sigma_{1x}\sigma_{2x} \rangle$, or equivalently J_x^2, is a natural choice as the observable O. We continue with this intuitive choice for all even gaps Δ_j^{j+2}, rather than performing a rigorous optimisation of the overlap $|O_{jk}|$.[3] We use a time-dependent coupling $\lambda(t)$ to excite our system and measure gaps at a target interaction strength λ_f. The system is initialised at $\lambda = 0$, followed by the use of one of three complementary methods:

1. Quench directly to $\lambda = \lambda_f$. This method is useful to probe the lowest gap Δ_0^2 in the paramagnetic regime, where method 2 is too gentle to create significant excitations.

2. Linearly ramp to λ_f at five times the ramp rate previously used for ground state preparation, leading to diabatic population of excited levels. This method works well to probe Δ_0^2 in the ferromagnetic regime, where method 1 is too violent.

3. Quench to an intermediate coupling λ_i, wait there for duration t_i, and then quench to λ_f. This method is convenient for higher gaps, as (λ_i, t_i) can be optimally chosen to target a given pair of levels.

The three methods are compared numerically in fig. 3.13, in terms of the figure of merit for the prepared state $A_{j,k} = |A_j A_k|$. As evident from the experimental findings below, these methods work well enough for our purposes, whereas a more sophisticated approach would be to choose the evolution of the classical control parameter $\lambda(t)$ based on quantum optimal control theory [156]. The entire process of nonclassical state preparation, suited for a particular application, followed by probing a well-constructed observable, can be generalised to a variationally optimised quantum circuit, as shown in the context of metrology in a recent work by Kaubruegger et al. [157].[4]

We now present our results. When the measured oscillations have only a single frequency component, as is the case for Δ_0^2 in fig. 3.14a, we extract the frequency from a sinusoidal fit to the data. When there are two or more components, as in fig. 3.14b, we instead locate peaks in the Fourier power spectrum. Such individual spectra were taken for gaps up to Δ_8^{10}, following which we combine the spectra to get a series of gaps for a particular value of the coupling λ/ω_z, as shown in fig. 3.15. The spectra measured for three different couplings $\lambda/\omega_z = 0.50(2), 1.00(2), 3.8(1)$ in fig. 3.16. Finally, fig. 3.17 summarises all the results on a energy level diagram, also including additional

[3] Such an optimisation would also need to account for the scaling of experimental uncertainties when measuring higher order spin moments.

[4] The authors considered applying J_x^2-type operators to a qubit ensemble, in order to maximise the sensitivity of the total spin to an external magnetic field. This proposal was subsequently implemented with trapped ions [158].

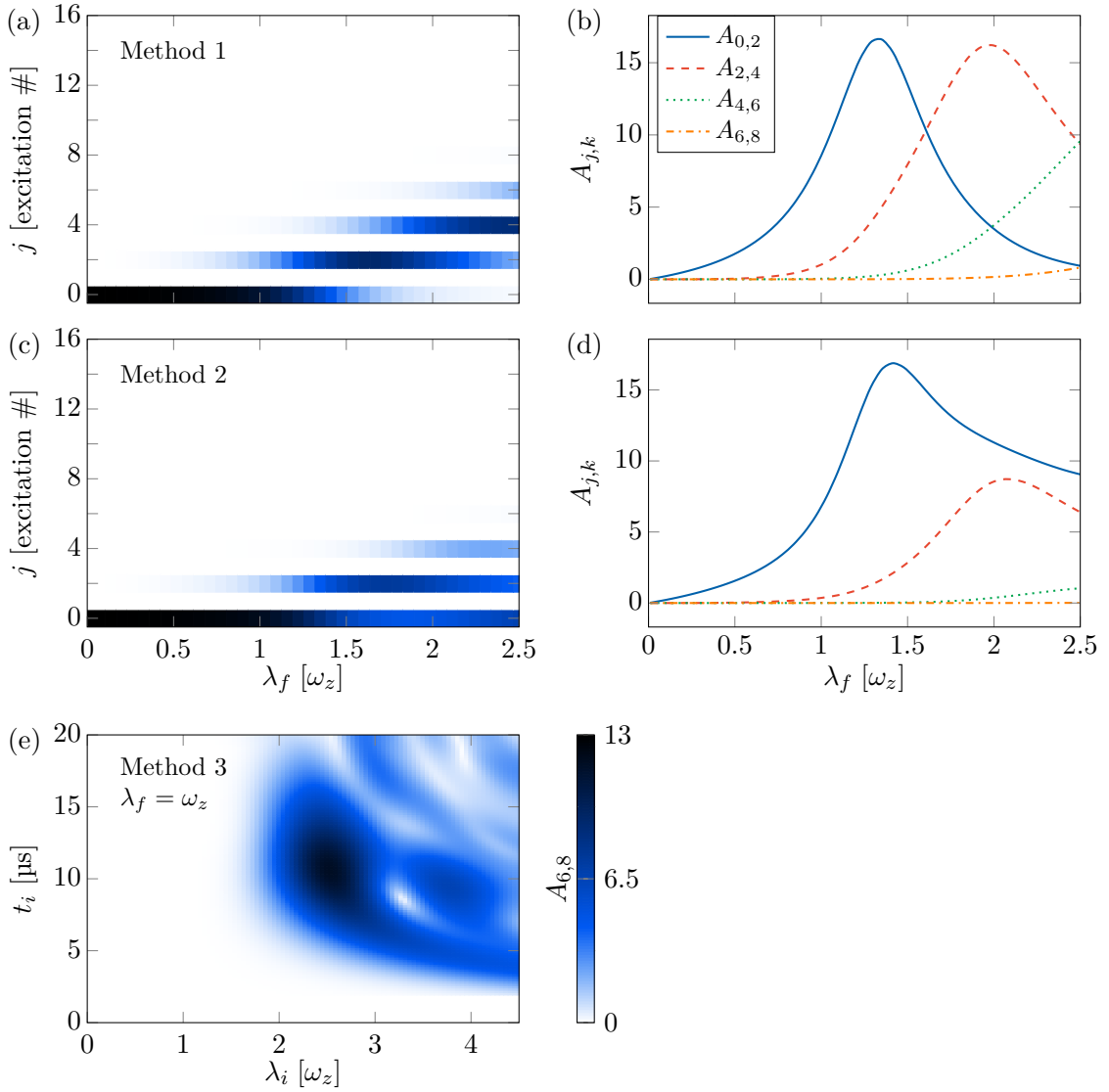

Figure 3.13: Comparison of the three methods to prepare superposition states for gap measurements at $\lambda = \lambda_f$. Method 1: Direct quench to λ_f. (a) The resulting relative occupation probabilities of the j^{th} excited level. (b) The corresponding amplitude $A_{j,k}$ for the observable J_x^2 at frequency Δ_j^k, linked to the energy gap between the j^{th} and k^{th} excited levels. Method 2: A fast (non-adiabatic) ramp to λ_f. (c),(d) The same quantities as above. Method 3: Quench to intermediate coupling λ_i for duration t_i, then quench to λ_f. As an example, we show in (e) the amplitude of the Δ_6^8 oscillation for $\lambda_f = \omega_z$. It is optimised at $(\lambda_i, t_i) \simeq (2.5\,\omega_z, 10.6\,\mu\text{s})$

measurements of Δ_0^2.[5] For these large data sets, we had to compromise between several experimental considerations, while keeping the total duration of a measurement run below 12 hours – the maximum reasonable continuous running period without recalibrations for our ultracold atom machine. Firstly, the time resolution must be sufficient to resolve higher energy gaps, and to rule out possible excitations there, even when our

[5] The Δ_0^2 measurements were also used as an absolute calibration of the coupling strength λ. We fit to the theoretically expected gap, with a single free parameter, namely the proportionality factor between λ and a photodiode voltage measured at a pick-up mirror on the path of the 626 nm beam.

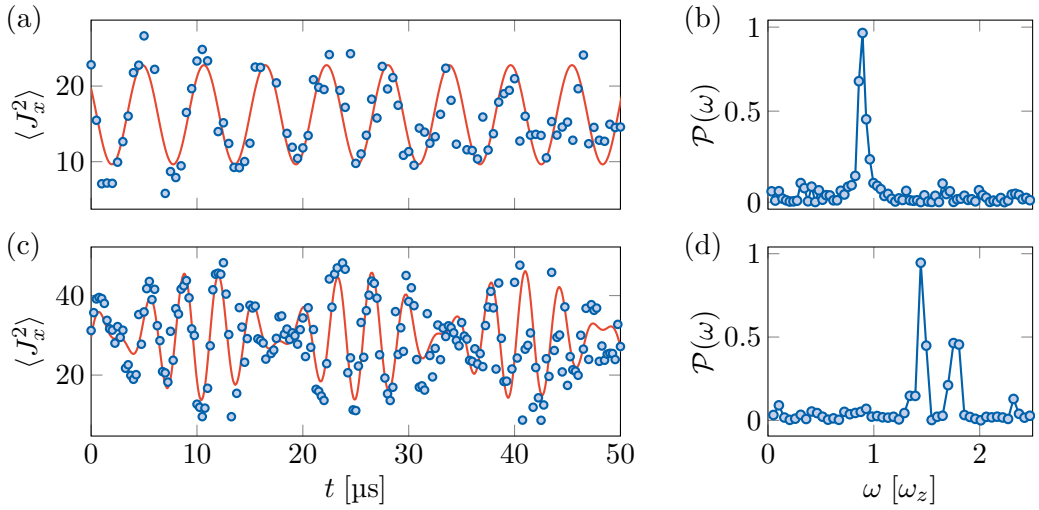

Figure 3.14: Measuring breathing mode frequencies. (a,c) Time evolution of the second moment $\langle J_x^2 \rangle$ for a coupling $\lambda = \omega_z$, following a weak excitation to populate levels $j = 0, 2$ (a) or a stronger excitation to levels $j = 2, 4, 6$ (c). (b,d) Respective Fourier spectra of the (a,c) evolutions.

protocol only targets lower frequencies. Secondly, the frequency resolution (limited by the maximum measured time) should allow separation of adjacent peaks in the spectrum. The final limitation is shot-to-shot fluctuations of the axial magnetic field along z at the 0.8 mG level. This leads to a typical effective broadening of $\delta\omega_z \, \mathrm{d}\Delta_j^k / \mathrm{d}\omega_z \simeq 0.02\,\omega_z$ for our parameters. These precautions, supplemented by numerical checks, justify the post hoc identification of spectral peaks with specific LMGm gaps.

We now interpret these spectra in terms of particle motion of the effective potentials introduced in section 3.6.2. In the paramagnetic phase ($\lambda = 0.5\,\omega_z$), the measured spacings remain close to each other, corresponding to a nearly harmonic trap (see fig. 3.16a). At the critical point $\lambda = \omega_z$, the successive spacings Δ_j^{j+2} increase more steeply with j (see fig. 3.16b), as expected for a particle evolving in the purely quartic potential [159] (see the Hamiltonian 3.22 at the critical point). This non-harmonic behaviour illustrates a defining property of quantum critical systems, whose low-energy spectra cannot be simply reduced to non-interacting excitation quanta [4]. Deep in the ferromagnetic phase ($\lambda = 3.8\,\omega_z$, fig. 3.16c and fig. 3.17), the spacings are not ordered monotonically and exhibit a minimum between the 6^{th} and 8^{th} levels. This can be explained by the fact that these energy levels are close to the tip of the corresponding double-well potential. Our observations are reminiscent of the divergence of the density of states at the tip of a macroscopic double-well potential [160], and are a signature of the occurrence of an excited-state quantum phase transition in the thermodynamic limit [141]. The lowest gap Δ_0^2, which is most directly relevant to the ground state phase transition, will be discussed further in the following section, where we contrast its behaviour with the parity gap Δ_0^1.

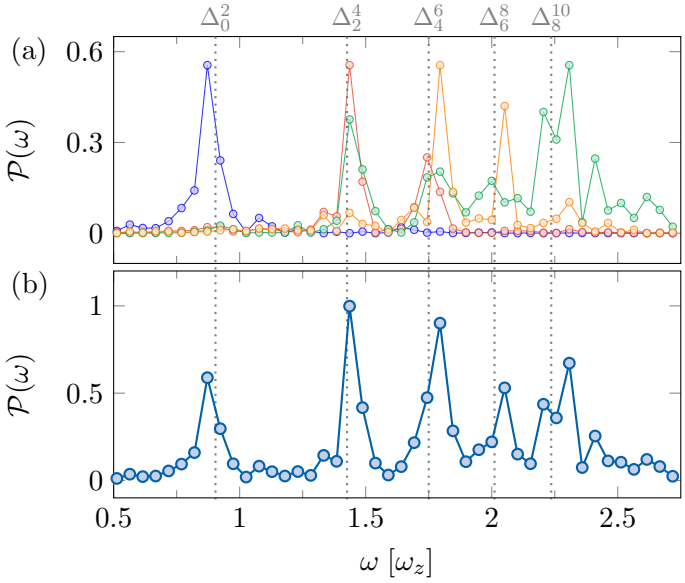

Figure 3.15: (a) Oscillation spectra measured at $\lambda/\omega_z = 1$, after an excitation pulse at intermediate coupling $\lambda_i/\omega_z = 1.2$, 2.1 2.66, and 3.25 for a duration $t_i = 11\,\mu s$, $7\,\mu s$, $13.5\,\mu s$ and $12\,\mu s$, plotted in indigo, red, green, and orange respectively. (b) Combined spectrum obtained by summing the previous four spectra. The theoretical values for the gaps Δ_k^j are denoted with grey dotted curves. On each spectrum, the background noise level is decreased by applying a Gaussian filter of rms width $0.5\,\omega_z$, centred on the most intense Fourier frequency.

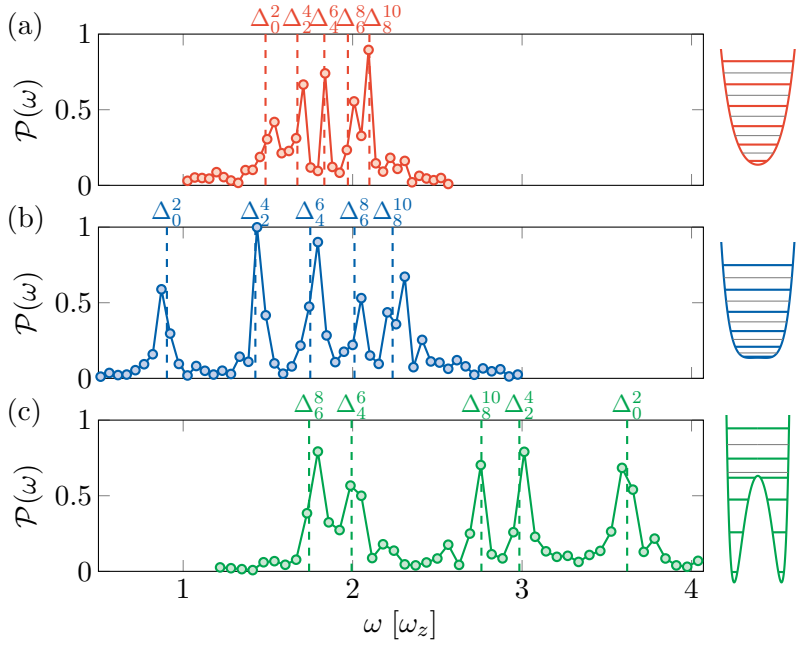

Figure 3.16: (a-c) Excitation Fourier spectra measured for $\lambda/\omega_z = 0.50(2)$ (a, red dots), 1.00(2) (b, blue dots) and 3.8(1) (c, green dots). The vertical dashed lines correspond to theoretical frequency spacings Δ_j^{j+2}. The right panels show the effective potentials and energy spectra for each interaction strength. The thin grey lines indicate odd-parity states, not excited with this protocol.

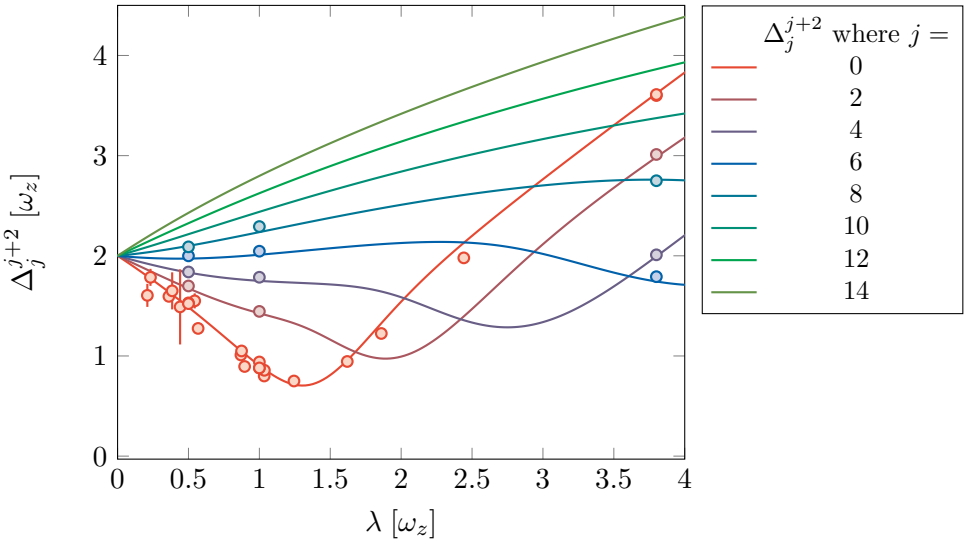

Figure 3.17: Summary of measured frequency spacings between even excited states compared to the LMGm (solid lines). Spectra taken at interaction strengths $\lambda/\omega_z = 0.50(2)$, $1.00(2)$ and $3.8(1)$ with method 3 (see text), are complemented with additional measurements of the lowest gap Δ_0^2 using methods 1 and 2.

3.7.2 *The dipole mode*

For the remainder of the chapter, we will study the effect of couplings which break the $\mathbb{Z}_2$ symmetry of our system. In a system of N independent qubits, such couplings could take the form $\hbar\omega_{x,i}\sigma_{x,i}$, where $\omega_{x,i}$ is a local magnetic field along x acting on the i^{th} qubit. Terms of this form in the Hamiltonian can flip individual qubits and do not conserve the total spin $\boldsymbol{J}^2$. Our large-spin realisation of the LMGm is intrinsically limited to a uniform x-field $\hbar\omega_x J_x = \sum_i \hbar\omega_x\sigma_{x,i}$, which only breaks the $\mathbb{Z}_2$ symmetry. Here we pulse this perturbation to create excitations in odd levels, while in the next section we will study the ground state properties in a static x-field.

Following the discussion on gap measurement from the previous section, we would ideally like to create a roughly equal superposition of the ground and first excited states without involving the higher levels. We choose a small magnetic pulse amplitude with pulse duration $t \simeq 3\,\mu\text{s}$, and experimentally verify that only the two states of interest are populated. A smaller pulse area is needed to achieve a good measurement in the ferromagnetic regime, where the state is more sensitive to B_x fields. We account for this by further halving the amplitude when working at $\lambda/\omega_z > 1$. We saw that the even excitations are breathing modes in the effective potential well picture, which lead to oscillations in the second-order moments. In contrast, odd excitations are dipole modes, and the natural observable to consider when probing the parity gap δ is the first-order moment $\langle J_x\rangle$.

In fig. 3.18a, we show an example of a measured oscillation, along with the fit used to extract the gap. Our results as a function of interaction strength are plotted in fig. 3.18b, where we also show the dynamical gap Δ for comparison. The dynamical

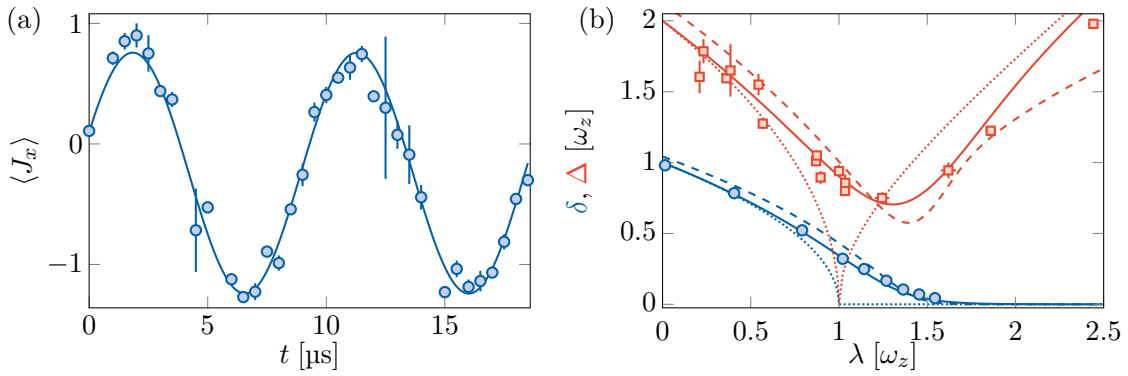

Figure 3.18: Dipole mode excitations and comparison to the breathing mode. (a) Dipole mode oscillation performed for $\lambda = 0.79(2)\,\omega_z$. The solid line is a sinusoidal fit to determine the gap δ. (b) Parity gap δ between even- and odd-parity sectors (blue disks) and dynamical gap Δ between the ground and first even-parity states (red squares), as a function of the coupling λ. The solid, dotted, and dashed lines are the exact LMGm, mean-field, and critical Hamiltonian predictions respectively.

gap Δ exhibits a minimum around the critical point, reminiscent of the gap closing in the thermodynamic limit at the transition point. The parity gap δ decreases when the coupling λ increases, in analogy with the softening of the spin dipole mode in quantum systems close to a ferromagnetic transition [161, 162]. The crossover from $\Delta/\delta \sim 2$ in the paramagnetic phase to a highly non-harmonic $\Delta/\delta \sim 3$ at the critical point reiterates the picture of emerging interacting quanta, as previously revealed by our measurements of the spectra of even gaps. As was the case for ground state properties, the deviations from the thermodynamic limit in the crossover region are well captured by the critical Hamiltonian.

For a finite system, the values of the gaps (and spin observables) at the critical point are described by the theory of finite-size scaling, introduced in section 3.3, which we investigate numerically for our system. The linear scaling of Hilbert space dimension with J and the decoupled odd and even parity sectors makes exact diagonalisation feasible up to $J \sim 2^{22}$.[6] As shown in fig. 3.19, for the parity gap we recover $\delta \sim J^{-1/3}$, a result initially proposed in ref. [56], which has since been analytically calculated by Dusuel and Vidal [137]. The same scaling exponent also seems to apply to the dynamical gap at the critical point. Our experimental measurements at $\lambda = \omega_z$ ($\Delta = 0.91(5)\,\omega_z, \delta = 0.33(1)\,\omega_z$) agree well with the numerical results, but deviate by about $0.1\,\omega_z$ from the limiting finite-size scaling behaviour. The finite-size scaling exponents are fundamental to the quantum critical point itself, with direct links to the critical exponents in the LMGm, and also to the exponents of the corresponding short-range model (i.e. the transverse-field Ising model introduced at the start of the chapter) [56, 136]. Indeed the scaling behaviour at $\lambda = \omega_z$ is drastically different to the paramagnetic phase ($\delta - \delta_\infty \sim J^{-1/2}$), and to the ferromagnetic phase, where $\delta \sim \mathrm{e}^{-aN}$ [163]. Let us take a closer look at the dynamical consequences of this exponentially small gap attained for $\lambda > \omega_z$.

[6] Conveniently, the Hamiltonian for the odd or even subspaces is tridiagonal in the z-Dicke basis.

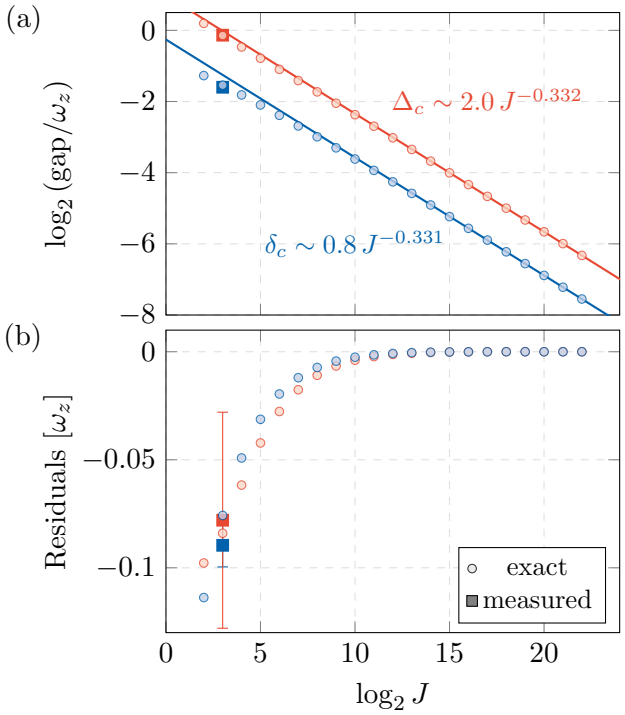

Figure 3.19: Finite size scaling of the gaps at the critical point (a) The parity (δ_c, blue) and dynamical (Δ_c, red) gaps at the critical point $\lambda/\omega_z = 1$ as a function of the system size J. We show exact diagonalisation (circles) and our experimental results at $J = 8$ (squares). Fitted scaling exponents are consistent with $1/3$ for both gaps. (b) Deviation of the numerics and experiments from the fitted universal behaviour in the thermodynamic limit.

3.7.3 *Tunnelling in the ferromagnetic phase*

We now focus on the dipole oscillation measurements in the ferromagnetic phase, where we measure a strong reduction of the parity gap (see fig. 3.20a) and a near-degeneracy of the even- and odd-parity ground states. Figure 3.20b,c compares the time evolution of the probability distributions $\Pi_m(\hat{x})$ during the dipole oscillation in the paramagnetic and ferromagnetic phases. In the paramagnetic phase, the distributions always exhibit a single peak, whose centre smoothly oscillates around zero. On the other hand, the ferromagnetic phase distributions exhibit two peaks at positive/negative large-$|m|$ values, with oscillations between these configurations, without significantly populating intermediate m levels. This qualitative change in the dynamics is well illustrated by the evolution of the most probable projection m^*, which only takes two possible values $m^* = \pm 6$ during the evolution shown in fig. 3.20c. These maximal projection values are close to the collective spin projections $\langle J_x \rangle = \pm 5.4(5)$ of the two corresponding mean-field broken-symmetry states. This behaviour can be interpreted as a 'macroscopic' quantum tunnelling between broken symmetry states – a phenomenon that has been extensively studied in single-molecule magnets [128, 164–166] and SQUID systems [167–169].

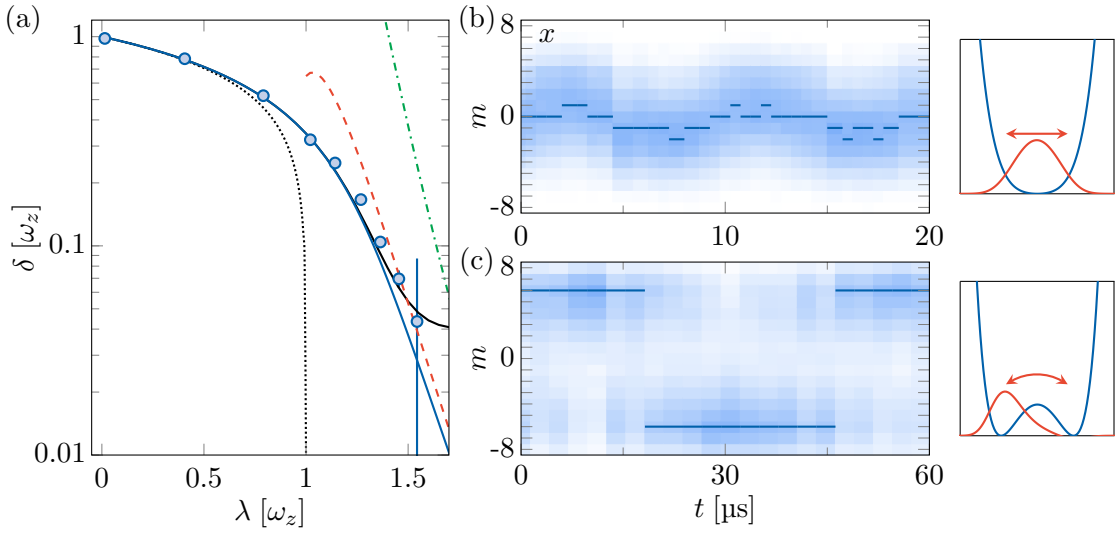

Figure 3.20: Tunnelling in the ferromagnetic phase (a) Parity gap δ as a function of λ (blue dots), compared with the $J = 8$ LMGm (blue line), mean-field theory (black dotted line), semi-classical tunnelling (red dashed line) and perturbation theories (green dash-dotted line). The solid black line is the mean value of δ expected from the LMGm and averaged over magnetic field fluctuations. (b,c) Time evolution of the projection probabilities $\Pi_m(\hat{x})$ during a dipole mode oscillation for $\lambda = 0.79(2)\,\omega_z$ (b) and $\lambda = 1.36(2)\,\omega_z$ (c). The most probable projection m^* is plotted as a blue line. The panels on the right use the effective 1-D potential to illustrate the change of dynamics from a simple dipole oscillation to a tunnelling behaviour.

Deep in the ferromagnetic phase, the dipole mode frequencies are consistent with the semi-classical theory of quantum tunnelling (see fig. 3.20a). This approach considers the problem of a particle in the double well potential equivalent to the LMGm, and applies the WKB approximation to calculate the tunnelling gap [170, 171], or uses a path-integral formalism with the instanton technique [172–174]. We also compare our results to perturbation theory calculations, which gives a simple picture of tunnelling in the limit $\lambda \gg \omega_z$. Here, the two broken-symmetry states $|\pm J\rangle_x$ are coupled by the z field via a process of order $2J$, leading to a high power-law scaling $\delta/\omega_z \propto (\omega_z/\lambda)^{2J-1}$. Deep in the ferromagnetic regime, our measured oscillation contrast decreases, and the frequency deviates from theory in a manner that can be understood in terms of magnetic field fluctuations along x (rms width 0.4 mG). These induce an energy offset between the two wells, which for $\lambda \gtrsim 1.5\,\omega_z$ dominates the tunnel splitting.

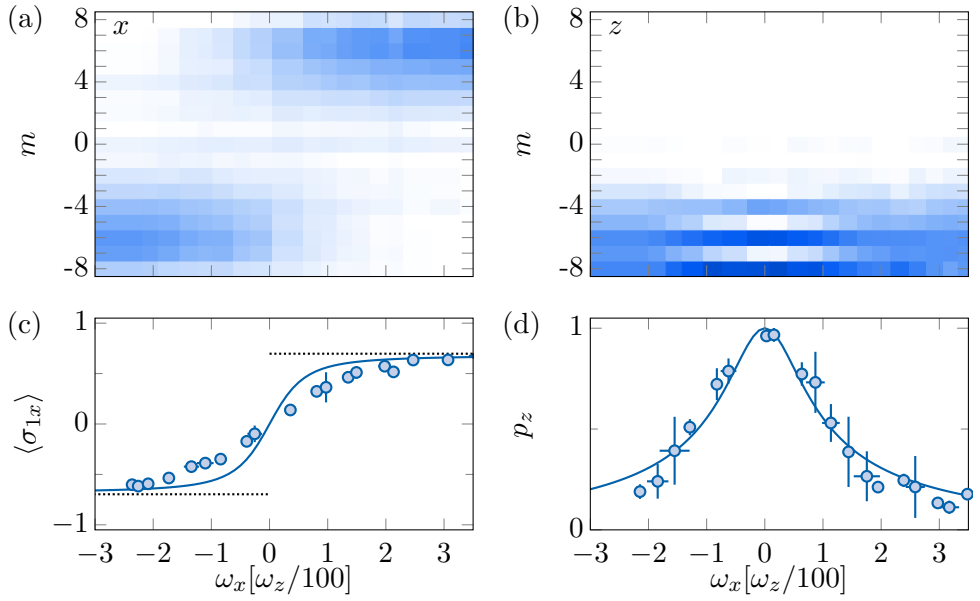

Figure 3.21: Link between symmetry breaking and a finite order parameter. (a,b) Projection probabilities $\Pi_m(\hat{x})$ (a) and $\Pi_m(\hat{z})$ (b) in the ground state as a function of ω_x, for $\lambda = 1.40(3)\,\omega_z$. (c,d) Order parameter $\langle\sigma_{1x}\rangle$ and mean parity p_z computed from (a,b) respectively, with comparison to the $J = 8$ LMGm (solid lines) and the mean-field order parameter (dotted lines in (c)).

3.8 SYMMETRY BREAKING

3.8.1 *In a static field*

We expand our discussion of symmetry breaking in the LMGm to consider the ground state properties of our system in the presence of a static transverse magnetic field ω_x, such that the Hamiltonian now reads

$$H = -\frac{\hbar\lambda}{2J-1}J_x^2 + \hbar\omega_z J_z - \hbar\omega_x J_x\,. \tag{3.25}$$

As before, we adiabatically ramp the coupling λ and probe the prepared ground state. Our results (see fig. 3.21) for a coupling strength $\lambda = 1.40(3)\,\omega_z$ show that the application of a small perturbation ω_x, on the order of a few per cent of ω_z causes significant polarisation of the total spin along x. This measurement is in the regime where the field is smaller than the parity gap, $\omega_x \lesssim \delta$, such that the effect of the x-field is essentially to tilt the equivalent 1-D potential and localise the ground state wavefunction to a single well, as sketched in the inset of fig. 3.22d. Hence, the magnetisation, i.e. the standard Ising order parameter, attains a value consistent with that of the mean-field broken symmetry state (at zero x-field) $\langle\sigma_{1x}\rangle = \mathrm{sgn}\,(\omega_x)\sqrt{1-(\omega_z/\lambda)^2}$.[7] Larger fields would

[7] Our projective Stern-Gerlach measurement is now the presence of a bias field along a direction $\boldsymbol{u} = \{\omega_x, 0, \omega_z\}$. As a result, the order parameter along $\mathbf{u}$ is given by $\langle\sigma_{1x}\rangle^{\boldsymbol{u}} = \langle\sigma_{1x}\rangle - \omega_x/\omega_z\langle\sigma_{1z}\rangle$. This leads to corrections of $\lesssim 3\,\%$ to our order parameter, which we wish to probe in the lab coordinate basis; we apply these corrections to our data when using them to fit the susceptibility.

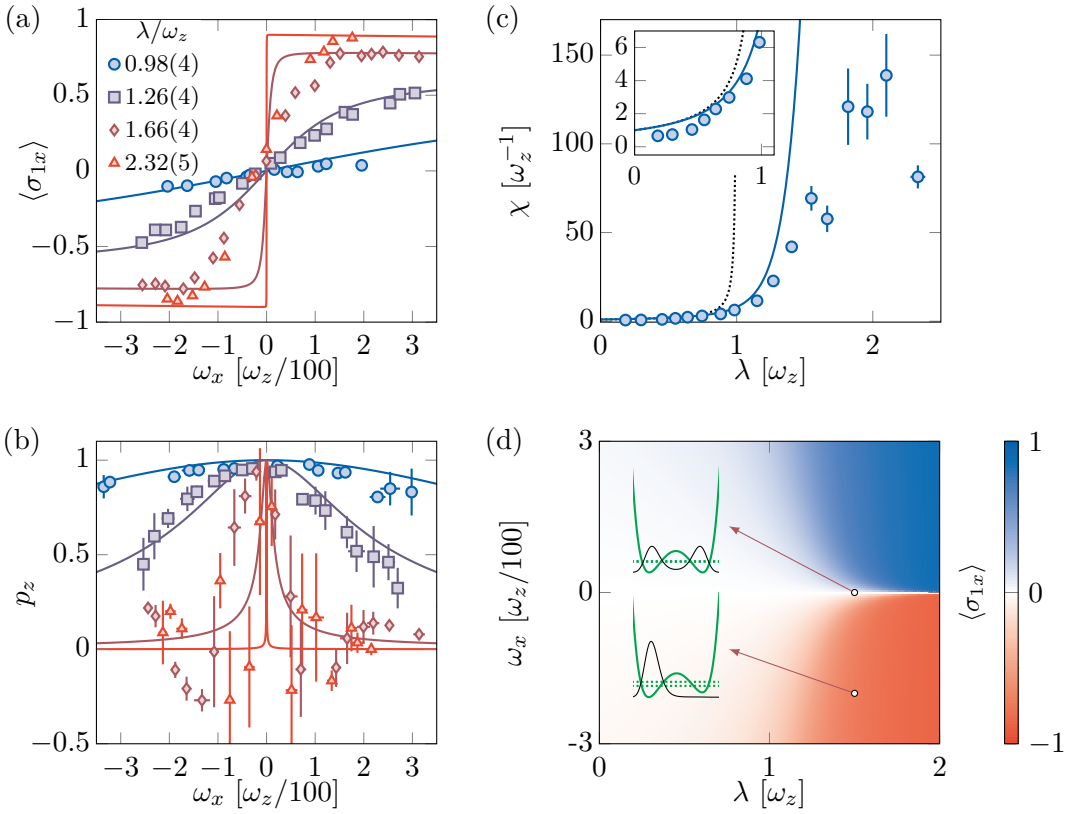

Figure 3.22: Symmetry breaking in a static field. (a) Order parameter $\langle\sigma_{1x}\rangle$ and (b) mean parity p_z as a function of the transverse magnetic field ω_x for different couplings λ. (c) The susceptibility χ compared to the $J = 8$ LMGm (solid blue) and the mean-field values (dotted black). The inset is a zoom-in on small χs. (d) The calculated order parameter $\langle\sigma_{1x}\rangle$ of the $J = 8$ LMGm ground state as a function of λ and the transverse field ω_x. The insets show the equivalent single-particle potentials (solid green), the energies of the ground and first excited states (dashed green), and the squared modulus of the ground state wavefunction (black) for the points $(\lambda/\omega_z, \omega_x/\omega_z) = (1.5, 0)$ and $(1.5, -0.02)$.

distort the effective double well, changing the position of the minimum, and allowing $\langle\sigma_{1x}\rangle$ to increase further – ultimately reaching $\pm J$ in the limit $\omega_x \gg \omega_z$.

Concurrently with this polarisation of the spin, we measure a loss of parity, as evident in the z-projection probabilities in fig. 3.21b. Increasing the field leads to a near-equal occupation of odd and even sublevels i.e. $p_z \sim 0$, implying the $\mathbb{Z}_2$ symmetry has been broken. This highlights the fundamental link between the breaking of symmetry and the appearance of a non-zero order parameter. In macroscopic systems, the symmetry itself is not an accessible observable: in a ferromagnet composed of N spin 1/2's, measuring the parity requires simultaneously measuring all individual polarisations σ_{iz}. Hence, the symmetry breaking can only be inferred indirectly from an order parameter. The mesoscopic nature of our system, effective averaging over the atomic cloud in a single shot, and single m-level detection make this striking measurement possible.[8]

[8] Such discrete symmetries can also be directly observed by probing spatially ordered phases with single-site detection, as shown for 1-D Rydberg arrays in ref. [175].

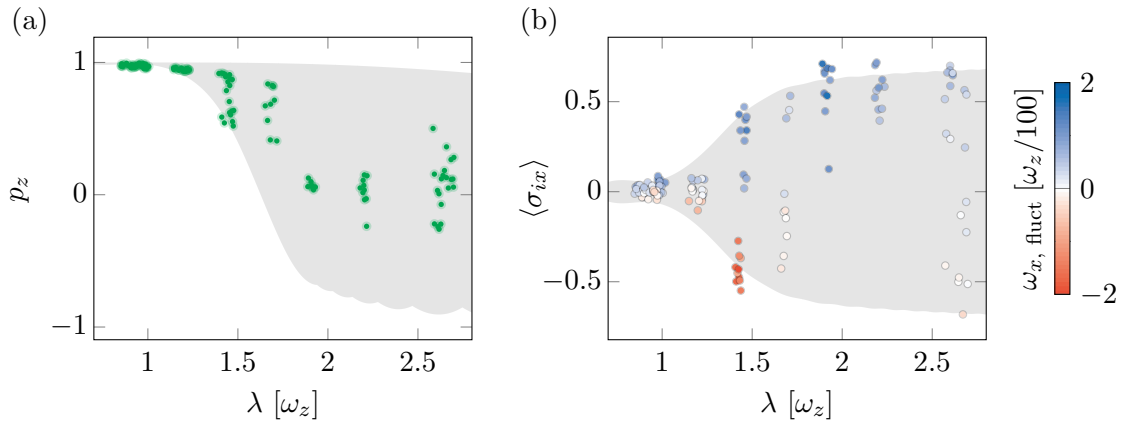

Figure 3.23: Spontaneous symmetry breaking due to environmental magnetic field fluctuations (a) The mean parity p_z associated with the $\mathbb{Z}_2$ symmetry of the LMGm phase transition after a slow ramp up of the coupling λ. Each point represents a single shot. (b) The order parameter $\langle\sigma_{ix}\rangle$, where the colour of the points encodes the independently recorded environmental magnetic field fluctuations along x, $\omega_{x,\mathrm{fluct}}$. Note that the lack of points with $\langle\sigma_{ix}\rangle < 0$ near $\lambda = 2$ occurred due to a slow global drift to positive values of the x-field during the experimental run. The shaded areas represent the expected effect (at 2-σ) of transverse field fluctuations of rms width $0.007\,\omega_z$.

We now extend these measurements to different interaction strengths. Our results in fig. 3.22a,b show the increasing sensitivity of the spin polarisation and mean parity to transverse perturbations as we go deeper into the ferromagnetic regime.[9] This effect is quantified by the susceptibility, $\chi = \mathrm{d}\langle\sigma_{1x}\rangle/\mathrm{d}\omega_x|_{\omega_x=0}$, which we determine by a linear fit to the x-magnetisation around $\omega_x = 0$. Although our experimental results are in good agreement with the LMGm in the paramagnetic phase, we observe an enhanced deviation upon increasing λ; this is caused by magnetic field fluctuations along x, which also limited the determination of the parity gap in the previous section. In the thermodynamic limit, χ diverges at the critical point as $(1-\lambda/\omega_z)^{-1}$, with critical exponent $\gamma = 1$.[10] The finite-size remnant of this behaviour is apparent in the sharp increase in susceptibility measured, and also in fig. 3.22d, where we plot the calculated magnetisation $\langle\sigma_{1x}\rangle(\lambda,\omega_x)$ of the ground state of eq. (3.25). In the thermodynamic limit, the quantum critical point at $\lambda/\omega_z = 1$ extends to a line of first-order phase transitions along the line $\omega_x = 0$, when $\lambda/\omega_z > 1$.

3.8.2 *Spontaneous symmetry breaking*

Another way to see symmetry breaking is using the shot-to-shot fluctuations of magnetic field inherent to our experimental setup, in particular by making their effect more pronounced by increasing the timescales involved. We show in fig. 3.23 the preparation of the LMGm ground state using a slow ramp of the coupling, with speed $\dot{\lambda} \simeq 0.006\,\omega_z^2$

[9] The negative values of parity at certain values of the field are an artefact resulting from imperfect adiabaticity of our ground state preparation ramp.
[10] This can be derived following the methods presented in section 3.6.1.

i.e. 2.5 times slower than the ramps used so far and corresponding to a total ramp time of $\simeq 360\,\mu s$ for the largest interaction strengths shown here. In this regime, we indeed recover spontaneous symmetry breaking for $\lambda \gtrsim 1.5\omega_z$, as evidenced by the sharp drop in the mean parity. Furthermore, we see a bifurcated distribution appearing in the order parameter $\langle \sigma_{ix} \rangle$ (cf. the bifurcation in projection probabilities in fig. 3.9, where the symmetry was not broken). As demonstrated in fig. 3.23b, the order parameter's sign is determined by the direction of the environmental B-field fluctuations $\omega_{x,\mathrm{fluct}}$, which are recorded with an independent magnetic probe adjacent to the science cell.

3.8.3 *Interaction-induced symmetry breaking*

Finally, we consider symmetry breaking due to interatomic interactions. By what mechanism can interactions cause symmetry breaking in our setup? Consider an ensemble where the spin state of each atom has been initialised to the ground state of the LMGm, deep in the ferromagnetic regime ($\lambda \gg \omega_z$). This ground state is roughly $|\psi_0\rangle = (|m_x = -J\rangle + |m_x = +J\rangle)/\sqrt{2}$, whereas the (nearly degenerate) first excited state of odd parity is $|\psi_1\rangle = (|m_x = -J\rangle - |m_x = +J\rangle)/\sqrt{2}$. Then, the scattering channel $|\psi_0\rangle_A \otimes |\psi_0\rangle_B \to |\psi_1\rangle_A \otimes |\psi_1\rangle_B$ for a pair of atoms A, B provides a clear candidate for a symmetry breaking process. The full treatment of this problem in the s-wave collision limit involves $J+1$ independent scattering lengths a_K, where $\boldsymbol{K} = \boldsymbol{J}_A + \boldsymbol{J}_B$ is the total electronic angular momentum of the colliding atoms.[11] Only one of these is known, $a_{2J} = 112(10)\,a_0$ [176], namely the background scattering length for two atoms in $m_z = -8$. So it is not feasible to make quantitative predictions about the expected rate of symmetry breaking processes. Instead, we give an order of magnitude estimate for two atoms in a BEC occupying the same spatial mode. Consider the evolution due to interactions for the initial state

$$|\psi_0\rangle_A \otimes |\psi_0\rangle_B = frac|-J\rangle_A\,|-J\rangle_B + |-J\rangle_A\,|J\rangle_B + |J\rangle_A\,|-J\rangle_B + |J\rangle_A\,|J\rangle_B 2\,.$$

The first and fourth terms only project onto the $K = 2J$ manifold, and the associated interaction energy scale is set by

$$E_{++} = \frac{4\pi\hbar^2 a_{2J}}{M}\,n\,, \tag{3.26}$$

where n is the atomic density. We are not as lucky for the corresponding energy E_{+-} of the second and third terms, which involves all K's. The dynamics of the mean parity is set by the phase difference induced by these energies: at time $t_{\mathrm{odd}} = \pi\hbar/|E_{+-} - E_{++}|$, we

[11] Dipolar relaxation process are negligible since $|\psi_0\rangle$ and $|\psi_1\rangle$ form the ground state manifold.

reach the odd-parity state $|\psi_1\rangle_A \otimes |\psi_1\rangle_B$. With no other prior information, a reasonable guess is[12]

$$E_{+-} - E_{++} \sim \frac{4\pi\hbar^2 a_{\mathrm{vdW}}}{M} n\,, \tag{3.27}$$

where $a_{\mathrm{vdW}} \simeq 160\, a_0$ is the van der Waal's length for dysprosium [110].

In our preliminary attempts to see symmetry breaking due to interactions, we used a BEC and prepared the LMGm ground state in the ferromagnetic regime, up to $\lambda/\omega_z \sim 2.5$. The density of the cloud was $n \sim 10^{14}\,\mathrm{cm}^{-3}$, corresponding to a symmetry breaking timescale $t_{\mathrm{odd}} \sim 0.7\,\mathrm{ms}$, i.e. a duration for which environmental transverse field fluctuations also play a significant role. Our measurements, when compared to our previous results with a thermal cloud, were not sufficient to identify an effect of interactions on the mean parity. Unfortunately, a thorough investigation was prevented by practical issues.

We note that the collisions considered here couple the internal state of each atom to the kinetic degrees of freedom of the cloud, and could potentially lead to the thermalisation of the spin degrees of freedom [178]. For the isolated LMGm studied in this chapter, thermalisation is precluded by the system's integrability [133, 134]. Finite-temperature effects would be most prominent near the critical point, where the spectrum is most dense, and they could be further boosted by increasing $k_{\mathrm{B}}T/\hbar\omega_z$. The restriction to the maximal spin sector $J = N/2$ changes the partition function of the system compared to the full N-qubit LMGm, and it has been theorised that this leads to fundamentally different finite-temperature properties [179].

[12] In fact, the scattering lengths are distributed according to $a_K \simeq 0.5\, a_{\mathrm{vdW}}(1 + \tan\Phi_K)$ [177], and we have no a priori knowledge of the Φ_K's, so the distribution has infinite variance!

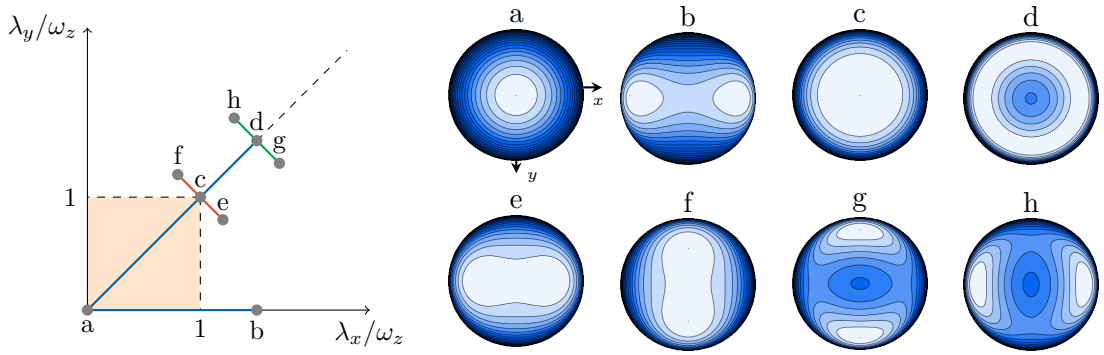

Figure 3.24: Phase transitions in the two-axis LMGm model, with ferromagnetic interactions $-\lambda_x J_x^2$ and $-\lambda_y J_y^2$. The panels on the right show semi-classical energy landscapes at the points labelled a-f in the λ_x-λ_y parameter space, with minima in white. The ground state is symmetric in the orange region, and leaving it (e.g. following the blue path a→b) leads to symmetry breaking by a 2nd order phase transition, i.e. the main subject of this chapter. The isotropic line $\lambda_x = \lambda_y$ is a special case where the ground state is always an eigenstate of J_z (see text). The blue path a→d also shows a 2nd order at transition at $\lambda_x = \lambda_y = \omega_z$, but of a different universality class. Crossing the isotropic line $\lambda_x = \lambda_y$ can also lead to 1st and 3rd order transitions between broken symmetry states (green and red paths respectively). Figure partly based on ref. [180].

3.9 PERSPECTIVES FOR STUDYING SPIN MODELS

In this chapter, I described a study of the ground state, dynamical and symmetry breaking properties $2J = 16$ interacting qubits in the Lipkin-Meshkov-Glick model, as realised with the large electronic ground state spin $J = 8$ of an ultracold dysprosium atom. A natural extension of our work is the realisation of the full LMGm Hamiltonian,

$$H = -\frac{\hbar}{2J-1}(\lambda_x J_x^2 + \lambda_y J_y^2) + \hbar\omega_z J_z\,, \tag{3.28}$$

with ferromagnetic interactions in both transverse directions. The phase transitions possible in this model are shown in fig. 3.24. For $\lambda_x \neq \lambda_y$, the physics is unchanged in the thermodynamic limit, and we still transition from a single minima at the south pole to double minima structure in the x-z ($\lambda_x > \lambda_y$) or y-z ($\lambda_x < \lambda_y$) plane. The line $\lambda_x = \lambda_y$ is the special isotropic case, where H commutes with J_z, and the ground state for $\lambda_x > \omega_z$ is simply the state $|m_z = m_0\rangle$, where m_0 varies discretely from $-J+1$ to 0 as we increase λ_x.[13] The nature of the phase transition is fundamentally altered on the semiclassical energy landscape – a sombrero potential opens rather than a double well. Indeed, the isotropic LMGm belongs to a different universality class of second-order phase transitions [56]. The isotropic line enriches the phase diagram in the λ_x-λ_y parameter space, where first- and third-order phase transitions are also possible [180] (see fig. 3.24). The structure of the excited levels also shows non-trivial behaviour, with four

[13] Such ground states are also interesting because they are protected from dipolar relaxation, which would quickly destroy a sample prepared in a $m \neq -8$ in the presence of a B_z field only. For instance, a degenerate gas in m could be used to probe the scattering lengths $a_{m,m}$, which are unknown for $m > -8$ (cf. discussion on symmetry breaking by interactions in section 3.8.3.)

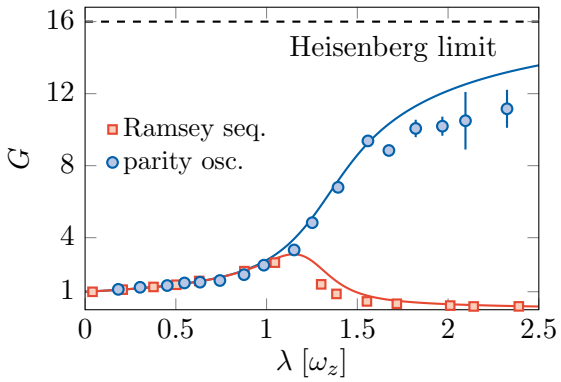

Figure 3.25: Quantum-enhanced sensing with ground states of the LMGm. The expected metrological gain G (relative to a coherent state at $G = 1$, which corresponds to the standard quantum limit) when using prepared ground states of the LMGm to measure a magnetic field, shown as a function of the coupling strength λ. We consider a standard Ramsey-like measurement, and a second protocol which exploits the high sensitivity of the mean parity p_z in the ferromagnetic regime. The fundamental upper bound on the gain is given by the Heisenberg limit $G = 2J = 16$.

different 'phases' classified according to divergences and discontinuities in the density of states [146]. The Hamiltonian 3.28 would be easy to implement in our experimental setup: for example, by adding another off-resonant beam propagating along z and linearly polarised along y we could create the required tensor light shift proportional to J_y^2.

Our system is also a promising platform for studying phase transition dynamics. For instance, non-adiabatic ramps across the transition, followed by a measurement of the depopulation of the ground level, could probe the validity of the Kibble-Zurek mechanism, whose relevance in systems with long-range interactions has been debated [181–185]. Here, the imposed conservation of $\boldsymbol{J}^2$ in our system is an asset. For example, the ramps of coupling simulated by Defenu et al. [183] could be implemented without the complications that would arise in trapped ion simulators due to spin-flip errors [186]. We mention that the LMGm can also act as a convenient toy system to study quantum annealing [187, 188] and dynamical phase transitions [189–192]. The tunable energy level landscape of the Hamiltonian 3.28 would be suited to measure the dynamical signatures of excited state phase transitions, such as 'capture' of the state near a classical stationary point following a quench, preventing the revival of the initial state [141].

Near criticality, our system is also interesting from a metrological point of view. Firstly, the LMGm's criticality can itself be used as a resource for quantum parameter estimation [193]. This can be used to determine the interaction anisotropy λ_y/λ_x (which is often unknown in systems like magnetic molecules) and for thermometry in finite-temperature systems. Secondly, the adiabatically prepared ground states are relevant for protocols for quantum-enhanced sensing of magnetic fields. We adiabatically prepare these states, in contrast to the most common method of using dynamical evolution under a one-axis twisting Hamiltonian $H = -\lambda J_x^2$ [194] (as previously studied in various AMO

systems [67, 68, 195] and also in our group [196, 197]).[14] More quantitatively, we measure a minimum variance $\Delta J_y^2 = 1.4(1)$ near the critical point, well below the value for the coherent spin state at $\lambda = 0$, which saturates the standard quantum limit $\Delta J_y^2 = J/2 = 4$. This relative increase in sensitivity to magnetic fields, for a hypothetical Ramsey-type measurement, is quantified by the metrological gain $G = \langle J_z \rangle^2 / (2J\Delta J_y^2)$ [199]; we reach a maximum value $G = 2.6(2)$, as shown in fig. 3.25. The squeezing observed is a manifestation of a general property of quantum critical points, namely an increase in fluctuations leading to the redistribution of quantum noise between observables [200]. In the ferromagnetic phase, the ground state is N00N-like, and the ideal observable is no longer the Ramsey phase, but rather the parity, which is highly sensitive to a rotation around the z-axis. This enhances the gain (see fig. 3.25), which tends to the ultimate Heisenberg limit $G_H = 2J$ in the limit $\lambda \gg \omega_z$ [201]. We will observe such a parity oscillation in a different context in the following chapter, where we probe the fundamental link between the nonclassicality of collective spin states and quantum entanglement.

[14] Ground state preparation of nonclassical states has also been achieved via spin mixing in BECs [198].

4

PARTITIONING DYSPROSIUM'S ELECTRONIC SPIN TO REVEAL ENTANGLEMENT

> If you try and take a cat apart to see
> how it works, the first thing you have
> in your hands is a nonworking cat.
>
> Douglas Adams, *The Salmon of Doubt*

In this chapter, I present an experimental study of nonclassicality and entanglement properties within the electronic spin of dysprosium atoms. I describe two protocols which partition the ensemble of $2J$ qubits encoded in the angular momentum, thereby giving a physical meaning to entanglement in this setting.

The work presented here has been published in the following article [202]:
Partitioning dysprosium's electronic spin to reveal entanglement in nonclassical states
T. Satoor*, A. Fabre*, J.-B. Bouhiron, A. Evrard, R. Lopes, S. Nascimbene
Physical Review Research 3 (1), 043001 (2021)
* These authors contributed equally

This chapter is structured as follows: we begin in section 4.1 with a general introduction to quantum entanglement and introduce some methods to detect and measure it. Section 4.2 then introduces a more general concept, nonclassicality, which applies to large-spin systems. We also detail the preparation of nonclassical states in our system. Next, we explain our method to partition dysprosium's electronic spin in section 4.3, which we apply to measurements of the nonclassicality of extracted qubit pairs in section 4.4. A direct probe of entanglement using the increase in entropy upon partition is explained in section 4.5. Section 4.6 presents a complementary set of experiments where we investigate the decoherence of nonclassical states upon the loss of qubit pairs. We give a summary in section 4.7 and suggest extensions of the results of this chapter, along with the relevance of our work in the ongoing debate on indistinguishable particle entanglement. Finally, we bring the themes of this chapter and the preceding one to a

close in section 4.8 by discussing general perspectives for many-body spin physics with dysprosium.

4.1 QUANTUM ENTANGLEMENT

A pure state of a system can be thought of as one that is as completely specified as the theory allows. Remarkably, quantum mechanics allows for pure states for which sub-parts of the system cannot themselves be assigned pure states: these states are called *entangled*, while all others are called *separable*. In other words, entanglement implies that "the best possible knowledge of a whole does not include the best possible knowledge of its parts" [203]. Consider a pure state $|\Phi\rangle$ of a system composed of subsystems A and B. Then, any state which cannot be expressed as a product of states associated with each subsystem i.e. $|\phi_A\rangle \otimes |\phi_B\rangle$ is said to be entangled. This definition can be generalised to define mixed entangled states: such states cannot be expressed as a classical distribution over product states of the type $\sum_i p_i \rho_{A,i} \otimes \rho_{B,i}$.

The theory of entanglement and its consequences for experiments are vast and multifaceted. We restrict our discussion to the aspects needed to contextualise our results. The interested reader can find detailed reviews in refs. [58, 204], and a description from a quantum information perspective in ref. [205].

4.1.1 *Bipartite systems*

This section introduces entanglement in quantum systems with two parts.

Concurrence

We begin — following the treatment of the short review [206] — by discussing a measure of entanglement called the concurrence. Consider a pure state $|\Phi\rangle$ of a system composed of subsystems A and B, spanned by the orthonormal bases $\left\{|\phi_1^A\rangle, \ldots, |\phi_n^A\rangle\right\}$ and $\left\{|\phi_1^B\rangle, \ldots, |\phi_n^B\rangle\right\}$ respectively. The bases can always be chosen such that the state $|\Phi\rangle$ takes the form

$$|\Phi\rangle = \sum_i^n c_i \, |\phi_i^A\rangle \otimes |\phi_i^B\rangle \, , \; c_i \geq 0 \tag{4.1}$$

which is called the Schmidt decomposition [207]. If there is more than one non-zero term in the above sum, A and B are entangled with each other. Then, the state of subsystem A (or B) is mixed, described by the density matrix $\rho_A = \mathrm{Tr}_B \, |\Phi\rangle \langle\Phi|$, obtained by performing a partial trace over B. This density matrix has eigenvalues c_i^2.

We might now ask how such entanglement could be detected and quantified. One approach is to define a particular entangled state, namely the singlet state of two qubits $(|\uparrow\downarrow\rangle - |\downarrow\uparrow\rangle)/\sqrt{2}$ as representing one 'unit' of entanglement. How many such singlet pairs, shared between participants Alice and Bob, are needed to create N copies of

$|\Phi\rangle$, such that Alice holds part A and Bob holds part B? Either participant is allowed local operations, like applying unitary operators or performing measurements, and they can exchange classical messages; these conditions are commonly referred to as local operations and classical communication (LOCC). The answer, $N \times E_f(\Phi)$, defines the entanglement of formation [208], given by

$$E_f(\Phi) = -\sum_{c_i \neq 0} c_i^2 \log_2 c_i^2 \,. \tag{4.2}$$

This quantity is in fact the von Neumann entropy of either reduced density matrix ρ_A or ρ_B.

Now consider the trickier case where the state of the composite system is mixed. Such a state ρ can be decomposed into pure states as

$$\rho = \sum_i p_i \, |\Phi_i\rangle \langle\Phi_i| \,, \tag{4.3}$$

where the p_i's are positive coefficients forming a probability distribution. This decomposition is not unique. For example, take the two-qubit state $(|\uparrow\uparrow\rangle\langle\uparrow\uparrow| + |\downarrow\downarrow\rangle\langle\downarrow\downarrow|)/2$: it could be seen as a mixture of the separable states $|\uparrow\uparrow\rangle$ and $|\downarrow\downarrow\rangle$, or equivalently as an equal mixture of the entangled states $(|\downarrow\downarrow\rangle + |\uparrow\uparrow\rangle)/\sqrt{2}$ and $(|\downarrow\downarrow\rangle - |\uparrow\uparrow\rangle)/\sqrt{2}$. For consistency, we want the entanglement of formation to vanish for separable states, and hence it is defined as

$$E_f(\rho) = \inf \sum_i p_i E_f(\Phi_i) \,, \tag{4.4}$$

where inf denotes the infimum, i.e. the minimum taken over all possible pure state decompositions of ρ. This method to generalise an entanglement measure to mixed states is called the convex roof construction, and it allows one to maintain certain desirable physical properties [204]. The disadvantage being that, in general, finding the optimal decomposition is not at all straightforward.

We now introduce the concurrence, an entanglement measure introduced by Hill and Wootters [209], which is very popular for bipartite systems. For a two-qubit pure state Φ, it is simply given by

$$\mathcal{C} = |\langle\Phi|\widetilde{\Phi}\rangle| \,. \tag{4.5}$$

Here, $|\widetilde{\Phi}\rangle = \sigma_y \otimes \sigma_y |\Phi^*\rangle$ represents the spin flip operation, where $|\Phi^*\rangle$ is the complex conjugate in the usual basis $\{|\downarrow\downarrow\rangle, |\downarrow\uparrow\rangle, |\uparrow\downarrow\rangle, |\uparrow\uparrow\rangle\}$. The concurrence vanishes for each of the separable basis states and equals unity for the maximally entangled singlet state

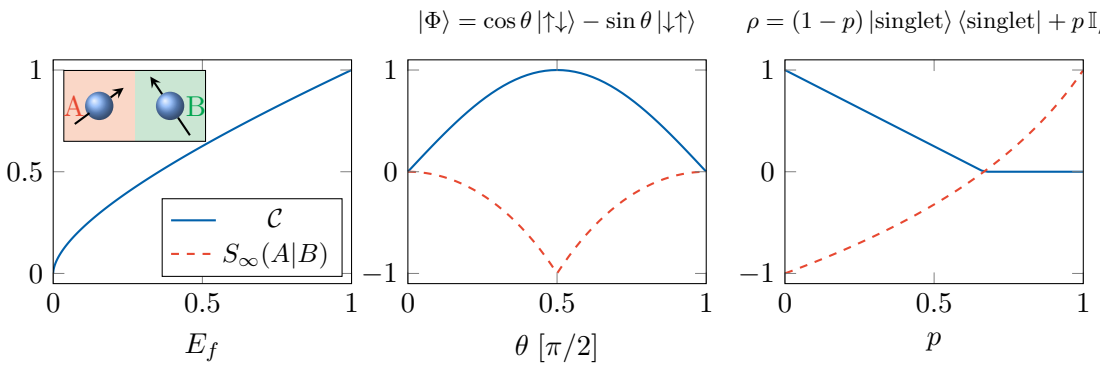

Figure 4.1: Entanglement of a pair of qubits A and B. Left: The entanglement of formation E_f is a simple monotonic function of the concurrence $\mathcal{C}$, which is an entanglement measure with an explicit formula even for mixed states (see text). Middle: The concurrence, evaluated for a pure state parametrised by θ. The maximally entangled singlet state is at $\theta = \pi/4$. We also show conditional entropy of the bipartition, as calculated using the Rényi entropy of infinite order S_∞. $S_\infty(A|B) < 0$ corresponds to an increase in entropy upon partition i.e. an entangled composite state. Right: The same quantities for a mixed state ρ, obtained by combining the singlet state (relative fraction p) with the identity $\mathbb{I}$.

(see fig. 4.1 for an example). The concurrence is directly linked to the entanglement of formation by the relation

$$E_f = h\left(\frac{1+\sqrt{1-\mathcal{C}^2}}{2}\right); \tag{4.6}$$
$$h(x) = -x\log_2 x - (1-x)\log_2(1-x),$$

which is a monotonic and convex function (see fig. 4.1). Remarkably, this result is also valid for mixed two-qubit states, where the concurrence has the explicit form [209]

$$\mathcal{C}(\rho) = \max\left\{0, \sqrt{\lambda_1} - \sqrt{\lambda_2} - \sqrt{\lambda_3} - \sqrt{\lambda_4}\right\}. \tag{4.7}$$

The λ_i's are the eigenvalues of $\rho\,\widetilde{\rho}$ in descending order, where $\widetilde{\rho}$ is the spin-flipped density matrix $\widetilde{\rho} = (\sigma_y \otimes \sigma_y)\rho^*(\sigma_y \otimes \sigma_y)$.

To summarise, the concurrence is special for two-qubit systems because it has an explicit form even for mixed states, bypassing the need to numerically perform the convex-roof minimisation given in eq. (4.4). Furthermore, the concurrence is directly linked to the entanglement of formation, a fundamental quantity with a clear operational definition.

Conditional entropy

The entanglement of formation and concurrence are not linear in the density matrix, as is clear from the above discussion. Accessing them experimentally is challenging, and can require tomographic reconstruction or specialised schemes involving many-body interference with multiple copies of the system [47, 210]. What if, rather than quantifying

entanglement, we are simply interested in verifying its presence? The most famous example of a criterion to achieve this, originally proposed to test local hidden-variable interpretations of quantum mechanics, is the violation of Bell inequalities [6]. We now introduce an entanglement criterion based on conditional entropy. For classical random variables X and Y, the conditional entropy is defined as

$$H(X|Y) \equiv H(X,Y) - H(Y)$$

and it quantifies the uncertainty in X if Y is known. Here $H(Y)$ is the Shannon entropy for the distribution of Y i.e. the classical analogue of the von Neumann entropy $S = -\mathrm{Tr}\,(\rho \log_2 \rho)$ from eq. (4.2) (see ref. [205] for a more detailed explanation). The classical conditional entropy is always non-negative, reflecting the fact that we cannot be more uncertain about the state of X than we are about the overall state of X and Y. This is no longer the case for entangled quantum systems, and

$$S(A|B) \equiv S(A,B) - S(B) < 0 \tag{4.8}$$

is a sufficient criterion to verify entanglement [211, 212]. Here $S(A,B)$ is defined on the composite state ρ, whereas $S(B)$ refers to the entropy of reduced state $\rho_B = \mathrm{Tr}_A\,\rho$.

The von Neumann entropy is in fact a limiting case ($\alpha \to 1^+$) of an entire class of Rényi entropy measures [213]

$$S_\alpha(\rho) = \frac{-1}{\alpha - 1}\mathrm{Tr}\,\rho^\alpha\,, \qquad \alpha > 1\,.$$

In our experiments, we make use of the Rényi entropy of infinite order[1], i.e. the limiting case $\alpha \to \infty$

$$S_\infty(\rho) = -\log_2 \lambda_{\max}(\rho) \tag{4.9}$$

where $\lambda_{\max}(\rho)$ is the largest eigenvalue of the density matrix. This eigenvalue corresponds to the maximum possible overlap of ρ with a pure state. The condition of increased disorder upon partition eq. (4.8), also works with this measure to demonstrate entanglement. The quantity S_∞ is plotted in fig. 4.1 for some pure and mixed two-qubit states.

4.1.2 *Multipartite systems*

In multipartite systems, the descriptors 'entangled' and 'separable' fail to tell the whole story. Consider three qubits in a pure state, distributed between three parties A, B and C. A fully separable state factorises into the form

$$|\Phi\rangle = |\alpha\rangle_A \otimes |\beta\rangle_B \otimes |\gamma\rangle_C\,,$$

[1] For pure states, this is equivalent to the min-entropy [214].

whereas a biseparable state can be written as

$$|\Phi\rangle = |\alpha\rangle_A \otimes |\delta\rangle_{BC},$$

where δ may be an entangled two-qubit state. Two other classes of bipartite entangled states can also be obtained by grouping parties AB or parties CA. Finally, states that fall into none of the above classes are said to exhibit genuine tripartite entanglement. In a landmark result, Dür et al. [75] showed that there are two distinct equivalence classes of genuinely tripartite entangled states. States within a class are equivalent in the sense that it is possible to transform one to another with local operations and classical communication (with a finite probability of success). For tripartite entangled states, the entanglement classes can be understood in terms of their respective paradigmatic states: firstly, the W state

$$|\mathrm{W}\rangle_3 = \frac{1}{\sqrt{3}}(|\downarrow\downarrow\uparrow\rangle + |\downarrow\uparrow\downarrow\rangle + |\uparrow\downarrow\downarrow\rangle) \tag{4.10}$$

and secondly, the Schrödinger cat-like state

$$|\mathrm{cat}\rangle_3 = \frac{1}{\sqrt{2}}(|\downarrow\downarrow\downarrow\rangle + |\uparrow\uparrow\uparrow\rangle) \tag{4.11}$$

The cat state, named as such since it is a superposition of maximally distinct states, is also commonly called the Greenberger–Horne–Zeilinger (GHZ) state or the N00N state, depending on the context. The classes' existence is reflected in distinct behaviours upon measurement of a subset of their qubits, as we shall see when studying their respective N-qubit versions in our experiments. The W state and cat state have been studied in a wide range of experimental settings (see refs. [215–222] and [132, 167, 196, 223–238] respectively).

Entanglement witnesses

Entanglement equivalence classes also complicate the experimental detection of multipartite entanglement. A convenient method, based on entanglement witnesses, is possible when we expect the prepared state ρ to be in the vicinity of a known multipartite entangled state $|\Psi\rangle$, up to the effect of experimental imperfections. In this context, an entanglement witness $\mathcal{W}$ is a carefully constructed observable such that

$$\mathrm{Tr}(\mathcal{W}\rho) \geq 0, \text{ for any } \rho \text{ without multipartite entanglement.} \tag{4.12}$$

Now, given our expectation that ρ has a significant overlap with $|\Psi\rangle$, we can construct our witness as

$$\mathcal{W} = \alpha\mathbb{I} - |\Psi\rangle\langle\Psi|,$$

where $\mathbb{I}$ is the identity operator and α is the smallest possible constant such that the condition 4.12 is satisfied. Hence, we need

$$\alpha = \max |\langle\Psi|\Phi\rangle|^2,$$

where the maximum is taken over all biseparable states $|\Phi\rangle$. We now determine α based on a simple method introduced by Bourennane et al. [239]. To be concrete, let us consider $|\Psi\rangle = |\text{cat}\rangle_3$. With respect to the bipartition $A : BC$, we can write the state as the Schmidt decomposition

$$|\text{cat}\rangle_3 = \frac{1}{\sqrt{2}}|\downarrow^A\rangle \otimes |\downarrow^B\downarrow^C\rangle + \frac{1}{\sqrt{2}}|\uparrow^A\rangle \otimes |\uparrow^B\uparrow^C\rangle .$$

The maximum overlap with a biseparable state of the type $A : BC$ is the largest Schmidt coefficient i.e. $1/\sqrt{2}$, and we get the same result for the other two bipartitions. Therefore, the global maximum across all states lacking genuine tripartite entanglement gives $\alpha = (1/\sqrt{2})^2$ and

$$\mathcal{W}_{\text{cat}} = \frac{1}{2}\mathbb{I} - |\text{cat}\rangle\langle\text{cat}| . \tag{4.13}$$

We have dropped the subscript 3 since this result also applies to general N-qubit cat states; as we shall see, this allows a link to our measurements. Note that witnesses can also be constructed with more sophisticated methods, for example, to optimise the number of measurement settings needed, or to distinguish specific classes of entangled states [240, 241].

4.2 NONCLASSICALITY AND LARGE-SPIN SYSTEMS

Entanglement has historically been the defining form of strangeness associated with quantum systems. However, since then, fundamentally nonclassical behaviour has been identified in a wide range of systems, even in cases where subsystems cannot be identified and entanglement is not obviously implicated.

Let us consider the state of a single mode of light within the framework of quantum optics [242]. Here, the family of quasi-classical states are the coherent states $|\alpha\rangle$ [243, 244]. When the number of photons in such a state is macroscopic ($|\alpha|^2 \gg 1$), quantum fluctuations are negligible and the system is well described by classical electromagnetic fields. Any state that is not coherent (or a classical distribution of coherent states) can be defined to be nonclassical. Some well-known examples are the Fock state, which has a given number of photons but maximal uncertainty on the phase, as well as the Schrödinger cat state, which is a quantum superposition of distinct coherent states $|\alpha\rangle$ and $|-\alpha\rangle$. We show in fig. 4.2 sketches of these states in phase space, as well as their Wigner function representations. Note that the Wigner representation is a quasi-probability

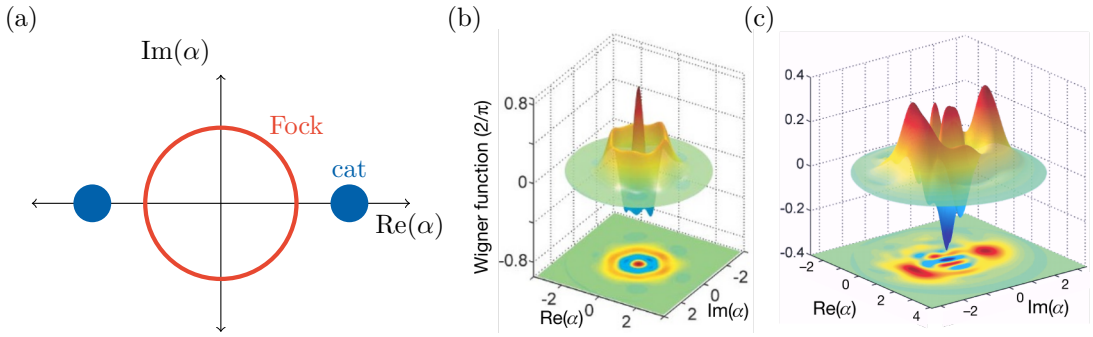

Figure 4.2: Nonclassical states of a single light mode. (a) Sketch in phase space of a Fock state and a Schrödiger cat-like state. (b,c) Experimentally reconstructed Wigner function of a Fock and cat state respectively, for light in a cavity, as measured by Deléglise et al. [237]. Negative regions result from quantum interferences.

distribution in phase space fully characterising the state [245]; its negativity signals distinctively quantum behaviour (see ref. [246] for further details).

Nonclassicality can also be understood in another class of non-composite systems: a single spin-J. The Hilbert space in this case is the finite-dimensional analogue of that of a light mode, allowing us to carry over the same formalism. Therefore, a spin state will be called classical if it can be expressed as a statistical mixture of coherent states [247], as

$$\rho^{(\text{classical})} = \sum_{\boldsymbol{n}} w_{\boldsymbol{n}} ||\boldsymbol{n}\rangle \langle \boldsymbol{n}||, \tag{4.14}$$

where $||\boldsymbol{n}\rangle$ is a spin-J coherent state pointing along the spatial direction $\boldsymbol{n}$ i.e. the maximally polarised state $|J, m = J\rangle_{\boldsymbol{n}}$. The sum is over positive weights $w_{\boldsymbol{n}} \geq 0$, with the normalisation condition $\mathrm{Tr}\,\rho = \sum_{\boldsymbol{n}} w_{\boldsymbol{n}} = 1$.[2] This decomposition of the state is called the Glauber-Sudarshan P-representation. Any state that cannot be represented in this form is called nonclassical.

Nonclassical correlations within a single spin have been shown to be fundamentally incompatible with a classical description (more precisely, non-contextual hidden-variable theories), as demonstrated by Lapkiewicz et al. [60] using a photonic qutrit violating a Bell-like inequality. Nonclassical squeezed and cat states have been produced with ground state atomic spins [196, 248, 249] and Rydberg atoms [132]. Nonclassicality can also manifest as macroscopic tunnelling, as seen with magnetic molecules [128] and our results in chapter 3. Nonclassical behaviour of the total spin of BECs of pseudo-spin 1/2 particles [63] is also closely linked to this category of systems, as we will discuss in detail in section 4.7.2.

[2] More generally, we can also replace the weights with a distribution $w(\boldsymbol{n})$, and the sum by an integral.

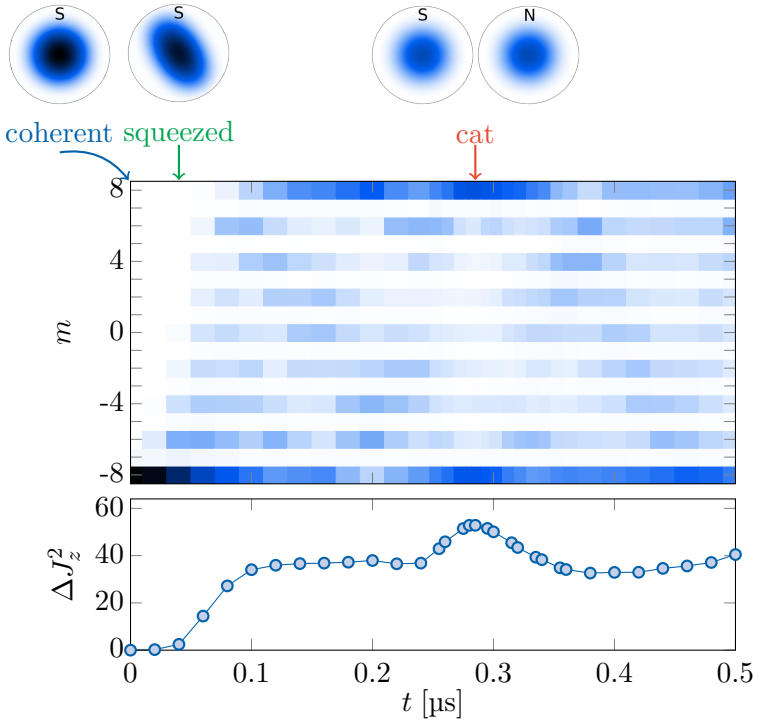

Figure 4.3: One axis twisting dynamics. Top: Spin projection probabilities Π_m along the z-axis under one-axis twisting dynamics $H = -\chi J_x^2$, in the presence of a finite z-field. The value of coupling is $\chi \simeq 0.9\,\mathrm{MHz}$. The initial Gaussian coherent state $|m = -J\rangle$ is squeezed at short times. At $t = \pi/(2\chi)$, we reach a Schrödinger cat-like state, close to the ideal cat state $(|m = -J\rangle + |m = +J\rangle)/\sqrt{2}$ in our system. The arrows mark the particular squeezed and cat states whose nonclassicality we discuss in detail later in this chapter. We also show the states as represented by their expected Husimi functions on the southern (S) and northern (N) hemispheres of the Bloch sphere. Below: The spin moment ΔJ_z^2 during the same evolution, showing an initial increase during squeezing, no evolution at intermediate times, and a revival when the cat is formed.

4.2.1 *Preparing nonclassical states*

The initial parameters for the dysprosium cloud here are similar to those used elsewhere in this thesis. We use a cloud of $1.0(1) \times 10^5$ atoms of ^{162}Dy, held in a crossed optical dipole trap at a temperature $T = 0.54(3)\,\mu\mathrm{K}$.[3]

Squeezed and cat states

A popular method for creating nonclassical spin states is the one-axis twisting dynamics, which requires a Hamiltonian of the type $H = -\chi J_x^2$ [194], as first implemented with atomic Bose-Einstein condensates [67, 68]. A detailed discussion of these dynamics in our system can be found in ref. [196]. Here, we generate this coupling using the spin-dependent light shift from a far-detuned 696 nm laser beam (excited level $J' = J - 1$), with a linear polarisation $\boldsymbol{e}_x$. Figure 4.3 shows the evolution of our system under such a

[3] Remember that, unless stated otherwise, the results should be understood by considering a single atom, with the ensemble only acting as an averaging mechanism.

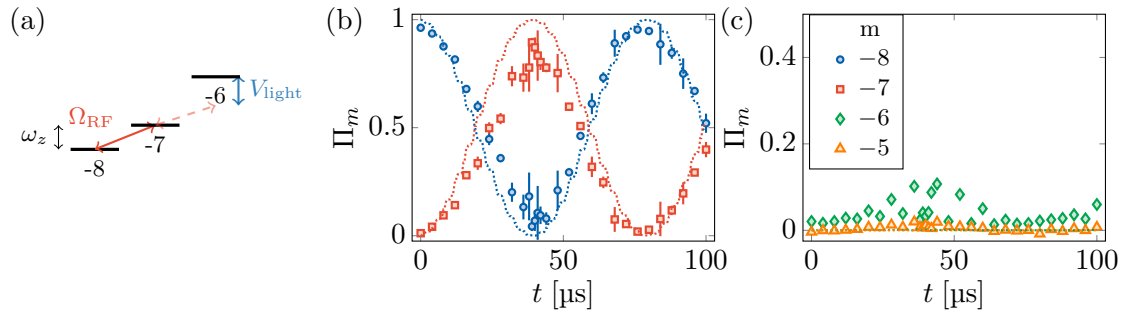

Figure 4.4: Preparation of the Dicke state $|J = 8, m = -7\rangle$. (a) A radio frequency coupling of strength Ω_{RF} at the Zeeman splitting frequency ω_z resonantly couples the initial coherent state $|m = -8\rangle$ to the target state $|m = -7\rangle$. The states $|m = -6\rangle$ and above are made off-resonant by light shifts from a laser beam at a frequency close to the 696 nm transition (see text). (b,c) Observed spin projection probabilities Π_m for $m \leq -5$ (marks, see legend) as a function of the RF pulse duration. The dotted curves show the simulated coherent evolution (considering all 17 states, without the rotating-wave approximation). The only fitted parameters are the RF coupling Ω_{RF} and its initial phase, whereas the light shifts and Zeeman splitting are determined independently. The deviation of the data from numerics is due to spin-changing collisions (see text).

light shift. The spin projection twists at short times ($\chi t \sim 0.05$), leading to the squeezing of a spin projection quadrature [194]. At intermediate times, there is no evolution of the moment ΔJ_z^2. Finally, a revival at a time $t_{\mathrm{cat}} = \pi/(2\chi)$, corresponds to a formation of a cat-like coherent superposition, dominated by stretched states $|m = \pm J\rangle$, with residual occupation of other even-m sublevels. The ideal cat state $|\mathrm{cat}\rangle = (|m = -J\rangle + |m = +J\rangle)/\sqrt{2}$ would be attained in the absence of a bias field along the z-direction. However, we apply a field $B = 50\,\mathrm{mG}$ to maintain a well-defined quantisation axis in the presence of shot-to-shot transverse field fluctuations. We will return to the squeezed and cat state indicated on fig. 4.3 later in this chapter to characterise them further and quantitatively probe their nonclassicality. Hereafter, the cat state we refer to is prepared with the parameters $\chi = 2\pi \times 1.25\,\mathrm{MHz}$ and $B = 53.7(1)\,\mathrm{mG}$ at $t = 200\,\mathrm{ns}$, whereas the squeezed state is prepared using a weaker coupling $\chi = 2\pi \times 32.1(4)\,\mathrm{kHz}$ with $B = 75(1)\,\mathrm{mG}$ at $t \simeq 700\,\mathrm{ns}$.

Dicke state $m = -7$

The Dicke states $|J, m\rangle$ are another family of states which are natural to consider for our setup. In analogy to the Fock states in quantum optics, these states are nonclassical (except at $m = \pm J$). The Dicke state $|m = -J + 1\rangle$ is of particular interest from a theoretical point of view: we explain in the next section that, in terms of the encoded spin-1/2's, it corresponds to a 16-qubit W state. To prepare it, we isolate the two levels $|m = -J\rangle$ and $|m = -J + 1\rangle$ by applying a strong quadratic light shift acting on the spin states $m > -J + 1$ only. This light shift is produced using the same laser beam used for one-axis twisting; it is far-detuned from the 696 nm transition, with polarisation σ_-, for which the states $|m = -J\rangle$ and $|m = -J + 1\rangle$ are dark. The beam parameters are chosen

to induce a detuning $V_{\text{light}} = 2\pi \times 320\,\text{kHz}$ for $|m = -J + 2\rangle$, in addition to the linear Zeeman splitting of $\omega_z = 2\pi \times 125\,\text{kHz}$ (see fig. 4.4a).

The two-level Rabi dynamics are induced by a single-loop RF antenna, which has not been introduced so far in this thesis. It is roughly rectangular, with dimensions $5\,\text{cm} \times 10\,\text{cm}$. To maximise the Rabi coupling, we place the antenna just outside the science cell, such that the atomic cloud is on the loop axis, at a distance of about 6 cm.[4] The antenna circuit is driven by a 30 W amplifier. Additionally, the loop's inductive impedance at the operating frequency ω_z is matched with a capacitance of about 760 nF, chosen by maximising the transfer to $|m = -J + 1\rangle$ at a fixed pulse duration, much shorter than the resulting optimised π-pulse duration of 40 µs.

The system's coherent evolution is described by the Hamiltonian

$$H_{\text{RF}} = \hbar\Omega_{\text{RF}} \cos(\omega_z t + \phi)\frac{J_x}{2} + V_0\frac{(J + J_z)(J - 1 + J_z)}{2J(2J - 1)}. \tag{4.15}$$

We will provide an intuitive explanation of the quadratic light shift term, which has zeros at $\langle J_z\rangle = -8,\ -7$, in section 4.4.3.

We fit a Rabi frequency $\Omega_{\text{RF}} \simeq 2\pi \times 12.6\,\text{kHz}$ to the dynamics (see fig. 4.4b,c). For our parameters, simulations indicate that $m = -6$ and higher sublevels should remain unoccupied. However, the maximum occupation of $|m = -7\rangle$ observed is $0.91(1)$, with residual overlaps on other Dicke states below 4%. We suspect that the fidelity is limited by inelastic collisions between atoms, which redistribute the spin among neighbouring m states.

4.3 PARTITIONING DYSPROSIUM'S ELECTRONIC SPIN

This section describes our method to give access to entanglement properties of the nonclassical states prepared above by using optical couplings to partition the electronic spin.

4.3.1 *Qubit mapping formalism*

The electronic ground state angular momentum $J = 8$ can be interpreted as the sum of $2J = 16$ virtual spin-1/2s, in a state symmetric upon exchange (as introduced for the LMG model in section 3.4). If these qubits were individually addressable, nonclassical spin-J states have a one-to-one mapping to entangled $2J$ qubit states. We discuss some related subtleties in a combined discussion of our results towards the end of the chapter. For now, we return to considering the partitioning of the qubit ensemble.

[4] The loop dimensions and distance to the atoms being much smaller than the RF wavelength, we must consider the near-field of an electrically short antenna. Here, the amplitude of the produced fields is given by their static values, which are maximal on the loop axis. This situation would be inverted in the far-field, where the field amplitude is maximal in the loop plane [250].

We will work with the basis of Dicke states. A Dicke state $|J, m\rangle$ has $m + J$ qubits pointing up and the remaining pointing down:

$$|J, m\rangle = \sum_{\text{sym.}} \frac{1}{\sqrt{{}^{2J}\mathrm{C}_{m+J}}} |\uparrow_1 \uparrow_2 \ldots \uparrow_{m+J} \downarrow_{m+J+1} \ldots \downarrow_{2J}\rangle \,. \tag{4.16}$$

The sum symmetrises the state over all permutations of $m + J$ qubits pointing up; there are ${}^{2J}\mathrm{C}_{m+J}$ terms, hence the normalising prefactor; note that ${}^{n}\mathrm{C}_{k}$ denotes binomial coefficients.

In the previous chapter, we studied a phase transition in the ensemble of $2J$ qubits. As long as the angular momentum J is conserved, the qubit ensemble cannot be partitioned, and the relevance of entanglement is disputable. Here, we access entanglement properties by experimentally performing a 2:14 partition of this ensemble through a coupling to an excited electronic level with angular momentum $J' = 7$. A pure 16-qubit state $|\psi\rangle$ (whose density matrix we denote ρ) can be decomposed with respect to this partition as

$$|\psi\rangle = \sum_{m'=-J'}^{J'} \sum_{q=-1}^{1} a_{m'q} \, |J', m'\rangle \otimes |1, q\rangle$$

where $|J', m'\rangle$ and $|1, q\rangle$ are Dicke states of $2J'$ and 2 qubits respectively and the $a_{m'q}$'s are complex coefficients. We show below how our experimental protocol gives access to the state of the 2-qubit subsystem, described by the pair density matrix ρ_{pair}, which is obtained by tracing out the remaining $2J'$ qubits i.e.

$$\rho_{\text{pair}} = \mathrm{Tr}_{2J'}(\rho) \tag{4.17}$$

It will be useful to represent the pair density matrix in the Dicke basis:

$$\langle 1, p|\rho_{\text{pair}}|1, q\rangle = \sum_{m'=-J'}^{J'} \langle J', m'; 1, p|\rho|J', m'; 1, q\rangle \tag{4.18}$$

$$= \sum_{m_a, m_b=-J}^{J} \sum_{m'=-J'}^{J'} \langle J', m'; 1, p|J, m_a\rangle \, \rho_{m_a, m_b} \, \langle J, m_b|J', m'; 1, q\rangle \,, \tag{4.19}$$

where we have expanded over the spin-J Dicke basis on the second line, with $\rho_{m_a,m_b} = \langle J, m_a|\rho|J, m_b\rangle$. The respective Clebsch-Gordan coefficients in the second equation above are only non-zero when $m_a = m' + p$ and $m_b = m' + q$.[5]

[5] Furthermore, we can use the form of the Dicke state given in eq. (4.16) to derive a simple explicit form for these Clebsch-Gordan coefficients:

$$\langle J', m'; j, p|J, m\rangle = \sqrt{\frac{{}^{2J'}\mathrm{C}_{m'+J} \, {}^{2j}\mathrm{C}_{2j+1}}{{}^{2J}\mathrm{C}_{m}}} \,,$$

with $m = m' + q$. This coefficient appears in the text with $J' = J - 1$ and $j = 1$; in general, this formula it is valid for $J' + j = J$.

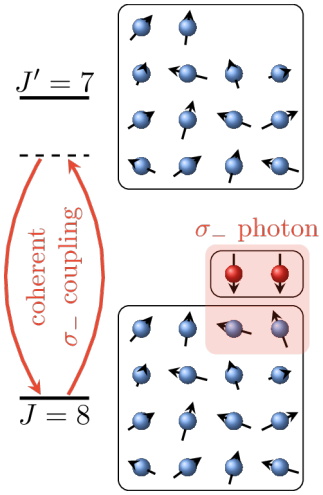

Figure 4.5: Scheme of the first protocol for manipulating qubit pairs in the electronic spin of dysprosium. An electronic spin of angular momentum J can be viewed as a set of $2J$ virtual qubits in a state symmetric upon exchange. The coherent coupling to an excited state $J' = J - 1$ with light polarised in a state $|\epsilon\rangle$ polarised light probes the probability of finding a qubit pair polarised in $|\epsilon^*\rangle$, itself equivalent to a 2-qubit symmetric state (see text). Here we show σ_- polarised light, for which $|\epsilon\rangle = |\downarrow\downarrow\rangle$ and $|\epsilon^*\rangle = |\uparrow\uparrow\rangle$.

4.3.2 *Implementing the partition*

For a practical realisation of the $2 : 2J'$ partition, we couple the ground state to an excited electronic level with angular momentum $J' = 7$, via the transition at 696 nm. Consider the resonant absorption of a photon, whose polarisation is defined by a complex unit vector $\boldsymbol{\epsilon}$. The polarisation defines the quantum state of an angular momentum $L = 1$, which we interpret as a symmetric 2-qubit state. This is evident from the mapping

$$\begin{aligned} |\uparrow\uparrow\rangle &\leftrightarrow \boldsymbol{\epsilon}_{+1} = (\hat{\boldsymbol{x}} + \mathrm{i}\hat{\boldsymbol{y}})/\sqrt{2} \\ (|\downarrow\uparrow\rangle + |\uparrow\downarrow\rangle)/\sqrt{2} &\leftrightarrow \boldsymbol{\epsilon}_0 = \hat{\boldsymbol{z}} \\ |\downarrow\downarrow\rangle &\leftrightarrow \boldsymbol{\epsilon}_{-1} = (\hat{\boldsymbol{x}} - \mathrm{i}\hat{\boldsymbol{y}})/\sqrt{2} \end{aligned}$$

corresponding to the usual σ_+, π, and σ_- polarisation states respectively. In this basis, we can decompose a general polarisation state as

$$\boldsymbol{\epsilon} = \sum_{q=-1}^{+1} \epsilon_q \, \boldsymbol{\epsilon}_q \tag{4.20}$$

For a given polarisation $|\epsilon\rangle$ and a given initial atomic state ρ in the ground level J, the allowed transitions are restricted by the conservation of the azimuthal angular momentum. Stated mathematically, the polarisation-dependent absorption cross-section is given by

$$\sigma(\boldsymbol{\epsilon}) = \sigma_0 \, \langle \boldsymbol{\epsilon}^* | \rho_{\text{pair}} | \boldsymbol{\epsilon}^* \rangle \,, \; \sigma_0 = \frac{3\lambda^2}{2\pi}. \tag{4.21}$$

Here, ρ_{pair} is the reduced 2-qubit density matrix, and $|\boldsymbol{\epsilon}^*\rangle$ is the complex-conjugate polarisation state with respect to the basis from eq. (4.20). Note that $|\boldsymbol{\epsilon}^*\rangle$ is the time-reversed photon state, whose z-angular momentum is flipped since $(\boldsymbol{\epsilon}^*)_q = (\boldsymbol{\epsilon}_{-q})^*$. We now give a physical justification for this expression.

Using eq. (4.21), the $J \to J' = J - 1$ process can be interpreted as follows: The photon, with associated two-qubit state $|\boldsymbol{\epsilon}\rangle$ annihilates a pair of qubits in state $|\boldsymbol{\epsilon}^*\rangle$ out of the total $2J$-qubit state ρ. The rate of this process is proportional to the probability of finding two randomly chosen qubits in the state $|\boldsymbol{\epsilon}^*\rangle$ i.e. the overlap $\langle\boldsymbol{\epsilon}^*|\rho_{\text{pair}}|\boldsymbol{\epsilon}^*\rangle$. Let us consider an example which is also simple to understand using angular momentum conservation. Take an incident σ_- polarised photon, in which case $|\boldsymbol{\epsilon}\rangle = |\downarrow\downarrow\rangle$ and hence $|\boldsymbol{\epsilon}^*\rangle = |\uparrow\uparrow\rangle$. If the dysprosium atom is initially in the coherent state $|J, m = -8\rangle$ ($2J$ qubits pointing down), the reduced pair state is $\rho_{\text{pair}} = |\downarrow\downarrow\rangle\langle\downarrow\downarrow|$. So there is no overlap, and the cross-section vanishes since there are no qubits pointing up which are available to be annihilated. Conversely, if the initial atomic state is $|J, m = +8\rangle$, we have $\rho_{\text{pair}} = |\uparrow\uparrow\rangle\langle\uparrow\uparrow|$ and the cross-section is maximal.

It is easier to measure off-resonant light shifts rather than an absorption cross section on our experimental setup. The qubit pair annihilation scheme using light shifts is illustrated in fig. 4.5. The physical origin of the light shift V is in fact virtual photon absorption processes, and so it is given by a similar polarisation-dependent formula

$$V = V_0 \langle\boldsymbol{\epsilon}^*|\rho_{\text{pair}}|\boldsymbol{\epsilon}^*\rangle, \quad V_0 = \frac{\hbar\Omega_R^2}{\Delta}, \tag{4.22}$$

where Δ is the detuning from resonance, and $\Omega_R = dE/2\hbar$ is the coupling Rabi frequency, $d = \langle J-1||\boldsymbol{d}||J\rangle$ being the reduced dipole matrix element, and E the light electric field amplitude. We will demonstrate in the coming pages how this relation provides a powerful tool to probe nonclassicality for states prepared in our experiments.

Derivation of the link to the reduced pair state

Here, we derive eq. (4.21) from the point of view of photon absorption probability in a coherent resonant process. This derivation is provided for the sake of completeness and is not needed to understand the results of the rest of the chapter. We follow the treatment from ref. [251].

Working within first-order perturbation theory and using rotating-wave approximation, the probability of absorption at short times is

$$P_{\text{abs}} = \langle\psi|\,(\boldsymbol{d}\cdot\boldsymbol{E})^\dagger\,\mathbb{P}_{J'=J-1}\,(\boldsymbol{d}\cdot\boldsymbol{E})\,|\psi\rangle\,t^2/\hbar^2,$$

where $\boldsymbol{d}$ is the electric dipole operator and $\mathbb{P}_{J'}$ projects on the excited electronic state manifold. Using the Wigner-Eckart theorem, we write the dipole q-component as

$$d_q = \langle J'||\boldsymbol{d}||J\rangle \sum_{m,m'} |J', m'\rangle\langle J, m; 1, q|J', m'\rangle\langle J, m|.$$

In terms of the polarisation components defined in eq. (4.20), we obtain the expression

$$P_{\text{abs}} = (\Omega t)^2 \sum_{q,q'} \epsilon^*_{q'} \epsilon_q a_{q,q'},$$

with the Rabi frequency $\Omega = \langle J-1||\boldsymbol{d}||J\rangle E/\hbar$ and the coefficients

$$a_{q,q'} = \sum_{m_1,m_2,m'} \langle\psi|J,m_1\rangle \langle J,m_2|\psi\rangle \langle J,m_1;1,q|J-1,m'\rangle \langle J-1,m'|J,m_2;1,q'\rangle .$$

Using the identity

$$\langle J,m;1,q|J-1,m'\rangle = (-1)^q \sqrt{\frac{2J-1}{2J+1}} \langle J,m|J-1,m';1,-q\rangle ,$$

we write

$$a_{q,q'} = \frac{2J-1}{2J+1}(-1)^{q+q'} \sum_{m_1,m_2,m'} \langle\psi|J,m_1\rangle \langle J,m_1|J-1,m';1,-q\rangle \times \langle J-1,m';1,-q'|J,m_2\rangle \langle J,m_2|\psi\rangle$$

which simplifies to

$$a_{q,q'} = \frac{2J-1}{2J+1}(-1)^{q+q'} \sum_{m'} \langle\psi|J-1,m';1,-q\rangle \langle J-1,m';1,-q'|\psi\rangle .$$

We now recognise the expression from eq. (4.18) for the reduced two-qubit density matrix, leading to

$$a_{q,q'} = \frac{2J-1}{2J+1}(-1)^{q+q'} \langle -q'|\rho_{\text{pair}}|-q\rangle .$$

Identifying the spin-1 state $|\boldsymbol{\epsilon}\rangle$ with the polarisation $\boldsymbol{\epsilon}$, we obtain the final expression

$$P_{\text{abs}} = (\Omega t)^2 \langle \boldsymbol{\epsilon}^*|\rho_{\text{pair}}|\boldsymbol{\epsilon}^*\rangle , \tag{4.23}$$

where we have used $(\boldsymbol{\epsilon}^*)_q = (\boldsymbol{\epsilon}_{-q})^*$, and also absorbed a factor $\sqrt{(2J-1)/(2J+1)}$ into the Rabi frequency. We can also interpret this polarisation-dependent absorption rate as a cross-section, which leads to the previously introduced formula eq. (4.21).

4.4 NONCLASSICALITY OF THE EXTRACTED QUBIT PAIR

Our first characterisation of entanglement of the $2J$-qubit state consists in revealing the nonclassical character of qubits pairs extracted from it.

4.4.1 *Pair Husimi function*

The pair Husimi function will be the primary quantity used to probe nonclassicality in this section. The Husimi Q-distribution is a quasi-probability distribution, defined over the domain $\{\alpha\}$ of coherent states as the squared overlap with the corresponding coherent state $|\alpha\rangle$. Hence, for a pair extracted from the $2J$-qubit ensemble, it is defined as

$$Q_{\text{pair}}(\boldsymbol{n}) = \langle \boldsymbol{n}|\rho_{\text{pair}}|\boldsymbol{n}\rangle \ , \tag{4.24}$$

where $|\boldsymbol{n}\rangle$ is a two-qubit state pointing along the spatial direction $\boldsymbol{n}$. Comparing this expression to the polarisation dependent light shift (eq. (4.22)), we see that by measuring the light shift for a σ_- polarisation, $|\boldsymbol{\epsilon}\rangle = |\downarrow\downarrow\rangle$, gives direct access to the Husimi function along the z-axis ($\boldsymbol{n} = \hat{\boldsymbol{z}}$), since

$$V/V_0 = \langle\uparrow\uparrow|\rho_{\text{pair}}|\uparrow\uparrow\rangle = Q_{\text{pair}}(\hat{\boldsymbol{z}}) \tag{4.25}$$

In section 4.4.3, we will show how measurements with σ_- polarised light can be combined with rotations of the spin-J state to measure the full pair Husmi function $Q_{\text{pair}}(\boldsymbol{n})$. We first explain the link of the Husimi function to nonclassicality.

4.4.2 *Nonclassicality and the link to concurrence*

At first sight, the Husimi function might seem ill-suited to probe nonclassicality, compared to the Wigner distribution mentioned in fig. 4.2. It is by definition positive-valued; furthermore, it cannot, for example, distinguish between a quantum superposition and an incoherent mixture of two coherent states, $|\boldsymbol{n}_1\rangle$ and $|\boldsymbol{n}_2\rangle$, which are distant in phase space. Here, we use the pair Husimi function to construct an inequality to detect nonclassicality of the state of the extracted pair ρ_{pair}. We will then explain how this leads to an elegant determination of the associated concurrence $\mathcal{C}(\rho_{\text{pair}})$. It is crucial to note that the $L = 1$ qubit pairs remain indivisible quantum objects in our system, such that the concurrence only quantifies the degree of nonclassical correlations.

The collective state ρ_{pair} of a qubit pair symmetric upon exchange can be written as the state of an angular momentum $L = 1$. The global spin-J state (see eq. (4.14)), the pair state will be called classical if it can be expressed as a statistical mixture of quasi-classical coherent states

$$\rho_{\text{pair}}^{(\text{classical})} = \sum_{\boldsymbol{n}} w_{\boldsymbol{n}} |\boldsymbol{n}\rangle\langle\boldsymbol{n}|, \tag{4.26}$$

with weights $w_{\boldsymbol{n}} \geq 0$, where $\sum_{\boldsymbol{n}} w_{\boldsymbol{n}} = 1$.

We now introduce a measure

$$Z(\boldsymbol{n}) \equiv 2\langle L_{\boldsymbol{n}}^2\rangle - \langle L_{\boldsymbol{n}}\rangle^2 - 1 \tag{4.27}$$

for arbitrary measurement axis $\boldsymbol{n}$. The key property we will use is as follows [247]: The existence of a strictly negative value $Z(\boldsymbol{n}) < 0$ is a necessary and sufficient criterion of nonclassicality. Note that coherent states satisfy $Z(\boldsymbol{n}) = 0$ for all $\boldsymbol{n}$. In fact, they are the only pure states with this property. Then, it follows by convexity that $Z(\boldsymbol{n}) \geq 0$ for classical states.

The link between $Z(\boldsymbol{n}) < 0$ and nonclassicality becomes more intuitive if we decompose the spin-1 into two virtual qubits, using

$$L_n = \frac{\sigma_{1n}}{2} + \frac{\sigma_{2n}}{2},$$

where σ_{in} is the Pauli operator along the direction $\boldsymbol{n}$ for the i^{th} qubit. This allows us to rewrite Z in a Cauchy-Schwarz-like form

$$Z = \langle \sigma_{in}\sigma_{jn} \rangle - \langle \sigma_{in} \rangle^2$$

where the 1- and 2-qubit correlators have the usual meanings, as previously used in chapter 3. Alternatively, we can factorise this expression as

$$Z = \langle A \otimes A \rangle, \text{ where } A = \sigma_{in} - \langle \sigma_{in} \rangle.$$

The existence of a one-qubit operator A satisfying $Z < 0$ also implies the nonclassicality of an exchange-symmetric state [252].

We now aim to express Z using the pair Husimi function, to make this criterion easily applicable to our system. Note that the Husimi function is simply the expectation value of the projector $|\boldsymbol{n}\rangle \langle \boldsymbol{n}|$. Furthermore, the eigenstates of L_n with non-zero eigenvalues are simply $|\boldsymbol{n}\rangle$ and $|-\boldsymbol{n}\rangle$. We can then write $L_n = |\boldsymbol{n}\rangle \langle \boldsymbol{n}| - |-\boldsymbol{n}\rangle \langle -\boldsymbol{n}|$, giving the expectation values

$$\begin{aligned} \langle L_n \rangle &= Q_{\text{pair}}(\boldsymbol{n}) - Q_{\text{pair}}(-\boldsymbol{n}), \\ \langle L_n^2 \rangle &= Q_{\text{pair}}(\boldsymbol{n}) + Q_{\text{pair}}(-\boldsymbol{n}). \end{aligned}$$

Substituting these into the definition of Z leads to the expression

$$Z(\boldsymbol{n}) = \gamma\, \mathcal{C}_n, \text{ where } \gamma = \left(\sqrt{Q_{\text{pair}}(-\boldsymbol{n})} - \sqrt{Q_{\text{pair}}(\boldsymbol{n})} \right)^2 - 1$$

We have introduced the nonclassicality measure

$$\mathcal{C}_n = 1 - \left(\sqrt{Q_{\text{pair}}(-\boldsymbol{n})} + \sqrt{Q_{\text{pair}}(\boldsymbol{n})} \right)^2. \tag{4.28}$$

The value of γ is negative by construction. Therefore, the state of the extracted qubit pair is nonclassical if and only if there exists a direction $\boldsymbol{n}$ for which $\mathcal{C}_n$ is strictly positive. This

criterion of nonclassicality is equivalent to the bipartite entanglement witness established by Korbicz et al. [253].

We now show that the distribution $\mathcal{C}_{\boldsymbol{n}}$ can be used to quantify the degree of nonclassicality of a quantum state, defined by its distance to the set of nonclassical states [254]. For a system of two qubits, this geometrical measure can be directly expressed in terms of the concurrence $\mathcal{C}$. As we saw in section 4.1.1, the concurrence can be explicitly written in terms of the density matrix, but it does not correspond to a directly accessible physical observable. Remarkably, the distribution $\mathcal{C}_{\boldsymbol{n}}$ can be used to retrieve the concurrence, as

$$\mathcal{C} = \max[0, \max_{\boldsymbol{n}} \mathcal{C}_{\boldsymbol{n}}]. \tag{4.29}$$

This relation was conjectured and numerically checked for randomly generated states in ref. [148]. As far as we are aware, it has not been proven.

4.4.3 *Application to the Dicke basis*

To access the Husimi function of qubit pairs extracted from nonclassical states, we begin by measuring light shifts to determine the Husimi function along the z-axis $Q_{\text{pair}}(\hat{\boldsymbol{z}})$ for all Dicke states $|J, m\rangle$; hereafter, these quantities are denoted Q_m i.e.

$$Q_m \equiv Q_{\text{pair}}(\boldsymbol{n} = \hat{\boldsymbol{z}}), \text{ for the state } \mathrm{Tr}_{2J'}\left(|J, m\rangle \langle J, m| \right) \tag{4.30}$$

The Dicke states are an appropriate starting point for generalising these measurements to all states, since they form an eigenbasis of the light shift operator for σ_- polarised light.[6]

The method for the Q_m measurement is shown in fig. 4.6a. After turning off the crossed dipole traps, we use spin rotations to prepare the coherent state $|m = J\rangle_{\boldsymbol{n}}$ polarised along a direction $\boldsymbol{n}$, parametrized by the spherical angles (θ, ϕ). The polar angle θ determines the projection probabilities Π_m along the Dicke states $|m\rangle$, which are significant for values of m close to $J \cos\theta$. We then pulse an off-centred laser beam with circular σ_- polarisation and blue detuning with respect to the 696 nm transition. The intensity gradient leads to a repulsive force along x proportional to the light shift (fig. 4.6a); the beam's offset is chosen as half its waist to maximise the force. After this kick, a magnetic field gradient separates the different m-components along z during a 2.3 ms long time-of-flight. Finally, we image the atoms to measure the x-displacement for each Dicke state $|m\rangle$ that is significantly populated, allowing us to retrieve their light shifts independently, and hence the respective values of Q_m. A typical single-shot absorption image is shown in fig. 4.6b.

Repeating the above measurement for various angles θ, we measure all the Q_m's, plotted in fig. 4.6c. In practice, the light shifts' amplitudes vary over several orders of

[6] This also ensures that the spin state does not evolve during Q_m measurement protocol.

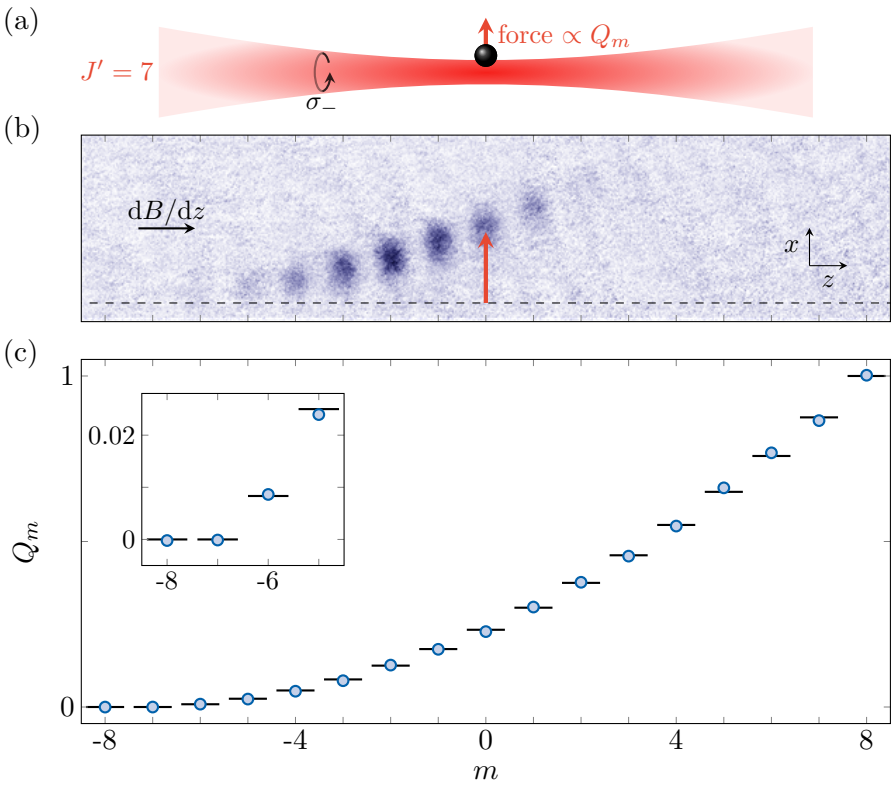

Figure 4.6: Measurement of pair Husimi function along the z-axis for Dicke states. (a) Scheme of the light shift measurement. We measure the force induced on the atoms by an off-centred laser beam, blue detuned with respect to the optical resonance to the excited level $J' = 7$. (b) Image of an atomic gas prepared in a coherent state of polar angle $\theta \simeq 100°$. The atoms are kicked along x by the laser beam. Subsequently, we apply a magnetic field gradient separating the magnetic sublevels $|m\rangle$ along z during time-of-flight. The dashed line indicates the mean x position in the absence of the repulsive laser beam. (c) Probability Q_m for a qubit pair taken in the Dicke state $|m\rangle$ to be in $|\uparrow\uparrow\rangle_z$, deduced from the kick amplitudes. The error bars here are smaller than the blue discs. The inset is a zoom near the dark states $m = -8, -7$. The black lines are the theoretical values computed from eq. (4.31).

magnitude as a function of m. To account for this, we vary the laser pulse duration in the range 10–100 µs and the detuning in the range 50 MHz – 1 GHz, in order to keep similar displacements for all m-states. For the smallest detunings, we also take into account the second-order corrections to the light shifts. The uncertainties in the laser beam's waist $w = 40(5)$ µm and on the excited state lifetime $\tau \simeq 11$ µs [109] lead to a systematic error. We correct an overall 20% error using the global constraint $\sum_m Q_m = (2J+1)/3$, which states that in a completely mixed state, a symmetric qubit pair has a probability $1/3$ to be in $|\uparrow\uparrow\rangle$.

Our measurements are consistent with an absence of light shifts for the states $|m = -J\rangle$ and $|m = -J+1\rangle$, i.e. these states are dark with respect to the $J \to J' = J-1$ optical transition for σ_- polarised light. In terms of the underlying qubits, the state $|m = -J\rangle$ only contains $|\downarrow\rangle$-polarised qubits, while the state $|m = -J+1\rangle$ has a single qubit in $|\uparrow\rangle$. In both cases, a qubit pair cannot be found polarised in $|\uparrow\uparrow\rangle$, and we have $Q_{-J} = Q_{-J+1} = 0$.

More generally, the state $|m\rangle$ has $J-m$ qubits in $|\downarrow\rangle$ and $J+m$ qubits in $|\uparrow\rangle$. Hence, the probability of picking a pair $|\uparrow\uparrow\rangle_z$ is given by a ratio of binomial coefficients,

$$Q_m = \frac{{}^{J+m}\mathrm{C}_2}{{}^{2J}\mathrm{C}_2} = \frac{(J+m)(J+m-1)}{2J(2J-1)}, \tag{4.31}$$

in good agreement with the measured values.

We now exploit these measurements to probe the pair Husimi function of arbitrary states. To this end, we measure the distribution of projection probabilities $\Pi_m(\boldsymbol{n})$ by combining spin rotations and Stern-Gerlach projective measurement along z. We then infer the Husimi function by weighting these probabilities with the Q_m values, as

$$Q_{\mathrm{pair}}(\boldsymbol{n}) = \sum_m Q_m \Pi_m(\boldsymbol{n}). \tag{4.32}$$

In the following, we use the theoretical values of eq. (4.31) rather than the measured ones to avoid propagating systematic errors.

4.4.4 *Coherent and W states*

We now apply the protocol described above to some well-known classes of N-qubit states. In each case, we measure the distribution Π_m and determine the pair Husimi function Q_{pair}. In turn, this gives access to the nonclassicality measure $\mathcal{C}_{\boldsymbol{n}}$, and the resulting concurrence $\mathcal{C}$.

We first consider the quasi-classical coherent spin state $|m=-J\rangle$ and the W state, which in our case is simply $|m=-J+1\rangle$. The coherent state can be viewed as a set of $2J$ qubits polarised in $|\downarrow\rangle$, forming a product state. On the other hand, the W state hosts a single qubit in $|\uparrow\rangle$, and is a paradigmatic state of a fundamental class of entanglement, as previously explained in section 4.1.2; the method to prepare the W state was explained in section 4.2.1.

Figure 4.7a,b shows the measured projection probabilities $\Pi_m(\theta)$ for these two states. For a given projection m, the coherent state probabilities feature a single peak centred on the expected maximum at $\theta_m = \cos^{-1}(m/J)$, shown as red lines. For the W state, we observe a double-peaked distribution for all $m \neq \pm J$. This behaviour results from the interference between two processes: the spin $|\uparrow\rangle_z$ can project onto $|\uparrow\rangle_\theta$ or $|\downarrow\rangle_\theta$. The first (second) process dominates for $\theta \simeq 0$ ($\theta \simeq \pi$), and the two processes interfere destructively at θ_m, as observed in our data.

Combining these measurements with the Q_m values using eq. (4.32), we infer the respective pair Husimi functions, finding good agreement with theory for both states (see fig. 4.7c). The coherent state obeys $Q_{\mathrm{pair}}(\theta) = \sin^4(\theta/2)$, corresponding to the probability that two qubits in $|\downarrow\rangle$ are projected onto $|\uparrow\rangle_\theta$.

Figure 4.7d shows the distribution $\mathcal{C}_{\boldsymbol{n}}$ computed from the measured Husimi functions of the coherent and W states. For the coherent state, the measured $\mathcal{C}_{\boldsymbol{n}}$ remains close to

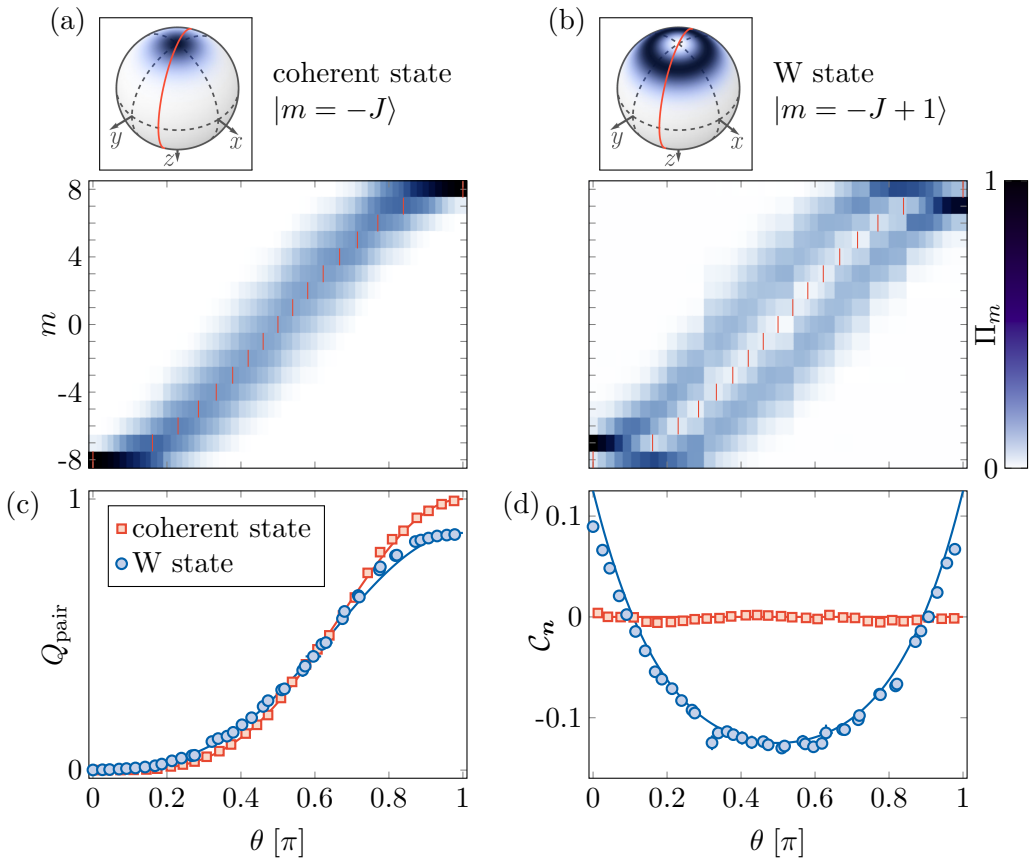

Figure 4.7: Qubit pair properties of coherent and W states. (a,b) Measured spin projection probabilities Π_m as a function of the polar angle θ, for a coherent spin state (a) and for the W state (b). The red vertical lines indicate the expected maxima for the coherent state, also corresponding to minima for the W state. The top panels represent the considered spin-J states on the generalised Bloch sphere; the red circles indicate the set of spanned measurement projection axis $\boldsymbol{n}$. (c) Pair Husimi function Q_{pair} computed from the (a) and (b) data (blue disks and red squares, respectively). The lines correspond to the expected functions $Q_{\text{pair}}(\theta)$ for the coherent and W states (red and blue lines). (d) Distribution $\mathcal{C}_{\boldsymbol{n}}$ of nonclassical correlations as a function of the polar angle θ. The W state's nonclassicality is evidenced by the points $\mathcal{C}_{\boldsymbol{n}} > 0$.

zero for all angles θ. The concurrence $\mathcal{C}$ is given by the global maximum of $\mathcal{C}_{\boldsymbol{n}}$ (or zero, if this maximum is negative). Our data are consistent with $\mathcal{C} = 0$. Indeed, the qubit pair drawn from this state itself forms a spin-1 coherent state, for which $\mathcal{C}_{\boldsymbol{n}}$ vanishes according to eq. (4.27).

We find that the prepared W state is not rotationally invariant along the z-axis; the projection probabilities show a small but significant variation with the azimuthal angle ϕ. This results from imperfections in the preparation protocol (see section 4.2.1), leading to a residual coherent admixture with other Dicke states. The quantities shown in fig. 4.7b,c,d are averaged over ϕ, with the error bars taking into account the dispersion. The measure $\mathcal{C}_{\boldsymbol{n}}$ takes significantly positive values for θ close to 0 and π, showing the state's nonclassical character. The azimuthal dependence is explicitly illustrated in fig. 4.8, where we show measurements for the azimuthal angles giving extremal values of $\mathcal{C}_{\boldsymbol{n}}$.

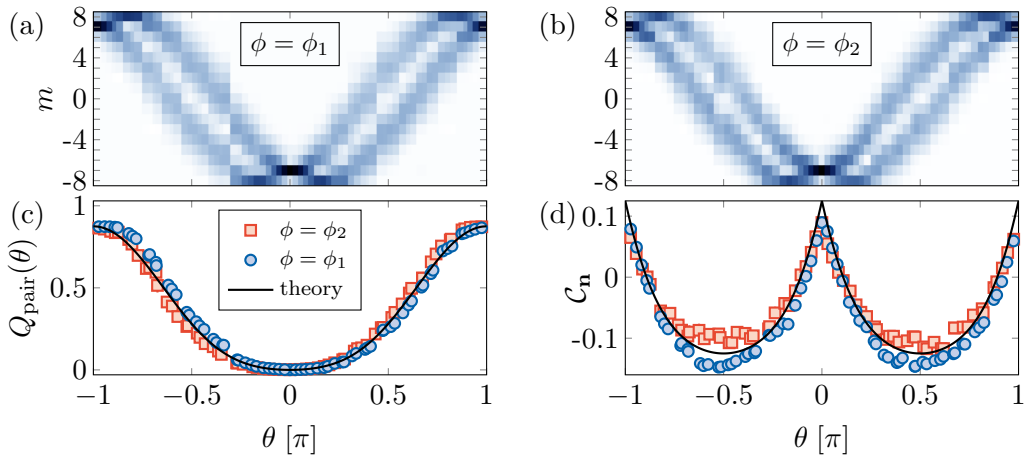

Figure 4.8: Deviation to z-rotation symmetry in the prepared W state. (a,b) Projection probabilities Π_m as a function of the polar angle θ, for $\phi_1 = 0.36(5)$ rad and $\phi_2 = \phi_1 - \pi/2$. (c) Pair Husimi functions Q_{pair} inferred from the (a) and (b) data (blue disks and red squared, respectively). The error bars (here, smaller than data markers) represent the statistical uncertainty from a bootstrap random sampling analysis. The solid line corresponds to the expected variation for the W state. (d) Distribution $\mathcal{C}_{\boldsymbol{n}}$ as a function of θ. The two azimuthal angles ϕ_1 and ϕ_2 are chosen to minimise and maximise the measured $\mathcal{C}_{\boldsymbol{n}}$ respectively.

The global maximum of $\mathcal{C}_{\boldsymbol{n}}$ is reached at the north pole $\theta = 0$, giving a concurrence $\mathcal{C} = 0.089(5)$. This is 71% of the maximum possible value $\mathcal{C} = 1/J = 0.125$ in a system of $2J$ qubits symmetric upon exchange [255], which would be reached for perfect preparation of the W state. Again, the limiting factor is imperfect state preparation, in particular the residual occupation $\Pi_{-J+2} \simeq 0.03$ and $\Pi_{-J+3} \simeq 0.01$ of the next Dicke states.[7]

4.4.5 *Squeezed state*

We now extend the study of qubit pair properties to states prepared by one-axis twisting dynamics (as introduced in section 4.2.1). The first of these is the squeezed state, which, unlike the Dicke states, is inherently asymmetric around the z-axis, since we can identify squeezed and anti-squeezed azimuthal directions. We denote these ϕ_{min} and $\phi_{\text{max}} = \phi_{\text{min}} + \pi/2$ respectively.

We show in fig. 4.9a,b the corresponding probabilities $\Pi_m(\theta, \phi)$. For $\theta = \pi/2$, a minimum spin projection uncertainty $\Delta J_{\text{min}} = 0.92(16)$ is measured at ϕ_{min} (see fig. 4.9c), in agreement with the value $\Delta J_{\text{min}} = 0.85$ expected for an optimally squeezed state (within the one-axis twisting dynamics). The measured distribution $\mathcal{C}_{\boldsymbol{n}}$ (fig. 4.9d) takes its maximum for $\theta = \pi/2$ and $\phi = \phi_{\text{min}}$, i.e. along the squeezed quadrature direction. This maximum gives a value for the concurrence $\mathcal{C} = 0.058(6)$, in agreement with the expected value of 0.055.

[7] Remember that the concurrence is not linear with respect to the prepared state or the pair density matrix. Here, we find that the concurrence is dramatically reduced by simultaneous residual occupation of the $m = -J$ and $m = -J + 3$ levels.

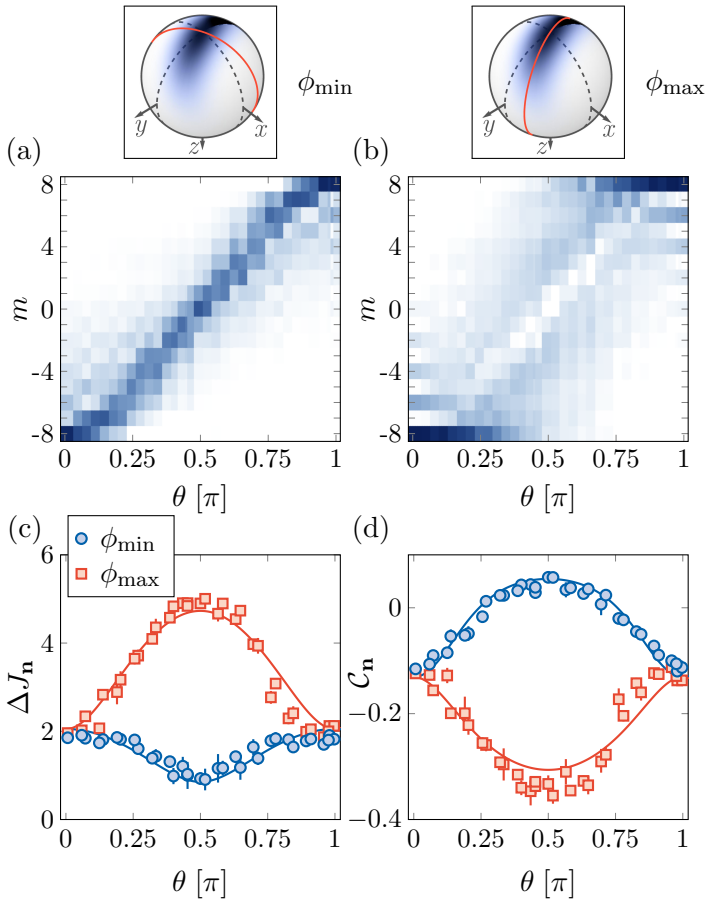

Figure 4.9: Qubit pair properties for a squeezed state. (a,b) Measured spin projection probabilities Π_m for a squeezed spin state, as a function of the polar angle θ with azimuthal angles (a) $\phi_{\min} = -0.4(2)$ rad and (b) $\phi_{\max} = \phi_{\min} + \pi/2$. These are the squeezed and anti-squeezed azimuthal directions. (c) Spin projection uncertainty $\Delta J_{\boldsymbol{n}}$ computed from the (a) and (b) data (blue disks and red squares, respectively). The lines correspond to the projection uncertainties expected for the targeted spin state. (d) Distribution $\mathcal{C}_{\boldsymbol{n}}$ of nonclassical correlations as a function of θ.

Our measurements can be used to check the direct link between quadrature squeezing and nonclassical pairwise correlations [59]. Indeed, for the states reached via the one-axis twisting dynamics, one expects the concurrence to be expressed in terms of the minimum spin projection uncertainty, as

$$\mathcal{C} = \frac{1 - 2\Delta J_{\min}^2/J}{2J-1}. \tag{4.33}$$

From the measured projection quadrature, we calculate a value of 0.053(5) for the right-hand side of eq. (4.33), in agreement with the direct concurrence measurement.

4.4.6 *Schrödinger cat state*

Finally, we apply the qubit pair protocol to the Schrödinger cat state. Figure 4.10a, shows the measured probabilities $\Pi_m(\boldsymbol{n})$ with respect to the polar angle θ. For $\theta = 0$, we confirm dominant population of the two stretched states, with $\Pi_{-J} = 0.38(2)$ and $\Pi_J = 0.42(2)$.

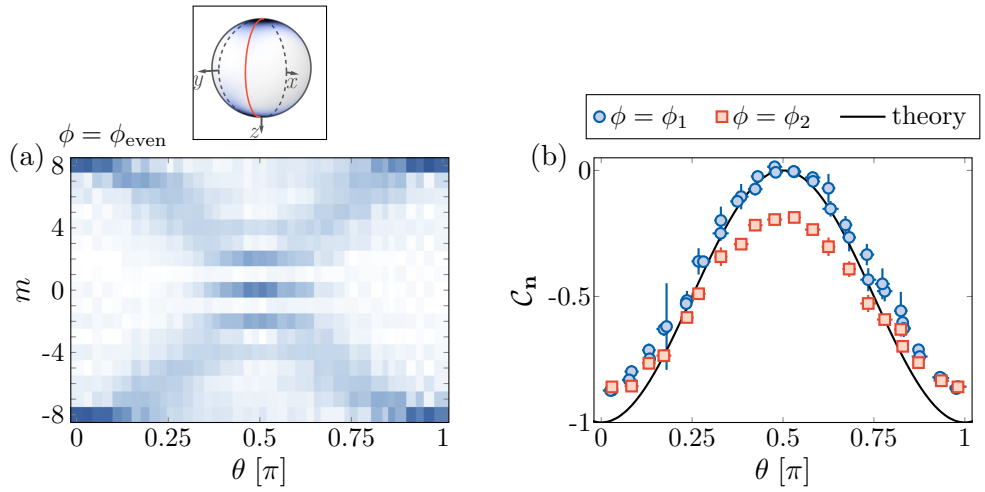

Figure 4.10: Qubit pair properties for a Schrödinger cat state. (a) Measured spin projection probabilities Π_m for a cat state, as a function of the polar angle θ. The azimuthal angle ϕ_{even} is chosen such that the two coherent state Husimi functions interfere destructively for odd-m values around $\theta = \pi/2$, giving an even parity. For the full ϕ-dependence of the state along the equator, see fig. 4.11a. (b) The nonclassicality measure $\mathcal{C}_n$ inferred from the projection probabilities like those shown in (a). We show measurements for the azimuthal angle $\phi_1 = 3.3(1)$ rad (blue disks), which shows maximal $\mathcal{C}_n$. This direction is most relevant for the determination of the concurrence. To illustrate the range of variation of $\mathcal{C}_n$, we also show measurements for $\phi_2 = \phi_1 - \pi/2$ (red squares). The solid line corresponds to the expected variation for a perfect cat state.

When varying θ, the distribution is a superposition of the contributions of each of the two coherent states forming the cat state. Interestingly, we observe interference between the two distributions when they overlap, i.e. for $\theta \simeq \pi/2$.

Similar to the W state, we measure a slight variation of pair properties with ϕ, as shown in fig. 4.10b. Since we focus on extracting the concurrence from the maximum of $\mathcal{C}_n$, we are most interested in the measurements for the azimuthal angle $\phi_1 = 3.3(1)$ rad that maximizes $\mathcal{C}_n$. To illustrate the range of variance, we also show results for $\phi_2 = \phi_1 - \pi/2$.

Our measurements are consistent with $\mathcal{C}_n < 0$ for all angles θ, showing that the reduced two-qubit state is classical. This measurement highlights a well-known property of the cat state, namely that any of its subsystems is classical. Revealing its entanglement properties requires going beyond pairwise measures, as we show in the following section.

4.5 PROBING ENTANGLEMENT VIA SUBSYSTEM ENTROPY

So far, we have studied the entanglement of $2J$-qubit states via the nonclassical character of their qubit pairs. In this section, we access entanglement more directly by probing whether a given state of the spin $J = 8$ is separable with respect to the 14 : 2 partition performed by the photon absorption. To prove entanglement with respect to this partition, we use the condition of negative conditional entropy

$$S_\infty(14|2) \equiv S_\infty(\rho) - S_\infty(\rho_{\text{pair}}) < 0 \tag{4.34}$$

which was introduced in section 4.1.1. Recall that the infinite-order Renyi entropies on the right hand side of the equation are each given by $-\log_2 \lambda_{\max}$, where $\lambda_{\max}$ is the largest eigenvalue of the respective density matrix.

Our method to evaluate the Rényi entropies is as follows. For the global $2J$-qubit state, we make use of the fact that $\lambda_{\max}$ is the maximum possible overlap of ρ with a pure state. We measure this overlap with respect to a well-chosen pure state to give a lower bound on $\lambda_{\max}$. For the extracted pair state, our method is based on the information encoded in the pair Husimi function measured in the previous section. This permits tomography of the pair density matrix [256]. We fit the measured Husimi function by a spherical harmonic expansion

$$Q_{\text{pair}}(\boldsymbol{n}) = \frac{1}{3} + \sqrt{\frac{4\pi}{3}} \sum_{\ell=1}^{2} \sum_{m=-\ell}^{\ell} \lambda_{\ell,m} Y_\ell^m(\boldsymbol{n}), \tag{4.35}$$

and infer the density matrix as

$$\rho_{\text{pair}} = \frac{1}{3}\mathbb{I} + \sum_{m=-1}^{1} \lambda_{1,m} \mathcal{L}_m + \sum_{m=-2}^{2} \lambda_{2,m} \mathcal{Q}_m, \tag{4.36}$$

where the $\mathcal{L}_m$ and $\mathcal{Q}_m$ matrices correspond to the $L = 1$ angular momentum components and quadrupole moments, respectively.[8]

4.5.1 *W state*

We perform the tomography for the pair state extracted from the W state, taking into account the slight variation of the Husimi function $Q_{\text{pair}}(\boldsymbol{n})$ with respect to the azimuthal angle ϕ in the prepared state. We infer a density matrix[9]

$$\rho_{\text{pair}} \simeq \begin{pmatrix} 0.88 & 0.01 + 0.05\,\mathrm{i} & -0.01 - 0.01\,\mathrm{i} \\ 0.01 - 0.05\,\mathrm{i} & 0.12 & 0.01\,\mathrm{i} \\ -0.01 + 0.01\,\mathrm{i} & -0.01\,\mathrm{i} & 0 \end{pmatrix},$$

[8] These operators are:

$$\mathcal{L}_0 = L_z, \quad \mathcal{L}_{\pm 1} = \mp(L_x \pm \mathrm{i} L_y)/\sqrt{2},$$
$$\mathcal{Q}_0 = \sqrt{\frac{5}{3}}(3L_z^2 - 2), \quad \mathcal{Q}_{\pm 1} = \mp\sqrt{\frac{5}{2}}[(L_x \pm \mathrm{i} L_y)L_z + L_z(L_x \pm \mathrm{i} L_y)], \quad \mathcal{Q}_{\pm 2} = \sqrt{\frac{5}{2}}(L_x \pm \mathrm{i} L_y)^2.$$

[9] Here, we work in basis of symmetric states: $|{\downarrow\downarrow}\rangle$, $(|{\downarrow\uparrow}\rangle\,|{\uparrow\downarrow}\rangle)/\sqrt{2}$, and $|{\uparrow\uparrow}\rangle$.

with typically 1% statistical uncertainty. The reconstructed matrix is visually represented in fig. 4.12, and it closely resembles the expected one

$$\rho_{\text{pair}} = \begin{pmatrix} 7/8 & 0 & 0 \\ 0 & 1/8 & 0 \\ 0 & 0 & 0 \end{pmatrix}.$$

Note that 7/8 is simply the probability of choosing both qubits in $|\downarrow\rangle$ when picking from an ensemble where one out of sixteen qubits is in $|\uparrow\rangle$. Diagonalization of the reconstructed density matrix gives a maximum eigenvalue $\lambda_{\max}(\rho_{\text{pair}}) = 0.882(5)$.

We now consider the global spin-J state. The projection probability $\Pi_{-J+1} = 0.91(1)$, onto the Dicke state $|m = -J+1\rangle$, straightforwardly provides a lower bound on the maximum overlap $\lambda_{\max}(\rho)$ with pure states.

Combining these results for the 2- and $2J$-qubit states according to eq. (4.34), we obtain the conditional entropy

$$S_\infty(14|2) < -0.03(1).$$

Its negative value shows that the prepared state is not separable with respect to a 14 : 2 partition, and is thus entangled.

4.5.2 *Schrödinger cat state*

We now consider the case of a Schrödinger cat state, for which the effect of the 14 : 2 partition is more striking. Extending the tomography protocol to the cat state, we obtain the reduced two-body density matrix

$$\rho_{\text{pair}} \simeq \begin{pmatrix} 0.46 & -0.01\,\mathrm{i} & -0.03 + 0.05\,\mathrm{i} \\ 0.01\,\mathrm{i} & 0.05 & -0.01\,\mathrm{i} \\ -0.03 - 0.05\,\mathrm{i} & 0.01\,\mathrm{i} & 0.49 \end{pmatrix},$$

that we compare to the expected matrix

$$\rho_{\text{pair}} = \begin{pmatrix} 1/2 & 0 & 0 \\ 0 & 0 & 0 \\ 0 & 0 & 1/2 \end{pmatrix} \tag{4.37}$$

obtained for a perfect cat state. The maximum eigenvalue of the reconstructed matrix is $\lambda_{\max}(\rho_{\text{pair}}) = 0.53(1)$.

The evaluation of the maximal eigenvalue of the prepared cat state is more involved. We evaluate its maximal overlap with the family of pure cat states $|\text{cat}_\beta\rangle = (|m = -J\rangle +$

$e^{i\beta}|m=J\rangle)/\sqrt{2}$. The simple form of these states in the Dicke basis allows us to express the overlap with a general state ρ as

$$\mathcal{O}_\beta = \langle \text{cat}_\beta | \rho | \text{cat}_\beta \rangle = \frac{\rho_{-J,-J} + \rho_{J,J} + 2\,\text{Re}(\rho_{-J,J}\, e^{i\beta})}{2},$$

where the diagonal elements $\rho_{m,m}$ are simply the spin projection probabilities Π_m, which we have already measured in section 4.4.6. The overlap $\mathcal{O}_\beta$ takes its maximum value $\mathcal{O}$ for $\beta = -\arg\rho_{-J,J}$, with

$$\mathcal{O} = \frac{\Pi_{-J} + \Pi_J + 2|\rho_{-J,J}|}{2}.$$

We present two protocols giving a lower bound on the extremal coherence $|\rho_{-J,J}|$, both based on the measurement of an observable A defined for the spin-J state. We consider its mean value in a state obtained after the cat state preparation, followed by a Larmor rotation around z of angle ϕ, as

$$\langle A \rangle(\phi) = \sum_{m,m'} a_{m,m'}\, \rho_{m',m}\, e^{i(m'-m)\phi}.$$

The extremal coherence can be singled out by measuring the Fourier coefficient $A_{2J} = |a_{J,-J}\,\rho_{-J,J}|$ at frequency $2J$ [231, 257]. We will use observables that can only take values in the interval $[-1,1]$, such that $|a_{J,-J}| \leq 1$. The coefficient A_{2J} then provides a lower bound on the extremal coherence $|\rho_{-J,J}|$.

The first observable we consider is the parity P of the spin projection along an equatorial direction $\boldsymbol{n} \perp \hat{\boldsymbol{z}}$, as a function of the azimuthal angle ϕ. We previously used the parity in chapter 3, where, for $\boldsymbol{n} = \hat{\boldsymbol{z}}$ it represented $\mathcal{Z}_2$ the symmetry of the LMG model. Note that the parity is commonly used to characterize cat states [224, 229–231, 233, 234, 238]. The parity is essentially recovered from the interference pattern between the $|m = \pm J\rangle$ projection distributions when they overlap at the equator $\theta \simeq \pi/2$ (cf. fig. 4.10a). We now measure this pattern with respect to the azimuthal angle ϕ (fig. 4.11a), observing an alternation between even- and odd-m projections with period $2\pi/(2J)$. We fit its oscillation, shown in fig. 4.11b, with a Fourier series, from which we extract the Fourier coefficient $P_{2J} = 0.26(1)$.

The second observable is measured following a non-linear evolution scheme [196, 258–261]. Firstly, the cat is prepared by a pulse of the one-axis twisting coupling (see fig. 4.11c, upper panel). This is followed by a waiting period, leading to a Larmor rotation by an angle ϕ around the z-axis. Finally, the same one-axis twisting pulse is reapplied. In the absence of imperfections, this procedure would create the superposition $\sin(J\phi)\,|m=-J\rangle + \cos(J\phi)\,|m=J\rangle$, allowing for extraction of the maximal coherence from the oscillation of z-projection probabilities of these two states only. In practice, we observe residual probabilities in other projection values m, as shown in fig. 4.11c. These

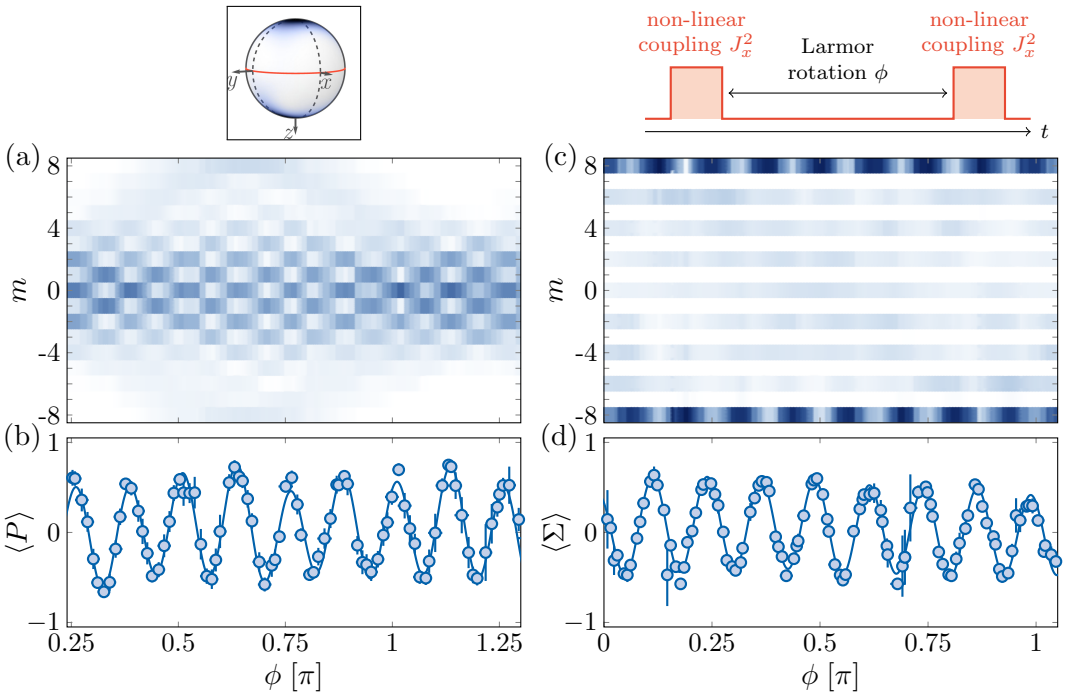

Figure 4.11: Two protocols for measuring the extremal coherence $|\rho_{-J,J}|$ of the prepared cat state. This allows a calculation of the overlap with respect to the family of ideal, pure cat states $|\mathrm{cat}(\beta)\rangle = (|m=-J\rangle + \mathrm{e}^{\mathrm{i}\beta}\,|m=J\rangle)/\sqrt{2}$. Parity protocol: (a) Projection probabilities Π_m measured along equatorial directions ($\theta = \pi/2$), parametrized by the azimuthal angle ϕ. (b) Evolution of the mean parity $\langle P \rangle$ deduced from (b). Non-linear detection protocol: (c) Projection probabilities Π_m measured after preparation of the cat using a one-axis twisting pulse $H \propto -J_x^2$, Larmor rotation of angle ϕ, and a second identical non-linear pulse. The protocol is shown in the top panel. (d) Evolution of the mean sign of even projections $\langle \Sigma \rangle$ deduced from (c). The solid lines in (b,d) are fits with a Fourier series. In either case, the amplitude of the component with period $2\pi/(2J)$ gives a lower bound on $|\rho_{-J,J}|$.

are in even m-states only, as expected from parity symmetry. We thus use an observable Σ defined as the sign of the spin projection on even states, with

$$\langle \Sigma \rangle = \sum_{m \text{ even}} \mathrm{sgn}(m)\Pi_m. \tag{4.38}$$

Its oscillation, shown in fig. 4.11d, gives a Fourier coefficient $\Sigma_{2J} = 0.247(5)$. The advantage of the sign observable Σ will become clear in the next section, where we consider a more complex quantum state.

The oscillations of the two observables, P and Σ, lead to comparable estimates of the extremal coherence. Using the measured probabilities $\Pi_{\pm J}$ quoted above, we infer a lower bound on the overlap $\mathcal{O} \geq 0.66(2)$ and thus on the eigenvalue $\lambda_{\max}(\rho)$. Combining this with the results of the pair state tomography, we get a conditional entropy

$$S_\infty(14|2) < -0.23(3),$$

Pair non-classicality

State ρ	Concurrence $\mathcal{C}(\rho_{\text{pair}})$
coherent	0
W	$0.71(4) \times \frac{1}{J}$
squeezed	0.058(6)
cat	0

Entanglement w.r.t. $14:2$ partition

State ρ	Max eigenvalue $\lambda_{\max}(\rho)$	Pair state ρ_{pair}	Conditional entropy $S_\infty(14\|2)$
W	$\geq 0.91(1)$	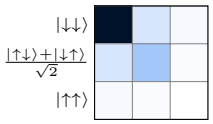	$< -0.03(1)$
cat	$\geq 0.66(2)$	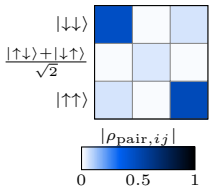	$< -0.23(1)$

Figure 4.12: Summary of results obtained by extraction of a polarised qubit pair $|\uparrow\uparrow\rangle$ from a $2J$-qubit state ρ, by coupling to excited state $J' = J - 1$.

which proves entanglement more evidently than for the W state. We note that the requirement $\mathcal{O} > \lambda_{\max}(\rho_{\text{pair}}) = 0.53(1)$, which we use to demonstrate the non-separability with respect to the $14:2$ partition, is consistent with the entanglement witness $\mathcal{O} > 0.5$ introduced in section 4.1.2.

Summary

Our results so far are summed up in fig. 4.12. We extracted a qubit pair ($L = 1$) in state $|\uparrow\uparrow\rangle$, defined externally by the polarisation of light, which couples the atom to an excited level $J' = J - 1$ with two fewer qubits. Since the amplitude of this process is proportional to the probability of finding such a polarised pair, our protocol gives direct information on the reduced pair state. This allowed us to extract the associated concurrence, quantifying the pair state's nonclassicality. In a second set of experiments, we reconstructed the qubit pair state, and combined this with purity measurements of the prepared 16-qubit state to give the conditional entropy of $14:2$ bipartition, which allowed us to detect entanglement.

4.6 DECOHERENCE ON QUBIT LOSS

We now consider the removal of a pair of qubits randomly drawn from the electronic spin state, irrespective of the pair's quantum state. For this purpose, we prepare a state of interest ρ' in an excited level of angular momentum $J' = 9$, corresponding to a symmetric state of $2J' = 18$ qubits (see fig. 4.13). The spontaneous emission of a photon drives the system to the ground state $J = 8$, which has two missing qubits. The emitted photon can, in general, carry an arbitrary polarisation, therefore the process allows for three independent quantum jumps associated with the polarisations $\boldsymbol{\epsilon}_{-1}, \boldsymbol{\epsilon}_0, \boldsymbol{\epsilon}_1$,

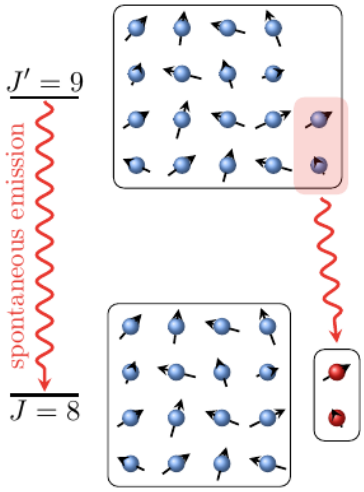

Figure 4.13: Scheme of the experiments to probe decoherence on qubit pair loss in the electronic spin of dysprosium. A symmetric state of $2J' = 18$ qubits is prepared in the excited manifold. A spontaneous emission process removes a random pair of qubits, following which we measure the reduced 16-qubit state in the ground level $J = 8$.

with $\boldsymbol{\epsilon}_{\pm 1} = (\boldsymbol{\epsilon}_x \pm \mathrm{i}\boldsymbol{\epsilon}_y)/\sqrt{2}$ and $\boldsymbol{\epsilon}_0 = \boldsymbol{\epsilon}_z$ (this is the same polarisation basis introduced in section 4.3.2). After spontaneous emission, the ground-state density matrix reads

$$\rho = \sum_{q=-1}^{1} \langle \boldsymbol{\epsilon}_q | \rho' | \boldsymbol{\epsilon}_q \rangle \,. \tag{4.39}$$

This is simply a trace over a qubit pair in the original state

$$\rho = \mathrm{Tr}_2 \, \rho'. \tag{4.40}$$

This corresponds to the loss of an arbitrary qubit pair. The pair is encoded in the photon (as the spin state corresponding to its polarisation, $\mathrm{Tr}_{16}\,\rho'$), which is lost to the environment in the results presented here. We probe the spin-J state ρ after decay, and use it to infer properties of the corresponding initial state ρ'.

4.6.1 *Robustness of pairwise correlations*

We first investigate the effect of particle loss on a W state prepared in an excited electronic level of angular momentum $J' = J + 1$, coupled to the ground state with an optical transition of wavelength 626 nm.[10] To produce the state $|m' = -J' + 1\rangle$ in the excited level, we start in the coherent state $|m = -J\rangle$ of the lowest energy manifold, and use π polarised resonant light to couple the system to the desired state (see fig. 4.14a). As shown in fig. 4.14b, we monitor the Rabi oscillation via the atom recoil upon light absorption.

[10] The light pulses are implemented with a laser locked to the atomic transition at 626 nm i.e. the MOT laser. An AOM allows for independent control of the beam's frequency, and also for the creation of the fast pulses needed; to this end, the beam is focussed at the AOM crystal.

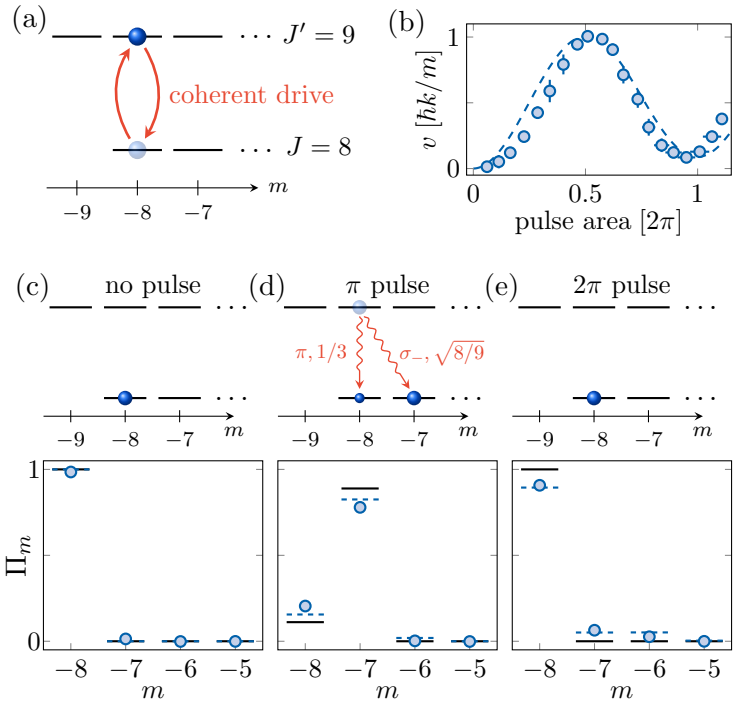

Figure 4.14: Loss of a qubit pair from a W state. (a) Scheme for the preparation of the W state in the excited electronic level. (b) Evolution of the mean atom velocity acquired due to the photon absorption recoil, as a function of the light pulse duration. The dashed line is a model taking into account spontaneous emission during the pulse. (c,d,e) Top panels: expected states, with a scheme of spontaneous emission in (d) showing the Clebsch-Gordan coefficients for the two possible quantum jumps. Bottom panels: spin projection probabilities (c) in the absence of the resonant light pulse, (d) for a π pulse and (e) a 2π pulse. The solid lines are the probabilities expected for a perfect W state, while the dashed lines use the same model as in (b).

The comparison with a master equation model, which takes into account spontaneous emission during the Rabi flopping, allows us to estimate a fidelity of 0.98 for a pulse duration $t_{\text{pulse}} \simeq 62\,\text{ns}$ – the excited state lifetime being $\tau_{\text{exc}} \simeq 1.2\,\mu\text{s}$ [262].

Following the light pulse, we wait for spontaneous emission to occur before measuring the spin state in the ground level. We observe significant populations only in the states $|m = -J\rangle$ and $|m = -J+1\rangle$, as expected from the selection rule $|m' - m| \leq 1$. The state $|m = -J+1\rangle$ is dominantly populated, showing that, in most cases, the $|\uparrow\rangle$ excitation of the W state is not removed upon the loss of a qubit pair. The projection probabilities, shown in fig. 4.14d, are close to the expected values $\Pi_{-J+1} = 1/(J+1)$ and $\Pi_{-J} = 1 - \Pi_{-J+1}$, with a residual difference mostly explained by the imperfect state preparation.

The nonclassicality of qubit pairs in the final state is probed via the distribution $\mathcal{C}_{\boldsymbol{n}}$ introduced in section 4.4.2. Recall that $\mathcal{C}_{\boldsymbol{n}}$ is obtained from the spin projection probabilities along $\boldsymbol{n}$. Since its maximum value is expected to be attained along z, we only consider projections along this direction, and obtain $\mathcal{C}_{\hat{z}} = 0.104(3)$. This value provides a lower bound on the qubit pair concurrence, expected to be $\mathcal{C} = 1/(J+1) \simeq 0.111$ in the initial state. The proximity of the initial state concurrence and the measured one after decay

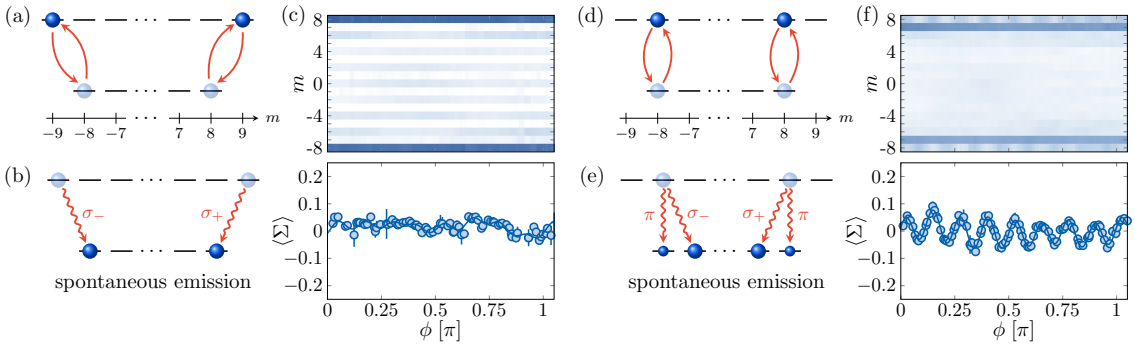

Figure 4.15: Loss of a qubit pair from superposition states. (a) Preparation of the Schrödinger cat state $|\psi_1\rangle$ in the excited electronic level. Given the small values of their Clebsch-Gordan coefficients, we neglect the couplings between $|m = \pm 8\rangle$ and $|m' = \pm 7\rangle$. (b) Scheme of the subsequent spontaneous emission. (c) Top panel: spin projection probabilities measured in the xy plane, as a function of the azimuthal angle ϕ. The corresponding sign observable $\langle\Sigma\rangle$ is shown below, together with a fit with a Fourier series. The y axis range has been reduced compared to fig. 4.11d to highlight the absence of oscillation. The panels (d,e,f) show the same information for the superposition state $|\psi_2\rangle = (|m' = -8\rangle + |m' = 8\rangle)/\sqrt{2}$.

illustrates that losing qubits does not alter nonclassicality of the remaining qubits pairs – this robustness to the loss of qubits is a defining property of the W state entanglement class (see section 4.1.2 and ref. [75]).

4.6.2 *Fragility of macroscopic coherence*

We contrast the W state's behaviour with that of coherent superpositions of states distant in phase space [263].

We consider two examples, namely a cat state

$$|\psi_1\rangle = (|m' = -J'\rangle + |m' = J'\rangle)/\sqrt{2}\,,$$

and the superposition

$$|\psi_2\rangle = (|m' = -J' + 1\rangle + |m' = J' - 1\rangle)/\sqrt{2}\,.$$

Their preparation consists in producing a cat state in the ground manifold $(|m = -J\rangle + |m = J\rangle)/\sqrt{2}$ (see section 4.2.1), and then resonantly to coupling it to the excited manifold. The state $|\psi_1\rangle$ is produced using an x-linear polarisation $\epsilon_x = (\epsilon_1 + \epsilon_{-1})/\sqrt{2}$, which dominantly couples the stretched states $|m = \pm J\rangle$ to states $|m' = \pm J'\rangle$ (see fig. 4.15a). Couplings to states $|m' = \pm(J' - 2)\rangle$ also occur, albeit with very small Clebsch-Gordan coefficients, such that these processes can be neglected.[11] The state $|\psi_2\rangle$ is obtained using a z-linear polarisation (see fig. 4.15d). In both cases, a coherent Rabi oscillation is

[11] The coupling amplitudes between $|m = \pm J\rangle$ and $|m' = \pm(J' - 2)\rangle$ are smaller than the couplings between $|m = \pm J\rangle$ and $|m' = \pm J'\rangle$ by a factor of $\sqrt{153}$. When the population of $|m' = \pm J'\rangle$ is maximised, we expect a residual population of the states $|m' = \pm(J' - 2)\rangle$ of 3% due to these small couplings.

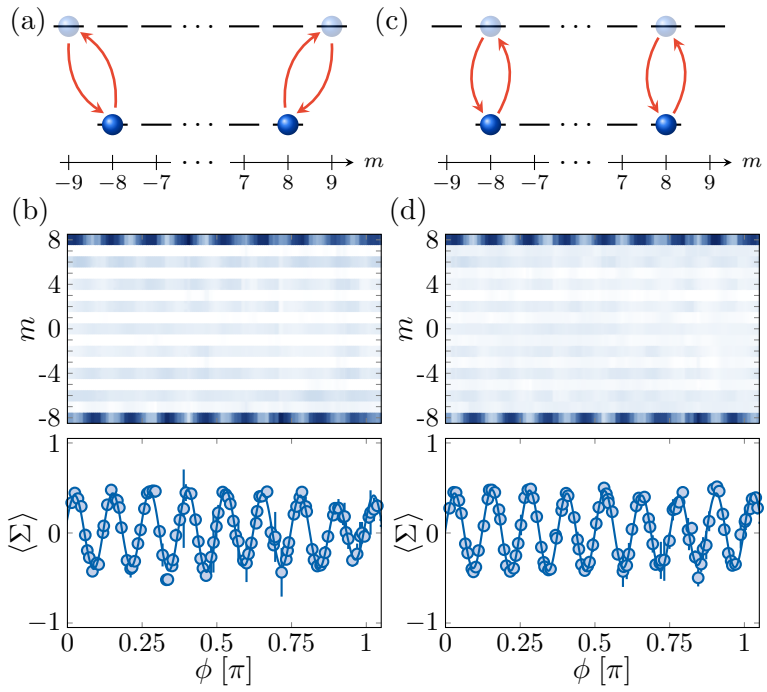

Figure 4.16: (a) Scheme of the 2π Rabi oscillation starting in a Schrödinger cat state of the electronic ground level, for an x-polarised laser excitation (state $|\psi_1\rangle$). (b) Top panel: spin projection probabilities measured after the non-linear detection protocol (see fig. 4.11), as a function of the azimuthal angle ϕ. The corresponding sign observable $\langle\Sigma\rangle$ is shown below, together with a fit with a Fourier series. The panels (c,d) show the same information for a z-polarised laser excitation (state $|\psi_2\rangle$). We find that the coherence $|\rho_{-J,J}|$, estimated by the Fourier component Σ_{2J}, is reduced to 0.202(2) (resp. 0.211(6)) for the x-polarised (resp. z-polarised) excitation, i.e. above 80% of the value obtained with no Rabi pulse. These measurements confirm that coherence is preserved during the Rabi oscillation.

observed when varying the pulse duration, and the fidelity of the preparation is limited by that of the cat state in the ground level. In fig. 4.16, we verify that the coherence of the superposition is maintained during Rabi flopping by studying the states reached after 2π pulses.

We study the effect of qubit loss, triggered by spontaneous emission, on the superposition states $|\psi_1\rangle$ and $|\psi_2\rangle$. For the cat state $|\psi_1\rangle$, we only expect population of the stretched states $|m = \pm J\rangle$ (see fig. 4.15b). To check the coherence between them, we measure the sign observable $\langle\Sigma\rangle$ as a function of the azimuthal angle ϕ. As shown in fig. 4.15c, its oscillation is completely washed out (cf. fig. 4.11). We determine the Fourier component $\Sigma_{2J} = 0.006(10)$, indicating an absence of coherence. For the superposition state $|\psi_2\rangle$, we observe dominant projection probabilities in the states $|m = \pm(J-1)\rangle$, corresponding to the spontaneous emission of a $\sigma_\mp$ polarised photons respectively (see fig. 4.15e). We do not measure any significant variation of these probabilities with the azimuthal angle ϕ, excluding coherence between them. We also measure residual projection probabilities in the stretched states $|m = \pm J\rangle$, which occur via the spontaneous emission of a π polarised photon. The advantage of our definition of the sign observable Σ (eq. (4.38)) becomes

clear here: it allows one to test the coherence between the states $|m = \pm J\rangle$, without being affected by the atoms populating odd-m states. The measured probabilities in stretched states coherently oscillate as a function of the angle ϕ (see fig. 4.15f). More quantitatively, the sign observable, which involves even-m only, evolves with a Fourier component $\Sigma_{2J} = 0.024(1)$.

The complete loss of coherence when starting in the cat state $|\psi_1\rangle$ can be interpreted as follows. The spontaneous decay involves two orthogonal polarisations, with a σ_+ polarised photon emitted when starting in the component $|m' = -J'\rangle$, while a σ_- polarised photon is associated with the decay of the state $|m' = J'\rangle$. The photon polarisation thus holds complete *which path* information on the spin state polarisation – a term referring to Einstein's version of the double-slit interference experiment [264, 265]. In this case, the coherence between the different paths is erased after spontaneous emission.

We contrast this with the state $|\psi_2\rangle$. The most probable quantum jumps still correspond to the emission of σ_+ and σ_- polarised photons, which carry information about the state polarisation (see fig. 4.15e). However, the quantum jump associated with the emission of a π polarised photon does not leak this information, which explains the residual coherence. The measured Fourier coefficient Σ_{2J} corresponds to 9.7(5)% of the value measured in the absence of the excitation. This reduction is consistent with the probability $1/(J+1) \simeq 11.1\%$ to scatter a π polarised photon for the considered state, showing that this channel fully preserves coherence.

4.7 PERSPECTIVES

Above, we considered the partition of an angular momentum $J' = J + 1$ of an excited electronic state. A random qubit pair is extracted by spontaneous emission towards the ground state J. We showed that nonclassical pairwise correlations of the W state are robust to particle loss. On the contrary, we observed that coherent superpositions of states distant in phase space are very fragile in this regard.

4.7.1 *Flexible manipulation of entangled states*

The study of light-spin interaction presented here is limited to measurements of the electronic spin. An interesting extension would be to collect the spontaneously emitted photon, whose polarisation is entangled with the dysprosium atom's spin state. For instance, the composite atom-photon state after decay of the excited level cat $|\psi_1\rangle$ is

$$\frac{|m = J\rangle \otimes |\sigma_+\rangle + |m = -J\rangle \otimes |\sigma_-\rangle}{\sqrt{2}} \tag{4.41}$$

The photon can then be seen as a 'flying qubit', capable of being transported over significant distances and being manipulated with standard quantum optics tools. Carrying

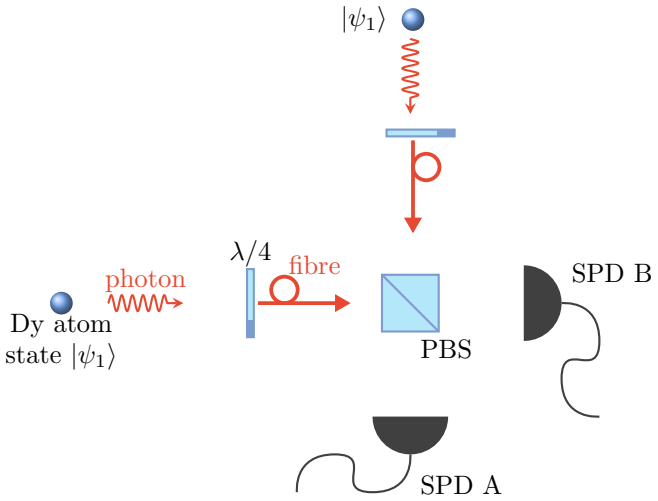

Figure 4.17: Scheme to create an entangled state of two distant dysprosium atoms. Both atoms are initialised in the cat state in the excited manifold $J' = 9$, with $|\psi_1\rangle = |m' = -J'\rangle + |m' = J'\rangle)/\sqrt{2}$. Spontaneously emitted photons are combined on a polarising beamsplitter (PBS). Simultaneous photon detection at both the single photon detectors (SPD) heralds atom-atom entanglement (see text for details).

forward the analogy with the double-slit experiment, the photon carries the *which path* information associated with the decay. In this spirit, spontaneous emission is a commonly used in protocols for entanglement manipulation (see, for example refs. [266–269]). Experiments in this area have been performed with trapped ions, neutral atoms or solid-state qubits acting as the 'stationary qubit(s)', typically with an effective spin of size 1 or 1/2 [270–275]. Such atom-light interfaces can form the building blocks of scalable quantum networks [276]. The large spin of dysprosium could provide several advantages here [277]: the enlarged Hilbert space implies increased information capacity, better resilience to noise, and more secure quantum cryptography. Furthermore, a superposition of states distant in phase space, such as our cat state, can itself act as a qubit with exceptional protection against certain decoherence channels – such systems have been dubbed 'cat qubits' [278, 279].

To conclude, we give a brief example of the kind of manipulations possible using the state 4.41 as a starting point; the example is closely related to a proposal in ref. [267] and the experiment in ref. [275]. Consider a pair of atoms, in two independent and spatially separated setups, each simultaneously initialised in the excited level cat state $|\psi_1\rangle$ (see fig. 4.17). We collect photons emitted along the z-direction and couple them into fibres.[12]The polarisations are rotated, such that upon arrival at a polarising beamsplitter, σ_- (resp. σ_+) photons are sent to photon detector A (resp. B). Assuming care is taken to

[12] The scheme's success rate could be greatly improved by placing each atom in an optical cavity; the resonant cavity mode establishes a direction for photon emission [272].

maintain the indistinguishability of photons arriving from the two atoms, simultaneous detection at both A and B projects the atom pair into the state

$$\frac{|m = J\rangle_1 \otimes |m = -J\rangle_2 + |m = -J\rangle_1 \otimes |m = J\rangle_2}{\sqrt{2}}.$$

This scheme has mapped photon-atom entanglement to atom-atom entanglement.

4.7.2 *Indistinguishable particle entanglement*

The discussion of nonclassicality and entanglement in this chapter uses a point of view equating a spin-J system to $2J$ indistinguishable qubits in a symmetric state. By construction, there is no meaningful way to label the qubits – and few-qubit observables are only accessible indirectly from measurements on the composite spin-J.

The fundamental nature of entanglement in systems of indistinguishable particles has been a subject of considerable theoretical discussion [280–286] (see also the recent review [76] and the references therein). Much of this debate has been motivated by experiments of BECs with two atomic states occupied, forming a pseudo-spin 1/2 [63]. If only a single spatial mode is occupied, quantum statistics dictate that the global spin state must be symmetrised – hence defining the Hilbert space as that of a total spin $J = N/2$ (see also the discussion for the LMG model in section 3.4). In this situation, it is natural to ask questions such as: is it meaningful to say that the two-particle state $(|\uparrow\downarrow\rangle + |\downarrow\uparrow\rangle)/\sqrt{2}$ entangled, since the superposition could be seen as a trivial consequence of the symmetry requirement? There have been several, at times contradictory, approaches to answer this question, each with implicitly different definitions of locality [76]. Another interesting question is the extent to which such entanglement is a useful resource for quantum information applications [287–289]. A few recent experiments have approached these issues by partitioning the system into distinguishable spatial modes [290–293].

We hope that our work brings a new perspective to this search for a consistent description of entanglement for identical particles. Although optically manipulated single spin-J systems are commonly used in entanglement generation protocols [266, 267, 270–275, 294], they have not, to our knowledge, been considered in the context of this debate. In this sense, our qubit loss experiments effectively distinguish a spin-1 subsystem by moving it to a separate mode (i.e. the photon polarisation). Our results also fit into the framework of conversion of nonclassicality into entanglement introduced in refs. [286, 295].

4.8 MANY-BODY SPIN PHYSICS WITH DYSPROSIUM

So far in this thesis, we have studied the LMG model and entanglement properties of the dysprosium's large electronic angular momentum. We have demonstrated how

optical couplings, specifically non-linear light shifts, are a powerful tool for producing nonclassical states in the ground and excited state manifolds. The robust single-state resolved detection techniques, averaged over the thermal cloud, allow for single/few-shot detection of the usual first- and second-order moments (e.g. J_n, J_n^2), as well as maximal-order moments 'custom designed' for a particular application (e.g. the parity P, and the sign variable Σ). A promising future direction would be to extend these ideas to systems of interacting dysprosium atoms. One option to engineer interactions would be via an optical cavity mode, as briefly discussed by us in ref. [202]. Here, we focus instead on the possibilities arising from direct atom-atom interactions, primarily considering the regime of a BEC with a spin degree of freedom, i.e. a spinor gas.

Spinor BECs are now a staple in the cold atoms community – see refs. [296, 297] for general reviews. Some common species used are ^{87}Rb ($F = 1, 2$) and ^{23}Na ($F = 1$), and the dipolar species ^{57}Cr ($F = 3$). Lanthanide species have remained largely unexplored, though there is considerable theoretical interest (see ref. [37] for a recent review). In the low-energy limit, the contact interactions for a pair of atoms with aribitrary spin states are fully characterised by a set of scattering lengths a_K, where $K = 0, 2 \ldots, 2F$ is the total angular momentum. For example, the spin-dependent interaction Hamiltonian for $F = 1$ is proportional to $(a_2 - a_0)\, F_1 \cdot F_2$. In this regard, ^{87}Rb is called ferromagnetic ($a_2 < a_0$) while ^{23}Na is antiferromagnetic ($a_2 > a_0$) .

Conceptually, the simplest situation for a spinor BEC is the mean-field limit, with atom number $N \gg F$, where all particles are condensed into a single spatial and spin state, in a vanishing external magnetic field. Then, the condensate spontaneously breaks the rotational SO(3) symmetry in addition to the usual U(1) gauge symmetry. The ground state phase diagram can host nonclassical states, such as the cat state or the $m = 0$ Dicke state [298, 299]. [13] Experimental realisation of such physics has tended to be with alkali atoms in finite fields, where the state observed instead depends on the sign and strength of Zeeman shifts [296], with weak dipole-dipole interactions preventing relaxation to the global ground state.

In strongly dipolar gases, the non-condensed state only has SO(3) symmetry in spherical trapping geometries. Dipolar interactions make relaxation of the total spin possible, which determines the dynamics of the spinor ground state and allows for thermalisation of the spin with kinetic degrees of freedom – as studied for chromium gases [300, 301]. Note that dipolar interactions can also lead to dramatic deviations from the single-mode approximation, for example, by the formation of spatially modulated spin textures [302].

For dysprosium, the large spin Hilbert space increases the potential for exotic spinor states. A convenient way to represent these is with a set of $2J = 16$ points on the Bloch sphere, called Majorana stars [145, 305]. These points give the directions opposite to where the underlying spin 1/2's point, and so they are also the roots of the spin-J Husimi

[13] In the terminology of $F = 2$ spinor physics, for example, these are called biaxial nematic and uniaxial nematic phases respectively.

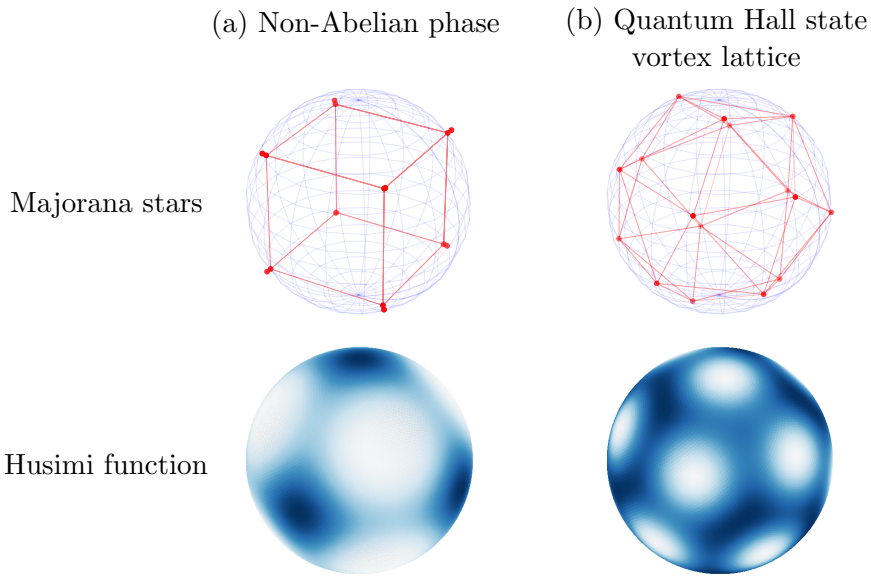

Figure 4.18: Spinor ground states for a $J = 8$ system, as represented by $2J$ Majorana stars on the Bloch sphere (top panels, red vertices), which lie at the zeros of the corresponding Husimi function (lower panels). (a) A state with non-Abelian character (see ref. [303] and the text). Pairs of Majorana stars lie at the vertices of a cube, giving O_h (octahedral) symmetry. (b) A state equivalent to a mean-field vortex lattice in a Hall system (see text). The vortex arrangement (calculated in ref. [304]), minimises effective repulsive contact interactions on the sphere. Mathematically, determining this vortex lattice configuration is also equivalent to the optimisation of electron positions in the Thomson plum-pudding model.

function. For example, the Dicke state $|m\rangle$ has $m + J$ stars at the north pole and $m - J$ stars at the south pole. The constellation of the Majorana stars reflects the symmetry of the spin state. In the mean-field and single-mode limit, a whole zoo of states is possible, depending on the scattering lengths a_K. If the symmetry group of the constellation is non-Abelian, the line-defects of the spinor BEC interact in unusual ways [306] – such states were classified in ref. [303] (see fig. 4.18a for an example), where the authors also discuss the detectable signatures of non-Abelian behaviour in the spin populations and the excitation spectrum. We mention that competition between multiple forms of magnetic order could be induced by additionally applying non-linear light shifts, as we did in our realisation of the LMG model.

The perspectives we discuss for dysprosium are necessarily speculative, since the spin-dependent scattering lengths a_K have not been measured for $K < 2J$. Nevertheless, we now discuss a special case $a_{2J} \gg a_K$, $a_{2J} > 0$ (for all $K < 2J$), since it is closely linked with the topic of the remainder of this thesis: artificial gauge fields. Indeed, the spin-J state can be represented by a wavefunction on the sphere, where Majorana stars are vortices of unit flux [307]. By this mapping, the spin can simulate the physics of the lowest Landau level in a spherical geometry pierced by total flux $2J$. The chosen scattering lengths correspond to repulsive contact interactions on the sphere: in the mean-field limit, the ground state minimises interaction energy in a configuration where the qubits (and

hence the vortices) have spread out in a configuration shown in fig. 4.18b, as discussed in ref. [308]. The situation is also interesting in the limit of low atom numbers, $N \sim J$, where quantum fluctuations are dominant and we leave the mean-field regime, such that the atoms are not all condensed into the same state. This can lead to the formation of highly correlated states: for example, in the case of exactly $J + 1$ atoms, the many-body ground state is in fact the bosonic Laughlin state at half filling [309, 310].

5

TOPOLOGY AND ENTANGLEMENT SPECTRUM OF A SYNTHETIC HALL SYSTEM

> Green in nature is one thing,
> green in literature another.
>
> Virginia Woolf, *Orlando*

In this chapter, I present the realisation of a quantum Hall system using a synthetic dimension encoded in the atomic spin of dysprosium. I will explain how distinct behaviour is observed at the edges, which host chiral states, and in the bulk, which shows a transverse response consistent with that of a topological band.

We begin with a brief overview of Hall physics (section 5.1) and explain how light-induced artificial magnetic fields are created in a synthetic dimension (section 5.2).

We then present our experimental findings (sections 5.3–5.6), in the form of an excerpt from our article [311]:
Probing chiral edge dynamics and bulk topology of a synthetic Hall system
T. Chalopin*, T. Satoor*, A. Evrard, V. Makhalov, J. Dalibard, R. Lopes, S. Nascimbene
Nature Physics 16, 1017–1021 (2020)
* These authors contributed equally

In particular, we explain the realisation of a Hall ribbon with atomic dysprosium, the properties of the ground band (analogous to the lowest Landau level), a study of the system's excitations (semi-classical cyclotron and skipping orbits), and the measurement of the Hall drift, quantified by the local Chern marker. This first half of the chapter aims to be concise while remaining self-contained. The topics covered formed a major part of T. Chalopin's PhD thesis [91], where in-depth explanations and experimental details can be found.

We take a more comprehensive approach in the chapter's second half (sections 5.8–5.9), where newer work is presented. We begin by examining the entanglement properties of many-body ground states, where the link to the themes of this chapter might not be evident at first. Then, we explain how a concept called the entanglement spectrum acts as an incisive probe of topological behaviour by linking entanglement in the bulk to the

behaviour of edge modes. This motivates a reinterpretation of our experimental results, where the signature of the entanglement spectrum at the single-particle level is revealed. Finally, we discuss how the entanglement properties could be probed directly in our system with future experiments, and conclude with a perspective on the realisation of many-body topological states with dysprosium.

5.1 INTRODUCTION TO QUANTUM HALL PHYSICS

The remarkable discovery of the integer quantum Hall effect in 1980 [9] kickstarted the study of topological states of matter. In that landmark experiment, K. v. Klitzing measured the transverse resistivity ρ_{xy} of a two-dimensional electron gas formed at the semiconductor-insulator interface in a transistor device. He observed plateaux at

$$\rho_{xy} = \frac{1}{\nu} \times \frac{h}{e^2} \tag{5.1}$$

as the magnetic field B applied perpendicular to the sample is varied. The parameter ν was found to take integer values at extremely high levels of precision ($\sim 10^{-10}$) , independent of microscopic sample properties or fine-tuning of the magnetic field. This was followed by the discovery of the fractional quantum Hall effect in 1982 [312], with plateaux at certain rational values of ν. Here, we provide a very brief introduction to Hall physics, focussing on the integer case, and highlight features that will reappear in our synthetic Hall system. In our explanations, we borrow freely from refs. [313–315].

Classical Hall system

Classically, the motion of an electron in a magnetic field takes the form of circular orbits at constant speed, at the cyclotron frequency $\omega_c = eB/M$, as sketched in fig. 5.1 (M is the electron mass and e is the electronic charge). The frequency is independent of the orbit radius. An additional external force F (e.g. from an electric field) causes a transverse displacement of the orbit's centre with velocity $\boldsymbol{v}_{\text{drift}} = -\boldsymbol{F} \times \boldsymbol{B}/(eB^2)$. The ratio of this drift velocity to the force gives the bulk Hall mobility, $\mu = -1/eB$. At a sharp repulsive boundary, the electron follows a skipping orbit along the edge (see fig. 5.1). Such skipping motion is less strongly affected by a force perpendicular to the edge, leading to a reduced mobility in this region. This picture also describes the motion of an electron wavepacket in the quantum case, such that we can refer to semiclassical cyclotron and skipping orbits.

In a translationally invariant Hall system, we can use Lorentz invariance to transform to a moving frame at velocity $-\boldsymbol{v}$, such that the electromagnetic fields transform as

$$(\boldsymbol{E} = \boldsymbol{0}, \boldsymbol{B} = B\hat{\boldsymbol{z}}) \longrightarrow (\boldsymbol{E} = -\boldsymbol{v} \times \boldsymbol{B}, \boldsymbol{B} = B\hat{\boldsymbol{z}})$$

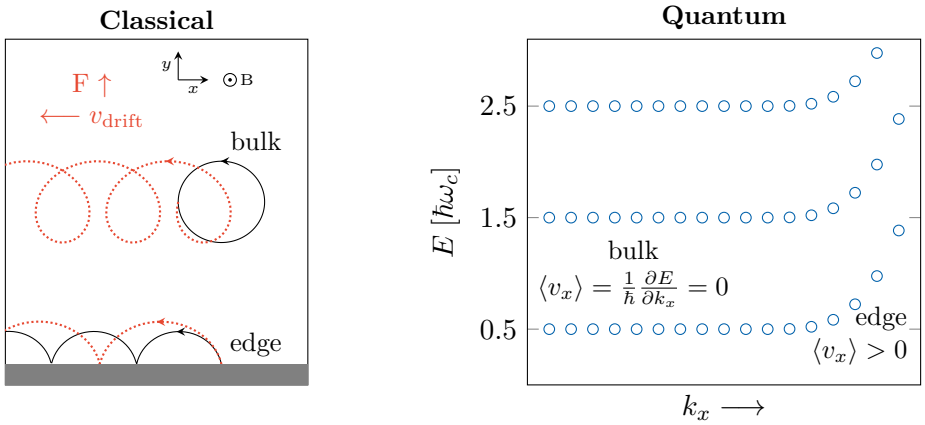

Figure 5.1: Two-dimensional Hall systems in the classical and quantum regimes. In the classical case, electron trajectories (solid black curves) take the form of circular cyclotron orbits in the bulk (at frequency ω_c) and skipping orbits at a hard edge. The application of a force causes a transverse drift of the orbits (dotted red curves). In the quantum case, the dispersion relation takes the form of evenly spaced Landau levels (at $(s+1/2)\hbar\omega_c$ for integer s) with a macroscopic degeneracy of stationary states in the bulk. The edges host chiral (unidirectional) states.

to lowest order in v/c. In the moving frame, the two-dimensional electron gas creates a current density $\mathcal{J} = -ne\boldsymbol{v}$, where n is the electron density. Using these equations and the definition of the resistivity tensor $\mathcal{J} = \boldsymbol{\rho} \cdot \boldsymbol{E}$, we can identify

$$\boldsymbol{\rho} = \frac{B}{ne}\begin{pmatrix} 0 & 1 \\ -1 & 0 \end{pmatrix}, \tag{5.2}$$

predicting a transverse resistivity linear in the field. Clearly, this approach does not predict the observed plateaux.

Quantum Hall system

For a single electron, quantum effects become relevant for motion at a lengthscale ℓ, which can be deduced by positing a Heisenberg-like relation $\Delta x \Delta p = \ell \times M\ell\omega_c = \hbar$. This gives an important quantity called the magnetic length $\ell = \sqrt{\hbar/eB}$. The magnetic field enters the quantum Hamiltonian as a coupling of the vector potential $\boldsymbol{A}$, with the canonical momentum $\boldsymbol{p}$:

$$H = \frac{(\boldsymbol{p} + e\boldsymbol{A}(\boldsymbol{r}))^2}{2M}.$$

We should remember that the kinetic momentum of the electron is given by $M\boldsymbol{v} = \boldsymbol{p} + e\boldsymbol{A}(\boldsymbol{r})$, and that given translational invariance, $\boldsymbol{p}$ is a conserved quantity. The solution of this single-particle Hamiltonian gives *Landau levels*. These form a harmonic spectrum

$$E_s = (s + 1/2)\,\hbar\omega_c\,, \quad \text{where } s = 0, 1, \ldots$$

as shown in fig. 5.1. Importantly, the spatial density of single-electron states in a single Landau level is $n_\phi = (2\pi\ell^2)^{-1} = B/\Phi_0$, where $\Phi_0 = h/e$ is the flux quantum. Hence,

a typical 2-D solid-state sample has a macroscopic degeneracy of each Landau level, tunable using the magnetic field.[1] Since the average electron density n of the sample remains fixed, we are able to tune the overall filling fraction $\nu = n/n_\phi$.

Transverse response

The argument leading to eq. (5.2) for the resistivity only depends on Lorentz invariance, and so it is also valid for a translationally invariant quantum system. Indeed, if we insert electron densities corresponding to a whole number of filled Landau levels, we recover the universal values of eq. (5.1). However, this explanation depends on the precise value of the magnetic field, and cannot account for the extreme robustness of the resistivity plateaux. In fact, the presence of disorder (which breaks translational invariance), and of states at the edge of real samples, play a crucial role in the integer quantum Hall effect.

We now compute the result of a transverse response measurement, working in a ribbon geometry i.e. with no boundaries along x, and a finite width L along y. We consider a smoothly varying confining potential $V(y)$. It is convenient to work in the Landau gauge, where $\boldsymbol{A} = eBy\,\hat{\boldsymbol{x}}$, and the single-particle wavefunctions have x-translational symmetry:

$$\psi_{p_x}(x,y) = \mathrm{e}^{\mathrm{i}p_x x/\hbar}\phi_{y_0}(y-y_0)\ \text{, with } y_0 = -p_x/eB \tag{5.3}$$

Here, the function $\phi_{y_0}(y-y_0)$ is localised in a region of width $\sim \ell$ around position $y = y_0$; its exact form is not important, and depends on $V(y)$. The dispersion relation $E(p_x)$ sharply rises when y_0 is close to the edges $y = 0, L$, where it is intersected by the Fermi level. The velocity of a wavepacket, $\boldsymbol{v}_{p_x} = \partial E/\partial p_x\,\hat{\boldsymbol{x}}$ has opposite sign at each edge, and is along the direction of the respective semiclassical skipping trajectories. Therefore, even without an external voltage, the ground state contains opposing chiral (unidirectional) edge currents.

The application of a voltage V_H across the sample can be treated as a chemical potential difference eV_H between the edges (see fig. 5.2). The resulting net transverse current at unit filling ($\nu = 1$) is obtained by integrating over the lowest Landau level (LLL)

$$I_H = -e\int_{\mathrm{LLL}} \mathrm{d}p_x \frac{1}{h}\frac{\partial E}{\partial p_x} = -\frac{e}{h}\int_{y=0}^{y=L} dE = -\frac{e^2}{h}V_H\,,$$

allowing us to recover the universal value for the resistivity.

What is the effect of disorder on this result? Disorder, ever-present in real samples due to imperfections, might be expected to reduce the transmitted current by backscattering the electrons off local kinks in the confining potential V. In the Hall system, the only state available into which an edge state can be backscattered is at the opposite edge of the sample. The probability for this process is close to zero if $L \gg \ell$. Hence, the chiral edge modes have a remarkable immunity from back scattering.

[1] The degeneracy is about 10^9 for a square sample of length 0.5 mm at a field of 10 T.

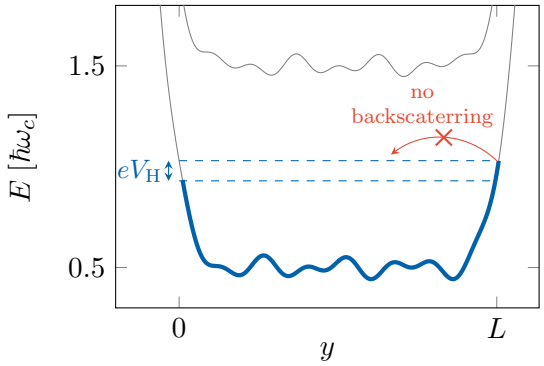

Figure 5.2: Transverse response of the lowest Landau level in a Hall system with disorder and edges. The Fermi level lies between the first two Landau levels. A voltage V_H applied across the edges of the sample at $y = 0, L$ can be interpreted as a difference of the Fermi levels at the two edges eV_H. The solid blue line shows the resulting filling of the band. The net current is then obtained by integrating the contributions of occupied states, resulting in a universal value h/e^2 for the resistivity (see text). The chiral edge modes are protected from backscattering, since there are no nearby unoccupied states with opposite momentum and the same energy.

The second key ingredient to recover the characteristic integer quantum Hall effect behaviour is the localisation of states in the bulk due to disorder. This broadens the delta functions of the density of states, located at the Landau level energies $(s + 1/2)\,\hbar\omega_c$ in the ideal case. These are spread over a finite energy range, given by the strength of disorder. Then, the chemical potential can vary smoothly with B, while the resistivity remains determined solely by the number of available edge channels, resulting in the famous plateaux.

Role of topology

Topology allows us to understand the quantum Hall effect in terms of bulk properties.

The formulation of the Berry (or geometric) phase [316] was an important step towards the application of topology to quantum systems. As an example, consider a pure coherent state of a spin-J system, described by a point on the Bloch sphere. We subject it to an adiabatic cycle of evolution, returning to the initial point in phase space. The system acquires the usual dynamical phase proportional to the respective eigenstate energies, and also a geometric factor $\exp(\mathrm{i}J\omega)$ which depends on the path followed in phase space. Using Stokes' theorem, the geometric phase is expressed in terms of ω, the solid angle subtended by the system's trajectory. In this case, the state resides on a spherical manifold, which has a number of holes, or genus $g = 0$. Hence, ω is ambiguous up to a multiple of the total curvature $(2 - 2g) \times 2\pi = 4\pi$, as given by the Gauss-Bonnet theorem. For the geometric phase factor to be physically meaningful, $2J$ must be an integer, which we know is the case for a quantum spin! This illustrates how the overall arrangement of the system's states can be given a precise meaning, fundamentally restricting the value of a global physical property. This property is then said to be topologically protected with respect to certain deformations of the system.

We now return to the quantum Hall system. In a landmark result, Thouless et al. [10] formulated an expression for the Hall conductance as an integral of a curvature F over the Brillouin zone, and noted that it takes the observed universal values for integer filling factors. In brief: this so-called TKNN expression uses Kubo linear response theory on a two-dimensional lattice, which, for a single band, gives a Hall conductance

$$\sigma^{xy} = \frac{e^2}{h}\left(\frac{1}{2\pi}\int_{\mathrm{BZ}} \mathrm{d}^2\boldsymbol{k}\; F(\boldsymbol{k})\right) = \frac{e^2}{h}\left(\frac{1}{2\pi}\oint_{\mathrm{BZB}} \mathrm{d}\boldsymbol{k}\cdot\boldsymbol{\mathcal{A}}(\boldsymbol{k})\right) \tag{5.4}$$

$$\text{where } \mathcal{A}^i(\boldsymbol{k}) = \frac{1}{2\mathrm{i}}\int_{\mathrm{MUC}} \mathrm{d}^2\boldsymbol{r}\left(u^*\frac{\partial u}{\partial k_i} - u\frac{\partial u^*}{\partial k_i}\right)$$

$$\text{and } F(\boldsymbol{k}) = \nabla_k \times \boldsymbol{\mathcal{A}}.$$

Here, F is called the Berry curvature, $\boldsymbol{\mathcal{A}}$ is a vector field called the Berry connection, and the u's (implicitly indexed by $\boldsymbol{k}$) are Bloch functions with the lattice's periodicity. The integrals are over the Brillouin zone (BZ), Brillouin zone boundary (BZB), and the magnetic unit cell (MUC) respectively. The term in brackets in eq. (5.4) was formally identified as a topological invariant taking integer values by Simon [317]; it is called the TKNN invariant or Chern number $\mathcal{C}$, which equals one for a Hall band. Through a general principle called the bulk-edge correspondence (see ref. [81] for a review), the presence of a gapless chiral edge mode for each band can be seen as a fundamental consequence of a boundary between a $\mathcal{C} = 1$ Hall system and the topologically trivial $\mathcal{C} = 0$ surroundings.

5.2 SYNTHETIC DIMENSION WITH INTERNAL STATES

An essential ingredient for Hall physics to emerge in a two-dimensional quantum system is the coupling of a momentum $\boldsymbol{p}$ to a vector field $\boldsymbol{A}$ (with $\nabla \times \boldsymbol{A} \neq \boldsymbol{0}$). In the spirit of quantum simulation and 'synthetic' systems, the two dimensions in question need not be spatial: here, we consider encoding one of them in the internal state of an ultracold atom. This concept of synthetic dimensions was proposed by Celi et al. [77] in 2014. Since the atom has no electric charge, a real magnetic field cannot create the required coupling; instead, the internal states are coupled to motion using optical transitions, creating an artificial magnetic field, as we now explain with a toy model.

Consider an atom with a two-level ground manifold ($J = 1/2$), described by the Hamiltonian

$$H = \frac{1}{2}Mv^2 - \frac{\hbar\Omega}{2}\left(\mathrm{e}^{-\mathrm{i}Kx}J_+ + \mathrm{e}^{\mathrm{i}Kx}J_-\right)$$

Here, M is the atom's mass and v is its velocity along x; motion along other axes is irrelevant. The resonant coupling of the $m = \pm 1/2$ levels (with strength Ω) has been achieved in Λ configuration with two-photon Raman transitions (see fig. 5.3). This uses counter-propagating laser beams along x, each with wavevector $K/2$. The phase factors $\mathrm{e}^{\pm\mathrm{i}Kx}$ arise from the interference of the beams. Any two-photon transition comes

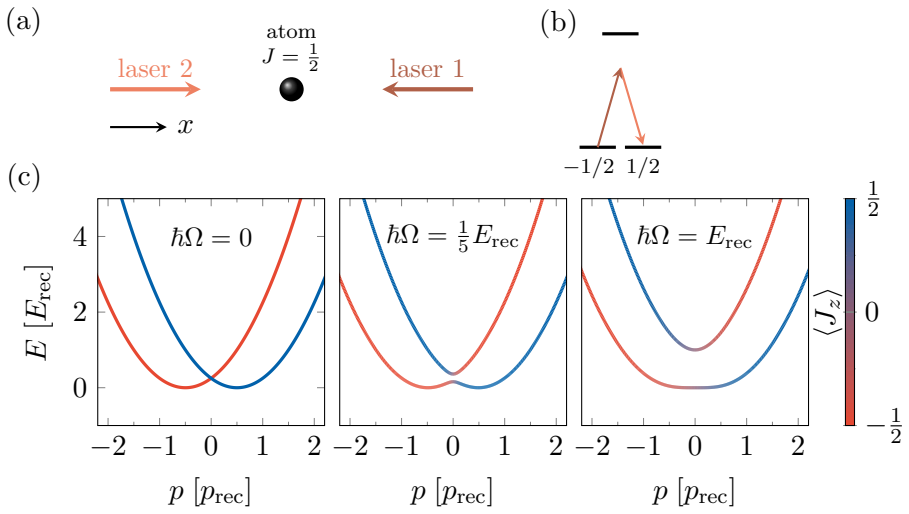

Figure 5.3: Toy model for synthetic dimension of size two encoded in the internal state of an atom. (a,b) Counterpropagating laser beams along a real dimension x, far-detuned from an excited state, induce coherent two-photon transitions between states $m = \pm 1/2$, coupling the 'position' in this internal synthetic dimension to the induced motion along x. The two-photon recoil momentum is denoted p_{rec}, and the associated recoil energy is E_{rec}. The coupling strength is $\hbar\Omega$. (c) Dispersion relation as a function of the coupling strength. The conserved canonical momentum is $p = Mv + p_{\mathrm{rec}} J_z$. The lower band is optimally flat at $\hbar\Omega = E_{\mathrm{rec}}$, where it is quartic to lowest order around $p = 0$.

along with a recoil momentum kick along x, with magnitude $p_{\mathrm{rec}} = \hbar K$, such that we can identify a conserved canonical momentum $p = Mv + p_{\mathrm{rec}} J_z$. Note that a large two-photon detuning from the single relevant excited level ensures that we can consider coherent dynamics in the ground manifold.[2]

We will now interpret J_z as the position in a discrete and finite synthetic dimension. Hopping along this dimension is associated with complex phase factors, which are analogous to the Aharonov-Bohm phase (more precisely, its counterpart in discretised systems, the Peierls phase). The natural length scale along the real dimension is $2\pi/K$, and we can identify a magnetic unit cell of dimensions $2\pi/K$ (real) $\times\, 1$ (synthetic), around which the total phase acquired is 2π. The link to the Hall Hamiltonian (in the Landau gauge) can be made more evident after a unitary transformation given by $U = \exp(\mathrm{i}Kx J_z)$, giving

$$H = \frac{(p - p_{\mathrm{rec}} J_z)^2}{2M} - \hbar\Omega J_x \,.$$

The J_x operator plays the role of the kinetic energy in the synthetic dimension, as it couples the position eigenstates $m = \pm 1/2$. We show the dispersion relation for different values of the coupling Ω in fig. 5.3b. We see how free-particle parabolic dispersions ($\Omega = 0$) are coupled for finite Ω, giving an optimally 'flat' lower band at $\hbar\Omega = E_{\mathrm{rec}}$ (here, it is quartic to lowest order around $p = 0$), analogous to the lowest Landau level. The average position in the synthetic dimension varies smoothly with p. The analogy with a

[2] In this toy model, we avoid specifying the details such as the beams' polarisations or the nature of the excited state manifold.

Hall system is rather overstated at this point; we will see that it is much more convincing for our larger synthetic dimension of size $2J+1 = 17$, where we can identify an extended and nearly dispersionless bulk, similar to a real Hall ribbon. Previous implementations of synthetic dimensions, of size three [84, 85, 318], were able to observe chiral edge modes.

Before presenting our experimental results, we note that the Hamiltonian presented above is part of the broader category of spin-orbit coupled systems, first implemented for ultracold atoms in a series of pivotal works in the Spielman group [319, 320], and developed further in refs. [321, 322]. Other than the synthetic dimension picture presented above, artificial gauge fields can also arise from a spatial variation of the coupling Ω (see ref. [323] for a review). We will revisit this approach for our system at the end of the chapter. The domain of artificial magnetic fields is rapidly growing, with advances in systems based on optical lattices [324–327], and synthetic dimensions encoded in photonic systems [328] or in the time domain [329].

Partial text of article begins here

This from our article ref. [311]. Note that the entire article, along with the methods and supplementary information sections referred to below, are included in appendix A.1.

5.3 IMPLEMENTING A SYNTHETIC HALL RIBBON

In this work, we engineer a topological system with ultracold bosonic ^{162}Dy atoms based on coherent light-induced couplings between the atom's motion and the electronic spin $J = 8$, with relevant dynamics along two dimensions – one spatial dimension and a synthetic dimension encoded in the discrete set of $2J + 1 = 17$ magnetic sublevels. These couplings give rise to an artificial magnetic field, such that our system realises an analogue of a quantum Hall ribbon. In the lowest band, we characterise the dispersionless bulk modes, where motion is inhibited due to a flattened energy band, and edge states, where the particles are free to move in one direction only. We also study elementary excitations to higher bands, which take the form of cyclotron and skipping orbits. We furthermore measure the Hall drift induced by an external force, and infer the local Hall response of the band via the local Chern marker, which quantifies topological order in real space [86]. Our experiments show that the synthetic dimension is large enough to allow for a meaningful bulk with robust topological properties.

The atom dynamics is induced by two-photon optical transitions involving counter-propagating laser beams along x (see fig. 5.4a), and coupling successive magnetic sublevels m [116, 320]. Here, the integer m ($-J \leq m \leq J$) quantifies the spin projection along the direction z of an external magnetic field. The spin coupling amplitudes then inherit the complex phase Kx of the interference between both lasers, where $K = 4\pi/\lambda$ and $\lambda = 626.1\,\mathrm{nm}$ is the light wavelength (see fig. 5.4b). Given the Clebsch-Gordan

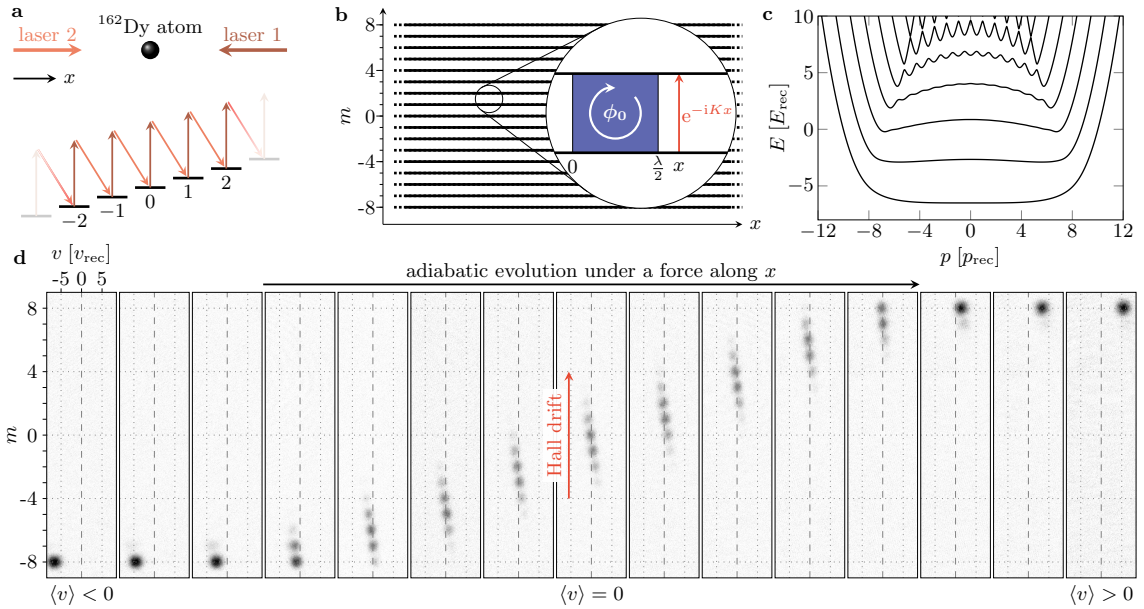

Figure 5.4: Synthetic Hall system. (a) Laser configuration used to couple the magnetic sublevels m of a ^{162}Dy atom (with $-J \leq m \leq J$ and $J = 8$, only a few m values represented). (b) Interpreting the spin projection as a synthetic dimension, the system is mapped to a two-dimensional ribbon of finite width. The photon recoil $p_{\text{rec}} = \hbar K$ imparted upon a spin transition leads to complex-valued hopping amplitudes along m, equivalent to the Aharonov-Bohm phase of a charged particle evolving in a magnetic field. The blue area represents a magnetic unit cell pierced by one flux quantum ϕ_0. (c) Dispersion relation describing the quantum level structure for $\hbar\Omega = E_{\text{rec}}$, with flattened energy bands reminiscent of Landau levels. (d) The lowest energy band is explored by applying an external force. We probe the velocity and magnetic projection distributions by imaging the atomic gas after an expansion under a magnetic field gradient. We find three types of behaviour: free motion with negative (positive) velocity on the bottom edge $m = -J$ (top edge $m = J$) and zero average velocity in the bulk. Each panel corresponds to a single-shot image.

algebra of atom-light interactions for the dominant optical transition, the atom dynamics is described by the Hamiltonian[3]

$$\hat{H} = \frac{1}{2}M\hat{v}^2 - \frac{\hbar\Omega}{2}\left(e^{-iK\hat{x}}\hat{J}_+ + e^{iK\hat{x}}\hat{J}_-\right) + V(\hat{J}_z) \tag{5.5}$$

where M is the atom mass, $\hat{v}$ is its velocity, $\hat{J}_z$ and $\hat{J}_\pm$ are spin projection and ladder operators. The coupling Ω is proportional to both laser electric fields, and the potential $V(\hat{J}_z) = -\hbar\Omega\hat{J}_z^2/(2J+3)$ stems from rank-2 tensor light shifts.

A light-induced spin transition $m \to m+1$ is accompanied by a momentum kick $-p_{\text{rec}} \equiv -\hbar K$ along x, such that the canonical momentum $\hat{p} = M\hat{v} + p_{\text{rec}}\hat{J}_z$ is a conserved quantity. After a unitary transformation defined by the operator $\hat{U} = \exp(iK\hat{x}\hat{J}_z)$, the Hamiltonian (5.5) can be rewritten, for a given momentum p, as

$$\hat{H}_p = \frac{(p - p_{\text{rec}}\hat{J}_z)^2}{2M} - \hbar\Omega\hat{J}_x + V(\hat{J}_z)\,. \tag{5.6}$$

[3] Within this excerpt, we use hats to denote quantum operators.

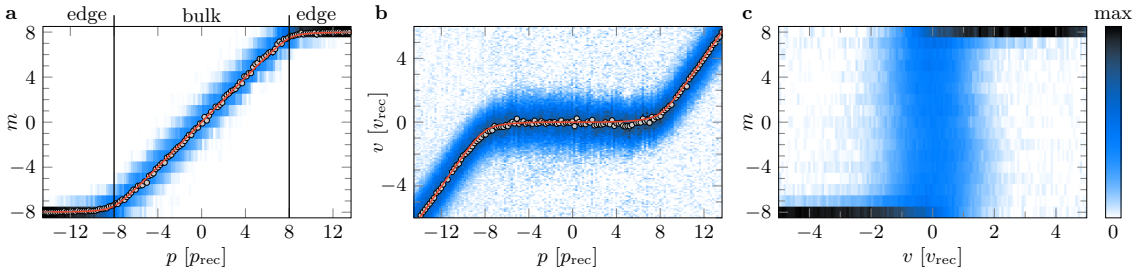

Figure 5.5: Ground band characterisation. (a) Spin projection distribution Π_m as a function of the momentum p, with the mean spin projection $\langle \hat{J}_z \rangle$ (grey dots) and the theoretical prediction $(p - M\partial_p E_0)/p_{\text{rec}}$ (red line). (b) Velocity distribution, together with the mean velocity $\langle \hat{v} \rangle$ (gray dots) and the expected value, given by the derivative of the band dispersion $\partial_p E_0$ (red line). (c) Local density of states obtained by integrating the measured distributions in (v, m) space over all momenta. All error bars in this section (here, smaller than data markers) are the 1-σ standard deviation of typically 5 measurement repetitions.

We can make an analogy between this Hamiltonian and the *ideal* Landau one, given by

$$\hat{H}_{\text{Landau}} = \frac{(\hat{p}_x - eB\hat{y})^2}{2M} + \frac{\hat{p}_y^2}{2M}, \tag{5.7}$$

which describes the dynamics of an electron evolving in 2D under a perpendicular magnetic field B. The analogy between both systems can be made upon the identifications $\hat{J}_z \leftrightarrow \hat{y}$ and $p_{\text{rec}} \leftrightarrow eB$. The term $\hat{J}_x$ in equation (5.6) plays the role of the kinetic energy along the synthetic dimension, since it couples neighbouring m levels with real positive coefficients, similarly to the discrete form of the Laplacian operator $\propto \hat{p}_y^2$ in equation (5.7) (see Supplementary Information). The range of magnetic projections being limited, our system maps onto a Hall system in a ribbon geometry bounded by the edge states $m = \pm J$. The relevance of the analogy is confirmed by the structure of energy bands $E_n(p)$ expected for the Hamiltonian (5.6) describing our system, shown in fig. 5.4c. The energy dispersion of the first few bands is strongly reduced for $|p| \lesssim J p_{\text{rec}}$, reminiscent of dispersionless Landau levels. A parabolic dispersion is recovered for $|p| \gtrsim J p_{\text{rec}}$, similar to the ballistic edge modes of a quantum Hall ribbon [79]. The flatness of the lowest energy band, for $\hbar\Omega \approx E_{\text{rec}}$, results from the compensation of two dispersive effects, namely the variation of $\hat{J}_x$ matrix elements and the extra term, $V(\hat{J}_z)$ (see appendix A.1).

5.4 GROUND BAND PROPERTIES

We first characterise the ground band using quantum states of arbitrary values of momentum p. We begin with an atomic gas spin-polarized in $m = -J$, and with a negative mean velocity $\langle \hat{v} \rangle = -6.5(1) v_{\text{rec}}$ (with $v_{\text{rec}} \equiv p_{\text{rec}}/M$), such that it corresponds to the ground state of (5.6) with $p = -14.5(1) p_{\text{rec}}$. The gas temperature $T = 0.55(6)$ µK is such that the thermal velocity broadening is smaller than the recoil velocity v_{rec}. We then slowly increase the light intensity up to a coupling $\hbar\Omega = 1.02(6) E_{\text{rec}}$, where $E_{\text{rec}} \equiv p_{\text{rec}}^2/(2M)$ is the natural energy scale in our system. Subsequently, we apply a

weak force F_x along x, such that the state adiabatically evolves in the ground energy band with $\dot{p} = F_x$, until the desired momentum is reached (see appendix A.1). We measure the distribution of velocity v and spin projection m by imaging the atomic gas after a free flight in the presence of a magnetic field gradient.

The main features of Landau level physics are visible in the raw images shown in fig. 5.4d. Depending on the momentum p, the system exhibits three types of behaviours. (i) When spin-polarized in $m = -J$, the atoms move with a negative mean velocity $\langle \hat{v} \rangle$, consistent with a left-moving edge mode. (ii) When the velocity approaches zero under the action of the force F_x, the system experiences a series of resonant transitions to higher m sublevels – in other words a transverse Hall drift along the synthetic dimension. In this regime the atom's motion is inhibited along x, as expected for a quasi non-dispersive band. (iii) Once the edge $m = J$ is reached, the velocity $\langle \hat{v} \rangle$ rises again, corresponding to a right-moving edge mode. Overall, while exploring the entire ground band under the action of a force along x, the atoms are pumped from one edge to the other along the synthetic dimension.

To distinguish between bulk and edge modes, we plot in fig. 5.5a the spin projection probabilities Π_m as a function of momentum p. We find that the edge probabilities $\Pi_{m=\pm J}$ exceed $1/2$ for $|p| > 8.0(1) p_{\mathrm{rec}}$, defining the edge mode sectors – with the bulk modes in between. We study the system dynamics via its velocity distribution and mean velocity $\langle \hat{v} \rangle$, shown in fig. 5.5b. We observe that the velocity of bulk modes remains close to zero, which shows via the Hellmann-Feynman relation $\langle \hat{v} \rangle = \partial E_0 / \partial p$ that the ground band is almost flat.

The measured residual mean velocities allow us to infer a dispersion $\Delta E_0^{\mathrm{pk-pk}} = 1.2(5)\, E_{\mathrm{rec}}$ in the bulk mode region – nearly 2% of the free-particle dispersion expected over the same range of momenta. On the contrary, edge modes are characterized by a velocity $\langle \hat{v} \rangle \simeq (p - p_0)/M$, corresponding to ballistic motion – albeit with the restriction $\langle \hat{v} \rangle < 0$ for edge modes close to $m = -J$, and $\langle \hat{v} \rangle > 0$ at the opposite edge. We also characterise correlations between velocity v and spin projection m over the full band, via the local density of states (LDOS) in (v, m) space, integrated over p. We stress here that the LDOS only involves gauge-independent quantities, and could thus be generalised to more complex geometries lacking translational invariance. As shown in fig. 5.5c, it also reveals characteristic quantum Hall behaviour, namely inhibited dynamics in the bulk and chiral motion on the edges.

5.5 EXCITATIONS: CYCLOTRON AND SKIPPING ORBITS

The ideal Landau level structure of a charged particle evolving in two dimensions in a transverse magnetic field is characterised by a harmonic energy spacing $\hbar\omega_c$, set by the cyclotron frequency $\omega_c = eB/M$. We test this behaviour in our system by studying elementary excitations above the ground band, via the trajectories of the centre of mass

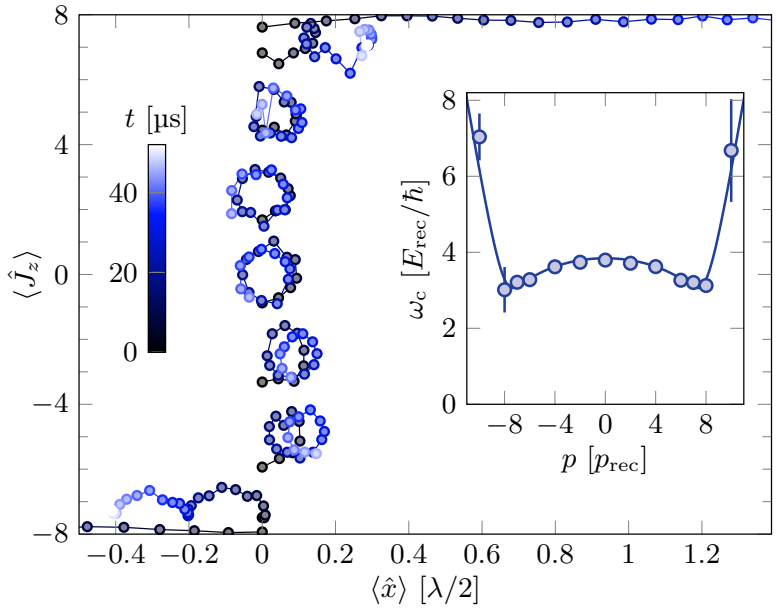

Figure 5.6: Cyclotron and skipping orbits. Trajectories in (x, m) space following a velocity kick $v_{\mathrm{kick}} \simeq v_{\mathrm{rec}}$, starting at $\langle \hat{x} \rangle = 0$, and for different initial momentum states (blue dots). The colour encodes the time evolution. Inset: Frequencies extracted from the velocity dynamics (blue dots), and compared with the expected cyclotron gap for $\hbar\Omega = E_{\mathrm{rec}}$ (blue line). The error bars are the 1-σ statistical uncertainty calculated from a bootstrap sampling analysis performed on more than a hundred pictures.

following a velocity kick $v_{\mathrm{kick}} \simeq v_{\mathrm{rec}}$. To access the real-space position of the atoms, we numerically integrate their centre-of-mass velocity evolution (see appendix A.1). As shown in fig. 5.6 (blue dots), we measure almost-closed trajectories in the bulk, consistent with the periodic cyclotron orbits expected for an infinite Hall system. We checked that this behaviour remains valid for larger excitation strengths, until one couples to highly dispersive excited bands (for velocity kicks $v_{\mathrm{kick}} \gtrsim 2v_{\mathrm{rec}}$, see appendix A.1). Close to the edges, the atoms experience an additional drift and their trajectories are similar to classical skipping orbits bouncing on a hard wall. In particular, the drift orientation only depends on the considered edge, irrespective of the kick direction. We report in the inset of fig. 5.6 the frequencies of velocity oscillations, which agree well with the expected cyclotron gap to the first excited band. We find that the gap is almost uniform within the bulk mode sector, with a residual variation in the range $\omega_c = 3.0(1) - 3.8(1)E_{\mathrm{rec}}/\hbar$.

5.6 TRANSVERSE HALL RESPONSE

We now investigate the key feature of Landau levels, namely their quantised Hall response, which is intrinsically related to their topological nature. In a ribbon geometry, the Hall response of a particle corresponds to the transverse velocity acquired upon applying a potential difference across the edges (see fig. 5.7a). In our system, such a

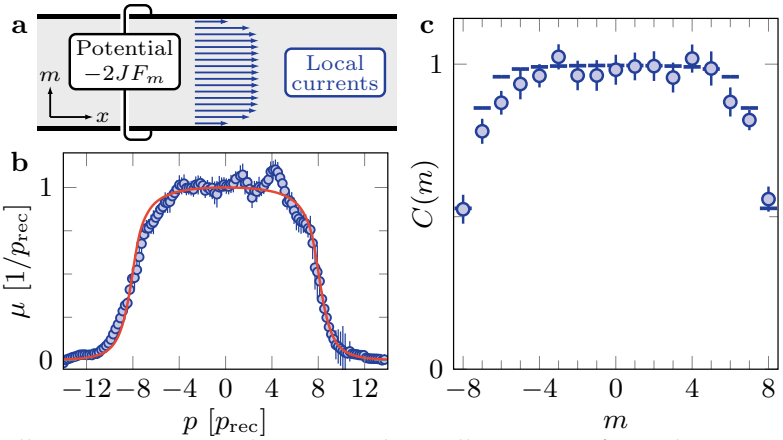

Figure 5.7: Hall response a. We determine the Hall response from the measurement of local currents in the real dimension, that result from the application, in synthetic space, of a potential difference $-2JF_m$ between the edges. b. Hall mobility $\mu(p)$ measured for states of momenta p, via their increase of velocity upon a small force F_m along m. c. Local Chern marker as a function of m, corresponding to the integrated mobility $\mu(p)$ weighted by the projection probability $\Pi_m(p)$. The error bars are the 1-σ statistical uncertainty calculated from a bootstrap sampling analysis over typically 100 pictures (b) and 1000 pictures (c).

potential corresponds to a Zeeman term $-F_m\hat{J}_z$ added to the Hamiltonian (5.6), which can now be recast as

$$\hat{H}_p - F_m\hat{J}_z = \hat{H}_{p+Mv'} - v'p, \quad \text{with} \quad v' = F_m/p_{\mathrm{rec}},$$

such that the force acts as a momentum shift Mv' in the reference frame with velocity v'. In the weak force limit, the perturbed state remains in the ground band, and its mean velocity reads

$$\langle\hat{v}\rangle = \langle\hat{v}\rangle_{F_m=0} - \mu F_m, \quad \text{where} \quad \mu = \frac{1}{p_{\mathrm{rec}}}\frac{\partial}{\partial p}(p - M\langle\hat{v}\rangle)$$

is the Hall mobility. This expression shows that the Hall response to a weak force can be related to the variation of the mean velocity within the ground band, that we show in fig. 5.5b. In practice, the velocity derivative at momentum p is evaluated using momentum states in the domain $(p - p_{\mathrm{rec}}, p + p_{\mathrm{rec}})$, corresponding to an evaluation of the Hall drift under a force $-2\,E_{\mathrm{rec}}/\ell < F_m < 2\,E_{\mathrm{rec}}/\ell$, where $\ell = 1$ is the unit length along the synthetic dimension. We present in fig. 5.7b the Hall mobility $\mu(p)$ deduced from this procedure. For bulk modes, it remains close to the value $\mu = 1/p_{\mathrm{rec}}$, which corresponds to the classical mobility $\mu = 1/(eB)$ in the equivalent Hall system. The mobility decreases in the edge mode sector, as expected for topologically protected boundary states whose ballistic motion is undisturbed by the magnetic field.

We use the measured drift of individual quantum states to infer the overall Hall response of the ground band. As for any spatially limited sample, our system does not exhibit a gap in the energy spectrum due to the edge mode dispersion. In particular, high-energy edge modes of the ground band are expected to resonantly hybridise with

excited bands upon disorder, such that defining the Hall response of the entire ground band is not physically meaningful. We thus only consider the energy branch $E < E^*$, where E^* lies in the middle of the first gap at zero momentum (see appendix A.1). We characterise the (inhomogeneous) Hall response of this branch via the local Chern marker

$$C(m) \equiv 2\pi \,\mathrm{Im}\, \langle m | \, [\hat{P}\hat{x}\hat{P}, \hat{P}\hat{J}_z\hat{P}] \, | m \rangle = \int_{E(p)<E^*} \mathrm{d}p \, \Pi_m(p)\mu(p),$$

where $\hat{P}$ projects on the chosen branch [86, 330]. This local geometrical marker quantifies the adiabatic transverse response in position space, and matches the integer Chern number $\mathcal{C}$ in the bulk of a large, defect-free system. Here, it is given by the integrated mobility $\mu(p)$, weighted by the spin projection probability $\Pi_m(p)$ (see appendix A.1). As shown in fig. 5.7c, we identify a plateau in the range $-5 \leq m \leq 5$. There, the average value of the Chern marker, $\overline{C} = 0.98(5)$, is consistent with the integer value $\mathcal{C} = 1$ – the Chern number of an infinite Landau level. This measurement shows that our system is large enough to reproduce a topological Hall response in its bulk. For positions $|m| \geq 6$, we measure a decrease of the Chern marker, that we attribute to non-negligible correlations with the edges.

Partial text of article ends here

5.7 A CYCLIC SYNTHETIC DIMENSION: THE TOPOLOGICAL LAUGHLIN PUMP

We have recently extended our study of Hall systems by realising a cyclic synthetic dimension encoded in dysprosium's electronic spin. The principle behind our experimental scheme was explained in our proposal ref. [331] (see appendix A.2 for the full article) and is illustrated in fig. 5.8a,b. In addition to the J_+ coupling used to create the Hall ribbon, we now include an additional frequency component in one of the Raman lasers to create J_-^2 couplings between all pairs of levels $m \to m-2$. Together, these hopping terms lead to the emergence of a triad of states $|r\rangle$, forming a cyclic synthetic dimension; together with the coordinate x, this creates a Hall system on a cylinder. Each state $|r\rangle$ projects only on the levels m mod $3 = r$. Hopping along the cylinder circumference i.e. from $|r\rangle$ to $|r+1\rangle$ is associated with a complex phase factor $\exp(\mathrm{i}(\phi - Kx))$, where ϕ is controlled using the relative phase of the Raman lasers, and provides a tunable axial magnetic field $B_\parallel$ through the cylinder (we also have the usual synthetic B-field in the radial direction).

We realised a topological Laughlin pump with this setup, described in our article ref. [332] (see appendix A.3 for the full article). This pump was conceived as a thought experiment by R. B. Laughlin in 1982 [78], setting the stage for understanding the quantisation of conductance in the integer quantum Hall effect observed two years earlier [9]. He pointed out that varying the axial flux $\Phi_\parallel$ controls quantised motion along the tube (see fig. 5.8c), later contextualised as a striking manifestation of the underlying

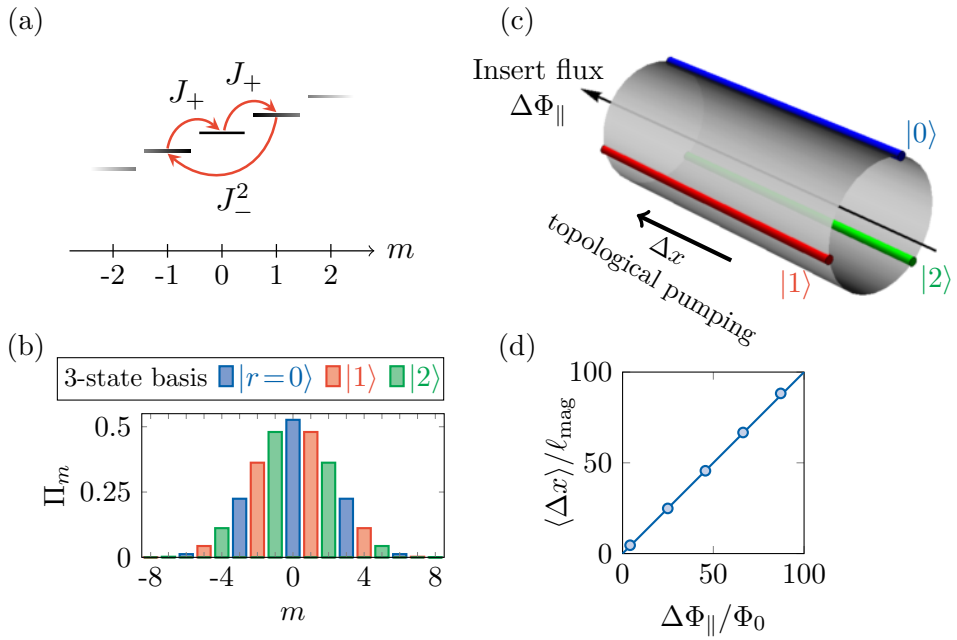

Figure 5.8: Topological pumping in a synthetic Hall cylinder. (a,b) Engineering a cyclic synthetic dimension of size three. (c,d) The experimental realisation of Laughlin's charge pump thought-experiment. See the text for details.

band topology. We realised this topological pump in our synthetic Hall cylinder by adiabatically ramping $\Phi_\parallel$, observing the predicted centre-of-mass motion along the cylinder axis, on average one magnetic length per inserted flux quantum, as shown in fig. 5.8d.

We are currently working on the realisation of a four-dimensional Hall system, exploiting r and m as independent synthetic dimensions, in addition to two spatial dimensions. A detailed discussion of the projects mentioned in this section is beyond the scope of this thesis. We now return to our two-dimensional Hall ribbon to discuss how topology relates to the structure of the entanglement of many-body states.

5.8 THE ENTANGLEMENT SPECTRUM AND TOPOLOGY

The identification of topological order in many-body systems is a challenging task. The inherent robustness of topological invariants makes systems immune to local probes and order parameters, which are used for phases emerging in conventional phase transitions. Moreover, the presence of strong correlations, with the associated exponentially large Hilbert space dimension, limits numerical methods. To tackle this problem, theoretical approaches have focussed on using the information encoded in the correlations of many-body ground states. The general idea is to cleverly construct quantities providing a concrete link to the system's physical properties. Beyond topology, these entanglement-based techniques provide important insights into disorder and impurity effects [333]. Here, we focus on one technique: the entanglement spectrum, introduced by Li and

Haldane [87] in 2008. We first introduce the topological entanglement entropy, which is closer to more familiar notions of entanglement. We then generalise this to the entanglement spectrum, following the treatment of ref. [334]. Next, we show how the results presented so far in this chapter already contain signatures of the entanglement spectrum at the single particle level. Finally, we discuss the possibility of directly probing the entanglement spectrum in our synthetic Hall system, inspired by a recent and as yet unrealised proposal [88].

5.8.1 *Topological entanglement entropy*

Consider a system in a many-body pure state $|\Psi\rangle$, whose topological nature we wish to probe. We apply a spatial bipartition $A : B$ on the system, such that the reduced density matrix for the region A is

$$\rho_A = \mathrm{Tr}_B \, |\Psi\rangle \langle\Psi| \, .$$

We can now wonder if the von Neumann entropy associated with this partition,

$$S_A = -\mathrm{Tr} \, (\rho_A \log \rho_A) = -\sum_i \lambda_i \log \lambda_i \, ,$$

can be used to probe topological properties. Note that $\{\lambda_i\}$ are the eigenvalues of the reduced density matrix ρ_A, and that we use the natural logarithm throughout this section. If the correlation length is finite, i.e. correlations between A and B are localised in a region around the cut separating them, we can argue that S_A must be proportional to the area of the cut. This is a $d-1$ dimensional area, where d is the dimensionality of the overall system. This statement is an example of an area law; such laws arise in diverse physical settings [335] and can be rigorously formulated in both classical and quantum contexts [336]. In fact, refs. [337, 338] showed that the deviation from this simple picture is given by a correction term $-\gamma$, called the topological entanglement entropy:

$$S_A \simeq c \, \mathcal{L}^{d-1} - \gamma \, .$$

Here c is a non-universal constant, and $\mathcal{L}$ is the characteristic size of the region A, which should be much larger than the correlation length. In two-dimensional systems, this statement becomes exact in the limit of large $\mathcal{L}$. Importantly, γ is a universal quantity associated with the structure of entanglement within the ground state $|\Psi\rangle$ [338]. For example, in the context of the fractional quantum Hall effect, it equals $\log \sqrt{3}$ for the Laughlin state at one-third filling.

Despite its elegant formulation, the topological entanglement entropy has a number of drawbacks. Since the above relation for S_A is only valid in the limit of an infinite system, it can be difficult to distinguish finite-size effects from the universal term [339, 340]. Moreover, in some cases, γ does not uniquely determine the topological order of

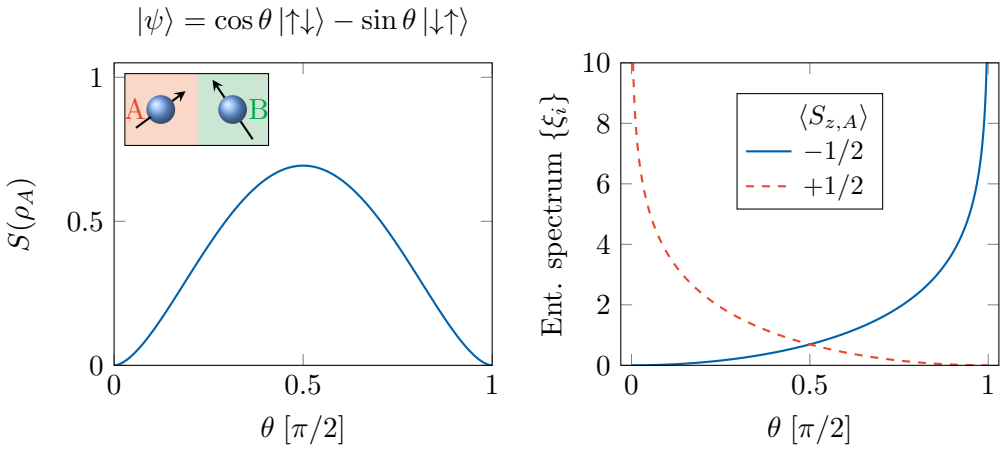

Figure 5.9: Entanglement of a pair of qubits denoted as subsystems A and B. Their state $|\psi\rangle$ is parametrised by the angle θ, with the maximally entangled singlet state at $\theta = \pi/4$. *Left*: The von-Neumann entropy S of the reduced density matrix ρ_A. If eigenvalues of ρ_A are $\{e^{-\xi_i}\}$, then $S = \sum \xi_i e^{-\xi_i}$ *Right*: The entanglement spectrum $\{\xi_i\}$ for different values of θ. The values in the spectrum are labelled by the respective eigenvalues of $S_{z,A}$, which remains a good quantum number in the subsystem A. This notion of labelling will be carried forward to more complicated systems. For the product states at $\theta = 0$ and $\theta = \pi/2$, there is only a single finite value in the entanglement spectrum, and it equals zero.

the state [334]. The entanglement spectrum is a generalisation which overcomes these difficulties: rather than condensing the information encoded in the reduced density matrix to a single quantity S_A, we will now exploit the structure of ρ_A's spectrum as a whole.

5.8.2 *Entanglement spectrum*

Li and Haldane initially proposed the entanglement spectrum in 2008 in the context of the fractional quantum Hall effect [87]. Since then, it has been applied to spin systems, topological insulators, Bose-Hubbard models, and complex paired superfluids (see ref. [334] and references therein).

We begin by writing our many-body state as a Schmidt decomposition over the bipartition $A : B$,

$$|\Psi\rangle = \sum_{i}^{\min(\dim_A, \dim_B)} \exp(-\xi_i/2)\,|\psi_{A,i}\rangle \otimes |\psi_{B,i}\rangle\,. \tag{5.8}$$

As introduced in chapter 4, $|\psi_{A/B,i}\rangle$ form orthonormal bases for the subsystems and $\{\xi_i\}$ is a set of real numbers. The maximal number of terms in this sum is given by the lesser of the Hilbert space dimensions of A and B. Now, the reduced density matrix has a simple form

$$\rho_A = \sum_i \exp(-\xi_i)\,|\psi_{A,i}\rangle\langle\psi_{A,i}|\,. \tag{5.9}$$

Both reduced states ρ_A, ρ_B have the same spectrum $\{\exp(-\xi_i)\}$ (if their dimensions are different, the 'missing' eigenvalues for the larger system are zero). The *entanglement spectrum* is simply the set of finite values $\{\xi_i\}$ i.e.

$$\text{entanglement spectrum} \equiv \{\xi_i\}\,.$$

Following Li and Haldane, we now consider a local operator O, such that it can be decomposed on the subsystems as $O = O_A + O_B$, where O_A acts only on A. Then, we can simultaneously diagonalise ρ_A and O_A, allowing us to label each value in the entanglement spectrum using the eigenvalues of O_A. We show a toy example for two-qubit states in fig. 5.9. In this case, we can take $O_A = \sigma_{z,A}$, giving two values in the spectrum, indexed by $\langle O_A \rangle = \pm 1/2$. Up to this point, the entanglement spectrum seems like an arbitrary construction – in the following, we will explain its utility by applying it to topological systems.

5.8.3 *Link to topology in an integer quantum Hall state*

In this section, we will consider a Hall system in two real spatial dimensions in a planar geometry. Our subsystem of interest A is the half plane $y > 0$. We aim to write the many-body state for a fermionic integer Hall state in the lowest Landau level as a Schmidt decomposition with respect to this bipartition, such that we can read off the entanglement spectrum using eq. (5.8). We will then highlight the link to topological properties by comparing the entanglement spectrum to the many-body spectrum of edge excitations.

Since our cut is along the line $y = 0$, it is natural to work in the Landau gauge,

$$H = \frac{(p_x - eBy)^2}{2M} + \frac{p_y^2}{2M}\,,$$

where the single-particle wavefunctions are translationally invariant along x, and indexed by their momentum component p_x:

$$\psi_{p_x}(x,y) = \mathrm{e}^{\mathrm{i}p_x x/\hbar}\phi_0(y - p_x/eB), \tag{5.10}$$

$$\phi_0(Y) = \frac{1}{\pi^{1/4}\sqrt{\ell}}\mathrm{e}^{-Y^2/2\ell^2}\,. \tag{5.11}$$

We show a scheme of the system in fig. 5.10a. The spatial extent of the wavefunction along y is set by the magnetic length $\ell = \sqrt{\hbar/eB}$. We associate the creation of a particle in this wavefunction with a fermionic operator $c^\dagger_{p_x}$. Then, the many-body ground state at unit filling $\nu = 1$ is a Slater determinant over all allowed momenta p_x in our system,

$$|\Psi\rangle = \left(\prod_{p_x} c^\dagger_{p_x}\right)|0\rangle\,. \tag{5.12}$$

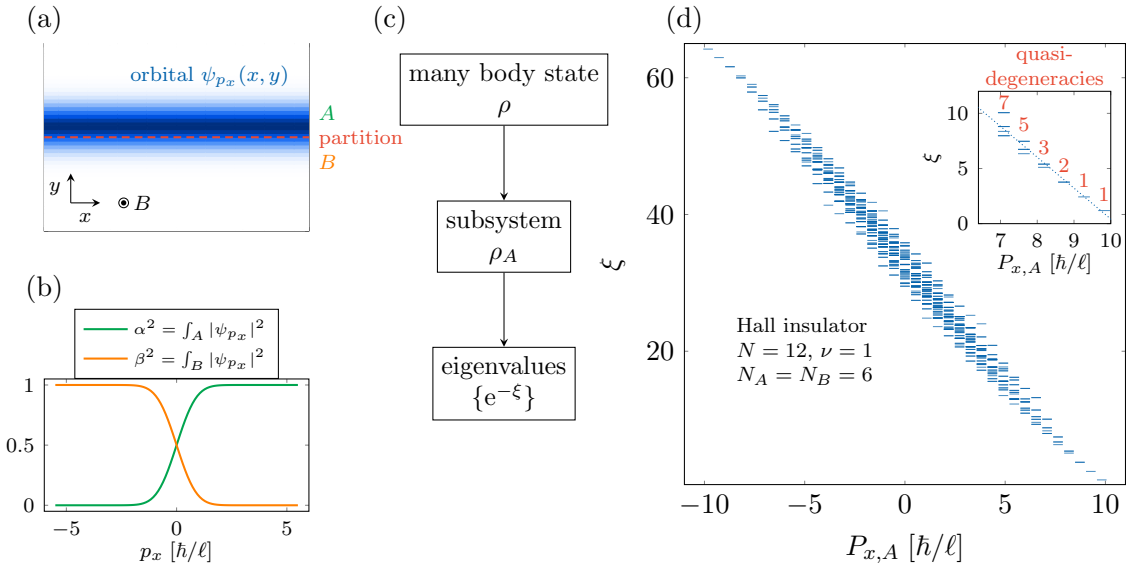

Figure 5.10: Entanglement spectrum of a Hall system. (a) A single-particle orbital $\psi_{p_x}(x,y)$ in the Landau gauge – along x it is a plane wave with momentum p_x, and along y it has a Gaussian spread of width ℓ centred at $y_0 = p_x/eB$. We partition the system with a cut along $y = 0$; p_x remains a good quantum number in subsystems A, B. (b) The norm of the single-particle orbital over the subsystems A, B are called α^2 and β^2 respectively. These quantities are useful when performing the Schmidt decomposition of a many body state ρ. (c) The set of non-trivial eigenvalues of the reduced density matrix ρ_A is $\{e^{-\xi}\}$, where $\{\xi\}$ is called the entanglement spectrum. (d) Example of a calculated entanglement spectrum for an integer quantum Hall state with $N = 12$ spin-polarised fermions completely filling the lowest Landau level ($\nu = 1$). The partition is performed at $y = 0$. We show the sector of the entanglement spectrum with fixed particle numbers $N_A = N_B = 6$ in the subsystems. We label the values ξ by the total momentum $P_{x,A} = \sum_A p_x$ of the particles in subsystem A, which is a good quantum number. *Inset*: Zoom on the lowest part of the entanglement spectrum, with a linear guide to the eye (dotted line). Crucially, the counting of the degeneracies (red text) of the smallest ξ's $(1, 1, 2, 3, 5, 7 \ldots)$ is exactly that of a chiral U(1) boson, i.e. an edge mode at the partition, providing a signature of the system's topological nature. Note that the degeneracies are only exact in the thermodynamic limit.

Note that we consider the spins to be polarised in a single state, and the proper anti-symmetrisation and normalisation is implicit here, and in the equations below. This ground state is equally valid in the interacting case.

The momentum p_x remains a good label after the partition at $y = 0$, and indeed the total momentum $P_x = \sum p_x$ is a good quantum number. Hence, we can make the form of the Schmidt decomposition clear by splitting each fermionic operator into two parts c_A and c_B, each of which create a particle in the upper and lower half plane respectively:

$$c^\dagger_{p_x} = \alpha_{p_x} c^\dagger_{p_x,A} + \beta_{p_x} c^\dagger_{p_x,B} \,. \tag{5.13}$$

From the anti-commutation relations for the c, c_A, and c_B operators, we can deduce that the coefficients satisfy $\alpha_{p_x}^2 + \beta_{p_x}^2 = 1$. In fact, the respective single-particle wavefunctions must decompose onto the same subsystems in the same way,

$$\psi_{p_x} = \alpha_{p_x}\, \psi_{p_x,A} + \beta_{p_x}\, \psi_{p_x,B}\,,$$

where $\psi_{p_x,A}$ is a normalised wavefunction localised to the upper half plane, and it is simply given by the product with a step function Θ i.e

$$\alpha_{p_x}\, \psi_{p_x,A} = \Theta(y)\, \psi_{p_x}\,.$$

Taking the squared norm, we get

$$\alpha_{p_x}^2 = \int_A \mathrm{d}x\, \mathrm{d}y\, |\psi_{p_x}|^2 = \frac{1 + \mathrm{erf}\,(p_x \ell/\hbar)}{2}\,, \text{ and } \beta_{p_x}^2 = \frac{1 - \mathrm{erf}\,(p_x \ell/\hbar)}{2}\,. \tag{5.14}$$

These real overlap coefficients are plotted in fig. 5.10b, and they take the form of smooth steps (of momentum width $\sim \hbar/\ell$) at $p_x = 0$, corresponding to the location of the orbital at the partition $y = 0$.

We are now ready to write the Schmidt decomposition of the integer Hall state, by substituting the split form of the fermionic creation operator 5.13 into the many-body ground state 5.12. We consider a lowest Landau level comprised of N orbitals, corresponding to a set of allowed x-momenta $\{p_i\}$, $i = 1, 2, \ldots, N$.

$$|\Psi\rangle = \left(\prod_{i=1}^{N} (\alpha_{p_i}\, c_{p_i,A}^\dagger + \beta_{p_i}\, c_{p_i,B}^\dagger) \right) (|0\rangle_A \otimes |0\rangle_B) \tag{5.15}$$

Upon expanding the product, we see that the state is a sum of terms, each corresponding to the creation of $0 \leq N_A \leq N$ particles in subsystem A, with the rest in B. Moreover, each term corresponds to the choice of a subset $\{p_j\}_A$ of N_A orbitals associated with subsystem A. Analogous quantities can be defined for B. Hence the state can be written as a sum over all such possible choices of subsets.

$$|\Psi\rangle = \sum_{\{p_j\}_A} \left(\prod_{\{p_j\}_A} \alpha_{p_j} \prod_{\{p_k\}_B} \beta_{p_k}\ |\{p_j\}_A\rangle \otimes |\{p_k\}_B\rangle \right) \tag{5.16}$$

Note that we have omitted factors of -1 from the ordering of $c^\dagger$ operators, which drop out anyways in the calculations below. By writing the state as a Schmidt decomposition, we have already done the required work for evaluating the entanglement spectrum. We can now just compare the prefactors in the above expression to eq. (5.8) to get

$$\xi_{\{p_j\}_A} = \log \left(\prod_{\{p_j\}_A} \alpha_{p_j}^{-2} \prod_{\{p_k\}_B} \beta_{p_k}^{-2} \right)\,, \tag{5.17}$$

where each choice of subset $\{p_j\}_A$ automatically specifies the complementary subset $\{p_k\}_B$, and thus gives us a value in the entanglement spectrum.

We can now apply a key insight of Li and Haldane, and focus on a given sector of the entanglement spectrum. To be concrete, in fig. 5.10d we show an evaluated spectrum for $N = 12$, $N_A = 6$, where we label the levels with the total momentum of orbitals filled in subsystem A; this quantity $P_{x,A}$ is simply a sum over the set $\{p_j\}_A$. For this calculation, we chose single-particle states evenly spaced between $\pm 3\hbar/\ell$.[4] The exact values in the spectrum depend on the discrete orbitals chosen, the number of particles, and the geometry of the cut (via the overlaps α, β). The key feature linked to topology is the structure of the low-lying levels, shown in the inset of fig. 5.10d. The characteristics emerging in the thermodynamic limit are: a linear dispersion in $P_{x,A}$, and the distinctive counting statistics of the degeneracies $(1, 1, 2, 3, 5, 7 \ldots)$. The precursors of these features are visible even for the modest system size considered: a rough overall linearity, and a bunching of levels for a given total momentum. Formally, these features are of a conformal field theory of a U(1) chiral bosonic mode, and they are exactly those found in the spectrum of excitations at the edge of an integer Hall system.[5] For the entanglement spectrum, they arise from an 'artificial edge' at $y = 0$ generated by our partition. This is the crux of the Li-Haldane conjecture: the entanglement spectrum of a gapped, bulk ground state describes the edge excitations. This can be seen as a bulk-edge correspondence for the entanglement spectrum.

Entanglement spectrum from single-particle psuedo-energies

We now provide an intuitive argument for the applicability of the Li-Haldane conjecture to the integer quantum Hall state. The simple Slater determinant form of the ground state considered here lends itself to an expression of the entanglement spectrum in terms of the sum of single-particle pseudo-energies [343, 344]. Consider the expression for the entanglement spectrum in terms of the overlap coefficients, given in eq. (5.17). Bringing a factor with all the β's outside the logarithm, we can write it in the form

$$\xi_{\{n_{p_x}\}} = \xi_0 + \sum_{p_x} n_{p_x}\, \epsilon(p_x)\,. \tag{5.18}$$

[4] The chosen momentum spacing in fact corresponds to a planar system with extent along x of $\sim 10\ell$, with a confining potential along y restricting the maximum allowed p_x. The situation we actually wish to consider, where a discrete finite set of momenta are allowed and the edges do not play a role, is better suited for a closed geometry such as a sphere. However, we treat the planar case here to make the connection with our experimental system more direct. The main physical insights gained are the same, and are valid in the bulk of a large finite system.

[5] The link to the properties of edge mode is explained further with fig. 5.11. For a more rigorous explanation, see ref. [341], appendix A.3. Similar results can also be obtained for the $\nu = 1/3$ Laughlin state, see ref. [342].

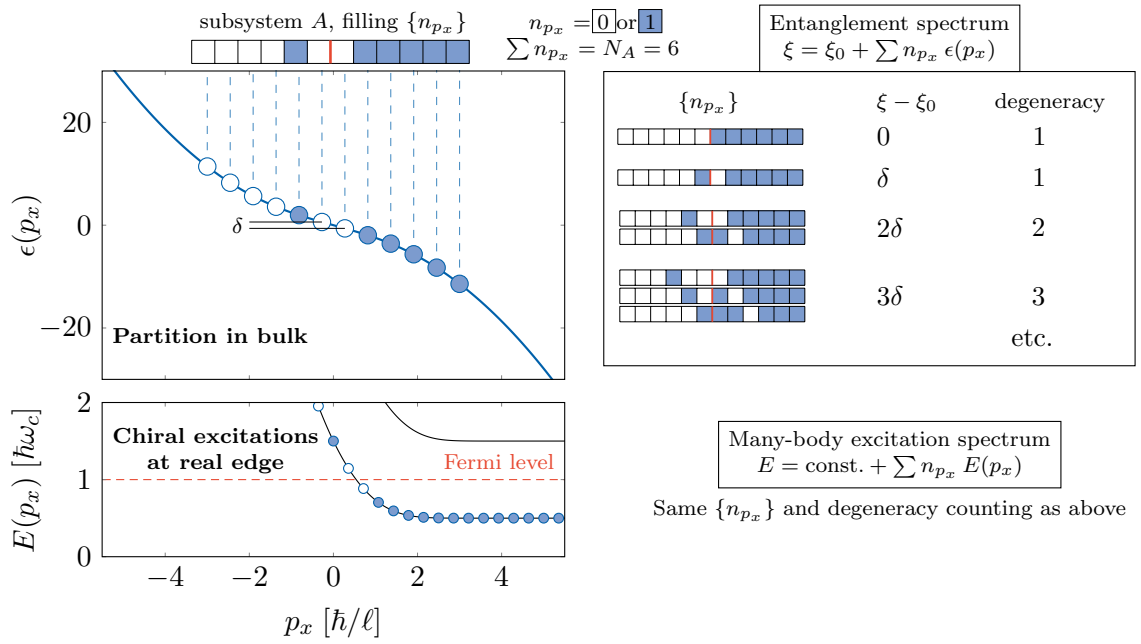

Figure 5.11: Calculation of entanglement spectrum $\{\xi\}$ from the 'dispersion relation' of single-particle pseudo-energies $\epsilon(p_x)$. We continue with the example of fig. 5.10: an integer quantum Hall state with $N = 12$ spin-polarised fermions completely filling the lowest Landau level. We consider the block of the entanglement spectrum with particle number $N_A = 6$ in the subsystem A ($y > 0$). *Top left*: The 12 orbitals considered are uniformly spaced in x-momentum around $p_x = 0$, with quasi-uniform spacing δ of the respective pseudo-energies $\epsilon(p_x)$. Note that $\epsilon(p_x)$ is calculated from the overlap a^2 of each orbital with the subsystem A (see text or fig. 5.10). The colouring of the circles gives an example of a filling configuration $\{n_{p_x}\}$, which we can easily sum to give an entanglement energy ξ (*Top right* formula). *Right*: The lowest lying configurations in the entanglement spectrum. As in the direct calculation in fig. 5.10, the counting of the degeneracies reveals an edge mode at the partition cut. *Lower left*: Analogy to the many-body edge excitation spectrum of an integer quantum Hall state (sharp edge at $y = 0$). The Fermi level intersects the the dispersion relation $E(p_x)$ in the edge region, such that lowest chiral edge excitation energies have a linear spectrum, with the same characteristic counting of degeneracies $(1, 1, 2, 3, 5, 7, 11, \ldots)$.

Here, the set of $n_{p_x} = 0$ or 1 is a configuration specifying which orbitals are occupied in subsystem A, with the constraint $\sum n_{p_x} = N_A$. The offset term is

$$\xi_0 = -\sum_{p_x} \log \beta_{p_x}^2 \,,$$

and more importantly, the single-particle pseudo-energy spectrum is given by

$$\epsilon(p_x) = \log\left(\frac{\beta_{p_x}^2}{\alpha_{p_x}^2}\right). \tag{5.19}$$

The computation of the entanglement spectrum from this point of view is illustrated in fig. 5.11. The function $\epsilon(p_x)$ is, to first order, linear at $p_x = 0$, such that we have a quasi-uniform spacing of the discrete allowed pseudo-energies (becoming exactly linear in the thermodynamic limit). We can then tabulate the possible filling configurations $\{n_{p_x}\}$ of subsystem A, and easily compute the corresponding levels in the entanglement

spectrum using eq. (5.19). It is visually clear why the lowest two energies have a single corresponding filling, while the next level is doubly degenerate, and so on. We recover both the roughly linear dispersion and the counting of degeneracies we already computed more explicitly in fig. 5.10.

We also show the direct analogy to the many-body edge excitation spectrum in fig. 5.11. There, we consider an integer Hall state in a large but finite system, with the Fermi level lying in between the lowest pair of Landau levels. Then, the dispersion relation at the edge plays a role analogous to $\epsilon(p_x)$, such that we would recover the same low-energy structure for the spectrum of the chiral edge excitations.

Applications of the entanglement spectrum

The single-particle spectrum discussed above provides an intuitive justification for the Li-Haldane conjecture for effectively non-interacting ground states, and we will use it in the next section. Furthermore, the partition we chose conserved translational symmetry, allowing for an analytic form of the entanglement spectrum. However, we stress that the entanglement spectrum is a valid probe of topological properties even in highly correlated systems, and it has been extensively investigated for states associated with the fractional quantum Hall effect, such as the Laughlin and Moore-Read states. Indeed, the entanglement spectrum even remains a useful probe of topology in the presence of disorder [345], or in more exotic systems such as fractional Chern insulators [346, 347]. More generally, the partition does not need to be spatial – the spectrum calculated with partitions in momentum space, or with respect to the orbitals themselves can provide complementary information on the ground state [87, 342, 348, 349]. The genus of the surface where the Hall system resides can itself play a role, with the entanglement spectrum on a torus revealing the two spatially separated edge modes associated with a partition [350]. There is an extensive literature which aims to prove or numerically verify the Li-Haldane conjecture in different settings [343, 349, 351–358]. Finally, the structure of the non-universal part of the entanglement spectrum [359] (where finite-size effects play a role) or the spectrum in the presence of pinned excitations [360] also have interesting properties. To summarise, the entanglement spectrum is a powerful new tool to access information encoded in many-body states, motivating experiments to probe it directly. We now discuss the first steps in this direction with our synthetic Hall system.

5.8.4 *Link to our synthetic Hall system*

We now perform a post hoc reinterpretation of the measured properties of the ground band of our system to 'create a partition', thereby revealing a link to the entanglement spectrum. Continuing the analogy with the real Hall system, where we chose a cut at $y = 0$, we partition our discrete synthetic dimension at $m^* = -0.5$, such that the levels $m = 0, 1, \ldots, J$ form the subsystem of interest A.

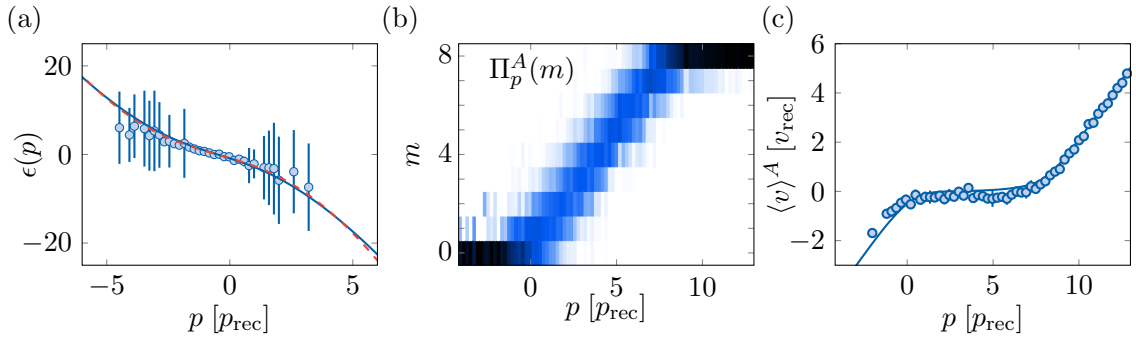

Figure 5.12: Partition of the synthetic Hall system with a cut along the line $m^* = -0.5$. (a) Single-particle entanglement psuedo-energies $\epsilon(p)$ associated with the partition. These are deduced from the projection probabilities (α_p^2, β_p^2) of single-particle states ψ_p on the two subsystems generated by the partition (see text). (b,c) Ground band properties of the state in the upper-half plane subsystem A. We show the spin projection probabilities (b) and the average velocities (c), indicating the appearance of an effective edge around the cut region at $p = -0.5\ p_{\mathrm{rec}}$. In all plots, we show data for a limited range of quasi-momenta over which the required projection probabilities to perform the post hoc partition are within our detection precision (see text).

We first clarify how the previously presented ground band properties (section 5.4 and fig. 5.5) were measured. In single experimental runs, we prepare a single-particle state ψ_p in the ground band with quasi-momentum p along the x-direction[6] (we drop the subscript x). Then, with our usual method of combining a Stern-Gerlach gradient with far-field time-of-flight expansion, we measure a distribution $n_p(m, v)$. This is the squared amplitude $|\psi_p(m, v)|^2$, over the continuous velocity v along x, and the synthetic dimension position over $2J + 1$ discrete m states. Let us consider a normalised distribution.

$$\sum_{m=-J}^{J} \int \mathrm{d}v\, n_p(m, v) = 1\,.$$

The quantities we plotted in fig. 5.5 are

$$\text{m distribution: } \Pi_p(m) = \int \mathrm{d}v\, n_p(m, v)$$

$$v \text{ distribution: } \mathcal{V}_p(v) = \sum_{m=-J}^{J} n_p(m, v)$$

$$\text{local density of states: } \mathrm{LDOS}(m, v) = \int \mathrm{d}p\, n_p(m, v)\,,$$

along with the calculated (p-dependent) mean values

$$\langle J_z \rangle = \sum_{m=-J}^{J} \Pi_p(m)\, m \quad \text{and} \quad \langle v \rangle = \int \mathrm{d}v\, \mathcal{V}_p(v)\, v$$

[6] There is in fact a small finite spread of quasi-momenta in a single shot because of thermal broadening, as mentioned in section 5.4. We can ignore in the discussion here for simplicity.

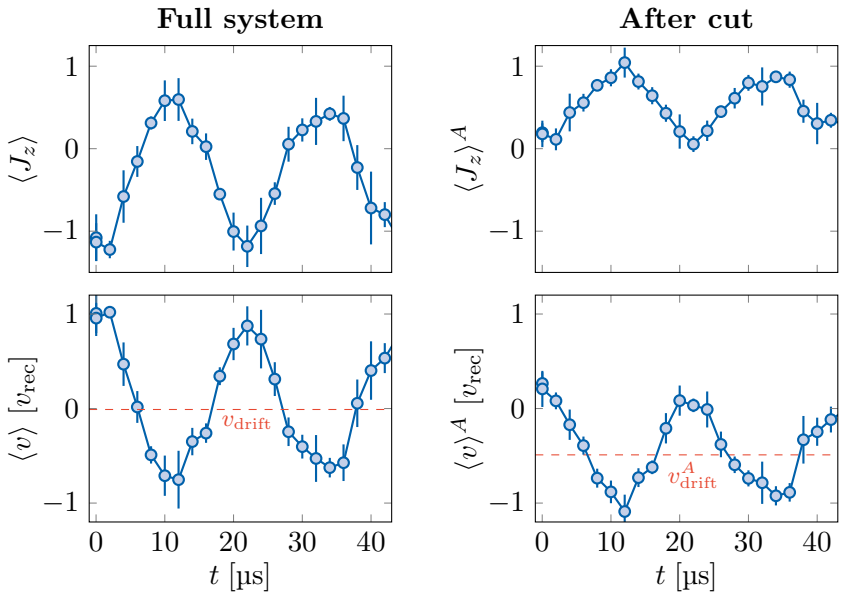

Figure 5.13: Appearance of edge-like dynamics in the partition region. *Left*: A cyclotron orbit in the bulk of the full system. This is similar to the closed orbits plotted in fig. 5.6, however here we directly show the evolution of the average magnetisation and velocity. The measured drift velocity is consistent with zero $v_{\mathrm{drift}} = -0.01(2)\ v_{\mathrm{rec}}$. *Right*: The same measurements, after the application of a partition at $m^* = -0.5$. This leads to skipping of the average magnetisation at the partition, along with the appearance of a negative average drift velocity $v^A_{\mathrm{drift}} = -0.49(2)\ v_{\mathrm{rec}}$.

We will now reinterpret these quantities in the upper half A of our Hall ribbon. Firstly, recall the convenient role played by the overlap coefficients α_p, β_p, defined in eq. (5.14). Since we have single-site resolution in m, these coefficients are easy to evaluate from the spin projection probabilities:

$$\alpha_p^2 = \sum_{m=0}^{J} \Pi_m \,, \text{ and } \beta_p^2 = \sum_{m=-J}^{-1} \Pi_m = 1 - \alpha_p^2 \tag{5.20}$$

This gives access to the single-particle entanglement pseudo-energies $\epsilon(p) = \log\left(\beta_p^2/\alpha_p^2\right)$, shown in fig. 5.12a. Since our absolute detection precision for the probabilities Π_m is at the per cent level, relative uncertainties in α (resp. β) increase sharply when the state ψ_p is largely localised to subsystem B (resp. A). Therefore, using this post hoc partitioning, we can only reliably measure $\epsilon(p)$ in a finite zone centred at $p = 0$, as reflected in fig. 5.12a. Since this zone is in the bulk of our system, the psuedo-energies are consistent with those of a real, infinite Hall system.

The spin and velocity distributions can be projected onto the subsystem A,

$$\Pi_p^A(m) = \frac{\Pi_p(m)}{\alpha_p^2} \,, \text{ for } 0 \leq m \leq J \tag{5.21}$$

$$\text{and } \mathcal{V}_p^A(v) = \frac{\sum_{m=0}^{J} n_p(m,v)}{\int \mathrm{d}v \sum_{m=0}^{J} n_p(m,v)} \tag{5.22}$$

following which the averaged quantities $\langle J_z \rangle^A$ and $\langle v \rangle^A$ of the cut state can be calculated similarly as for the full system. In fig. 5.12b,c, we focus on the spin distribution $\Pi_p^A(m)$ and the average velocity $\langle v \rangle^A$, which reveal the behaviour of an effective edge appearing at the partition. At this edge, the spin states saturates in $m = 0$, as for the real boundary at $m = -8$ in the full system (cf. fig. 5.5a). Moreover, the finite and negative average velocities at $p < 0$ correspond to the chiral edge mode (cf. fig. 5.5b). This edge behaviour is also apparent in fig. 5.13, which shows the effect of taking a closed cyclotron orbit centred near the cut $m^* = -0.5$ in the full system, and projecting it onto subsystem A. A skipping behaviour at $m = 0$ is apparent in the evolution of the average magnetisation, along with the appearance of a negative average drift velocity $v^A_{\text{drift}} = -0.49(2)\ v_{\text{rec}}$.

5.8.5 *Towards direct realisation of the entanglement Hamiltonian*

Given the ground band properties associated with the upper half of our Hall system following our applied 'partition', it is interesting to look for a Hamiltonian where such properties would appear naturally. This is in fact called the entanglement Hamiltonian.

Let us take a step back and reconsider the general many-body Hamiltonian H with a ground state ρ. As before, we consider a spatial biparition $A : B$. The *entanglement Hamiltonian* $\widetilde{H}$ is associated to the reduced state ρ_A, and it is defined by the relation

$$\rho_A = \exp\left(-\widetilde{H}\right) = \sum_i \exp\left(-\xi_i\right) |\psi_{A,i}\rangle \langle \psi_{A,i}| \ . \tag{5.23}$$

Recall that the states $|\psi_{A,i}\rangle$ are an orthonormal basis in which the Schmidt decomposition of the overall state ρ is expressed (see eq. (5.8)). Hence, the eigenvalues of the entanglement Hamiltonian form the entanglement spectrum. This is the key motivation to directly realise $\widetilde{H}$ in experiments. Compared to the tomographic reconstruction of ρ_A, which requires a number of measurements exponentially large in the system size, an implementation of the entanglement Hamiltonian would reduce this problem to one of spectroscopy of many-body excitations.

In 2018, Dalmonte et al. [88] addressed a series of challenges regarding the implementation of entanglement Hamiltonians as follows: firstly, $\widetilde{H}$ is unknown for a general system, and it is not even clear whether it can be represented in a closed, physically realisable form. If this was the case, the story would stop here, and the entanglement Hamiltonian would remain a useful theoretical tool. In fact, a result from axiomatic field theory, called the Bisognano-Wichmann (BW) theorem [361, 362], provides a way out. Roughly speaking, it states that the entanglement Hamiltonian in an infinite, continuous,

Lorentz invariant system, for a spatial partition along $y = 0$ takes the form of a local, linear spatial deformation of the original Hamiltonian,[7]

$$\widetilde{H} = yH + \text{const.} \tag{5.24}$$

The authors then showed that such an ansatz for the entanglement Hamiltonian of discrete, moderately sized systems gives very accurate entanglement spectra for some important classes of models. Moreover, they identified that modern quantum simulators based on trapped ions arrays, Rydberg dressings, or laser-assisted tunnelling in optical lattices are well suited for the implementation of the required position-dependent couplings. This work has since led to many interesting theoretical developments and proposals, including methods to efficiently reconstruct the entanglement Hamiltonian [363], or to estimate it variationally [364] (see ref. [365] for a review). We highlight ref. [341], where these methods are discussed for topological systems; the effective edge state at the partition, which we discussed in the previous section, also appears in this work.

Our synthetic Hall system is well suited to a direct implementation of the entanglement Hamiltonian in a BW-like form. Recall from eq. (5.5) that the Hamiltonian we implemented takes the form

$$H = \frac{(p - p_{\text{rec}} J_z)^2}{2M} - \hbar\Omega \left(J_x + \frac{J_z^2}{2J+3} \right) \tag{5.25}$$

For a cut at $m^* = -0.5$ across the synthetic dimension, the BW theorem provides an ansatz of the entanglement Hamiltonian for subsystem A,

$$\widetilde{H} = c_1 \left(\frac{1}{E_{\text{rec}}} \frac{\{J_z - m^\star, H\}}{2} + c_2 (J_z - m^\star) \right) .$$

Here the curly braces denote the anti-commutator, which accounts for the fact that H does not commute with $(J_z - m^*)$. The constant c_2 represents an offset of original Hamiltonian not expressed in eq. (5.25), whereas c_1 ensures the correct overall scaling of the entanglement spectrum, maintaining $\text{Tr}(\rho_A) = 1$. Note that the entanglement Hamiltonian is defined over the subsystem A only, such that $\widetilde{H}$ more accurately refers to the block of the above operator acting on the $m \geq 0$ subspace. Expanding the above ansatz gives terms of the form J_z^3 and pJ_z^2, whose implementation is not obvious with the spin-dependent light shifts and Raman coupling techniques discussed so far. Realising higher order couplings using additional degrees of freedom like intensity modulation of the light shift beams is a work in progress in our group. Once realised, these will provide couplings that would be unphysical in a real Hall system, where $p^2 J_z$ maps to $p_x^2 y$.

Figure 5.14 summarises calculations checking the validity of the BW ansatz in our system, in the picture of single-particle states of the ground band indexed by the quasi-momentum p. We compare the ground band dispersion of the ansatz $\widetilde{H}$ with the

[7] The constant offset merely ensures consistency with eq. (5.23) by maintaining $\text{Tr}\,(e^{-\widetilde{H}}) = 1$.

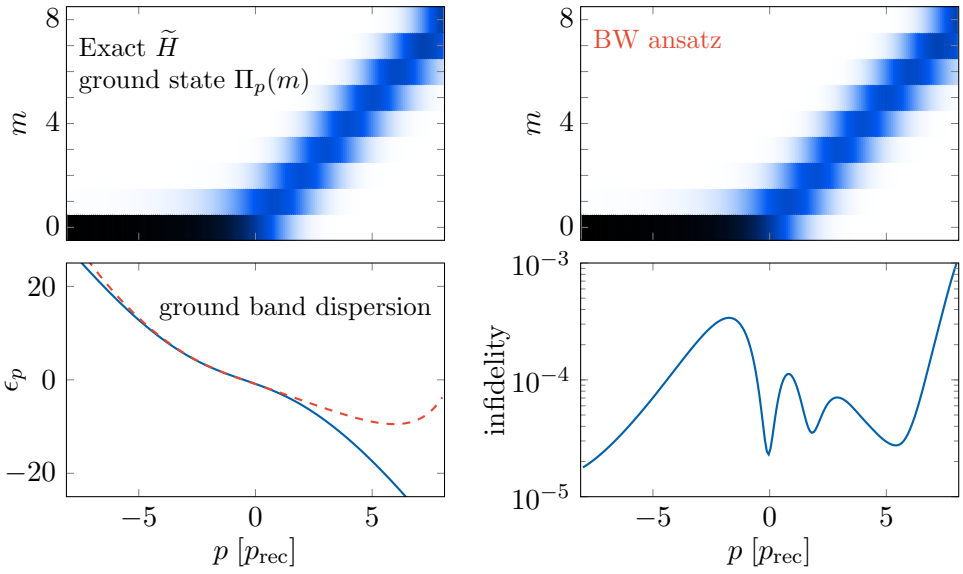

Figure 5.14: Numerical check of the validity of the ansatz for the entanglement Hamiltonian $\widetilde{H}$ given by Bisognano-Wichmann (BW) theorem in the synthetic Hall system. *Top left*: Ground band projection probabilities $\Pi_p(m)$ for the exact entanglement Hamiltonian $\widetilde{H}$. This is obtained by projecting the ground state of the Hall Hamiltonian into the upper half plane $m \geq 0$ i.e. this is the theory plot for the data in shown in fig. 5.12b. *Top right*: Ground band projection probabilities for a BW ansatz entanglement Hamiltonian. *Bottom right*: The difference between the states depicted in the top two panels is quantified by the infidelity, defined here as the squared Hellinger distance between the spin projection probability distributions, $d_{\mathrm{H}}^2(\Pi_m, \Pi'_m) = \sum_m (\sqrt{\Pi_m} - \sqrt{\Pi'_m})^2$. We choose this measure as it would be an experimentally convenient figure of merit for a variational optimisation of the entanglement Hamiltonian (see text). Note that the states we are comparing here only have real coefficients. *Bottom left*: The ground band dispersion of the exact entanglement Hamiltonian (solid blue curve), compared to the BW ansatz Hamiltonian (dashed red curve). The exact results are simply the single-particle pseudo-energies ϵ_p for the full synthetic Hall Hamiltonian.

pseudo-energies ϵ_p, finding reasonable agreement around the partition region, which could be improved by adjusting couplings to account for effects from the finite and discrete synthetic dimension. We also compare the eigenstates of the ansatz $\widetilde{H}$ to theory, again finding a good agreement, as quantified by the low infidelity in fig. 5.14. Hence, our synthetic Hall system is a promising platform for the first experimental implementation of the entanglement Hamiltonian in a topological system, providing a direct link to the Li-Haldane conjecture. We conclude this section on the entanglement spectrum by emphasising that the longer-term experimental perspective for this section, and indeed of all the work presented in this chapter, is the extension of these techniques to many-body topological states, which are discussed below.

5.9 TOWARDS MANY-BODY TOPOLOGICAL STATES

So far, we have discussed the creation of light-induced artificial magnetic fields in a system with a large synthetic dimension. We observed the characteristic topological response of the system's bulk as well as the chiral nature of the edge states. However, our measurements were limited to single-particle states. The most exciting future direction for this work would be the realisation of strongly correlated states in the regime of the fractional quantum Hall effect; these exotic states famously host elementary excitations with anyonic statistics [366]. In this regime, our techniques would give access to complex correlation effects, such as flux attachment via cyclotron orbits [367], and charge fractionalisation via adiabatic pumping [368] or centre-of-mass Hall response [369]. Our techniques could also be extended to fermionic isotopes of dysprosium, where the bulk response of the Fermi sea at a given filling fraction could be probed. The fermions also provide a larger bulk in the synthetic dimension i.e. $F = 21/2$ for ^{161}Dy.

We now discuss an important preliminary step towards the fractional quantum Hall regime, namely the realisation of many-body states at large filling factors. Here, the ground state can be described by a mean-field approach, with the insertion of magnetic flux causing Abrikosov vortices to form, as originally described for type-II superconductors [370]. With ultracold atoms, such systems were first realised with rotating Bose-Einstein condensates [371, 372], where the Sagnac phase associated with particle motion in the rotating frame plays the role of the Aharonov-Bohm phase. In an essential precursor to our work, artificial gauge fields were subsequently realised by optical coupling of internal states in alkali species [319]. Compared to the above studies, our system has a number of advantages when trying to approach the strongly-correlated regime, where the atomic density n is comparable to the gauge field's flux density n_ϕ. We need the interaction and thermal energy scales to be smaller than the Landau level splitting, to permit a description restricted to a single band. Our large cyclotron energy, $\hbar\omega_c \simeq k_B \times 1.8 - 2.3\,\mu K$, allows this to be realised for realistic temperatures. This creation of flat, well-separated bands is enabled by the advantageous parameters of light-spin interactions for lanthanides, allowing large couplings without significant heating[8], as we discussed in chapter 2. Our synthetic dimension provides an additional advantage: as we will see below, the large manifold of internal states can boost the effective magnitude of the light-induced gauge fields. However, when it comes to interactions, the synthetic dimension has some peculiar features: since atoms interact when they are nearby in real space, the effective 'length scale' of interactions in the synthetic dimension is infinite. Although this can lead to an interesting phenomenology [375], we now discuss a setup which circumvents this issue by associating a fixed spin state to each position in real space.

[8] The creation of gauge fields using complex-valued hopping amplitudes in optical lattices [326, 373, 374] is also limited by heating effects.

To conclude, we briefly describe a proposed experiment inspired by ref. [376] (where a synthetic dimension of size two was considered). As shown in fig. 5.15a, two laterally offset counter-propagating light beams, with opposite circular polarisations, pass near a Bose-Einstein condensate of dysprosium, creating a spatially varying polarisation field. We work near the transition at $\lambda = 833\,\mathrm{nm}$, with excited level angular momentum $J' = J = 8$. The ground state of the off-resonant spin-light coupling is a polarisation-dependent dark state, introduced in chapter 2, varying smoothly in space between $m = \pm 8$ depending on the relative intensities of the two beams (see fig. 5.15b). An atom moving adiabatically, following this ground state, acquires a geometric Berry phase, which manifests as an artificial gauge field, as originally pointed out in ref. [377] (see ref. [115] for a review). The total flux in a region between the beams, and of length λ, is $N_\phi \sim h \times 2J$ [376], emphasising the advantage of the large synthetic dimension. We show in fig. 5.15c a numerically computed mean-field ground state of such a system. It shows a pattern of Abrikosov lattices, identified as points of vanishing density and non-trivial phase winding in the spinor ground state. Beyond the content of this thesis, the realisation of this experiment would require further developments on cancelling magnetic field fluctuations, for detecting the spin and spatial state, and for understanding the spin-dependent interactions – constituting a practical roadmap for the realisation of many-body topological states.

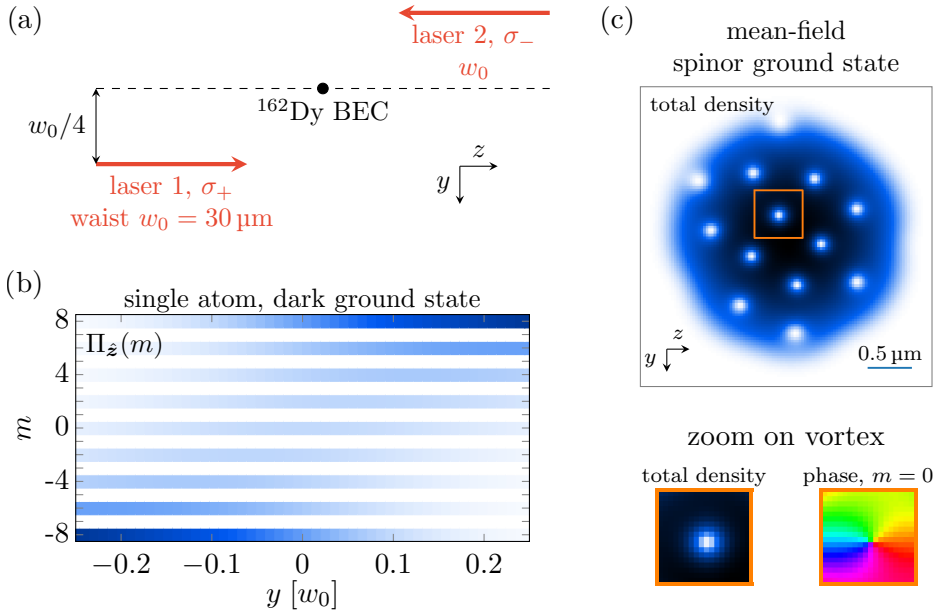

Figure 5.15: A scheme for creating a many-body topological state in the limit of large filling fraction. (a) Two counter-propagating laser beams, far-detuned from the $J' = J = 8$ transition at 833 nm are focussed with waist w_0 near a dysprosium BEC. The beams are laterally separated and carry opposing circular polarisations, creating a spatially varying polarisation field across the BEC, as a function of the relative intensities of the Gaussian beams. (b) Spin projection probabilities of the dark ground state of the atom-light coupling with respect to the 833 nm transition, as a function of the coordinate y. The ground state is $m = \pm 8$ for pure $\sigma_\pm$-polarised light respectively. Here, we see the intermediate states between these limits. (c) The adiabatic following of the ground state leads to an artificial gauge field along x (see text). Numerical simulation of the mean-field ground state using imaginary time evolution of a two-dimensional Gross-Pitaevskii equation, for a $2J + 1$ component spinor wavefunction. We consider a BEC of 10^4 atoms in a spherically symmetric trap $\omega_{x,y,z} = 2\pi \times 0.7\,$kHz. The spin-dependent interactions for dysprosium are not known; here, we consider all scattering lengths to be equal, with $a = 110\,a_0$. Dipolar interactions are not considered, we do not expect them to significantly affect the observed behaviour. The light-shift amplitude at the focus of each beam is $V_0 \simeq 10^5 E_{\text{rec}}$, corresponding to a detuning of 2.5 GHz and a power of 4 W. The repulsive scalar potential accompanying the gauge field is compensated by an additional trapping potential along the y-axis. The overall spatial form of the wavefunction is well described by a Thomas-Fermi profile with a radius of $R_{\text{TF}} \simeq 1.5\,\mu$m; the chemical potential is $\mu \simeq 9\,$kHz. The spin state converges everywhere to the local dark state, with squared fidelity greater than 99%. We observe vortices in the calculated wavefunction: points of vanishing total density and a phase winding of 2π in all populated spin components. The lower panels show a zoomed-in view of one such vortex. The extent of the vortex is comparable to the expected healing length $\xi = (8\pi n_{2\text{D}}\, a / R_{\text{TF}})^{-1/2} \simeq 90\,$nm.

A

APPENDIX: PUBLICATIONS

This appendix contains articles published during this thesis which were not fully discussed in the main text.

A.1 PROBING CHIRAL EDGE DYNAMICS AND BULK TOPOLOGY OF A SYNTHETIC HALL SYSTEM

The following pages contain the full text of the article [311], including the Methods and Supplementary Materials. An excerpt from this article was presented in sections 5.3–5.6.

Probing chiral edge dynamics and bulk topology of a synthetic Hall system
T. Chalopin*, T. Satoor*, A. Evrard, V. Makhalov, J. Dalibard, R. Lopes, S. Nascimbene
Nature Physics 16, 1017–1021 (2020)
* These authors contributed equally

nature physics

LETTERS

https://doi.org/10.1038/s41567-020-0942-5

Check for updates

Probing chiral edge dynamics and bulk topology of a synthetic Hall system

Thomas Chalopin[1,3], Tanish Satoor[1,3], Alexandre Evrard[1], Vasiliy Makhalov[1,2], Jean Dalibard[1], Raphael Lopes[1] and Sylvain Nascimbene[1]✉

Quantum Hall systems are characterized by quantization of the Hall conductance—a bulk property rooted in the topological structure of the underlying quantum states[1]. In condensed matter devices, material imperfections hinder a direct connection to simple topological models[2,3]. Artificial systems, such as photonic platforms[4] or cold atomic gases[5], open novel possibilities by enabling specific probes of topology[6–13] or flexible manipulation, for example using synthetic dimensions[14–21]. However, the relevance of topological properties requires the notion of a bulk, which was missing in previous works using synthetic dimensions of limited sizes. Here, we realize a quantum Hall system using ultracold dysprosium atoms in a two-dimensional geometry formed by one spatial dimension and one synthetic dimension encoded in the atomic spin $J=8$. We demonstrate that the large number of magnetic sublevels leads to distinct bulk and edge behaviours. Furthermore, we measure the Hall drift and reconstruct the local Chern marker, an observable that has remained, so far, experimentally inaccessible[22]. In the centre of the synthetic dimension—a bulk of 11 states out of 17—the Chern marker reaches 98(5)% of the quantized value expected for a topological system. Our findings pave the way towards the realization of topological many-body phases.

In two-dimensional (2D) electron gases, quantization of the Hall conductance results from the non-trivial topological structuring of the quantum states of an electron band. For an infinite system, this topological character is described by the Chern number C, a global invariant taking a non-zero integer value that is robust to relatively weak disorder[1]. In a real finite-sized system, the non-trivial topology further leads to in-gap excitations delocalized over the edges, characterized by unidirectional motion exempt from backscattering[3]. Such protected edge modes, together with their generalization to topological insulators, topological superconductors or fractional quantum Hall states[23,24], lie at the heart of possible applications in spintronics[25] or quantum computing[26].

In electronic quantum Hall systems, the topology manifests itself via the spectacular robustness of the Hall conductance quantization to finite-size or disorder effects[27]. Nonetheless, such perturbations typically lead to conducting stripes surrounding insulating domains of localized electrons, making the comparison with simple defect-free models challenging. In topological insulators or fractional quantum Hall systems, topological properties are more fragile, and can only be revealed in very clean samples[23,24]. Recent experiments with topological quantum systems in photonic or atomic platforms[5,28] have created new possibilities, from the realization of emblematic models of topological matter[6,29,30] to the application of well-controlled edge and disorder potentials. In such systems, internal degrees of freedom can be used to simulate a synthetic dimension of finite size with sharp-edge effects[14–21]. Encoding a synthetic dimension in the time domain can also give access to higher-dimensional physics[31,32].

In this work, we engineer a topological system with ultracold bosonic ^{162}Dy atoms based on coherent light-induced couplings between an atom's motion and the electronic spin $J=8$, with relevant dynamics along two dimensions—one spatial dimension and a synthetic dimension encoded in the discrete set of $2J+1=17$ magnetic sublevels. These couplings give rise to an artificial magnetic field, such that our system realizes an analogue of a quantum Hall ribbon. In the lowest band, we characterize the dispersionless bulk modes, where motion is inhibited due to a flattened energy band, and edge states, where the particles are free to move in one direction only. We also study elementary excitations to higher bands, which take the form of cyclotron and skipping orbits. We furthermore measure the Hall drift induced by an external force, and infer the local Hall response of the band via the local Chern marker, which quantifies topological order in real space[22]. Our experiments show that the synthetic dimension is large enough to allow for a meaningful bulk with robust topological properties. Numerical simulations of interacting bosons moreover show that our system can host quantum many-body systems with non-trivial topology, such as mean-field Abrikosov vortex lattices or fractional quantum Hall states.

The atom dynamics is induced by two-photon optical transitions involving counter-propagating laser beams along x (Fig. 1a), and coupling of successive magnetic sublevels m (refs. [33,34]). Here, the integer m ($-J\leq m\leq J$) quantifies the spin projection along the direction z of an external magnetic field. The spin coupling amplitudes then inherit the complex phase Kx of the interference between both lasers, where $K=4\pi/\lambda$ and $\lambda=626.1$ nm is the light wavelength (Fig. 1b). Given the Clebsch–Gordan algebra of atom–light interactions for the dominant optical transition, the atom dynamics is described by the Hamiltonian

$$\hat{H}=\frac{1}{2}M\hat{v}^2-\frac{\hbar\Omega}{2}\left(\mathrm{e}^{-iK\hat{x}}\hat{J}_+ + \mathrm{e}^{iK\hat{x}}\hat{J}_-\right)+V(\hat{J}_z) \qquad (1)$$

where M is the atom mass, $\hat{v}$ is its velocity and $\hat{J}_z$ and $\hat{J}_\pm$ are the spin projection and ladder operators. The coupling Ω is proportional to both laser electric fields, and the potential $V(\hat{J}_z)=-\hbar\Omega\hat{J}_z^2/(2J+3)$ stems from rank-2 tensor light shifts (see Methods and Supplementary Information).

A light-induced spin transition $m\rightarrow m+1$ is accompanied by a momentum kick $-p_{\mathrm{rec}}\equiv-\hbar K$ along x, such that the canonical

[1]Laboratoire Kastler Brossel, Collège de France, CNRS, ENS-PSL University, Sorbonne Université, Paris, France. [2]Present address: ICFO-The Institute of Photonic Sciences, Barcelona, Spain. [3]These authors contributed equally: Thomas Chalopin, Tanish Satoor. ✉e-mail: sylvain.nascimbene@lkb.ens.fr

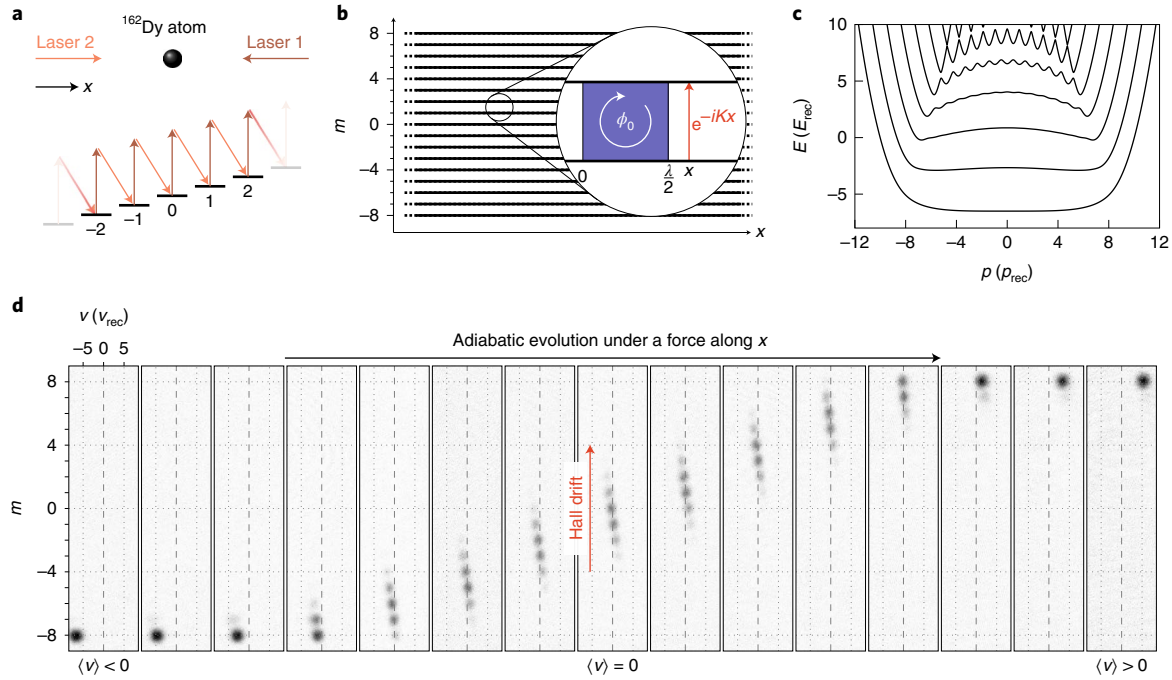

Fig. 1 | Synthetic Hall system. a, Laser configuration used to couple the magnetic sublevels m of a ^{162}Dy atom (with $-J \leq m \leq J$ and $J=8$; only a few m values are represented). **b**, Interpreting the spin projection as a synthetic dimension, the system is mapped to a 2D ribbon of finite width. The photon recoil $p_{rec}=\hbar K$ imparted on a spin transition leads to complex-valued hopping amplitudes along m, equivalent to the Aharonov–Bohm phase of a charged particle evolving in a magnetic field. The blue area represents a magnetic unit cell pierced by one flux quantum ϕ_0. **c**, Dispersion relation describing the quantum level structure for $\hbar\Omega=E_{rec}$, with flattened energy bands reminiscent of Landau levels. **d**, The lowest energy band is explored by applying an external force. We probe the velocity and magnetic projection distributions by imaging the atomic gas after an expansion under a magnetic field gradient. We find three types of behaviour: free motion with negative (positive) velocity on the bottom edge $m=-J$ (top edge $m=J$) and zero average velocity in the bulk. Each panel corresponds to a single-shot image.

momentum $\hat{p} = M\hat{v} + p_{rec}\hat{J}_z$ is a conserved quantity. After a unitary transformation defined by the operator $\hat{U} = \exp(iK\hat{x}\hat{J}_z)$, the Hamiltonian (1) can be rewritten, for a given momentum p, as

$$\hat{H}_p = \frac{(p - p_{rec}\hat{J}_z)^2}{2M} - \hbar\Omega\hat{J}_x + V(\hat{J}_z) \qquad (2)$$

We can make an analogy between this Hamiltonian and the ideal Landau one, given by

$$\hat{H}_{Landau} = \frac{(\hat{p}_x - eB\hat{y}^2)}{2M} + \frac{\hat{p}_y^2}{2M} \qquad (3)$$

which describes the dynamics of an electron of charge $-e$ evolving in the x–y plane under a perpendicular magnetic field B. The analogy between the two systems can be made upon the identifications $\hat{J}_z \leftrightarrow \hat{y}$ and $p_{rec} \leftrightarrow eB$. The term $\hat{J}_x$ in equation (2) plays the role of the kinetic energy along the synthetic dimension, because it couples neighbouring m levels with real positive coefficients, similarly to the discrete form of the Laplacian operator $\propto \hat{p}_y^2$ in equation (3) (see Supplementary Information). The range of magnetic projections being limited, our system maps onto a Hall system in a ribbon geometry bounded by the edge states $m=\pm J$. The relevance of the analogy is confirmed by the structure of energy bands $E_n(p)$ expected for the Hamiltonian (2) describing our system, shown in Fig. 1c. The energy dispersion of the first few bands is strongly reduced for $|p| \lesssim Jp_{rec}$, reminiscent of dispersionless Landau levels. A parabolic dispersion is recovered for $|p| \gtrsim Jp_{rec}$, similar to the ballistic edge modes of a quantum Hall ribbon[3]. The flatness of the lowest energy band, for $\hbar\Omega \approx E_{rec}$, results from the compensation of two dispersive effects, namely the variation of $\hat{J}_x$ matrix elements and the extra term, $V(\hat{J}_z)$ (see Supplementary Information).

We first characterize the ground band using quantum states of arbitrary values of momentum p. We begin with an atomic gas spin-polarized in $m=-J$, and with a negative mean velocity $\langle\hat{v}\rangle = -6.5(1)v_{rec}$ (with $v_{rec} \equiv p_{rec}/M$), such that it corresponds to the ground state of equation (2) with $p=-14.5(1)p_{rec}$. The gas temperature $T=0.55(6)\,\mu$K is such that the thermal velocity broadening is smaller than the recoil velocity v_{rec}. We then slowly increase the light intensity up to a coupling $\hbar\Omega=1.02(6)E_{rec}$, where $E_{rec} \equiv p_{rec}^2/(2M)$ is the natural energy scale in our system. Subsequently, we apply a weak force F_x along x, such that the state adiabatically evolves in the ground energy band with $\dot{p} = F_x$, until the desired momentum is reached (see Methods). We measure the distribution of velocity v and spin projection m by imaging the atomic gas after a free flight in the presence of a magnetic field gradient.

The main features of Landau level physics are visible in the raw images shown in Fig. 1d. Depending on the momentum p, the system exhibits three types of behaviour. (1) When spin-polarized in $m=-J$, the atoms move with a negative mean velocity $\langle\hat{v}\rangle$, consistent with a left-moving edge mode. (2) When the velocity approaches zero under the action of the force F_x, the system experiences a series of resonant transitions to higher m sublevels—in other words a transverse Hall drift along the synthetic dimension. In this regime the atom's motion is inhibited along x, as expected for a quasi non-dispersive band. (3) Once the edge $m=J$ is reached, the velocity $\langle\hat{v}\rangle$ rises again, corresponding to a right-moving edge mode. Overall, while exploring the entire ground band under the action of a force along x, the atoms are pumped from one edge to the other along the synthetic dimension.

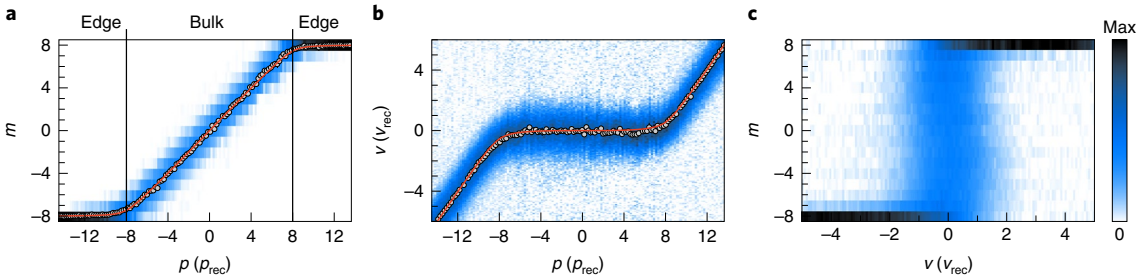

Fig. 2 | Ground band characterization. a, Spin projection distribution Π_m as a function of momentum p, with the mean spin projection $\langle \hat{J}_z \rangle$ (grey dots) and the theoretical prediction $(p - M\partial_p E_0)/p_{\mathrm{rec}}$ (red line). **b**, Velocity distribution, together with the mean velocity $\langle \hat{v} \rangle$ (grey dots) and the expected value, given by the derivative of the band dispersion $\partial_p E_0$ (red line). **c**, Local density of states obtained by integrating the measured distributions in (v, m) space over all momenta. All error bars are the $1-\sigma$ s.d. of typically five measurement repetitions.

To distinguish between bulk and edge modes, Fig. 2a shows the spin projection probabilities Π_m as a function of momentum p. We find that the edge probabilities $\Pi_{m=\pm J}$ exceed 1/2 for $|p| > 8.0(1)p_{\mathrm{rec}}$, defining the edge mode sectors—with the bulk modes in between. We study the system dynamics via its velocity distribution and mean velocity $\langle \hat{v} \rangle$, shown in Fig. 2b. We observe that the velocity of bulk modes remains close to zero, which shows via the Hellmann–Feynman relation $\langle \hat{v} \rangle = \partial E_0/\partial p$ that the ground band is almost flat.

The measured residual mean velocities allow us to infer a dispersion $\Delta E_0^{\mathrm{pk-pk}} = 1.2(5)\ E_{\mathrm{rec}}$ in the bulk mode region—nearly 2% of the free-particle dispersion expected over the same range of momenta. By contrast, edge modes are characterized by a velocity $\langle \hat{v} \rangle \simeq (p - p_0)/M$, corresponding to ballistic motion, albeit with the restriction $\langle \hat{v} \rangle < 0$ for edge modes close to $m = -J$ and $\langle \hat{v} \rangle > 0$ at the opposite edge. We also characterize correlations between velocity v and spin projection m over the full band, via the local density of states (LDOS) in (v, m) space, integrated over p. We stress here that the LDOS only involves gauge-independent quantities and could thus be generalized to more complex geometries lacking translational invariance. As shown in Fig. 2c, it also reveals characteristic quantum Hall behaviour, namely inhibited dynamics in the bulk and chiral motion on the edges.

The ideal Landau level structure of a charged particle evolving in two dimensions in a transverse magnetic field is characterized by a harmonic energy spacing $\hbar\omega_c$, set by the cyclotron frequency $\omega_c = eB/M$. We test this behaviour in our system by studying elementary excitations above the ground band, via the trajectories of the centre of mass following a velocity kick $v_{\mathrm{kick}} \simeq v_{\mathrm{rec}}$. To access the real-space position of the atoms, we numerically integrate their centre-of-mass velocity evolution (see Methods). As shown in Fig. 3 (blue dots), we measure almost closed trajectories in the bulk, consistent with the periodic cyclotron orbits expected for an infinite Hall system. We checked that this behaviour remains valid for larger excitation strengths, until one couples to highly dispersive excited bands (for velocity kicks $v_{\mathrm{kick}} \gtrsim 2v_{\mathrm{rec}}$, see Methods). Close to the edges, the atoms experience an additional drift and their trajectories are similar to classical skipping orbits bouncing on a hard wall. In particular, the drift orientation only depends on the considered edge, irrespective of the kick direction. We report in the inset of Fig. 3 the frequencies of velocity oscillations, which agree well with the expected cyclotron gap to the first excited band. We find that the gap is almost uniform within the bulk mode sector, with a residual variation in the range $\omega_c = 3.0(1)$–$3.8(1)E_{\mathrm{rec}}/\hbar$.

We now investigate the key feature of Landau levels, namely their quantized Hall response, which is intrinsically related to their topological nature. In a ribbon geometry, the Hall response of a particle corresponds to the transverse velocity acquired upon applying a potential difference across the edges (Fig. 4a). In our system,

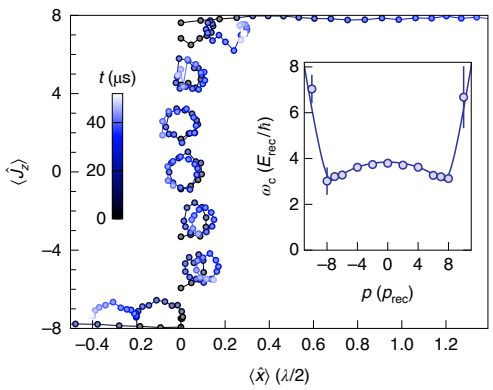

Fig. 3 | Cyclotron and skipping orbits. Trajectories in (x, m) space following a velocity kick $v_{\mathrm{kick}} \simeq v_{\mathrm{rec}}$, starting at $\langle \hat{x} \rangle = 0$, and for different initial momentum states (blue dots). The colour encodes the time evolution. Inset: frequencies extracted from the velocity dynamics (blue dots) and compared with the expected cyclotron gap for $\hbar\Omega = E_{\mathrm{rec}}$ (blue line). Error bars show the $1-\sigma$ statistical uncertainty calculated from a bootstrap sampling analysis performed on more than 100 pictures.

such a potential corresponds to a Zeeman term $-F_m\hat{J}_z$ added to Hamiltonian (2), which can now be recast as

$$\hat{H}_p - F_m\hat{J}_z = \hat{H}_{p+Mv'} - v'p \quad \text{with} \quad v' = F_m/p_{\mathrm{rec}}$$

such that the force acts as a momentum shift Mv' in the reference frame with velocity v'. In the weak force limit, the perturbed state remains in the ground band, and its mean velocity reads

$$\langle \hat{v} \rangle = \langle \hat{v} \rangle_{F_m=0} - \mu F_m, \quad \text{where} \quad \mu = \frac{1}{p_{\mathrm{rec}}}\frac{\partial}{\partial p}(p - M\langle \hat{v} \rangle)$$

is the Hall mobility. This expression shows that the Hall response to a weak force can be related to the variation of the mean velocity within the ground band, which we show in Fig. 2b. In practice, the velocity derivative at momentum p is evaluated using momentum states in the domain $(p - p_{\mathrm{rec}}, p + p_{\mathrm{rec}})$, corresponding to an evaluation of the Hall drift under a force $-2E_{\mathrm{rec}}/\ell < F_m < 2E_{\mathrm{rec}}/\ell$, where $\ell = 1$ is the unit length along the synthetic dimension. We present in Fig. 4b the Hall mobility $\mu(p)$ deduced from this procedure. For bulk modes, it remains close to the value $\mu = 1/p_{\mathrm{rec}}$, which corresponds to the classical mobility $\mu = 1/(eB)$ in the equivalent Hall system. The mobility decreases in the edge mode sector, as expected

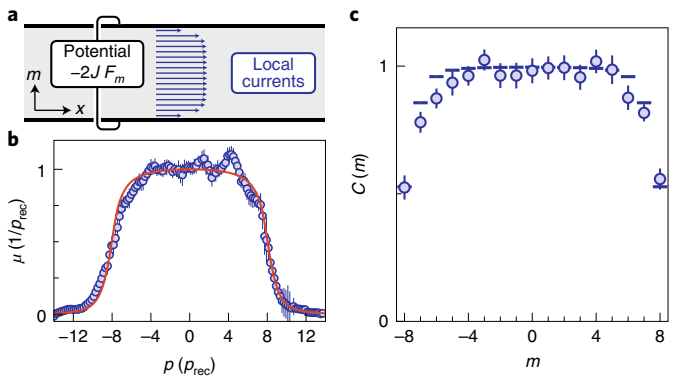

Fig. 4 | The Hall response. a, The Hall response is determined from the measurement of local currents in the real dimension that result from the application, in synthetic space, of a potential difference $-2JF_m$ between the edges. **b**, Hall mobility $\mu(p)$ measured for states of momenta p via their increase of velocity on application of a small force F_m along m. **c**, Local Chern marker as a function of m, corresponding to the integrated mobility $\mu(p)$ weighted by the projection probability $\Pi_m(p)$. Error bars represent the $1-\sigma$ statistical uncertainty calculated from a bootstrap sampling analysis over typically 100 pictures (**b**) and 1,000 pictures (**c**).

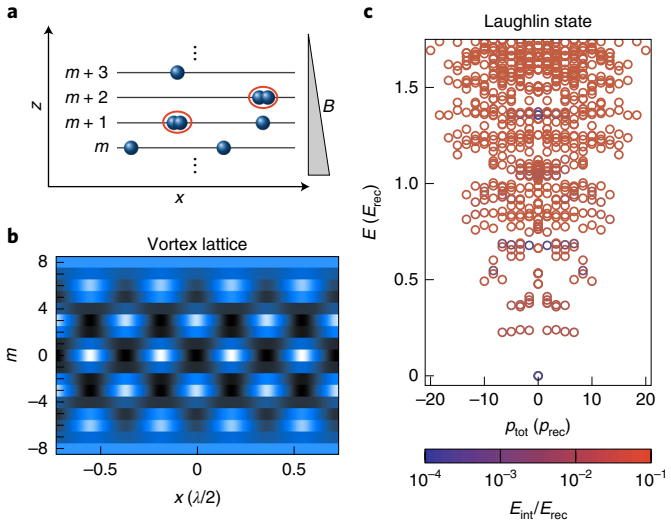

Fig. 5 | Simulations of topological many-body systems. a, Proposed scheme to engineer contact interactions along both directions x and m. A magnetic field gradient spatially separates the different m states along z, such that collisions (represented by the red ellipses) only occur for atoms in the same magnetic sublevel m. **b**, Density distribution of a Bose–Einstein condensate, with a chemical potential at ~$2E_{rec}$ above the single-particle ground-state energy. **c**, Many-body spectrum of a system of $N=5$ interacting atoms, where the colour encodes the interaction energy. We use periodic boundary conditions along x, with a circumference $L=0.6(\lambda/2)$ allowing for $N_{orb}=9$ orbitals at low energy, compatible with the Laughlin state. The residual energy dispersion between these orbitals is minimized by using a coupling strength $\Omega=0.5E_{rec}/\hbar$.

for topologically protected boundary states whose ballistic motion is undisturbed by the magnetic field.

We use the measured drift of individual quantum states to infer the overall Hall response of the ground band. As for any spatially limited sample, our system does not exhibit a gap in the energy spectrum due to the edge mode dispersion. In particular, high-energy edge modes of the ground band are expected to resonantly hybridize with excited bands upon disorder, such that defining the Hall response of the entire ground band is not physically meaningful. We thus only consider the energy branch $E<E^*$, where E^* lies in the middle of the first gap at zero momentum (see Methods). We characterize the (inhomogeneous) Hall response of this branch via the local Chern marker

$$C(m) \equiv 2\pi \mathrm{Im}\langle m|[\hat{P}\hat{x}\hat{P}, \hat{P}\hat{J}_z\hat{P}]|m\rangle = \int_{E(p)<E^*} \mathrm{d}p\ \Pi_m(p)\mu(p)$$

where $\hat{P}$ projects on the chosen branch[22,35]. This local geometrical marker quantifies the adiabatic transverse response in position space and matches the integer Chern number $\mathcal{C}$ in the bulk of a large, defect-free system. Here, it is given by the integrated mobility $\mu(p)$, weighted by the spin projection probability $\Pi_m(p)$ (see Methods). As shown in Fig. 4c, we identify a plateau in the range $-5\leq m\leq 5$. There, the average value of the Chern marker, $\overline{C}=0.98(5)$, is consistent with the integer value $\mathcal{C}=1$, the Chern number of an infinite Landau level. This measurement shows that our system is large enough to reproduce a topological Hall response in its bulk. For positions $|m|\geq 6$, we measure a decrease of the Chern marker, which we attribute to non-negligible correlations with the edges.

Such a topological bulk is a prerequisite for the realization of emblematic phases of 2D quantum Hall systems, as we now confirm via numerical simulations of interacting quantum many-body systems. In our system, collisions between atoms a priori occur when they are located at the same position x, irrespective of their spin projections m, m', leading to highly anisotropic interactions. Although this feature leads to an interesting phenomenology[36], we propose to control the interaction range by spatially separating the different m states using a magnetic field gradient, suppressing both contact and dipole–dipole interactions for $m\neq m'$, as illustrated in Fig. 5a (see Methods and Supplementary Information). The system then becomes truly 2D and closely related to the seminal work of ref. [33], albeit with a discrete spatial dimension with sharp walls. In the following, we discuss the many-body phases expected for bosonic atoms with such short-range interactions, assuming, for simplicity, repulsive interactions of equal strength for each projection m.

We first consider the case of a large filling fraction $\nu\equiv N_{at}/N_\phi\gg 1$, where N_ϕ is the number of magnetic flux quanta in the area occupied by N_{at} atoms, as realized in previous experiments on rapidly rotating gases[37,38]. In this regime and at low temperature, the system forms a Bose–Einstein condensate that spontaneously breaks translational symmetry, leading to a triangular Abrikosov lattice of quantum vortices (Fig. 5b). Owing to the hard-wall boundary along m, one expects phase transitions between vortex lattice configurations when tuning the coupling strength Ω and the chemical potential, similar to the phenomenology of type-II superconductors in confined geometries[39] (see Methods).

For lower filling fractions $\nu\approx 1$, one expects strongly correlated ground states analogous to fractional quantum Hall states[40]. We present in Fig. 5c a numerical calculation of the many-body spectrum for $N_{at}=5$ atoms with periodic boundary conditions along x, corresponding to a cylinder geometry. We choose the circumference such that the number of orbitals $N_{orb}=9$ in the bulk region of the lowest band matches the number $N_{orb}=2N_{at}-1$ required to construct the Laughlin wavefunction. For contact interactions parametrized by a Haldane pseudopotential of amplitude $U=E_{rec}$, we numerically find a ground state separated by an energy gap $E_{gap}\simeq 0.23E_{rec}=k_B\times 140\,\mathrm{nK}$ from the rest of the excitations. It also exhibits a very small interaction energy E_{int}, indicating anti-bunching between atoms, which is a hallmark of the Laughlin state.

The realization of a quantum-Hall system based on a large synthetic dimension, as discussed here, is a promising setting for future realizations of topological quantum matter. An important asset

of our set-up is the large cyclotron energy, measured in the range $\hbar\omega_c \simeq k_B \times 1.8 - 2.3\,\mu K$, much larger than the typical temperatures of quantum degenerate gases, thus enabling the realization of strongly correlated states at realistic temperatures. The techniques developed here could give access to complex correlation effects, such as flux attachment via cyclotron orbits[41] or charge fractionalization via adiabatic pumping[42] or the centre-of-mass Hall response[43]. Our protocol could also be extended to fermionic isotopes of dysprosium, with a synthetic dimension given by the hyperfine spin of the lowest energy state, $F = 21/2$ for ^{161}Dy, leading to an even larger bulk. At low temperature and unit filling of the ground band, the Fermi sea would exhibit an almost quantized Hall response akin to the integer quantum Hall effect.

Online content

Any methods, additional references, Nature Research reporting summaries, source data, extended data, supplementary information, acknowledgements, peer review information; details of author contributions and competing interests; and statements of data and code availability are available at https://doi.org/10.1038/s41567-020-0942-5.

Received: 13 December 2019; Accepted: 20 May 2020;
Published online: 22 June 2020

References

1. Thouless, D. J., Kohmoto, M., Nightingale, M. P. & denNijs, M. Quantized Hall conductance in a two-dimensional periodic potential. *Phys. Rev. Lett.* **49**, 405–408 (1982).
2. Laughlin, R. B. Quantized Hall conductivity in two dimensions. *Phys. Rev. B* **23**, 5632–5633 (1981).
3. Halperin, B. I. Quantized Hall conductance, current-carrying edge states, and the existence of extended states in a two-dimensional disordered potential. *Phys. Rev. B* **25**, 2185–2190 (1982).
4. Ozawa, T. et al. Topological photonics. *Rev. Mod. Phys.* **91**, 015006 (2019).
5. Goldman, N., Budich, J. C. & Zoller, P. Topological quantum matter with ultracold gases in optical lattices. *Nat. Phys.* **12**, 639–645 (2016).
6. Jotzu, G. et al. Experimental realization of the topological Haldane model with ultracold fermions. *Nature* **515**, 237–240 (2014).
7. Aidelsburger, M. et al. Measuring the Chern number of Hofstadter bands with ultracold bosonic atoms. *Nat. Phys.* **11**, 162–166 (2015).
8. Hu, W. et al. Measurement of a topological edge invariant in a microwave network. *Phys. Rev. X* **5**, 011012 (2015).
9. Mittal, S., Ganeshan, S., Fan, J., Vaezi, A. & Hafezi, M. Measurement of topological invariants in a 2D photonic system. *Nat. Photon.* **10**, 180–183 (2016).
10. Wu, Z. et al. Realization of two-dimensional spin–orbit coupling for Bose–Einstein condensates. *Science* **354**, 83–88 (2016).
11. Fläschner, N. et al. Experimental reconstruction of the Berry curvature in a Floquet Bloch band. *Science* **352**, 1091–1094 (2016).
12. Ravets, S. et al. Polaron polaritons in the integer and fractional quantum Hall regimes. *Phys. Rev. Lett.* **120**, 057401 (2018).
13. Schine, N., Chalupnik, M., Can, T., Gromov, A. & Simon, J. Electromagnetic and gravitational responses of photonic Landau levels. *Nature* **565**, 173–179 (2019).
14. Celi, A. et al. Synthetic gauge fields in synthetic dimensions. *Phys. Rev. Lett.* **112**, 043001 (2014).
15. Mancini, M. et al. Observation of chiral edge states with neutral fermions in synthetic Hall ribbons. *Science* **349**, 1510–1513 (2015).
16. Stuhl, B. K., Lu, H.-I., Aycock, L. M., Genkina, D. & Spielman, I. B. Visualizing edge states with an atomic Bose gas in the quantum Hall regime. *Science* **349**, 1514–1518 (2015).
17. Livi, L. F. et al. Synthetic dimensions and spin–orbit coupling with an optical clock transition. *Phys. Rev. Lett.* **117**, 220401 (2016).
18. Kolkowitz, S. et al. Spin–orbit-coupled fermions in an optical lattice clock. *Nature* **542**, 66–70 (2017).
19. An, F. A., Meier, E. J. & Gadway, B. Direct observation of chiral currents and magnetic reflection in atomic flux lattices. *Sci. Adv.* **3**, e1602685 (2017).
20. Lustig, E. et al. Photonic topological insulator in synthetic dimensions. *Nature* **567**, 356–360 (2019).
21. Ozawa, T. et al. Topological photonics. *Rev. Mod. Phys.* **91**, 015006 (2019).
22. Bianco, R. & Resta, R. Mapping topological order in coordinate space. *Phys. Rev. B* **84**, 241106 (2011).
23. Stormer, H. L., Tsui, D. C. & Gossard, A. C. The fractional quantum Hall effect. *Rev. Mod. Phys.* **71**, S298–S305 (1999).
24. Hasan, M. Z. & Kane, C. L. Colloquium: topological insulators. *Rev. Mod. Phys.* **82**, 3045–3067 (2010).
25. Pesin, D. & MacDonald, A. H. Spintronics and pseudospintronics in graphene and topological insulators. *Nat. Mater.* **11**, 409–416 (2012).
26. Kitaev, A. Y. Fault-tolerant quantum computation by anyons. *Ann. Phys.* **303**, 2–30 (2003).
27. Klitzing, K. V., Dorda, G. & Pepper, M. New method for high-accuracy determination of the fine-structure constant based on quantized Hall resistance. *Phys. Rev. Lett.* **45**, 494–497 (1980).
28. Lu, L., Joannopoulos, J. D. & Soljačić, M. Topological photonics. *Nat. Photon.* **8**, 821–829 (2014).
29. Aidelsburger, M. et al. Realization of the Hofstadter Hamiltonian with ultracold atoms in optical lattices. *Phys. Rev. Lett.* **111**, 185301 (2013).
30. Miyake, H., Siviloglou, G. A., Kennedy, C. J., Burton, W. C. & Ketterle, W. Realizing the Harper Hamiltonian with laser-assisted tunneling in optical lattices. *Phys. Rev. Lett.* **111**, 185302 (2013).
31. Lohse, M., Schweizer, C., Price, H. M., Zilberberg, O. & Bloch, I. Exploring 4D quantum Hall physics with a 2D topological charge pump. *Nature* **553**, 55–58 (2018).
32. Zilberberg, O. et al. Photonic topological boundary pumping as a probe of 4D quantum Hall physics. *Nature* **553**, 59–62 (2018).
33. Lin, Y.-J., Jiménez-García, K. & Spielman, I. B. Spin–orbit-coupled Bose–Einstein condensates. *Nature* **471**, 83–86 (2011).
34. Cui, X., Lian, B., Ho, T.-L., Lev, B. L. & Zhai, H. Synthetic gauge field with highly magnetic lanthanide atoms. *Phys. Rev. A* **88**, 011601 (2013).
35. Kitaev, A. Anyons in an exactly solved model and beyond. *Ann. Phys.* **321**, 2–111 (2006).
36. Barbarino, S., Taddia, L., Rossini, D., Mazza, L. & Fazio, R. Magnetic crystals and helical liquids in alkaline-earth fermionic gases. *Nat. Commun.* **6**, 8134 (2015).
37. Schweikhard, V., Coddington, I., Engels, P., Mogendorff, V. P. & Cornell, E. A. Rapidly rotating Bose–Einstein condensates in and near the lowest Landau level. *Phys. Rev. Lett.* **92**, 040404 (2004).
38. Bretin, V., Stock, S., Seurin, Y. & Dalibard, J. Fast rotation of a Bose–Einstein condensate. *Phys. Rev. Lett.* **92**, 050403 (2004).
39. Abrikosov, A. A. On the magnetic properties of superconductors of the second group. *Sov. Phys. JETP* **5**, 1174–1182 (1957).
40. Kane, C. L., Mukhopadhyay, R. & Lubensky, T. C. Fractional quantum Hall effect in an array of quantum wires. *Phys. Rev. Lett.* **88**, 036401 (2002).
41. Goldman, V. J., Su, B. & Jain, J. K. Detection of composite fermions by magnetic focusing. *Phys. Rev. Lett.* **72**, 2065–2068 (1994).
42. Zeng, T.-S., Wang, C. & Zhai, H. Charge pumping of interacting fermion atoms in the synthetic dimension. *Phys. Rev. Lett.* **115**, 095302 (2015).
43. Taddia, L. et al. Topological fractional pumping with alkaline-earth-like atoms in synthetic lattices. *Phys. Rev. Lett.* **118**, 230402 (2017).

Publisher's note Springer Nature remains neutral with regard to jurisdictional claims in published maps and institutional affiliations.

© The Author(s), under exclusive licence to Springer Nature Limited 2020

Methods

Details on the experimental protocol. Our experiments began by preparing an ultracold gas of $8(2)\times10^4$ ^{162}Dy atoms at a temperature $T=0.55(6)\,\mu$K, which was then held in an almost symmetrical optical dipole trap with frequency $\bar{\omega}=2\pi\times150\,$Hz, leading to a peak density of $n_0\approx10^{13}\,$cm^{-3}. The atoms were placed in a magnetic field $B=172(2)\,$mG along the z axis, corresponding to a Zeeman splitting of frequency $\omega_Z=2\pi\times298(3)\,$kHz, with the electronic spin polarized in the absolute ground state $m=-J$. We then turned off the trap and turned on the two laser beams shown in Fig. 1, which differed in frequency by $\omega_{12}=\omega_1-\omega_2$. When ω_{12} was close to the Zeeman splitting ω_Z, a spin transition $m\rightarrow m+1$ occurred via the absorption of one photon from beam 1 and the stimulated emission of one photon in beam 2. In such processes and in the absence of additional external forces, the canonical momentum $\hat{p}=M\hat{v}+\hbar K\hat{J}_z$ is conserved.

The laser beam frequencies were set close to the optical transition at 626.1 nm, which couples the electronic ground state $J=8$ to an excited level $J'=9$. The beams were detuned by $\Delta=2\pi\times22\,$GHz with respect to resonance and were linearly polarized along orthogonal directions, each being at 45° with respect to the z axis. The algebra of the Clebsch–Gordan coefficients of $J\rightarrow J'=J+1$ transitions led to Hamiltonian (2) at resonance ($\omega_{12}=\omega_Z$), with

$$\Omega=\frac{2J+3}{4(J+1)(2J+1)}V_0,\quad V_0=\frac{3\pi c^2\Gamma}{2\omega_0^3}\frac{\sqrt{I_1I_2}}{\Delta}$$

where $I_{1,2}$ are the laser intensities on the atoms, $\Gamma\simeq2\pi\times135\,$kHz is the transition linewidth and ω_0 is its resonant frequency. The value of the coupling Ω was calibrated using an independent method and remained constant over the experimental sequence because the waists of both laser beams were much larger than the region of atomic motion. The Larmor frequency ω_Z was calibrated from the resonance of the Raman transition between $m=-8$ and $m=-7$.

The non-resonant case ($\omega_{12}\neq\omega_Z$) can be reduced to the resonant case in a reference frame moving at a velocity $v_{\mathrm{frame}}=(\omega_Z-\omega_{12})/K$. Note that the required change of frame means that fluctuations of ω_Z contribute to the uncertainties of the measured velocities. We first slowly increased the intensity up to a coupling $\hbar\Omega=1.02(6)E_{\mathrm{rec}}$, where $E_{\mathrm{rec}}\equiv p_{\mathrm{rec}}^2/(2M)$, and then applied an external force F_x on the system via the inertial force resulting from a time-dependent frequency difference, with $F_x=(M/K)\partial_t\omega_{12}$. The preparation of a state in the lowest band with a given momentum p was performed by adiabatically ramping the frequency difference to a final value

$$\omega_{12}=\omega_Z+2\left(\frac{p}{p_{\mathrm{rec}}}+J\right)\frac{E_{\mathrm{rec}}}{\hbar}\qquad(4)$$

We used the relation (4) to define, from the final frequency difference ω_{12}, the quasi-momentum p parametrizing the experimental data. We used a constant ramp rate $\partial_t\omega_{12}\simeq0.22\ \omega_{\mathrm{c,min}}^2$, where $\omega_{\mathrm{c,min}}\simeq3.06\ E_{\mathrm{rec}}/\hbar$ is the minimum cyclotron frequency separating the two lowest energy bands for $\Omega=E_{\mathrm{rec}}/\hbar$. Depending on the target p state, the preparation took between 150 µs and 550 µs. Shot-to-shot fluctuations of the ambient magnetic field induce fluctuations of the Zeeman frequency splitting, hence an error in the value of the prepared momentum p. As shown in Extended Data Fig. 1, the measured error in momentum remains small compared to the recoil momentum p_{rec}, and its root mean square (r.m.s.) deviation $\Delta p\simeq0.06p_{\mathrm{rec}}$ is compatible with the magnetic field fluctuations $\sigma_B=0.7\,$mG measured independently.

We numerically checked the adiabaticity of the state preparation protocol. While preparing $m=+J$, which requires crossing all momentum states, the squared overlap with the ground band remains greater than 0.96 and the deviation of the mean spin projection $\langle\hat{J}_z\rangle$ from the corresponding ground state value is always less than 0.08. The largest deviations occur near $m\simeq\pm7$, where the energy gap to the first excited band is the smallest. This behaviour is consistent with our measurements, showing that the adiabatic transfer to $m=J$ after exploring the entire band is above 97%.

At the end of the experiment, we probed the velocity and spin projection distributions. For this, we abruptly switched off the Raman lasers and subsequently ramped up an inhomogeneous magnetic field that split the different magnetic sublevels along z. After a 4-ms expansion, we took a resonant absorption picture. The measured atom density was split along z according to the magnetic projection m, and the density along x corresponds to the distribution of velocity v ($\omega t_{\mathrm{tof}}\approx4$). Our imaging set-up was such that the 17 magnetic sublevels had different cross-sections. We calibrated the relative cross-sections such that the calculated atom number remained constant for all momentum states, irrespective of their spin composition.

Cyclotron orbits. To probe the excitations of the system we performed a velocity quench, which couples the lowest Landau level to the next higher energy band. The system then responds periodically with a frequency set by the energy difference between the two bands, which for the case of an ideal Hall system would correspond to the cyclotron frequency ω_c. Experimentally, we performed the velocity kick by quenching the detuning ω_{12}, which in practice settles to a steady value after 4 µs. We show in Extended Data Fig. 2a,b an example of coherent oscillations of both magnetization and velocity. We computed the response of the system in real space, x, via a numerical integration of the velocity evolution as shown in Extended Data Fig. 2c. The uncertainty on the Larmor frequency leads to a systematic error on the velocity on the order of $0.1v_{\mathrm{rec}}$, consistent with the small drift of some cyclotron orbits in the bulk.

The response of the system was probed after a velocity kick $v_{\mathrm{kick}}\approx v_{\mathrm{rec}}$. This kick ensures a negligible overlap with the second excited band (smaller than 4%). Although, in an ideal Hall system, all bulk excitations evolve periodically at the cyclotron frequency $\omega_c=qB/M$ due to the harmonic spacing of successive Landau levels, this is not exactly the case in our system. We tested this behaviour by varying the strength of the excitation, which relates to the magnitude of the velocity kick. As shown in Extended Data Fig. 2d, we find that the trajectories cease to be closed and start to drift along the kick direction as the excitation strength exceeds $1.5v_{\mathrm{rec}}$ (Extended Data Fig. 2f). This regime corresponds to the onset of a significant population of higher energy bands $n\geq2$, which illustrates the non-harmonic spectrum of our system.

It is important to note that the excitation protocol described so far is inefficient for large values of p, where the energy gap is much larger. In that regime, a quench of the coupling amplitude Ω leads to a more efficient overlap with higher energy bands. This is shown in Extended Data Fig. 2e, for the case of a sudden branching of the coupling strength to $\hbar\Omega=E_{\mathrm{rec}}$. The system initially at $p=-Jp_{\mathrm{rec}}$ is then effectively coupled to higher energy bands and the bouncing on the hard wall characteristic of classical skipping orbits is clearly visible.

Transverse drift in a Hall system. Our system is analogous to a Hall system in a ribbon geometry (see Supplementary Information for a discussion in the case of a disk geometry). To understand the role of a sharp edge on the physical quantities measured in the main text, we consider an electronic Hall system in a semi-infinite geometry, described by the Landau Hamiltonian (3), written as

$$\hat{H}=\frac{\hat{p}_y^2}{2M}+\frac{1}{2}M\omega_c^2(\hat{y}-\hat{p}_x\ell^2/\hbar)^2$$

with a hard-wall restricting motion to the half-plane $y>0$. Here, we introduce the cyclotron frequency $\omega_c=eB/M$ and the magnetic length $\ell=\sqrt{\hbar/eB}$, assuming a magnetic field B along z.

We first consider semiclassical trajectories in the absence of external forces, which are either closed cyclotron orbits or skipping orbits bouncing on the edge, parametrized by the rebound angle θ (Extended Data Fig. 3a). Applying a perturbative force F along y leads to a drift of cyclotron orbits of velocity $v_d=-F/eB$ along x, corresponding to a Hall mobility $\mu=1/eB$. For skipping orbits, the Hall drift can be expressed analytically as

$$\mu=\frac{1}{eB}\left[1-\left(\frac{\sin\theta}{\theta}\right)^2\right]\qquad(5)$$

The factor of reduction compared to cyclotron orbits, plotted in Extended Data Fig. 3a, smoothly interpolates between 1 for almost closed orbits ($\theta\rightarrow\pi$) and 0 for almost straight orbits ($\theta\rightarrow0$). This behaviour provides a simple explanation of the reduced Hall mobility of edge modes (Fig. 4b).

We extend this reasoning to the quantum dynamics in the lowest energy band. In a semi-infinite geometry, the eigenstates of Hamiltonian (5) can be indexed by the momentum p along x, and are expressed as[44]

$$\begin{aligned}\psi_p(x,y)&=\tfrac{e^{ipx/\hbar}}{\sqrt{2\pi\hbar}}\phi_p(y)\\ \phi_p(y)&\propto D_{\epsilon(p)-1/2}\left[\sqrt{2}(y-p\ell^2/\hbar)/\ell\right]\end{aligned}\qquad(6)$$

where $D_\epsilon(z)$ is the parabolic cylinder function and $\epsilon(p)=E_0(p)/\hbar\omega_c$ is the reduced energy determined by the boundary condition $D_{\epsilon(p)-1/2}(-\sqrt{2}p\ell/\hbar)=0$ (Extended Data Fig. 3b). By summing over all momentum states of the ground band, we compute the local density of state in (v_x, y) coordinates plotted in Extended Data Fig. 3d. Far from the edge $y\gg\ell$, the velocity distribution is a Gaussian centred on $v_x=0$, of r.m.s. width $\delta v_x=\hbar/(M\ell)$. The distribution is shifted to negative velocities when approaching the edge $y=0$, as expected for chiral edge modes.

We now consider the Hall response of the system by studying the perturbative action of a force F along y, described by the Hamiltonian

$$\begin{aligned}\hat{H}'_p&=\tfrac{\hat{p}_y^2}{2M}+\tfrac{1}{2}M\omega_c^2(\hat{y}-p\ell^2/\hbar)^2-F\hat{y}\\&=\tfrac{\hat{p}_y^2}{2M}+\tfrac{1}{2}M\omega_c^2\left(\hat{y}-\tfrac{p\ell^2}{\hbar}-\tfrac{F}{M\omega_c^2}\right)^2+\mathcal{E}(p)\\ \mathcal{E}(p)&=-\tfrac{pF}{M\omega_c}-\tfrac{F^2}{2M\omega_c^2}\end{aligned}$$

We identify the perturbed Hamiltonian $\hat{H}'_p$ as $\hat{H}_{p+F/\omega_c}$, with an additional energy shift $\mathcal{E}(p)$. Assuming the system to remain in the ground band, the group velocity of a localized wavepacket becomes

$$\langle\hat{v}\rangle'=v_0(p+F/\omega_c)-\frac{F}{M\omega_c},\quad v_0(p)=\frac{\mathrm{d}E_0(p)}{\mathrm{d}p}$$

Assuming a small force, we expand the velocity as $\langle\hat{v}\rangle' = v_0(p) - \mu(p)F$, with the mobility

$$\mu(p) = \frac{1}{eB}\left(1 - M\frac{\mathrm{d}v_0}{\mathrm{d}p}\right)$$

This formula is analogous to the expression for the Hall mobility in our synthetic system. As shown in Extended Data Fig. 3c, it is close to the classical Hall drift in an infinite plane in the bulk mode region $p \gtrsim \hbar/\ell$, while it decreases towards zero in the edge mode region $p < 0$.

The overall response of an energy branch in the ground band can be obtained by summing the drifts of all populated eigenstates, such that the centre of mass drift reads

$$\langle v(t)\rangle' = \langle v(t)\rangle_0 - F\int \mathrm{d}p\; n(p)\mu(p)$$

where we assume the normalization $\int \mathrm{d}p\; n(p) = 1$ for the occupation number $n(p)$. We consider a uniform occupation of the lowest energy band, restricted to the energy branch $E_0(p) < \hbar\omega_c$, that is, in the middle of the bulk gap to the first excited band in the bulk. This condition corresponds to momentum states $p > p^\star \simeq 0.54\hbar/\ell$ of the ground band. Assuming an upper momentum cutoff p' in the bulk region, we obtain the Hall drift

$$\langle v(t)\rangle' = \langle v(t)\rangle_0 - \frac{F}{eB}\left(1 - M\frac{v_0(p') - v_0(p^*)}{p' - p^*}\right)$$

As long as $p' \gg \hbar/\ell$, the second term can be neglected, and one recovers the Hall drift of a topological band of Chern number $\mathcal{C} = 1$.

We finally consider the local Hall response in the ground band, quantified by the local Chern marker[22]

$$C(x,y) = 2\pi\mathrm{Im}\langle x,y|[\hat{P}\hat{x}\hat{P}, \hat{P}\hat{y}\hat{P}]|x,y\rangle$$

where $\hat{P}$ projects on the considered branch of states and $|x,y\rangle$ are localized in (x, y). The calculation of the Chern marker starts by decomposing position states into momentum states, as

$$C(x,y) = \frac{2}{\hbar}\;\mathrm{Im}\left[\int \mathrm{d}p\;\mathrm{d}q\; e^{i(p-q)x/\hbar}\phi_p(y)\phi_q^*(y)\tilde{c}(p,q)\right]$$

where $\tilde{c}(p,q) \equiv \langle\psi_p|\hat{x}\hat{P}\hat{y}|\psi_q\rangle$, which can be evaluated using the explicit form of equation (6) for momentum states as

$$\tilde{c}(p,q) = i\hbar\;\langle y\rangle_q\langle\phi_p|\phi_q\rangle\delta'(p-q)$$

where $\langle y\rangle_q$ is the mean y position in the wavefunction ϕ_q. Using the general formula

$$\int \mathrm{d}u\;\mathrm{d}v\, f(u,v)\delta'(u-v) = \int \mathrm{d}u\;\mathrm{d}v\frac{\partial_v f(u,v) - \partial_u f(u,v)}{2}\delta(u-v)$$

we obtain the expression for the Chern marker

$$C(x,y) = \int \mathrm{d}p\;|\phi_p(y)|^2\frac{\mathrm{d}\langle y\rangle_p}{\mathrm{d}p}$$

The relation $p = Mv_0 + qB\langle y\rangle_p$ then leads to

$$C(x,y) = \int \mathrm{d}p\;|\phi_p(y)|^2\mu(p) \qquad (7)$$

a relation analogous to the local Chern marker expression for our synthetic Hall system. We show in Extended Data Fig. 3e the Chern marker calculated for an energy branch $E(p) < \hbar\omega$, which is close to 1 for $y \gtrsim \ell$, and decreases towards zero when approaching the edge $y = 0$, similarly to the decrease of the Chern marker close to the edges shown in Fig. 4c.

Local Chern marker in synthetic dimension. In the synthetic Hall system, the expression of the local Chern marker reads

$$C(x,m) = 2\pi\mathrm{Im}\langle x,m|[\hat{P}\hat{x}\hat{P}, \hat{P}\hat{J}_z\hat{P}]|x,m\rangle \qquad (8)$$

Translation invariance along x ensures that the Chern marker only depends on the coordinate m. In the main text, the notation $|m\rangle$ refers to an arbitrary $|x,m\rangle$ state, the choice of x being irrelevant. The derivation of the Chern marker $C(m) = \int \mathrm{d}p\; \Pi_m(p)\mu(p)$ is obtained following the same procedure as for a standard Hall system, discussed above. So far, we have only considered one component μ_{xm} of the mobility tensor—the one that measures the drift along x resulting from a force along m. One can also consider the other component, which quantifies the magnetization drift $\mathrm{d}\langle\hat{J}_z\rangle/\mathrm{d}t$ that results from a force F_x along x. In a linear response, it is defined as $\langle\hat{J}_z\rangle = \langle\hat{J}_z\rangle_0 - \mu_{mx}(p)F_x t$, where μ_{mx} explicitly designates the mobility component considered here, and $\langle\hat{J}_z\rangle_0$ is the unperturbed magnetization. Its expression is given by

$$\mu_{mx} = -\frac{\mathrm{d}}{\mathrm{d}F_x}\frac{\mathrm{d}\langle\hat{J}_z\rangle}{\mathrm{d}t} = -\frac{\mathrm{d}\langle\hat{J}_z\rangle(p)}{\mathrm{d}p}$$

where we used $F_x = \dot{p}$ and the fact that $\langle\hat{J}_z\rangle_0$ is time-independent. The expression $\hat{p} = M\hat{v} + p_{\mathrm{rec}}\hat{J}_z$ allows us to recover the relation $\mu_{mx} = -\mu_{xm}$ between the two transverse mobilities.

We show in Extended Data Fig. 4b,c the measurements of both mobilities as a function of p, and find good agreement between them. We also present in Extended Data Fig. 4d the local Chern markers computed using the data of each mobility.

In the main text, the Chern marker is evaluated over a branch of the ground band, below an energy threshold shown in Extended Data Fig. 4a (at half the cyclotron gap at $p = 0$). We also show the Chern marker computed using all momentum states (grey points). Compared to the restricted branch, we only find a discrepancy on the edges of the ribbon. In the region $-5 \leq m \leq 5$, the values are nearly identical, showing that the bulk topological response is insensitive to the momentum cutoff.

We also evaluate theoretically the effect of disorder on the Chern marker. For this, we consider a finite-sized system of length $L = 5\lambda/2$, with periodic boundary conditions along x, and discretized on a grid $(x_n = n\delta x, m)$ of spacing $\delta x = \lambda/40$. The atom dynamics is described by Hamiltonian (2) with an additional disorder potential, taken as a random energy at each site (x_n, m) drawn according to a normal distribution of r.m.s. Δ. We calculate the energy spectrum and the local Chern marker using the equation (8), where $\hat{P}$ projects on the eigenstates of energy $E < E^\star$, where $E^\star = \hbar\omega_c$ is the middle of the bulk gap. We show in Extended Data Fig. 5a an example of Chern marker distribution in the region $|x_n| < \lambda/2$ for a disorder strength $\Delta = E_{\mathrm{rec}}$. We define a coarse-grained average at the centre of the synthetic dimension as

$$\bar{C}(m=0) = \langle C(x_n, m=0)\rangle_{|x_n|\,<\,\lambda/4}$$

We show in Extended Data Fig. 5b the variation of $\bar{C}(m=0)$ with the disorder strength Δ, averaged over 100 disorder realizations for each value of Δ. We find that the central Chern marker is almost unchanged for disorder strengths $\Delta \lesssim 2E_{\mathrm{rec}}$, demonstrating the robustness of the Chern marker in the bulk of the sample.

Abrikosov vortex lattices. The role of interactions in the ground band is assumed to be governed by a single parameter g, which describes contact interactions in both the real and synthetic dimensions (see Supplementary Information). We consider a gas of bosonic atoms with high filling fractions, for which the many-body ground state is well captured by mean-field theory. The system is described by a spinor classical field $(\psi_m(x))$ (with $-J \leq m \leq J$), whose dynamics is governed by the Gross–Pitaevskii equation

$$i\hbar\dot{\psi}_m = \tfrac{\hbar^2}{2M}(i\partial_x + Km)^2\psi_m - \hbar\Omega\left(\tfrac{\sqrt{J(J+1) - m(m+1)}}{2}\psi_{m-1} + \tfrac{\sqrt{J(J+1) - m(m-1)}}{2}\psi_{m+1} + \tfrac{m^2}{2J+3}\psi_m\right) + g|\psi_m|^2\psi_m$$

From the phenomenology of Abrikosov vortex lattices, we expect the ground state to break translational invariance along the real dimension, with an unknown periodicity L_0. To find L_0, we numerically calculate the ground state on a cylinder of circumference L, corresponding to periodic boundary conditions along the real dimension, by evolving the Gross–Pitaevskii equation in imaginary time. We find that the ground-state energy is minimized for a set of circumferences L, integer multiples of a length that we identify as L_0.

The thermodynamic properties are determined by the coupling Ω and the interaction energy scale $g\langle n\rangle$, where $\langle n\rangle$ is the mean atom density, or equivalently by the chemical potential μ_{chem}. Here we explore situations in which the chemical potential lies in the gap between the lowest Landau level and the first excited band (Extended Data Fig. 6b).

For large enough interactions, we always find ground-state configurations in the shape of Abrikosov triangular vortex lattices, such as the ones presented in the main text (Fig. 5). We give in Extended Data Fig. 6a,b another example of such a ground state, represented here by both the density profile and the phase associated to the wavefunction. Around each local minimum of the density, the phase profile is reminiscent of the phase winding of a quantum vortex in a continuous 2D system.

The hard walls in the synthetic dimension have a strong impact on the vortex lattice geometry. We distinguish the different configurations by counting the number of vortex lines along x. For example, in Extended Data Fig. 6a we identify a configuration made of three vortex lines. The phase diagram, shown in Extended Data Fig. 6c, shows a large variety of vortex configurations. Typically, the distance between lines is set by the magnetic length ℓ_{m} in the synthetic dimension. The reduction of the number of vortex lines with Ω is thus explained by the increase of ℓ_{m}. Similarly to type-II superconductors in a confined geometry, the different vortex configurations are separated by first-order transition lines.

The observation of such vortex lattices demands a high-resolution in situ imaging resolved in m space. However, the spontaneous breaking of translational symmetry can be revealed in the momentum distribution—accessible in standard

time-of-flight experiments—via the occurrence of Bragg diffraction peaks at multiples of the momentum $p_0 = h/L_0$. As shown in Extended Data Fig. 6d, the expected variation of p_0 with the coupling Ω indirectly reveals the occurrence of phase transitions between different vortex configurations.

Data availability

Source data, as well as other datasets generated and analysed during the current study, are available from the corresponding author upon request. Source data are provided with this paper.

Code availability

The source code for the numerical simulations of the Abrikosov vortex lattices and the Laughlin states are available from the corresponding author upon request. Source data are provided with this paper.

References

44. De Bièvre, S. & Pulé, J. V. Propagating edge states for a magnetic Hamiltonian. *Math. Phys. Electron. J* **2002**, 39–55 (2002).

Acknowledgements

We thank J. Beugnon, N. Cooper, P. Delpace, N. Goldman, L. Mazza and H. Price for stimulating discussions. We acknowledge funding from the EU under ERC projects 'UQUAM' and 'TOPODY', and PSL research university under the project 'MAFAG'.

Author contributions

All authors contributed to the set-up of the experiment, data acquisition, data analysis and the writing of the manuscript.

Competing interests

The authors declare no competing interests.

Additional information

Supplementary information is available for this paper at https://doi.org/10.1038/s41567-020-0942-5.

Correspondence and requests for materials should be addressed to S.N.

Reprints and permissions information is available at www.nature.com/reprints.

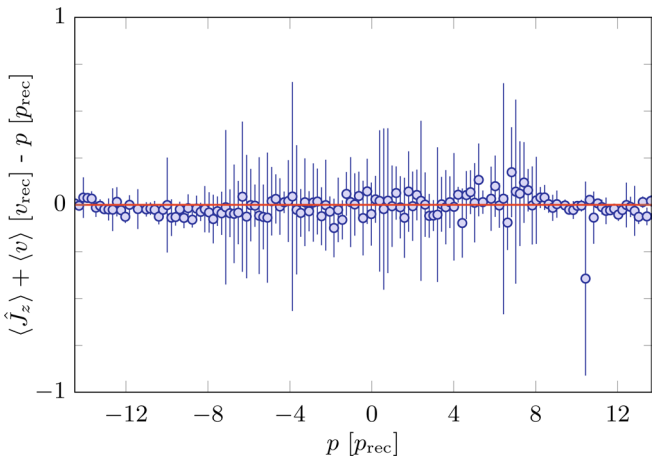

Extended Data Fig. 1 | Conservation of canonical momentum. Difference between the measured canonical momentum $p_{\mathrm{rec}}\langle \hat{J}_z \rangle + M\langle \hat{v} \rangle$ and the targeted value p defined by the state preparation protocol. All error bars are the 1-σ standard deviation of typically 5 measurement repetitions.

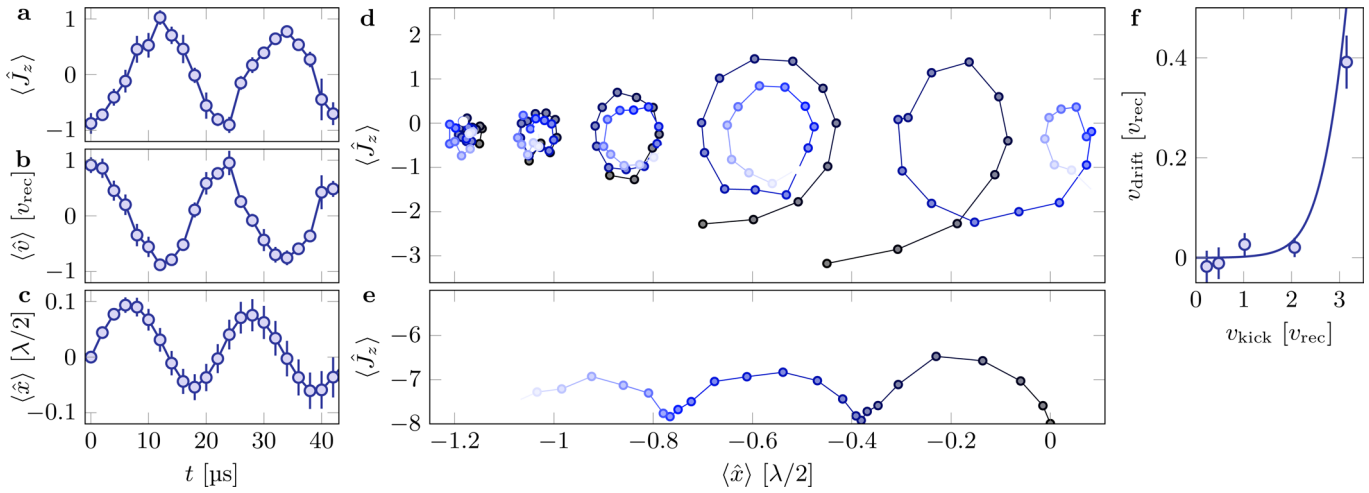

Extended Data Fig. 2 | Cyclotron orbits measurements. a, **b**, **c**, Magnetization, velocity and position response as a function of time after application of a velocity kick $v_{\mathrm{kick}} \approx v_{\mathrm{rec}}$. **d**, Bulk excitations corresponding to different velocity kicks, $v = 0.23$, 0.48, 1.02, 2.06, and 3.15 v_{rec}, from left to right. The orbits are off-centred in real space for visual clarity. **e**, Skipping orbit for the momentum state $p = -J\,p_{\mathrm{rec}}$ following a sudden jump of the coupling strength Ω. **f**, Velocity drift of the orbits as a function of the amplitude kick. The solid line corresponds to the expected drift due to the non-harmonic spectrum of the energy bands. All error bars are the 1-σ standard deviation of typically 5 measurement repetitions.

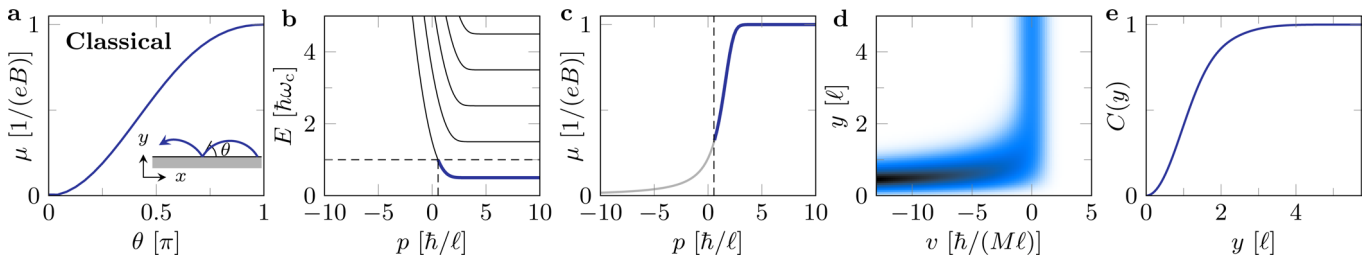

Extended Data Fig. 3 | Hall system in real dimensions. a, Variation of the Hall mobility for classical skipping orbits, depending on the angle of rebound on a hard wall. The case of closed cyclotron orbits corresponds to $\theta = \pi$. **b**, Dispersion relation of a quantum Hall system in a semi-infinite geometry $y > 0$. The blue line indicates the energy branch used for the Chern marker calculation, defined by $E_0(p) < \hbar\omega_c$. **c**, Hall mobility μ as a function of momentum p. **d**, Local density of state in the (v, y) plane. **e**, Local Chern marker $C(y)$ for the energy branch defined in **b**.

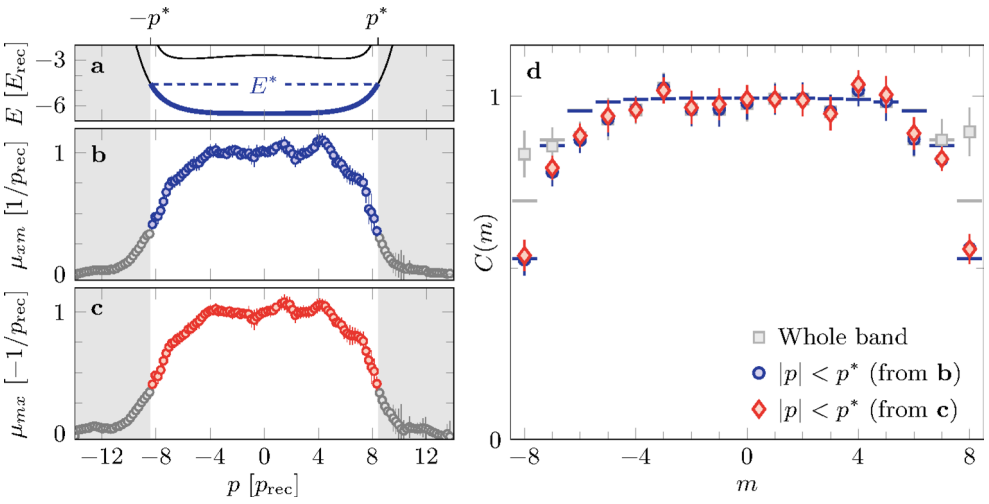

Extended Data Fig. 4 | Hall mobility and local Chern markers. a, Predicted dispersion relation for $\hbar\Omega = E_{\rm rec}$. The branch pictured in blue, chosen as $E(p) < E^*$ with E^* at half the gap, is used for the computation of the local Chern marker. **b**, Measured mobility in x resulting from the application of a force along m, as presented in the main text. The points in blue, corresponding to $|p| < p^*$ (white area), are the ones considered for the Chern marker presented in the main text (see Fig. 4). **c**, Measured mobility in m resulting from the application of a force along x. As for **b**, the points in red are associated to momentum states lying below E^*. **d**, Chern marker obtained from the measured mobility, using the whole energy branch ($-\infty < p < \infty$, gray squares, using data in **b**), or using the branch defined in **a** ($-p^* < p < p^*$). For the latter, the blue dots correspond to the data in **b**, and are identical to Fig. 4. The red diamonds correspond to the data in **c**. Solid lines are theoretical values. The error bars are the 1-σ statistical uncertainty calculated from a bootstrap sampling analysis over typically 100 pictures (**b**,**c**) and 1000 pictures (**d**).

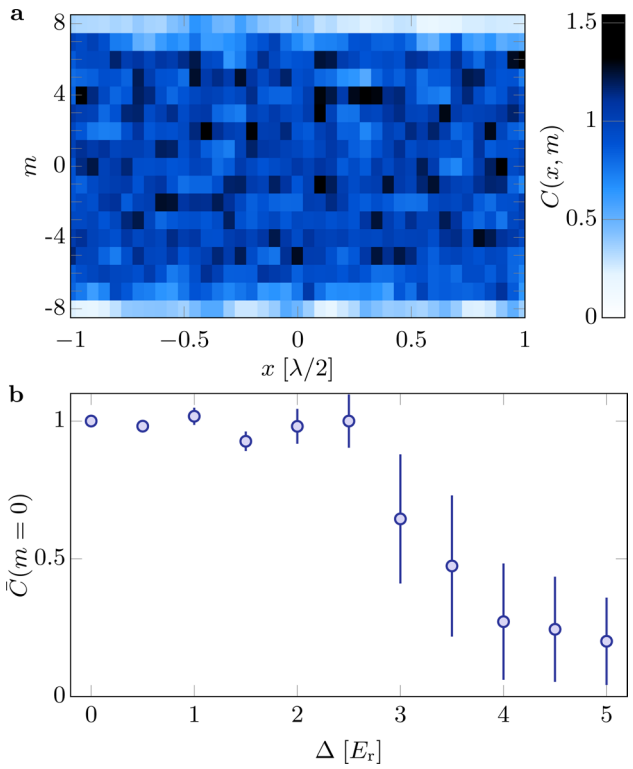

Extended Data Fig. 5 | Effect of disorder. a, Example of Chern marker distribution in the presence of disorder of strength $\Delta = E_{\mathrm{rec}}$. **b**, Chern marker $\bar{C}(m = 0)$ averaged over the region $|x| < \lambda/4$ as a function of the disorder strength Δ. Each point is the average of 100 disorder realizations, the error bar showing the standard deviation of the mean.

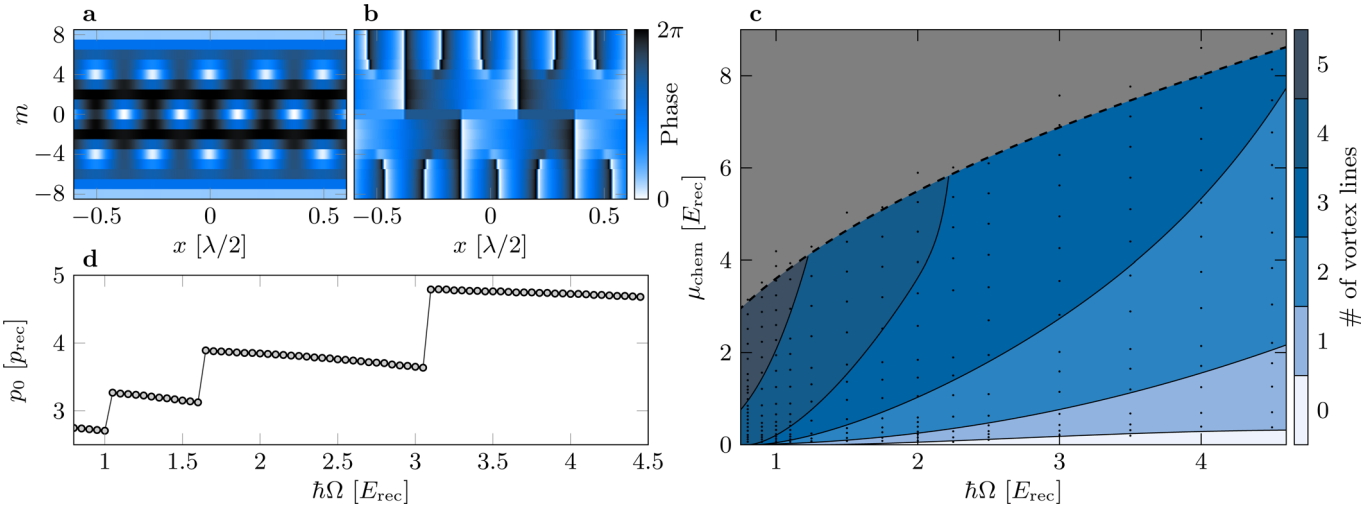

Extended Data Fig. 6 | Abrikosov vortex lattices. a, Ground state density profile and **b**, associated phase, for $\hbar\Omega = 3E_{\rm rec}$ and for $\mu_{\rm chem} \approx 4E_{\rm rec}$. The local minima of the density exhibit a phase winding around them, and thus correspond to quantum vortices. **c**, Number of vortex lines as a function of the Raman coupling Ω and the chemical potential $\mu_{\rm chem}$. The dots identify the configurations for which a simulation was realized. The color encodes the number of vortex lines that characterizes the low-energy vortex lattice configuration. The phase separation lines are guides to the eye. The dashed line identifies the gap to the first excited band above which the atoms significantly occupy higher Landau levels. **d**, Momentum p_0 associated to the spontaneous breaking of the translational invariance resulting from the appearance of a vortex lattice, as a function of Ω. The points were taken at a chemical potential corresponding to half the gap.

Supplementary information
Probing chiral edge dynamics and bulk topology of a synthetic Hall system

Thomas Chalopin,* Tanish Satoor,* Alexandre Evrard, Vasiliy Makhalov,† Jean Dalibard, Raphael Lopes, and Sylvain Nascimbene‡
Laboratoire Kastler Brossel, Collège de France, CNRS, ENS-PSL University, Sorbonne Université, 11 Place Marcelin Berthelot, 75005 Paris, France
(Dated: May 15, 2020)

I. ATOM LIFETIME IN THE GROUND BAND

As explained in the main text (Methods), we experimentally find that we can adiabatically prepare the ground state for any value of p, which suggests the absence of significant inelastic processes leading to higher band population. We confirmed such an observation by measuring the atom lifetime, following a preparation in the states $p = 0$ and $p = 12\hbar K$. Experimentally, this amounts to measuring the remaining number of atoms after a holding time, in the presence of the Raman coupling at $\hbar\Omega = E_{\rm rec}$ (see Fig. S1).

We measure a lifetime of approximately 4 ms, for $p = 0$, which cannot be simply attributed to incoherent Rayleigh scattering processes associated to the Raman coupling. Indeed, we estimate numerically the spontaneous emission rate to be, at most, on the order of $15\,\mathrm{s}^{-1}$, corresponding to a timescale larger than ~ 60 ms, an order of magnitude larger than the one reported in Fig. S1. However, we notice that the lifetime is significantly larger for $p = 12\hbar K$, which suggests the presence of dipolar relaxation [1]. We find numerically that the typical loss rate associated to the dipolar relaxation, for a density of $10^{13}\,\mathrm{cm}^{-3}$, varies between $\sim 70\,\mathrm{s}^{-1}$ and $\sim 230\,\mathrm{s}^{-1}$ (depending on the spin state), which is consistent with our measurements. This loss mechanism could be inhibited in a modified protocol, in which the Hamiltonian (2) (main text) is realized in the absence of external magnetic field, which requires a different laser configuration.

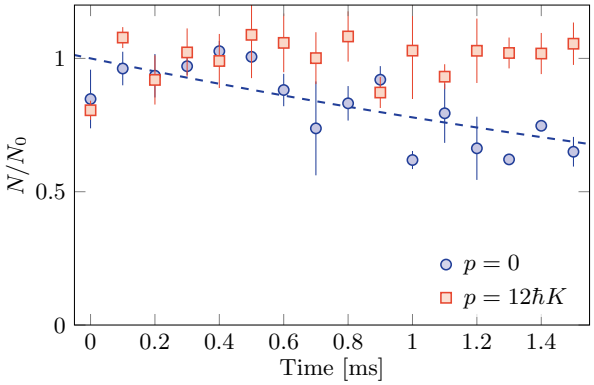

Fig. S1. Lifetime in the ground band. Remaining atom number N for a state prepared at $p = 0$ (blue) and $p = 12\hbar K$ (red), in the presence of the Raman coupling at $\hbar\Omega = E_{\rm rec}$. The atom numbers are normalized by N_0, the value at the origin of the fit (dashed line) which indicates a 1/e time constant of 4 ms. The error bars are the 1-σ standard deviation of typically 5 measurement repetitions.

II. EMERGENCE OF LANDAU LEVELS

In Fig. S2, we show the dispersion relation of the Hamiltonian (2) (see main text) calculated for different couplings Ω. In the absence of the light coupling, $\Omega = 0$, the Hamiltonian reduces to the kinetic energy term $(\hat{p} - p_{\rm rec}\hat{J}_z)^2/(2M)$, leading to $2J+1$ parabolas shifted along p. All energy crossings become avoided for $\Omega \neq 0$, leading to flattened energy bands akin to Landau levels. Achieving a flat ground band dispersion in the bulk region requires couplings that are large enough ($\hbar\Omega \gtrsim 0.2\,E_{\rm rec}$) to reduce short-$p$ oscillations, while still being sufficiently small ($\hbar\Omega \lesssim E_{\rm rec}$) to minimize longer-scale curvature.

The large spin $J = 8$ allows for a simplified semi-classical description, where the spin is represented by a point on the generalized Bloch sphere, parametrized by its spherical angles (θ, ϕ). The spin projection is mapped on a continuous variable $m = J\cos\theta$, with the azimuthal angle ϕ being its conjugated variable (up to a factor $\hbar$). The semi-classical Hamiltonian corresponding to the quantum Hamiltonian (2) (see main text) then reads

$$\mathcal{H}_p = \frac{(p-\hbar K m)^2}{2M} - \hbar\Omega\left(\sqrt{J^2-m^2}\cos\phi + \frac{m^2}{2J+3}\right).$$

This energy functional being minimized for $\phi = 0$, one can assume $\phi \ll 1$ and obtain a low-energy expansion

$$\mathcal{H}_p = \frac{(p-\hbar K m)^2}{2M} + \frac{\hbar^2\phi^2}{2M'(m)} + V(m),$$
$$M'(m) = \hbar/\left(\Omega\sqrt{J^2-m^2}\right),$$
$$V(m) = -\hbar\Omega\left(\sqrt{J^2-m^2} + \frac{m^2}{2J+3}\right),$$

which is exactly the Landau Hamiltonian (3) (see main text), albeit with a position-dependent mass $M'(m)$ and a confining potential $V(m)$ in the synthetic dimension.

* These two authors contributed equally.
† Present address: ICFO-The Institute of Photonic Sciences, 08860 Castelldefels (Barcelona), Spain
‡ sylvain.nascimbene@lkb.ens.fr

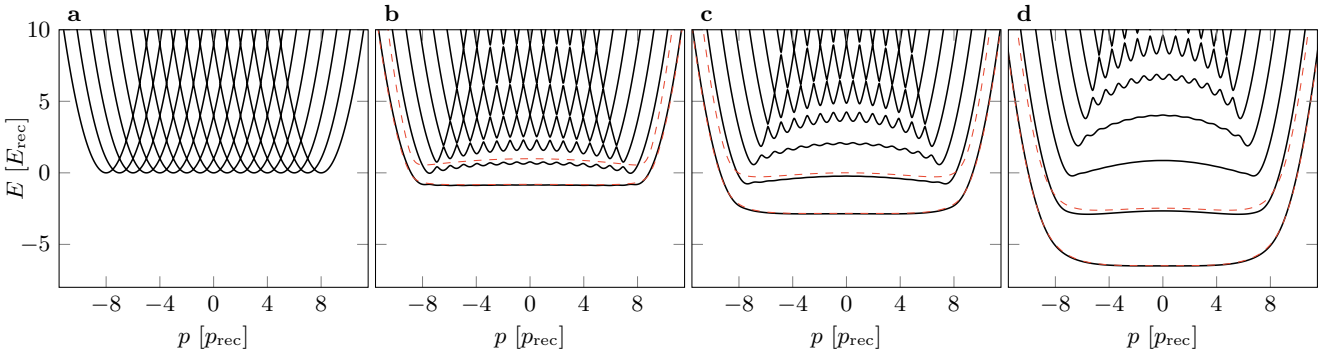

Fig. S2. **Emergence of synthetic Landau levels. a-d.** Dispersion relations for coupling strengths $\hbar\Omega/E_{\rm rec} = 0, 0.2, 0.5$ and 1 (solid lines). The dashed red lines correspond to the first two energy bands of a semi-classical theory, including first-order quantum corrections.

The divergence of the mass $M'(m)$ for $|m| \to J$ leads to an effective hard-wall condition.

In the middle of the bulk, at $m = 0$, in the semi-classical model, we deduce the cyclotron frequency $\omega_c = \sqrt{2J\Omega E_{\rm rec}/\hbar}$, and we expect a value $\omega_c = 4E_{\rm rec}/\hbar$ for $\hbar\Omega = E_{\rm rec}$, which is close to the exact value $\omega_c = 3.84E_{\rm rec}/\hbar$ (see inset of Fig. 3, see main text). We also infer the expressions for magnetic lengths

$$\ell_m = \sqrt[4]{\frac{J\hbar\Omega}{2E_{\rm rec}}} \quad \text{and} \quad \ell_x = \frac{1}{K\ell_m}$$

in the synthetic and real dimensions respectively. These lengths are the characteristic sizes of the quantum vortices shown in Fig. 5b (see main text). For the coupling $\hbar\Omega = E_{\rm rec}$ used in the simulations, we obtain magnetic lengths $\ell_m \simeq 1.41$ and $\ell_x \simeq 0.11\lambda/2$.

The approximate analogy between the Hamiltonians (2) and (3) (see main text) can also be inferred using quantum operators, as we explain now assuming $p \simeq 0$ for simplicity. In that case, we expect the system to be polarized in $m = J$ along x, such that the commutator

$$[\hat{J}_z, \hat{J}_y] = -\mathrm{i}\hat{J}_x \simeq -\mathrm{i}J$$

is a c-number. The operator $-\hat{J}_y/J$ is then canonically conjugated to the spin projection $\hat{J}_z$. We then use the Holstein-Primakoff approximation at second order to express the spin projection $\hat{J}_x$ as

$$\hat{J}_x = J + \frac{1}{2} - \frac{\hat{J}_y^2 + \hat{J}_z^2}{2J},$$

leading to the Hamiltonian

$$\hat{H} = \frac{(p - p_{\rm rec}\hat{J}_z)^2}{2M} + \frac{\hbar\Omega}{2J}\hat{J}_y^2 + \frac{3\hbar\Omega}{2J(2J+3)}\hat{J}_z^2 - \hbar\Omega\left(J + \frac{1}{2}\right).$$

This Hamiltonian corresponds to the Landau Hamiltonian (3) (see main text), with an additional $\hat{J}_z^2$ term. This approximation can be generalized to all values of momentum p. We show in Fig. S2 the first two energy bands calculated within this approximation, together with the exact spectrum.

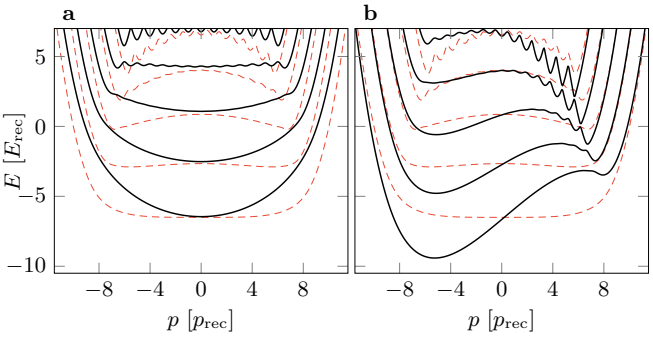

Fig. S3. **Ground band flatness. a.** Dispersion relation after addition of a harmonic confining potential proportional to J_z^2 (solid lines), which cancels $V(\hat{J}_z)$ of Eq. (2) (see main text). **b.** Dispersion relation in case of using Raman laser beams in a σ-π configuration (solid lines). In both panels, the red dashed lines correspond to the dispersion relation of the Hamiltonian (2) (see main text).

III. GROUND BAND FLATNESS AND SYMMETRY

The flatness of the ground band and the uniformity of the cyclotron frequency in our system arise from the partial cancellation of the dispersive effects from the kinetic term $-\hbar\Omega\hat{J}_x$ and the light shift term $V(\hat{J}_z) = -\hbar\Omega\hat{J}_z^2/(2J+3)$ in the Hamiltonian (2) (see main text). To illustrate this, we show the effect of removing the term $V(\hat{J}_z)$ from the Hamiltonian in Fig. S3a – clearly resulting in a highly dispersive lowest band. This is equivalent to an additional harmonic confining potential along the synthetic dimension, which is achievable in practice using an additional laser beam linearly polarized along z, and far-detuned from both Raman beams.

Furthermore, the symmetry of the ground band about $p = 0$ depends on the polarization of the two coupling lasers. The Raman transition scheme we use (Fig. 1a, see main text) could also be achieved using a polarization $u_1 = y = (\hat{\sigma}_+ - \hat{\sigma}_-)/\sqrt{2}\mathrm{i}$ for laser 1 and $u_2 = z = \hat{\pi}$

for laser 2. However, this σ-π configuration results in a highly asymmetric dispersion relation, as shown in Fig. S3b. In our experimental scheme, we recover symmetric bands by allowing equal contributions from σ-π and π-σ arrangements, which corresponds to having orthogonal linear polarizations at 45° to the z-axis. Imperfections in the orientation of the polarizations could explain the slight asymmetries we measure in velocity and the Hall mobility.

IV. CHERN MARKER IN A HALL DISK

We extend the discussion of the main text (Methods) to the transverse response properties of a Hall system confined in a finite area, taking the example of a disk geometry. Writing the vector potential in the symmetric gauge, the Schrödinger equation reads

$$\mathrm{i}\partial_t\psi = \frac{\hbar^2}{2M}\left[-\frac{1}{r}\partial_r(r\partial_r) + \left(\frac{-\mathrm{i}\partial_\theta}{r} - \frac{r}{2\ell^2}\right)^2\right]\psi$$

in polar coordinates. Its eigenstate wavefunctions $\psi_{n,m}(r,\theta) = \phi_{n,m}(r)\mathrm{e}^{\mathrm{i}m\theta}$, indexed by an integer $n \in \mathbb{N}$ and the angular momentum projection $m \in \mathbb{Z}$, are solutions of the radial equation

$$E_{n,m}\phi_{n,m} = \frac{\hbar^2}{2M}\left[-\frac{1}{r}\partial_r(r\partial_r) + \left(\frac{m}{r} - \frac{r}{2\ell^2}\right)^2\right]\phi_{n,m}.$$

For $R \to \infty$, the states for a given n are degenerate and form the n^{th} Landau level. The wavefunction $\phi_{n,m}(r)$ takes significant values around the radius $r \simeq \sqrt{2m}\ell$. For a finite disk of radius R, we thus expect the states $\phi_{n,m}$ to remain almost degenerate for $m \lesssim (R/\ell)^2/2$. We show in Fig. S4a the energy spectrum for a disk of radius $R = 10\,\ell$, consistent with this expectation.

We now consider the transverse response of a system in which the states of energy $E_{n,m} < \hbar\omega_\mathrm{c}$ (i.e. with $n = 0$ and $m \leq m^*$) are uniformly occupied (see Fig. S4a). The local Chern marker can be expressed in terms of the radial wavefunctions as

$$C(\mathrm{r}) = C_0(r) + C_1(r),$$
$$C_0(r) = \sum_{m\leq m^*} \mu_m |\phi_{0,m}(r)|^2,$$
$$C_1(r) = \frac{|\phi_{0,m^*}(r)|^2 + |\phi_{0,m^*+1}(r)|^2}{4} |\langle\phi_{0,m^*}|\hat{r}|\phi_{0,m^*+1}\rangle|^2,$$

where we introduce

$$\mu_m = \frac{1}{2}(|\langle\phi_{0,m}|\hat{r}|\phi_{0,m+1}\rangle|^2 - |\langle\phi_{0,m}|\hat{r}|\phi_{0,m-1}\rangle|^2).$$

The first term $C_0(r)$ is the sum of contributions from all occupied orbitals, analogously to the equation (7) (Methods) obtained in the half-plane geometry. It remains close to one in the bulk, and decreases to zero close to the edge $r = R$ over a length scale ℓ. The term $C_1(r)$ remains negligible in the bulk, and takes negative values of order $R/\ell \gg 1$ close to the edge. One checks that the spatial averages of the two terms are opposite, such that

$$\int \mathrm{d}^2 r\, C(r) = 0,$$

as required for the Chern marker on a finite geometry [2]. Such a zero average does not occur in the experimental system, since the atom dynamics is not confined in the real dimension x.

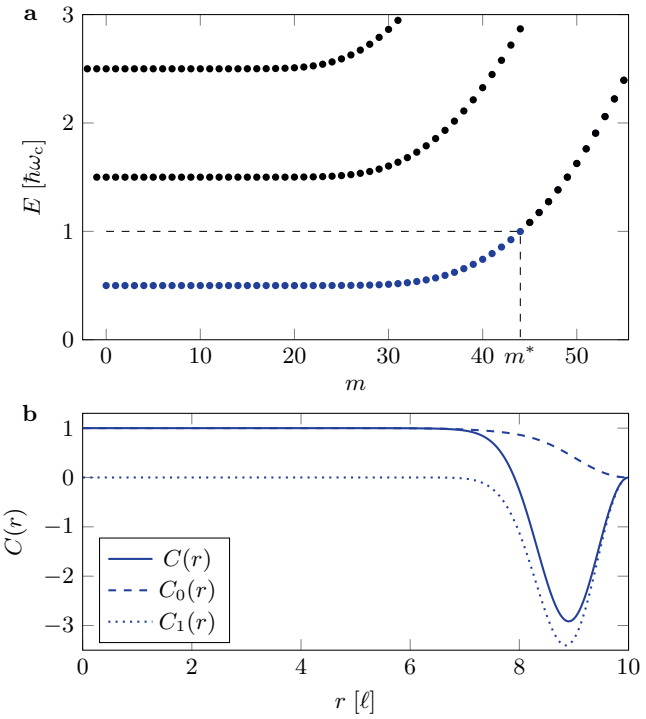

Fig. S4. Spectrum and Chern marker in a Hall disk. **a.** Energy spectrum of a Hall disk of radius $R = 10\,\ell$, indexed by the angular momentum projection m. The blue dots correspond to the states of energy $E_{n,m} < \hbar\omega_\mathrm{c}$ considered for the Chern marker evaluation. **b.** Chern marker $C(r)$ in the same geometry, together with the two contributions $C_0(r)$ and $C_1(r)$.

V. INTERACTIONS IN THE LOWEST ENERGY BAND

Interactions are typically short-ranged in atomic gases. In our system, interactions are thus local in x, but they can occur between any pair of spin projections m_1, m_2, corresponding to highly long-range interactions along the synthetic dimension. To recover short-range interactions, we propose to spatially separate the different m states using a magnetic field gradient oriented along another direction z. The resulting system is thus constituted of $2J + 1 = 17$ one-dimensional tubes, offset in position along z. For a transverse confinement of frequency

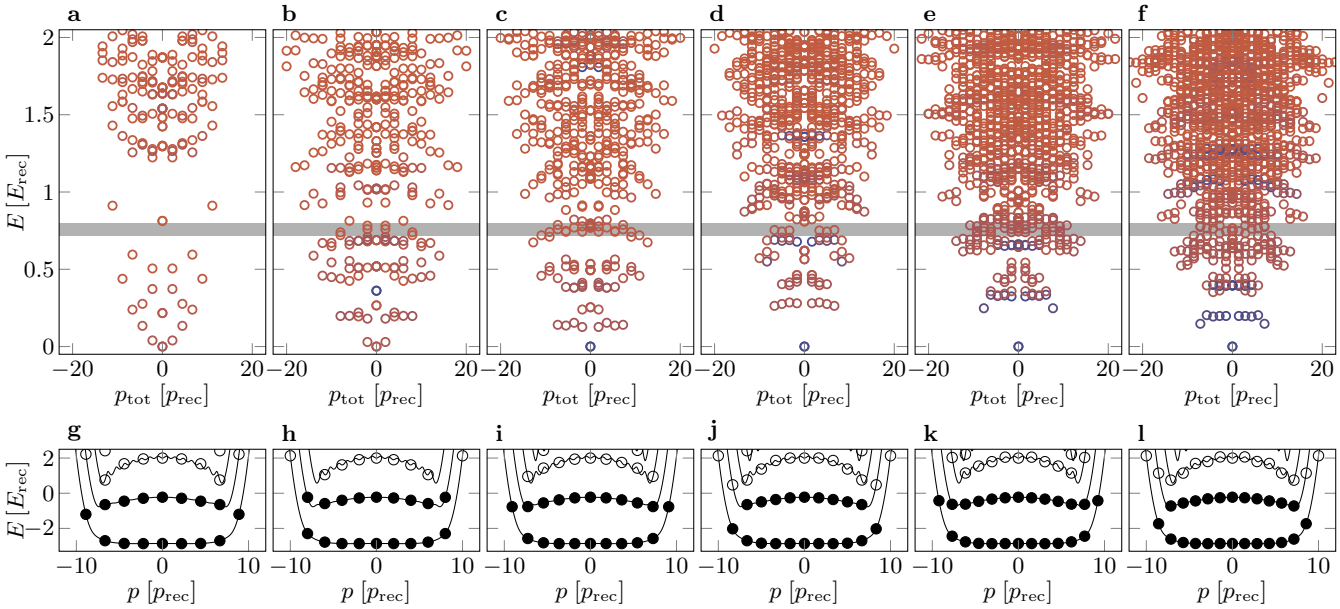

Fig. S5. Laughlin-like states at low filling. a-f. Many-body energy spectra calculated for $N_{\rm at} = 5$ atoms on cylinders, of circumferences $L = 0.45, 0.5, 0.55, 0.6, 0.65, 0.7\,\lambda/2$, respectively. We identify a Laughlin-like state with very small interaction energy and at zero momentum, separated in energy from other eigenstates for $L \geq 0.55\,\lambda/2$. For $L = 0.7\,\lambda/2$ we recognize an energy branch of edge excitations of the Laughlin state. The gray area marks the bulk gap of the Laughlin state $\Delta = 0.60(3)\,U$ expected in dispersionless Landau levels and in the thermodynamic limit [3]. The color scale is identical to the one used in Fig. 5c. **g-l.** Single-particle states included in the simulations are shown as solid dots.

$\omega_z = 2\pi \times 1\,$kHz, corresponding to a ground-state extent $\Delta z = \sqrt{\hbar/M\omega_z} \simeq 250\,$nm, the interactions become short-ranged for moderate magnetic field gradients $\nabla B \gtrsim 30\,$G/cm. For such gradients, the distance between subsequent tubes is $\gtrsim 320\,$nm, such that the spatial overlap of neighbouring wavefunctions is negligible, thus making contact interactions only possible between atoms within the same tube. At such spatial separations, the long-range dipole-dipole interactions (DDI) furthermore remains limited to a few tens of Hz ($h = 1$), which is also much weaker than the contact interaction within each tube.

The interaction between atoms in a given m state is then described by a short-range potential $g_m\delta(x_1 - x_2)$ with coupling constant g_m, proportional to the s-wave scattering length a_m. At low magnetic field, rotational symmetry ensures that $a_m = a_{-m}$, such that interactions are described by $J + 1$ independent scattering lengths. While the a_m constants are uniform between all nuclear spin levels for two-electron atoms, we do not expect such a SU(N) symmetry for lanthanide atoms such as dysprosium, for which only the coupling constant $a_8 = 140(20)\,a_0$ has been measured [4]. All the other a_m constants remain unknown and we plan to investigate them in the future. Nonetheless, if all values a_m are positive, the system will be protected from collapse, making many-body phases experimentally accessible.

In lanthanide atoms, interactions between magnetic dipoles enrich the situation discussed above. These interactions offer an additional degree of freedom that could be used to stabilize the system in case of attractive s-wave interaction channels.

For simplicity, we neglect dipolar interactions in the numerical simulations presented in the main text (Methods) and consider that all scattering lengths are equal and positive, such that the interaction potential reads $g\,\delta(x_1 - x_2)\delta_{m_1,m_2}$. For such contact interactions, one expects interactions restricted to the lowest Landau level to reduce to a single Haldane pseudo-potential [5, 6]

$$U = \frac{g}{4\pi}\frac{1}{\ell_x \ell_m} = \frac{gK}{4\pi}.$$

VI. LAUGHLIN-LIKE STATE AT LOW FILLING

We consider in this section bosonic atoms at low filling fractions, for which one expects strongly-correlated ground states. We calculate the many-body spectrum of this system using exact diagonalization. The stability of Laughlin-like quantum states is based on limited energy dispersion in the ground band, which is improved by considering a coupling $\hbar\Omega = 0.5\,E_{\rm rec}$, i.e. half of the value used in the experiment. We use a cylindrical geometry to avoid edge effects along x, and restrict the basis of single-particle levels to an energy $E = 3\,E_{\rm rec}$ above the single-particle ground state, which includes bulk states of the ground and first excited bands, with a few edge modes depending on the circumference L of the cylinder

(see Fig. S5g-l). We calculate the energy spectrum of $N_{\rm at}$ bosonic atoms interacting at short range, with an interaction strength $U = E_{\rm rec}$. The many-body eigenstates are indexed by the total momentum $p_{\rm tot}$, a conserved quantity that permits us to subdivide the Hilbert space into independent sectors, limiting the involved matrices to dimensions less than 4000.

We show in Fig. S5a-f six energy spectra calculated for cylinder circumferences in the range $L = 0.45 - 0.7\,\lambda/2$. For $L = 0.45\,\lambda/2$, the ground state does not exhibit any of the characteristics of the Laughlin state: sizeable interaction energy $E_{\rm int} \simeq 0.03\,E_{\rm rec}$ and phonon-like low-energy excitations. This behavior stems from the limited number of single-particle orbitals at low energy $N_{\rm orb} = 7$, smaller than the number $N_{\rm orb} = 2N_{\rm at} - 1 = 9$ of distinct orbitals involved in the Laughlin wavefunction [7, 8]. For circumferences $L \geq 0.55\,\lambda/2$, we find a ground state with a very small interaction energy $E_{\rm int} \simeq 1.5 \times 10^{-4}\,E_{\rm rec}$, indicating anti-bunching between atoms, as expected for the Laughlin state. This state is separated from excited levels by an energy gap of maximum value $\simeq 0.27\,E_{\rm rec}$ (reached for $L = 0.63\,\lambda/2$), without featuring a low-energy phonon branch. For longer circumferences $L \geq \lambda/2$, the low-energy excitations also exhibit very small interaction energy, as expected for edge excitations of the Laughlin state occurring for a number of low-energy orbitals $N_{\rm orb} > 2N_{\rm at} - 1$ [9, 10].

[1] Burdick, N. Q., Baumann, K., Tang, Y., Lu, M. & Lev, B. L. Fermionic Suppression of Dipolar Relaxation. *Phys. Rev. Lett.* **114** (2015).

[2] Bianco, R. & Resta, R. Mapping topological order in coordinate space. *Phys. Rev. B* **84**, 241106 (2011).

[3] Regnault, N. & Jolicoeur, T. Quantum Hall Fractions in Rotating Bose-Einstein Condensates. *Phys. Rev. Lett.* **91**, 030402 (2003).

[4] Tang, Y., Sykes, A., Burdick, N. Q., Bohn, J. L. & Lev, B. L. s-wave scattering lengths of the strongly dipolar bosons Dy 162 and Dy 164. *Phys. Rev. A* **92** (2015).

[5] Haldane, F. D. M. Fractional Quantization of the Hall Effect: A Hierarchy of Incompressible Quantum Fluid States. *Phys. Rev. Lett.* **51**, 605–608 (1983).

[6] Cooper, N. R. Rapidly rotating atomic gases. *Adv. Phys.* **57**, 539–616 (2008).

[7] Laughlin, R. B. Anomalous Quantum Hall Effect: An Incompressible Quantum Fluid with Fractionally Charged Excitations. *Phys. Rev. Lett.* **50**, 1395–1398 (1983).

[8] Rezayi, E. H. & Haldane, F. D. M. Laughlin state on stretched and squeezed cylinders and edge excitations in the quantum Hall effect. *Phys. Rev. B* **50**, 17199–17207 (1994).

[9] Wen, X.-G. Theory of the edge states in fractional quantum hall effects. *Int. J. Mod. Phys. B* **06**, 1711–1762 (1992).

[10] Soulé, P. & Jolicoeur, T. Edge properties of principal fractional quantum Hall states in the cylinder geometry. *Phys. Rev. B* **86**, 115214 (2012).

A.2 SIMULATING TWO-DIMENSIONAL DYNAMICS WITHIN A LARGE-SIZE ATOMIC SPIN

The following pages contain the text of the article [331], which was briefly discussed in section 5.7.

Simulating two-dimensional dynamics within a large-size atomic spin
A. Fabre, J.-B. Bouhiron, T. Satoor, R. Lopes, S. Nascimbene
Physical Review A 105 (1), 013301 (2022)

Simulating two-dimensional dynamics within a large-size atomic spin

Aurélien Fabre, Jean-Baptiste Bouhiron, Tanish Satoor, Raphael Lopes, and Sylvain Nascimbene*
Laboratoire Kastler Brossel, Collège de France, CNRS, ENS-PSL University, Sorbonne Université, 11 Place Marcelin Berthelot, 75005 Paris, France

(Received 11 October 2021; accepted 9 December 2021; published 5 January 2022)

Encoding a dimension in the internal degree of freedom of an atom provides an interesting tool for quantum simulation, facilitating the realization of artificial gauge fields. We propose an extension of the synthetic dimension toolbox, making it possible to encode two dimensions within a large atomic spin. The protocol combines first- and second-order spin couplings such that the spin projection m and the remainder $r = m \pmod 3$ of its Euclidian division by 3 act as orthogonal coordinates on a synthetic cylinder. It is suited for an implementation with lanthanide atoms, which feature a large electronic spin and narrow optical transitions for applying the required spin couplings. This method is useful for simulating geometries with periodic boundary conditions and engineering various types of topological systems evolving in high dimensions.

DOI: 10.1103/PhysRevA.105.013301

Ultracold atomic gases provide a versatile playground for the study of various types quantum many-body physics. The simulation of artificial gauge fields enables the realization of systems exhibiting a nontrivial topological character [1,2]. A well-developed protocol for their implementation is based on light-induced couplings between the atom motion and its spin. This technique enables the realization of a synthetic dimension, fully encoded in the internal degree of freedom of the atom, namely, its electronic and/or nuclear spin [3]. The dynamics of atoms subjected to such a spin-orbit coupling can be described by an effective gauge field [4,5], which has been used to engineer two-dimensional quantum Hall systems, with one spatial dimension and another synthetic one [6,7]. Synthetic dimensions are also promising for the realization of high-dimensional systems that would feature a topological character with no equivalent in lower dimensions [8–10].

The most natural implementation of a synthetic dimension consists in considering the spin projection m of the atomic spin J (with $|m| \leqslant J$, m integer [11]) as the coordinate of an artificial dimension [6,7]. Motion along this dimension then occurs via spin transitions $m \to m'$, for example, induced by radio-frequency or two-photon optical transitions. The range $|m - m'|$ of spin transitions is then limited by selection rules to nearest ($|m - m'| = 1$) or next-nearest ($|m - m'| = 2$) neighbor hoppings. This constraint restricts the simulation of periodic boundary conditions to small-spin systems [12–14]. Indeed, a coupling between stretched states $m = \pm J$ requires a $2J$-photon optical transition, which is experimentally unrealistic for $J \gg 1$. In the absence of such coupling, the synthetic dimension features sharp edges [6,7], such that the bulk physics is limited to projection states m far enough from edges [15]. The concept of synthetic dimension was also generalized to atomic momentum states [16] and has also been developed in photonic systems [17]. Recently, a pair of synthetic dimensions was simulated in a temporally modulated ring resonator [18].

In this article we propose a protocol to simulate dynamics in two dimensions within the atomic spin only. It applies to atomic species possessing a large spin $J \gg 1$. We propose to combine spin couplings of ranks 1 and 2, such that the spin projection m and the remainder $r \equiv m \pmod 3$ of its Euclidian division by three evolve independently, thus acting as the two orthogonal coordinates describing the surface of a cylinder (see Fig. 1). We discuss the conditions of applicability of this description and the requirements for its practical implementation in cold atom experiments. We also describe its extension for the simulation of quantum Hall physics on a cylinder, with one spatial dimension x and another one encoded in the remainder r, which naturally features periodic boundary conditions (the coordinate m adding another degree of freedom, nonrelevant in this case since it is uncoupled to the x and r dynamics).

I. BASIC DESCRIPTION OF THE PROTOCOL

The protocol combines linear and quadratic spin couplings, described by the Hamiltonian

$$H = -U_a \frac{J_+}{J} - U_b \frac{J_-^2}{J(J-1/2)} + \text{H.c.} \tag{1}$$

The transitions between magnetic sublevels $|m\rangle$ induced by these couplings are shown in Fig. 1(a). They enable nontrivial cycles between triples of spin states $m \to m+1 \to m+2 \to m$, leading to the emergence of a cyclic synthetic coordinate, independent from the magnetic projection m, and encoded in the division remainder $r = m \pmod 3$.

The projection m and remainder r obviously do not evolve independently under the action of either the linear or quadratic spin couplings considered independently. Indeed, the linear coupling J_+ increases both m and r by one unit, while the quadratic one J_-^2 decreases m by 2 and increases r by one

*sylvain.nascimbene@lkb.ens.fr

 ©2022 American Physical Society

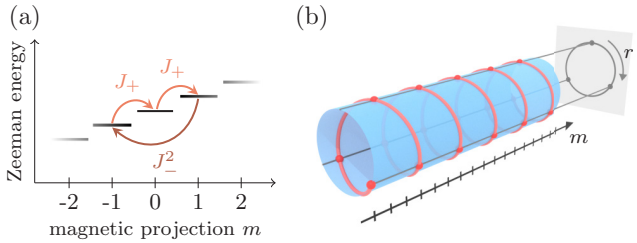

FIG. 1. (a) Scheme of the spin transitions between the projection states $|m\rangle$ of an angular momentum J. Combining first- and second-order couplings leads to nontrivial three cycles $m \to m+1 \to m+2 \to m$. (b) Scheme of the emergent synthetic cylinder for $J = 8$, where the projection m plays the role of the axial coordinate, and the remainder $r \equiv m \pmod 3$ of its Euclidian division by 3 acts as the azimuthal cyclic coordinate.

unit. The occurrence of decoupled m and r dynamics relies on the proper combination of both processes.

In order to understand the condition for independent dynamics, we first give a hand-waving argument—a more rigorous treatment being given in Sec. II. We treat m and r as continuous variables and approximate the action of the spin operators as

$$\frac{J_+ + J_-}{J}\psi(m,r) \simeq \psi(m+1,r+1) + \psi(m-1,r-1) \simeq \left(2 + \partial_m^2 + 2\partial_m\partial_r + \partial_r^2\right)\psi(m,r) \quad (2)$$

and

$$\frac{J_+^2 + J_-^2}{J\left(J-\frac{1}{2}\right)}\psi(m,r) \simeq \psi(m+2,r-1) + \psi(m-2,r+1) \simeq \left(2 + 4\partial_m^2 - 4\partial_m\partial_r + \partial_r^2\right)\psi(m,r) \quad (3)$$

at the first nontrivial order in m and r. The Hamiltonian then takes the expression

$$H = -2(U_a+U_b) - (U_a+4U_b)\partial_m^2 - (U_a+U_b)\partial_r^2 - 2(U_a-2U_b)\partial_m\partial_r. \quad (4)$$

The coupling between the m and r dynamics stems from the last term $\propto \partial_m\partial_r$, which cancels for the coupling ratio

$$U_b/U_a = 1/2. \quad (5)$$

Under this condition, the m and r dynamics become approximately separable, mimicking the motion of a particle on a cylindrical surface with an axial coordinate m and an azimuthal coordinate r [see Fig. 1(b)]. Unless explicitly specified, we assume in the following this condition to be fulfilled and define a single coupling amplitude $U \equiv U_a = 2\,U_b$.

II. SEMICLASSICAL ANALYSIS AND EMERGENCE OF A SYNTHETIC CYLINDER

A more precise understanding of the spin dynamics can be obtained by performing a semiclassical analysis, which is legitimate for a large spin size $J \gg 1$.

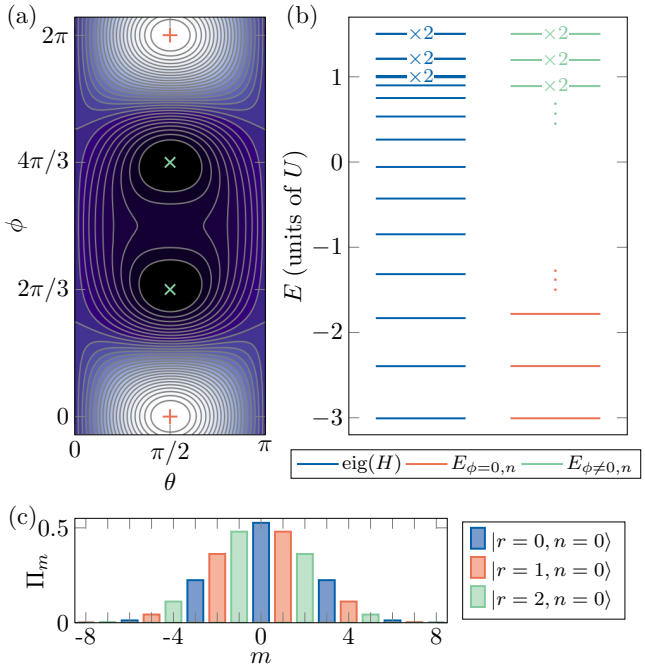

FIG. 2. (a) Semiclassical energy functional corresponding to the energy of a coherent spin state of spherical angles (θ, ϕ). The red plus sign indicates the energy minimum at $\theta = \pi/2$ and $\phi = 0$. The green crosses show the two degenerate maxima at $\phi = 2\pi/3$ and $4\pi/3$. (b) Energy-level spectra of the actual Hamiltonian (1) (dark blue lines) and of its harmonic approximation around the energy minimum (medium red lines) or maxima (light green lines) for a spin length $J = 8$. The label $\times 2$ indicates doubly degenerate levels. The degeneracy is not exact for the spectrum of H, and the label is shown when two levels are separated by less than the linewidth. (c) Spin projection probabilities Π_m for the states $|r, n\rangle$, with $n = 0$ and $r = 0, 1, 2$ (dark blue, medium red, and light green bars).

A. Semiclassical ground state

We first carry out a variational study of the ground state, restricted to the family of coherent spin states. A coherent spin state is defined as a maximally polarized state $|\theta, \phi\rangle$, parametrized by the orientation of its polarization, labeled by the spherical angles (θ, ϕ) [19]. The energy associated with a coherent state is described by the functional

$$E(\theta,\phi) \equiv \langle\theta,\phi|H|\theta,\phi\rangle = -2U\,\sin\theta\cos\phi - U\,\sin^2\theta\cos(2\phi), \quad (6)$$

shown in Fig. 2(a). It features a single minimum oriented along x, that is, $\theta = \pi/2, \phi = 0$.

B. Harmonic low-energy dynamics

In order to understand the low-energy dynamics, we expand the Hamiltonian around the semiclassical ground state, assuming that the spin states remain highly polarized along x. The z and y spin components then exhibit a commutator

$$[J_z, J_y] = -i\hbar J_x \simeq -i\hbar J, \quad (7)$$

such that J_z and $(-J_y/J)$ can be considered as canonically conjugated. Expanding the Hamiltonian in powers in these

operators, we obtain at the lowest nontrivial order a quadratic Hamiltonian

$$H \simeq U\left(-3-\frac{5}{2J}+\frac{4J_z^2+6J_y^2}{2J^2}\right).$$

It describes the dynamics of a harmonic oscillator of spectrum

$$E_{\phi=0,n} = E_0 + n\hbar\omega, \tag{8}$$

$$E_0 = [-3+(2\sqrt{6}-5)/(2J)]U, \tag{9}$$

$$\hbar\omega = (2\sqrt{6}/J)U, \tag{10}$$

where $n \geqslant 0$ is an integer and ω is the effective oscillator frequency. We discuss in Appendix A an alternative derivation, based on a Holstein-Primakoff transform of spin operators in terms of a bosonic degree of freedom [20].

C. Extension to high-energy states

The variational analysis can also be used to get the highest energy states. The energy functional $E(\theta,\phi)$ exhibits two degenerate maxima, at $\theta=\pi/2$ and $\phi = 2\pi/3$ or $4\pi/3$ [see Fig. 2(a)]. The dynamics around these maxima can also be approximated by a harmonic spectrum, which turns out to be linked to the spectrum calculated around the ground state $\phi = 0$, as $E_{\phi\neq 0,n} = -E_{\phi=0,n}/2$. Overall, the harmonic spectra calculated around the energy minimum ($\phi = 0$) or maxima ($\phi = 2\pi/3, 4\pi/3$) can be recast into a single expression:

$$E_{\phi,n} = (E_0 + n\hbar\omega)\cos\phi, \quad n\in\mathbb{N}, \quad \phi\in\left\{0,\frac{2\pi}{3},\frac{4\pi}{3}\right\}. \tag{11}$$

We show in Fig. 2(b) a comparison between the spectrum of the actual Hamiltonian (1) and the approximated spectrum (11), calculated for $J = 8$. The harmonic spectrum accounts well for the first levels above the ground state and the states below the highest energy levels. We checked that the number of levels well described by the harmonic spectrum increases when increasing the spin length J, as expected for a semiclassical analysis.

D. Interpretation as a cylindrical geometry

The spectrum (11) obtained from the semiclassical analysis is relevant to describe spin dynamics at low and high energies but does not apply in the intermediate-energy regime. Still, we consider here the effective spin dynamics restricted to the semiclassical spectrum and interpret it in terms of motion on a synthetic cylinder. This approach will become fully justified when coupling the spin to a spatial degree of freedom, such that the three coherent states indexed by ϕ occur at low energy on equal footings (see Sec. IV B).

The semiclassical spectrum (11), proportional to $\cos\phi$ with $\phi = 0, 2\pi/3, 4\pi/3$, is reminiscent of the dispersion relation $E(q) \sim -2t\cos(qa)$ of a particle evolving on a one-dimensional ring lattice of length L, where t is the tunnel coupling and a is the lattice constant. The quasimomentum q takes the discrete values $(2\pi j)/L$, with $0 \leqslant j < L/a$ an integer. By analogy, the three discrete angles ϕ involved in our problem play the role of the momenta conjugated to a cyclic dimension of length $L/a = 3$.

This motivates the definition of a basis of position states $|r,n\rangle$, where r is the coordinate of the synthetic dimension, by the inverse Fourier transform

$$|r,n\rangle = \frac{1}{\sqrt{3}}\sum_{\phi=0,\frac{2\pi}{3},\frac{4\pi}{3}} e^{-i\phi r}|\phi,n\rangle. \tag{12}$$

The spin projection probabilities Π_m of the states $|r,n\rangle$, shown in Fig. 2(c) for $n = 0$, only involve projections m such that $m \pmod 3 = r$, justifying the r notation. The spectrum (11), associated to an effective Hamiltonian diagonal in the $|\phi,n\rangle$ basis, can be recast in terms of the $|r,n\rangle$ states as

$$\begin{aligned} H_{\text{eff}} &= \sum_{n\geqslant 0}\sum_{\phi=0,\frac{2\pi}{3},\frac{4\pi}{3}} (E_0+n\hbar\omega)\cos\phi|\phi,n\rangle\langle\phi,n| \\ &= \sum_{n\geqslant 0}\sum_{r=0}^{2}\frac{E_0+n\hbar\omega}{2}|r+1,n\rangle\langle r,n| + \text{H.c.} \end{aligned} \tag{13}$$

We recognize the Hamiltonian of a particle on a cylinder, with free dynamics along the azimuthal direction r and harmonic trapping along the axis m.

III. LOW-ENERGY DYNAMICS

A. Excitation protocol

We illustrate the independent motion along the two directions m and r with simulations of spin dynamics. Starting in the ground state of the Hamiltonian (1), we apply a weak perturbation that induces a nonzero velocity either along m or along r. The velocity along m is defined as

$$v_m \equiv \frac{i}{\hbar}[H,J_z] \tag{14}$$

$$= U_a\frac{iJ_+}{J} + U_b\frac{-2iJ_-^2}{J(J-1/2)} + \text{H.c.} \tag{15}$$

The cyclic coordinate r, which can be viewed as an angular variable, cannot be expressed in terms of an Hermitian operator [21,22]. To obtain the expression of the velocity along r, we replace the prefactor -2 in front of the J_-^2 coupling by 1 to account for the different hopping values $\Delta m = -2$ and $\Delta r = 1$. Since the J_+ coupling induces identical hoppings $\Delta m = \Delta r = 1$, its prefactor remains the same for the two velocities. This leads to the expression [23]

$$v_r = U_a\frac{iJ_+}{J} + U_b\frac{iJ_-^2}{J(J-1/2)} + \text{H.c.} \tag{16}$$

The velocity kick along m is applied by evolving a Zeeman field along z,

$$V_{\text{pert}}^{(m)} = V_z J_z, \tag{17}$$

corresponding to a linear potential in m.

To induce a velocity along r, we need to couple the ground state $|\phi = 0, n = 0\rangle$ to the states $|\phi\neq 0, n = 0\rangle$. Since the states $|\phi, n = 0\rangle$ are coherent spin states spread along the equator with azimuthal angles $2\pi/3$, two states with different angles ϕ are very distant in phase space for $J \gg 1$ and thus cannot be coupled with low-order spin couplings. To excite the r velocity, we apply a time-dependent perturbation involving the high-order coupling $V_{\text{pert}}^{(r)}(t) = V_r\cos(2\pi J_z/3 - \alpha t)$.

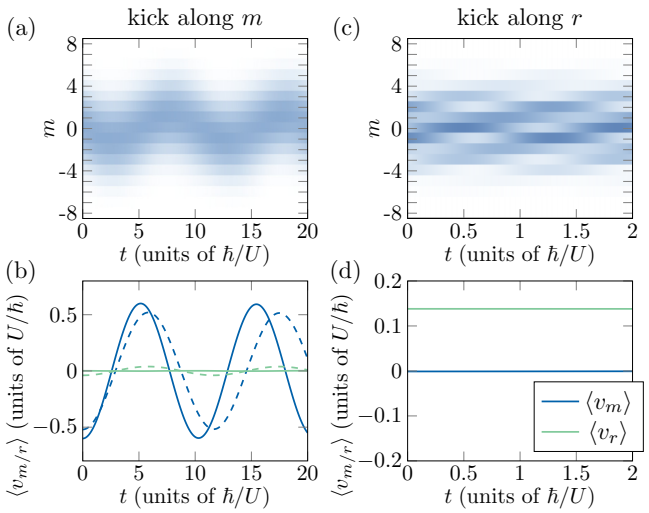

FIG. 3. Simulated spin dynamics following a velocity kick along m or r for $U_b/U_a = 0.5$ (left and right columns, respectively). (a, c) Evolution of the spin projection probabilities Π_m. (b, d) Evolution of the mean velocities $\langle v_m\rangle$ (dark blue lines) and $\langle v_r\rangle$ (light green lines) for the same evolutions. The dashed lines in (b) are calculated with $U_b/U_a = 0.4$.

This coupling, diagonal in the $|m\rangle$ projection state basis, is three-periodic in m, such that it takes a value depending on r only, as

$$V_{\text{pert}}^{(r)}(t) = V_r \cos(2\pi r/3 - \alpha t). \tag{18}$$

This potential corresponds to a perturbation in r moving at the speed $3\alpha/(2\pi)$, which drives the system to a nonzero velocity $\langle v_r\rangle \neq 0$.

B. Decoupling of m and r dynamics

We show in Fig. 3 the dynamics subsequent to the m and r velocity kicks for $U_b = U_a/2$. For a weak excitation along m, the projection probabilities Π_m and the mean velocity $\langle v_m\rangle$ oscillate consistently with harmonic trapping along m. The oscillation frequency matches the value of ω given in (10). In contrast, the mean velocity $\langle v_r\rangle$ remains close to zero.

An opposite behavior occurs for a weak excitation along r: the spin distribution Π_m becomes modulated in m with a period 3, and this modulation coherently evolves in time with a given chirality. The mean velocity $\langle v_r\rangle$ remains stationary at a nonzero value, consistently with the absence of trapping along r. The mean velocity $\langle v_m\rangle$ remains close to zero. These two evolutions are thus consistent with independent dynamics of the two coordinates m and r.

We present in Appendix B a study of the spin dynamics as a function of the strength of the excitation along m. When the oscillation amplitude along the m axis becomes comparable to the spin length J, the spin projection probabilities do not remain Gaussian and exhibit more complex dynamics. In this nonlinear regime, the r velocity does not vanish, showing that the m and r dynamics are no longer independent.

We also studied the effect of a departure from the relation $U_b/U_a = 0.5$ by repeating the simulation with $U_b/U_a = 0.4$ [dashed lines in Fig. 3(b)]. For an excitation along m, we obtain a nonzero oscillation of $\langle v_r\rangle$, which confirms that the m and r dynamics are rigorously decoupled under the condition $U_b/U_a = 0.5$ only, as found in Sec. I. Nevertheless, we expect that the interpretation of spin dynamics in terms of motion in two dimensions remains valid away from the condition $U_b/U_a = 0.5$, albeit with m and r not orthogonal.

IV. IMPLEMENTATION WITH COLD ATOMS

A. Implementation with lanthanide atoms

This proposal requires using an atomic species with an internal spin $J \gg 1$. Lanthanide atoms exhibit a large electronic spin in the ground state, namely, $J = 8$, $J = 6$, and $F = 4$ for dysprosium, erbium, and thulium—the species brought to quantum degeneracy so far [24–26]. The levels spectra shown in Fig. 2 and the low-energy dynamics shown in Fig. 3 were calculated for $J = 8$ and are thus relevant for a practical implementation with dysprosium atoms. Fermionic isotopes of erbium and dysprosium, which were also produced in the quantum degeneracy regime [27,28], feature a hyperfine structure with an even larger total spin length.

The spin couplings involved in the Hamiltonian (1) can be implemented using the ac-Stark shift produced by off-resonant lasers [29]. In general, second-order light shifts produce spin couplings described by tensors of rank 0, 1, and 2 [30]. For alkali or two-electron atoms, the electronic ground state is isotropic (s valence shell with an orbital angular momentum $L = 0$), prohibiting spin-dependent light shifts. Spin transitions can arise from higher-order processes involving the fine or hyperfine couplings, albeit with significant values only close to optical resonances [31]. Lanthanide atoms exhibit a more favorable electronic structure for the realization of spin-dependent light shifts, thanks to the anisotropic electronic orbitals in their electronic ground state. The interaction with light inherits a significant spin dependency from this anisotropy, even for light far detuned from resonances [32]. Furthermore, spin couplings can be further enhanced using light close to a single narrow optical transition [33].

In practice, the spin couplings can be produced using resonant optical transitions in the presence of a quantization magnetic field along z. Denoting ω_{L} the Larmor frequency, a two-photon process involving two light frequencies of difference $\Delta\omega$ will produce a first- (second-) order spin coupling for $\Delta\omega = \omega_{\text{L}}$ ($\Delta\omega = 2\omega_{\text{L}}$, respectively). An important asset of this protocol is its protection from magnetic field fluctuations. Indeed, the $|r, n\rangle$ basis states are not magnetized along z [see Fig. 2(c)], such that magnetic field perturbations cancel at first order.

B. Coupling to a spatial dimension: Example of a quantum Hall cylinder

When the spin couplings are induced by two-photon optical transitions from a single laser spatial mode, they are not coupled to the atom motion. The dynamics can be enriched when they involve light beams propagating along different directions, such that spin transitions occur together with a momentum kick exchanged with light. We present in this section an application of such a spin-orbit coupling, yielding dynamics mimicking a quantum Hall cylinder, with an additional

harmonic degree of freedom. This protocol has recently been implemented experimentally by our group [34]. Quantum Hall cylinders have also been recently realized by directly coupling a small number of spin levels [12–14].

We assume the spin couplings to be driven by two-photon optical transitions using a pair of laser beams counterpropagating along the spatial coordinate x. The couplings then inherit the complex phase factor e^{2ikx} from the laser beam interference, where k is the light momentum. The atom dynamics is governed by the Hamiltonian

$$H = \frac{p_x^2}{2M} + V, \tag{19}$$

$$V = -\left[U_a \frac{J_+}{J} + U_b \frac{J_-^2}{J(J-1/2)}\right] e^{-2ikx} + \text{H.c.}, \tag{20}$$

where p_x is the x momentum and M is the atom mass. The two processes increasing the remainder r thus acquire a common phase factor e^{-2ikx}, leading to a gauge field in the xr plane. On the contrary, the two processes increasing the projection m have opposite phase factors $e^{\pm 2ikx}$, with a zero mean effect for $U_a = 2\,U_b$. Under this condition that we assume in the following, we do not expect the occurrence of an effective magnetic field in the xm plane. Therefore we expect the system to behave as a quantum Hall cylinder in the two variables (x, r), with another degree of freedom m acting as the coordinate of an independent harmonic oscillator [from the term $n\hbar\omega$ in the spectrum (11)].

In order to reveal this behavior, we generalize the semiclassical treatment discussed above. For each position x, we calculate the semiclassical energy functional

$$\begin{aligned} V_{\text{cl}}(\theta, \phi, x) = &-2U \sin\theta \cos(\phi - 2kx) \\ &-U \sin^2\theta \cos(2\phi + 2kx), \end{aligned} \tag{21}$$

which always features three extrema for the same orientations, namely, $\theta = \pi/2$ and $\phi = 0$, $2\pi/3$, or $4\pi/3$. Expanding the spin operators around these three extrema, we obtain the harmonic spectra

$$V_{\phi,n}(x) = (E_0 + n\hbar\omega)\cos(\phi - 2kx), \tag{22}$$

which we compare to the x-dependent eigenstates of $V(x)$ in Fig. 4(a). We find an excellent agreement for $n = 0$ and 1, and observe a visible departure for $n = 2$, signaling the onset of anharmonic effects.

The energies $V_{\phi,n}(x)$ play the role of cosine lattice potentials, the angle ϕ defining the x position of the energy minima. Importantly, the three angles ϕ play a symmetric role, such that they are all involved in the effective low-energy dynamics—contrary to the purely spin dynamics studied in Sec. II.

The dynamics induced by the potentials $V_{\phi,n}(x)$ on the r coordinate is better visualized in the $|r, n\rangle$ position state basis, as

$$\begin{aligned} V_{\text{eff}} &= \sum_{n\geqslant 0} \sum_{\phi=0,\frac{2\pi}{3},\frac{4\pi}{3}} (E_0 + n\hbar\omega)\cos(\phi - 2kx)|\phi, n\rangle\langle\phi, n| \\ &= \sum_{n\geqslant 0} \sum_{r=0}^{2} \frac{E_0 + n\hbar\omega}{2} e^{-2ikx}|r+1, n\rangle\langle r, n| + \text{H.c.} \end{aligned} \tag{23}$$

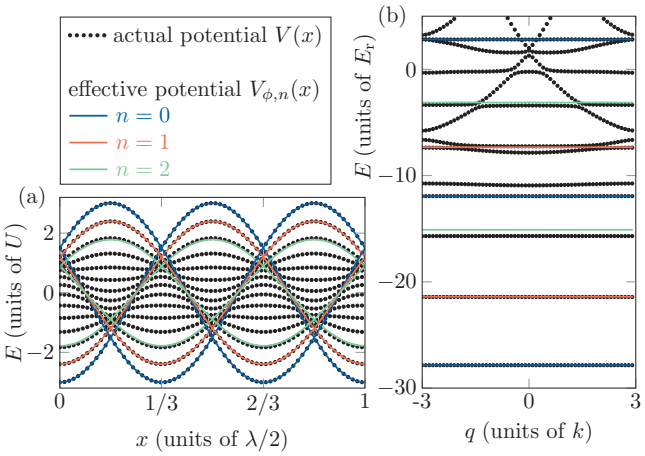

FIG. 4. (a) Energy spectrum of the coupling $V(x)$ as a function of x (black dots), compared with the effective potentials $V_{\phi,n}(x)$ with $n = 0, 1, 2$ (dark blue, medium red, and light green lines). (b) Band structures calculated using the actual potential $V(x)$ (black dots) and the effective ones $V_{\phi,n}(x)$, with $n = 0, 1, 2$ (dark blue, medium red, and light green lines).

This potential describes hopping dynamics along r, with an x-dependent complex phase that mimics the Aharonov-Bohm phase associated to a magnetic field in the xr plane. The full atom dynamics, described by the effective Hamiltonian $H_{\text{eff}} = p_x^2/2M + V_{\text{eff}}$, then maps to the motion of a charged particle on a Hall cylinder along x and r, with an additional harmonic degree of freedom n.

We validate this description by comparing the energy-level structure of the actual Hamiltonian (19) with the effective model (23). Both models are invariant upon the discrete magnetic translation

$$T_{\text{mag}} = T_{x,\lambda/6} R_{z,-2\pi/3}, \tag{24}$$

which combines a $\lambda/6$ translation along x and rotation of the spin around z of angle $-2\pi/3$. This symmetry leads to the conservation of the quasimomentum,

$$q \equiv \frac{M v_x}{\hbar} + 2kJ_z \ (\text{mod } 6k), \tag{25}$$

defined over the magnetic Brillouin zone $-3k \leqslant q < 3k$. The Hamiltonian spectra organize in magnetic Bloch bands, shown in Fig. 4(b) for a coupling strength $U = 12\,E_r$, where $E_r = \hbar^2k^2/(2M)$ is the single-photon recoil energy. The spectrum of the Hamiltonian (19) exhibits very flat lowest energy bands, well reproduced by the bands of the effective model for $n = 0, 1, 2$. This comparison confirms the relevance of the description of low-energy dynamics as that of a quantum Hall cylinder.

V. CONCLUSION

To conclude, we have shown that by combining first- and second-order spin couplings, one can simulate two-dimensional dynamics within a large-size atomic spin. One of the two coordinates consists in a three-site cyclic dimension. Extending our protocol to larger circumferences $L > 3$ requires implementing a coupling J_+^{L-1}, which cannot be

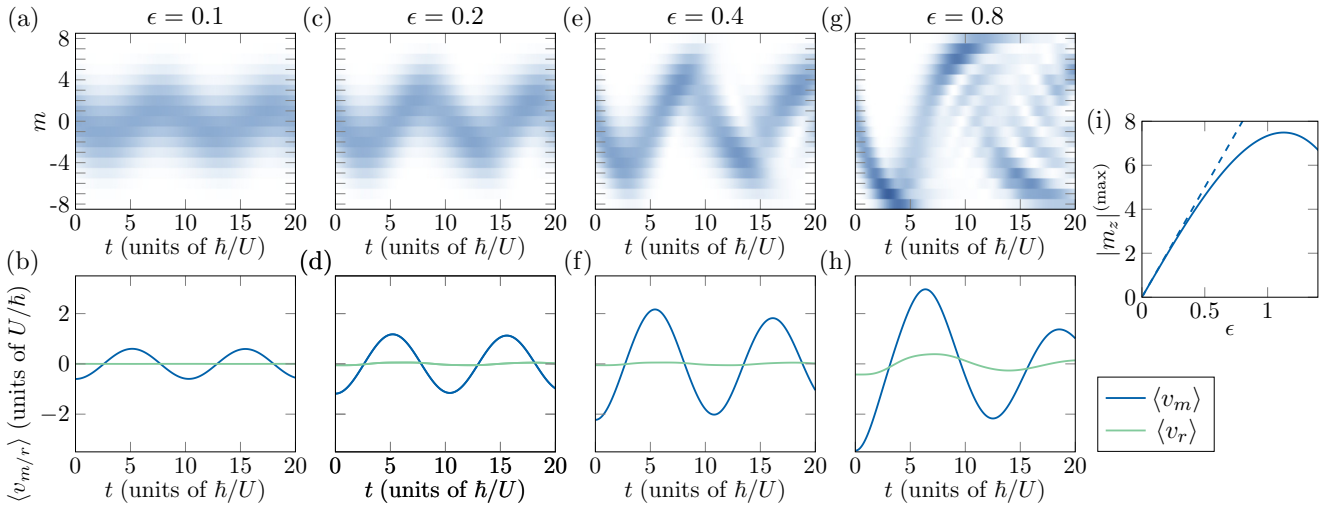

FIG. 5. (a, c, e, g) Evolution of the spin projection probabilities for various excitation strengths $\epsilon = 0.1, 0.2, 0.4, 0.8$. The corresponding evolutions of velocities $\langle v_m \rangle$ (dark blue lines) and $\langle v_r \rangle$ (light green lines) are shown in (b, d, f, h). (i) Evolution of the magnetization amplitude $|m_z|^{(\max)}$ as a function of ϵ. The dashed line is the linear response valid for small ϵ.

achieved with a two-photon process due to selection rules but could be realized using higher-order processes.

Our technique extends the synthetic dimension toolbox and could be applied to simulate various types of topological systems. We described the extension of the method to engineer a quantum Hall cylinder with an additional harmonic degree of freedom. The simulation of two-dimensional dynamics in a single spin will become even more useful for realizing other types of topological systems in higher dimensions $D > 3$, such as four-dimensional quantum Hall systems [9] or five-dimensional Weyl semimetals [10]. Our method could also be applied to other physical platforms making use of synthetic dimensions [5].

Synthetic dimensions appear as a versatile tool for engineering complex single-particle Hamiltonians with nontrivial topology. Such systems could serve as a ground to study interacting topological systems. Importantly, synthetic dimensions encoded in the spin degree of freedom naturally lead to infinitely ranged interactions, as long as the different spin states are allowed to be in contact. A control of the interaction range in such systems could be achieved by imposing a spatial separation between the different spin states or using suitable interaction time modulations close to Feshbach resonances [35].

ACKNOWLEDGMENTS

We thank Jean Dalibard for stimulating discussions and careful reading of the manuscript. This work is supported by European Union through Grant No. TOPODY 756722 from the European Research Council.

APPENDIX A: LOW-ENERGY DYNAMICS

We give an alternative derivation of the low-energy dynamics of the Hamiltonian (1). The ground state obtained from the semiclassical analysis is the coherent spin state polarized along x. We use a Holstein-Primakoff transform to express the spin operators in terms of a bosonic degree of freedom [20] as

$$J_x = J - a^\dagger a, \tag{A1}$$

$$J_z - iJ_y = \sqrt{2J - a^\dagger a}\, a, \tag{A2}$$

$$J_z + iJ_y = a^\dagger \sqrt{2J - a^\dagger a}, \tag{A3}$$

where a is a bosonic annihilation operator. To lowest order, the z spin component

$$J_z \simeq \sqrt{\frac{J}{2}}(a + a^\dagger) \tag{A4}$$

maps to the position operator of the harmonic oscillator associated with a. Expanding the Hamiltonian in power series in $1/J$, we obtain at first order

$$H/U \simeq -3 + \frac{10a^\dagger a - a^2 - a^{\dagger 2}}{2J}. \tag{A5}$$

This quadratic Hamiltonian can be diagonalized using a Bogoliubov transform by defining new bosonic operators

$$b = u\, a + v\, a^\dagger, \tag{A6}$$

$$b^\dagger = v^* a + u^* a^\dagger, \tag{A7}$$

with $u^2 - v^2 = 1$. For $u = [1/2 + 5/(4\sqrt{6})]^{1/2} \simeq 1.005$ and $v = -\sqrt{u^2 - 1} \simeq -0.102$, the Hamiltonian takes the canonical form

$$H = E_0 + \hbar\omega\, b^\dagger b, \tag{A8}$$

with

$$E_0 = \left(-3 + \frac{2\sqrt{6} - 5}{2J}\right)U, \tag{A9}$$

$$\hbar\omega = \frac{2\sqrt{6}}{J}U. \tag{A10}$$

This expansion can be reproduced around the semiclassical energy maxima, leading to the complete harmonic spectrum (11) discussed in the main text.

APPENDIX B: EXCITATION ALONG *m* IN THE NONLINEAR REGIME

We studied the atom dynamics following an excitation along m as a function of the excitation strength. Starting in the ground state $|\psi_0\rangle$ of the unperturbed Hamiltonian (1), we excite the system by applying a short pulse of potential J_z, resulting in a state $|\psi_i\rangle = \exp(-i\epsilon J_z)|\psi_0\rangle$, from which we evolve the Hamiltonian (1). We show in Fig. 5 the spin dynamics calculated for excitation strengths $\epsilon = 0.1, 0.2, 0.4, 0.8$.

For $\epsilon = 0.1$, the spin projection probabilities $\Pi_m(t)$ remain close to a Gaussian. Its center sinusoidally evolves around zero, with an amplitude $|m_z|^{(\max)} \simeq 1$, much smaller than the spin length $J = 8$ [see Fig. 5(a)]. In this linear regime, the amplitude $|m_z|^{(\max)} \simeq 1$ is proportional to the excitation strength ϵ [see Fig. 5(i)].

The spin dynamics departs from this simple behavior for larger excitation strengths, as soon as the oscillation amplitude $|m_z|^{(\max)}$ becomes comparable to J. In this nonlinear regime, the spin projection probabilities cease to be Gaussian, and the spin dynamics is more complex [see Figs. 5(e) and 5(g)]. While the r velocity remains negligible in the linear regime, it becomes significant in the nonlinear domain, showing that m and r dynamics are coupled at high energy.

[1] J. Dalibard, F. Gerbier, G. Juzeliūnas, and P. Öhberg, Colloquium: Artificial gauge potentials for neutral atoms, Rev. Mod. Phys. **83**, 1523 (2011).

[2] N. R. Cooper, J. Dalibard, and I. B. Spielman, Topological bands for ultracold atoms, Rev. Mod. Phys. **91**, 015005 (2019).

[3] O. Boada, A. Celi, J. I. Latorre, and M. Lewenstein, Quantum Simulation of an Extra Dimension, Phys. Rev. Lett. **108**, 133001 (2012).

[4] A. Celi, P. Massignan, J. Ruseckas, N. Goldman, I. B. Spielman, G. Juzeliūnas, and M. Lewenstein, Synthetic Gauge Fields in Synthetic Dimensions, Phys. Rev. Lett. **112**, 043001 (2014).

[5] T. Ozawa and H. M. Price, Topological quantum matter in synthetic dimensions, Nat. Rev. Phys. **1**, 349 (2019).

[6] M. Mancini, G. Pagano, G. Cappellini, L. Livi, M. Rider, J. Catani, C. Sias, P. Zoller, M. Inguscio, M. Dalmonte, and L. Fallani, Observation of chiral edge states with neutral fermions in synthetic Hall ribbons, Science **349**, 1510 (2015).

[7] B. K. Stuhl, H.-I. Lu, L. M. Aycock, D. Genkina, and I. B. Spielman, Visualizing edge states with an atomic Bose gas in the quantum Hall regime, Science **349**, 1514 (2015).

[8] X.-L. Qi, T. L. Hughes, and S.-C. Zhang, Topological field theory of time-reversal invariant insulators, Phys. Rev. B **78**, 195424 (2008).

[9] H. M. Price, O. Zilberberg, T. Ozawa, I. Carusotto, and N. Goldman, Four-Dimensional Quantum Hall Effect with Ultracold Atoms, Phys. Rev. Lett. **115**, 195303 (2015).

[10] B. Lian and S.-C. Zhang, Five-dimensional generalization of the topological Weyl semimetal, Phys. Rev. B **94**, 041105(R) (2016).

[11] We consider here the case of an integer spin length J, but the proposal can be straightforwardly extended to a half-integer spin.

[12] C.-H. Li, Y. Yan, S. Choudhury, D. B. Blasing, Q. Zhou, and Y. P. Chen, A Bose-Einstein condensate on a synthetic Hall cylinder, arXiv:1809.02122.

[13] J. H. Han, J. H. Kang, and Y. Shin, Band Gap Closing in a Synthetic Hall Tube of Neutral Fermions, Phys. Rev. Lett. **122**, 065303 (2019).

[14] Q.-Y. Liang, D. Trypogeorgos, A. Valdés-Curiel, J. Tao, M. Zhao, and I. B. Spielman, Coherence and decoherence in the Harper-Hofstadter model, Phys. Rev. Research **3**, 023058 (2021).

[15] T. Chalopin, T. Satoor, A. Evrard, V. Makhalov, J. Dalibard, R. Lopes, and S. Nascimbene, Probing chiral edge dynamics and bulk topology of a synthetic Hall system, Nat. Phys. **16**, 1017 (2020).

[16] F. A. An, E. J. Meier, and B. Gadway, Direct observation of chiral currents and magnetic reflection in atomic flux lattices, Sci. Adv. **3**, 4 (2017).

[17] L. Yuan, Q. Lin, M. Xiao, and S. Fan, Synthetic dimension in photonics, Optica **5**, 1396 (2018).

[18] A. Dutt, Q. Lin, L. Yuan, M. Minkov, M. Xiao, and S. Fan, A single photonic cavity with two independent physical synthetic dimensions, Science **367**, 59 (2020).

[19] F. T. Arecchi, E. Courtens, R. Gilmore, and H. Thomas, Atomic coherent states in quantum optics, Phys. Rev. A **6**, 2211 (1972).

[20] T. Holstein and H. Primakoff, Field dependence of the intrinsic domain magnetization of a ferromagnet, Phys. Rev. **58**, 1098 (1940).

[21] S. M. Barnett and D. T. Pegg, Quantum theory of rotation angles, Phys. Rev. A **41**, 3427 (1990).

[22] R. Lynch, The quantum phase problem: A critical review, Phys. Rep. **256**, 367 (1995).

[23] The velocity along r can be recovered using the unitary angle operator $\exp(i\frac{2\pi}{3}J_z)$, from its commutator with the Hamiltonian, as

$$v_r \equiv \frac{i}{\hbar}\frac{1}{\sqrt{3}}\left\{\exp\left(-i\frac{2\pi}{3}J_z\right),\left[H,\exp\left(i\frac{2\pi}{3}J_z\right)\right]\right\}$$
$$= U_a\frac{iJ_+}{J} + U_b\frac{iJ_-^2}{J(J-1/2)} + \text{H.c.},$$

which coincides with the expression given in (16).

[24] M. Lu, N. Q. Burdick, S. H. Youn, and B. L. Lev, Strongly Dipolar Bose-Einstein Condensate of Dysprosium, Phys. Rev. Lett. **107**, 190401 (2011).

[25] K. Aikawa, A. Frisch, M. Mark, S. Baier, A. Rietzler, R. Grimm, and F. Ferlaino, Bose-Einstein Condensation of Erbium, Phys. Rev. Lett. **108**, 210401 (2012).

[26] E. T. Davletov, V. V. Tsyganok, V. A. Khlebnikov, D. A. Pershin, D. V. Shaykin, and A. V. Akimov, Machine learning for achieving Bose-Einstein condensation of thulium atoms, Phys. Rev. A **102**, 011302(R) (2020).

[27] M. Lu, N. Q. Burdick, and B. L. Lev, Quantum Degenerate Dipolar Fermi Gas, Phys. Rev. Lett. **108**, 215301 (2012).

[28] K. Aikawa, A. Frisch, M. Mark, S. Baier, R. Grimm, and F. Ferlaino, Reaching Fermi Degeneracy via Universal Dipolar Scattering, Phys. Rev. Lett. **112**, 010404 (2014).

[29] R. Grimm, M. Weidemüller, and Y. B. Ovchinnikov, Optical dipole traps for neutral atoms, Adv. At. Mol. Opt. Phys. **42**, 95 (2000).

[30] C. Cohen-Tannoudji and J. Dupont-Roc, Experimental study of zeeman light shifts in weak magnetic fields, Phys. Rev. A **5**, 968 (1972).

[31] B. S. Mathur, H. Tang, and W. Happer, Light shifts in the alkali atoms, Phys. Rev. **171**, 11 (1968).

[32] M. Lepers, J.-F. Wyart, and O. Dulieu, Anisotropic optical trapping of ultracold erbium atoms, Phys. Rev. A **89**, 022505 (2014).

[33] W. Kao, Y. Tang, N. Q. Burdick, and B. L. Lev, Anisotropic dependence of tune-out wavelength near Dy 741-nm transition, Opt. Express **25**, 3411 (2017).

[34] A. Fabre, J.-B. Bouhiron, T. Satoor, R. Lopes, and S. Nascimbene, Laughlin's topological charge pump in an atomic Hall cylinder, arXiv:2110.12971.

[35] L. Barbiero, L. Chomaz, S. Nascimbene, and N. Goldman, Bose-Hubbard physics in synthetic dimensions from interaction Trotterization, Phys. Rev. Research **2**, 043340 (2020).

A.3 LAUGHLIN'S TOPOLOGICAL CHARGE PUMP IN AN ATOMIC HALL CYLINDER

The following pages contain the text of the article [332], which was briefly discussed in section 5.7.

Laughlin's topological charge pump in an atomic Hall cylinder
A. Fabre, J.-B. Bouhiron, T. Satoor, R. Lopes, S. Nascimbene
Physical Review Letters 128 (17), 173202 (2022)

Editors' Suggestion | Featured in Physics

Laughlin's Topological Charge Pump in an Atomic Hall Cylinder

Aurélien Fabre, Jean-Baptiste Bouhiron, Tanish Satoor, Raphael Lopes, and Sylvain Nascimbene*
Laboratoire Kastler Brossel, Collège de France, CNRS, ENS-PSL University, Sorbonne Université, 11 Place Marcelin Berthelot, 75005 Paris, France

(Received 17 November 2021; accepted 25 February 2022; published 25 April 2022)

The quantum Hall effect occurring in two-dimensional electron gases was first explained by Laughlin, who developed a thought experiment that laid the groundwork for our understanding of topological quantum matter. His proposal is based on a quantum Hall cylinder periodically driven by an axial magnetic field, resulting in the quantized motion of electrons. We realize this milestone experiment with an ultracold gas of dysprosium atoms, the cyclic dimension being encoded in the electronic spin and the axial field controlled by the phases of laser-induced spin-orbit couplings. Our experiment provides a straightforward manifestation of the nontrivial topology of quantum Hall insulators, and could be generalized to strongly correlated topological systems.

DOI: 10.1103/PhysRevLett.128.173202

The quantization of Hall conductance observed in two-dimensional electronic systems subjected to a perpendicular magnetic field [1] is intimately linked to the nontrivial topology of Bloch bands [2] and the occurrence of chiral edge modes protected from backscattering [3]. The first step in its understanding was provided by Laughlin, who gave an elegant argument by considering a Hall system in a cylindrical geometry (Fig. 1) [4]. Besides the radial magnetic field $\mathbf{B}_\perp$ yielding the Hall effect, this geometry authorizes an axial field $\mathbf{B}_\parallel$, which does not pierce the surface but threads the cylinder with a flux $\Phi_\parallel$. Varying the flux $\Phi_\parallel$ controls a quantized electronic motion along the tube, which is directly linked to the underlying band topology. Such quantization of transport was later generalized by Thouless to any physical system subjected to a slow periodic deformation [5], as implemented in electronic quantum dots [6,7], photonic waveguides [8], and ultracold atomic gases [9,10].

So far, the topology of magnetic Bloch bands has been revealed in planar systems only, by measuring the quantization of transverse response [1,11–13] or observing chiral ballistic edge modes [14–16]. The realization of Laughlin's pump experiment requires engineering periodic boundary conditions, which is challenging when using genuine spatial dimensions. The concept of a synthetic dimension encoded in an internal degree of freedom provides an alternative method for the generation of gauge fields [17]. Synthetic dimensions were first implemented with open boundary conditions, leading to the observation of chiral edge modes [18,19]. More recently, synthetic Hall cylinders were engineered using several spin states coupled in a cyclic manner [20–22]. Nevertheless, the realization of Laughlin's topological charge pump was not realized yet, due to the absence of control over an axial magnetic field $\mathbf{B}_\parallel$.

In this Letter, we use an ultracold gas of ^{162}Dy atoms to engineer a Hall cylinder whose azimuthal coordinate is encoded in the electronic spin $J = 8$ [23]. We manipulate the spin using coherent optical transitions, such that a triplet of internal states coupled in a cyclic manner emerges at low energy, leading to an effective cylindrical geometry [24]. The exchange of momentum between light and atoms leads to a spin-orbit coupling that mimics a radial magnetic field $\mathbf{B}_\perp$ [25]. The phases of the laser electric fields also control an effective axial field $\mathbf{B}_\parallel$, which is the crucial ingredient to implement Laughlin's thought experiment and reveal the underlying topology. The topological character of the

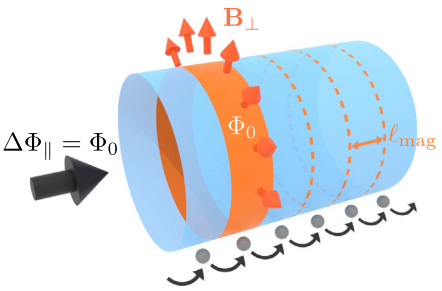

FIG. 1. Laughlin's thought experiment. Scheme of a two-dimensional electronic system in a cylindrical geometry, with a radial magnetic field $\mathbf{B}_\perp$ producing a quantum Hall effect. The orange area, pierced by one magnetic flux quantum Φ_0, defines the length ℓ_{mag} of the magnetic unit cell—each cell being filled with one electron in a quantum Hall insulator. Laughlin's thought experiment consists of performing an adiabatic cycle by threading one flux quantum $\Delta\Phi_\parallel = \Phi_0$ through the cylinder. The cycle shifts electron occupations by one unit cell, such that a single electron is pumped from one edge to the other, or equivalently the center-of-mass position is displaced by ℓ_{mag}.

 © 2022 American Physical Society

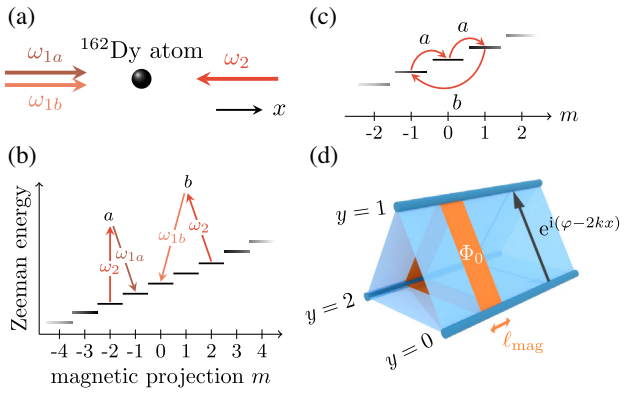

FIG. 2. Emerging quantum Hall cylinder. (a) Sketch of the laser configuration involving two beams counterpropagating along x and sent on a thermal sample of dysprosium atoms—one beam having two frequency components. (b) Scheme of the two-photon optical transitions resonantly driving first- and second-order spin transitions, labeled a and b, respectively. (c) Representation of a nontrivial 3-cycle between magnetic sublevels induced by the light couplings. (d) Scheme of the Hall cylinder dynamics emerging at low energy, involving three spin states $|y\rangle$ (with $y = 0$, 1, and 2). The hopping amplitudes have a complex phase $\varphi - 2kx$, where $2\hbar k$ plays the role of a radial magnetic field $B_\perp$ and φ is linked to an axial field $B_\parallel$. The orange area, of length $\ell_{\rm mag} = \lambda/6$ is threaded by one unit of magnetic flux quantum Φ_0.

ground Bloch band manifests as well in a complementary pump experiment driven by Bloch oscillations.

In our experimental protocol, we apply a magnetic field in order to lift the degeneracy between the magnetic sublevels m (with $-J \le m \le J$ and integer m). Spin transitions of first and second order, i.e., $\Delta m = \pm 1$ and ± 2, are induced by resonant two-photon optical transitions, using a pair of laser beams counterpropagating along x [Fig. 2(a)] [26]. The configuration of laser frequencies is chosen such that the atoms undergo a momentum kick $-2\hbar k$ upon either resonant process $m \to m+1$ or $m \to m-2$, shown in Fig. 2(b). Here, $k = 2\pi/\lambda$ is the photon momentum for the laser wavelength $\lambda = 626.1$ nm. The resulting spin-orbit coupling breaks continuous translation symmetry, but conserves the quasimomentum $q = Mv_x/\hbar + 2km \pmod{6k}$, defined over the magnetic Brillouin zone $-3k \le q < 3k$, where M and v_x are the atomic mass and velocity. The atom dynamics is described by the Hamiltonian

$$H = \frac{1}{2}Mv_x^2 + V, \tag{1}$$

$$V = -\mathcal{T}_y e^{-2ikx} + \text{H.c.}, \quad \mathcal{T}_y = t_a e^{i\varphi_a}\frac{J_+}{J} + t_b e^{i\varphi_b}\frac{J_-^2}{J^2}, \tag{2}$$

where J_+ and J_- are the spin ladder operators, and $t_a, t_b > 0$ are the strengths of the first- and second-order transitions. The phase difference $\varphi_a - \varphi_b$ can be gauged away using a suitable spin rotation, such that we retain hereafter a single phase $\varphi \equiv \varphi_a = \varphi_b$.

The combination of the two types of transitions induces nontrivial 3-cycles $m \to m+1 \to m+2 \to m$ [Fig. 2(b)], with chiral dynamics in the cyclic variable $y = m \pmod 3$—each step increasing y by one unit. As explained in a previous theoretical work [24] and in the Supplemental Material [26], this dynamics leads to the emergence at low energy of a closed subsystem of dimension 3, spanned by three spin states $|y\rangle$, with $y = 0$, 1, 2 and where $|y\rangle$ expands on projection states $|m\rangle$ with $m = y \pmod 3$ only. The $|y\rangle$ states are obtained by linear combinations of three coherent spin states oriented along equatorial directions of azimuthal angles $\phi = \varphi + \{0, 2\pi/3, 4\pi/3\}$. Hence, they only involve magnetic projections m around 0, with a rms width $\Delta m = \sqrt{J/2} = 2$. The $|y\rangle$ states will be interpreted in the following as position eigenstates along a cyclic synthetic dimension of length $Y = 3$. The operator $\mathcal{T}_y$ involved in the spin coupling [Eq. (2)] then acts as a translation $\mathcal{T}_y|y\rangle = t|y+1\rangle$, with a hopping amplitude $t = t_a + t_b$. The low-energy spin dynamics is described by the effective potential

$$V_{\rm eff} = -t\sum_{y=0}^{2}(e^{i(\varphi-2kx)}|y+1\rangle\langle y| + \text{hc}). \tag{3}$$

Together with the kinetic energy $\frac{1}{2}Mv_x^2$, it describes the motion of a particle on a cylinder discretized along its circumference [see Fig. 2(c)]. The complex phase $2kx$ mimics the Aharonov-Bohm phase associated with a radial magnetic field $B_\perp = 2\hbar k$ (assuming a particle charge $q = -1$). It defines a magnetic length $\ell_{\rm mag} = \lambda/6$, such that the magnetic flux $\Phi_\perp = \ell_{\rm mag} Y B_\perp$ through a portion of cylinder of length $\ell_{\rm mag}$ equals the flux quantum $\Phi_0 = h/|q|$.

Experimentally, we use a gas of about 4×10^4 atoms, initially prepared at a temperature $T = 0.54(3)$ μK, such that the thermal momentum width $\sigma_q \simeq 1.3k$ is much smaller than the Brillouin zone extent $6k$, and interaction effects can be neglected on the time scale of our experiments. The atoms are adiabatically loaded in the ground Bloch band with $t_a = 11.5(3)E_r$ and $t_b = 7.1(2)E_r$, by ramping the light coupling parameters. Here, $E_r = \hbar^2k^2/(2M)$ is the single-photon recoil energy. The mean quasimomentum $\langle q \rangle$ is controlled by applying a weak force F_x after the loading (see the Supplemental Material [26]). We simultaneously probe the distribution of velocity v_x and spin projection m. For this, we abruptly switch off the light couplings and ramp up a magnetic field gradient that spatially separates the different magnetic sublevels along z. The velocity distribution is obtained from the density

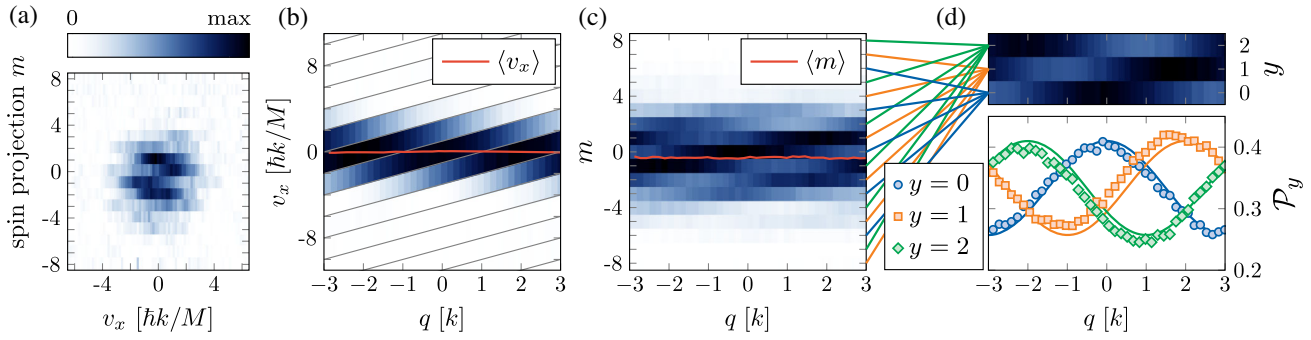

FIG. 3. Ground band characterization. (a) Spin-resolved velocity distribution measured for a gas of mean quasimomentum $\langle q \rangle \simeq 2k$. (b) Distribution of discrete velocity components $v_x = \hbar(q + 2kp)/M$ (with integer p) for states of quasimomentum q. The red line shows the mean velocity $\langle v_x \rangle$. (c) Spin projection probabilities Π_m measured as a function of q. The red line stands for the mean spin projection $\langle m \rangle$. (d) Probabilities $\mathcal{P}_y$ of projection on $y = m (\mathrm{mod}\ 3)$. The blue circles, orange squares, and green diamonds correspond to $y = 0$, 1, and 2, respectively. Statistical error bars, computed from a bootstrap random sampling analysis, are smaller than the symbols. The lines are calculated from the expected band structure.

profile along x measured after a 2.3 ms expansion. A typical spin-resolved velocity distribution is shown in Fig. 3(a).

The velocity distribution, plotted in Fig. 3(b) as a function of q, exhibits a period $2k$, similar to the case of a simple $\lambda/2$-lattice. The mean velocity $\langle v_x \rangle$, shown as a red line, remains close to zero. Since it is linked to the slope of the ground-band energy $\partial_q E_0(q) = \hbar \langle v_x \rangle$, this shows that the band is quasiflat. In fact, the band's flatness is protected from pertubations, such as external magnetic field fluctuations, by the zero net magnetization of the $|y\rangle$ spin states—a similar effect has been used in another implementation of a Hall cylinder using dynamical decoupling techniques [22].

The probabilities Π_m of projection on each sublevel m reveal a longer periodicity $6k$ [Fig. 3(c)], corresponding to the full extent of the magnetic Brillouin zone. It experimentally confirms the spatial separation of magnetic orbitals $\ell_{\mathrm{mag}} = 2\pi/(6k) = \lambda/6$ introduced above. The Π_m measurements also give access to the probabilities $\mathcal{P}_y$ of projection on the synthetic coordinate y, by summing the Π_m's with $m = y (\mathrm{mod}\ 3)$ [Fig. 3(d)]. The q variation of these distributions reveals a chirality typical of the Hall effect: when increasing the momentum by $2k$, the $\mathcal{P}_y$ distributions cycle along the synthetic dimension in a directional manner, as $\mathcal{P}_y \to \mathcal{P}_{y+1}$ [30,31]. We stress that such a drift does not occur on the mean spin projection $\langle m \rangle$, which remains close to zero [red line in Fig. 3(c)].

The adiabatic y drift occurring during Bloch oscillations provides a first insight into the topological character of the lowest energy band—similar to the quantized flow of Wannier function charge centers in Chern insulators [32]. To quantify this drift, we cannot rely on the mean y position, which is ill defined for a cyclic dimension [33]. Instead, it is reconstructed by integrating the anomalous velocity $\langle v_y \rangle \equiv \partial_\varphi H/\hbar$ induced by the force F_x driving the Bloch oscillation. For this purpose, we conduct a separate experiment, in which we suddenly switch off the force F_x, such that the center of mass undergoes a cyclotron oscillation, with the x and y velocities oscillating in quadrature. More precisely, the rate of change of the x velocity gives access to the y velocity, via the exact relation

$$\partial_t \langle v_x \rangle = \frac{i}{\hbar}[H, v_x] = -\frac{2\hbar k}{M}\langle v_y \rangle.$$

Hence, the velocity $\langle v_y \rangle$ induced by the force F_x is given by the initial slope of $\langle v_x \rangle$ [Fig. 4(b)].

The center-of-mass drift $\langle \Delta y \rangle$, obtained upon integration of $\langle v_y \rangle$ is shown in Fig. 4(a). We find that it varies linearly with the quasimomentum variation Δq [Fig. 4(a)], such that the drift per Bloch oscillation cycle reads

$$\frac{\langle \Delta y \rangle}{Y} = 0.97(5), \tag{4}$$

consistent with a unit winding around the cylinder of circumference Y [26]. The rotation along y occurring over a Bloch oscillation cycle is thus quantized, providing a first manifestation of the nontrivial band topology.

We now characterize the global band topology by implementing Laughlin's charge pump experiment, and extend the protocol to reveal the local geometrical properties. To simulate the axial magnetic field used to drive the pump, we interpret the complex phase φ involved in the y hoppings [see Eq. (3)] as the Peierls phase associated with the field $\mathbf{B}_\parallel$ threading the cylinder with a flux

$$\Phi_\parallel = \frac{3\varphi}{2\pi}\Phi_0. \tag{5}$$

We vary $\Phi_\parallel$ by adjusting the phase difference φ between the laser electric fields involved in the spin transitions using acousto-optic modulators.

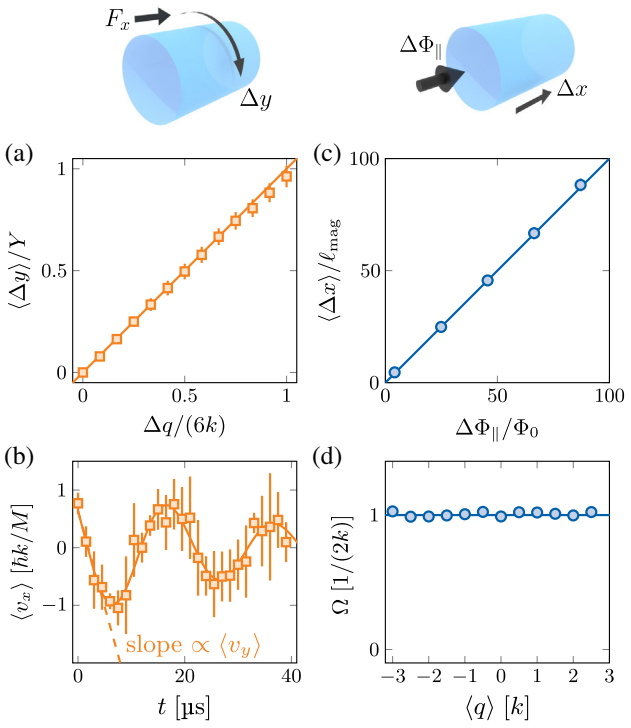

FIG. 4. Topological charge pumps. (a) Center-of-mass displacement $\langle\Delta y\rangle$ as a function of the quasimomentum shift Δq induced by a force F_x (orange squares), together with a linear fit (orange line). (b) Evolution of the mean velocity $\langle v_x\rangle$ immediately after switching off the force F_x (orange squares), fitted with a damped sine (solid line). The velocity $\langle v_y\rangle$ is obtained from the initial slope of the fit (dashed line). (c) Displacement of the center of mass $\langle\Delta x\rangle$ induced by an axial magnetic flux $\Phi_\parallel$ and averaged over the magnetic Brillouin zone (blue circles). The blue line is a linear fit. (d) Berry curvature Ω measured as a function of the mean quasimomentum $\langle q\rangle$ (blue circles). The solid line is the expected Berry curvature, which is not distinguishable from the constant value $\Omega(q) = 1/(2k)$.

We drive the pump by slowly ramping the phase φ, and measure the induced shift of the center of mass along the real dimension x. The experiment is performed for various values of the quasimomentum $\langle q\rangle$ uniformly spanning the magnetic Brillouin zone. The q-averaged drift, shown in Fig. 4(c), is consistent with a linear variation

$$\frac{\langle\Delta x\rangle}{\ell_{\mathrm{mag}}} = \mathcal{C}\frac{\Phi_\parallel}{\Phi_0}, \qquad \mathcal{C} = 1.00(4),$$

in agreement with the expected quantization of transport by the Chern number $\mathcal{C} = 1$. The pump adiabaticity is checked by repeating the experiment for various speeds of the flux ramp, and measuring identical responses for slow enough ramps [26].

Our experiments also give access to the anomalous drift of individual momentum states $\Delta x = \Omega(q)\varphi$, proportional to the Berry curvature $\Omega(q)$ that quantifies the local geometrical properties of quantum states [34]. As shown in Fig. 4(d), the measured Berry curvature is flat within error bars, consistent with theory, which predicts $\Omega(q) = 1/(2k)$ with negligible q variation. The flatness of the Berry curvature is a consequence of the continuous translation symmetry along x, making our system similar to continuous two-dimensional systems with flat Landau levels. In contrast, discrete lattice systems, such as Hofsdtater and Haldane models [35,36], or previous implementations of synthetic Hall cylinders [20–22], exhibit dispersive bands with inhomogeneous Berry curvatures.

We have shown that implementing a quantum Hall cylinder gives direct access to the underlying topology of Bloch bands. Our realization of Laughlin's pump protocol could be generalized to interacting atomic systems, which are expected to form strongly correlated topological states of matter at low temperature. In particular, at fractional fillings, one expects the occurrence of charge density waves as one-dimensional precursors of two-dimensional fractional quantum Hall states [37]. The pumped charge would then be quantized to a rational value, revealing the charge fractionalization of elementary excitations [38].

We thank Jean Dalibard for insightful discussions and careful reading of the manuscript, and Thomas Chalopin for discussions at an early stage of this work. This work is supported by the European Union (Grant No. TOPODY 756722 from the European Research Council).

*sylvain.nascimbene@lkb.ens.fr

[1] K. v. Klitzing, G. Dorda, and M. Pepper, New Method for High-Accuracy Determination of the Fine-Structure Constant Based on Quantized Hall Resistance, Phys. Rev. Lett. **45**, 494 (1980).
[2] D. J. Thouless, M. Kohmoto, M. P. Nightingale, and M. den Nijs, Quantized Hall Conductance in a Two-Dimensional Periodic Potential, Phys. Rev. Lett. **49**, 405 (1982).
[3] B. I. Halperin, Quantized Hall conductance, current-carrying edge states, and the existence of extended states in a two-dimensional disordered potential, Phys. Rev. B **25**, 2185 (1982).
[4] R. B. Laughlin, Quantized Hall conductivity in two dimensions, Phys. Rev. B **23**, 5632 (1981).
[5] D. J. Thouless, Quantization of particle transport, Phys. Rev. B **27**, 6083 (1983).
[6] M. Switkes, C. M. Marcus, K. Campman, and A. C. Gossard, An adiabatic quantum electron pump, Science **283**, 1905 (1999).
[7] S. K. Watson, R. M. Potok, C. M. Marcus, and V. Umansky, Experimental Realization of a Quantum Spin Pump, Phys. Rev. Lett. **91**, 258301 (2003).
[8] Y. E. Kraus, Y. Lahini, Z. Ringel, M. Verbin, and O. Zilberberg, Topological States and Adiabatic Pumping in Quasicrystals, Phys. Rev. Lett. **109**, 106402 (2012).

[9] M. Lohse, C. Schweizer, O. Zilberberg, M. Aidelsburger, and I. Bloch, A Thouless quantum pump with ultracold bosonic atoms in an optical superlattice, Nat. Phys. **12**, 350 (2016).

[10] S. Nakajima, T. Tomita, S. Taie, T. Ichinose, H. Ozawa, L. Wang, M. Troyer, and Y. Takahashi, Topological Thouless pumping of ultracold fermions, Nat. Phys. **12**, 296 (2016).

[11] C. R. Dean, L. Wang, P. Maher, C. Forsythe, F. Ghahari, Y. Gao, J. Katoch, M. Ishigami, P. Moon, M. Koshino, T. Taniguchi, K. Watanabe, K. L. Shepard, J. Hone, and P. Kim, Hofstadter's butterfly and the fractal quantum Hall effect in moiré superlattices, Nature (London) **497**, 598 (2013).

[12] L. A. Ponomarenko, R. V. Gorbachev, G. L. Yu, D. C. Elias, R. Jalil, A. A. Patel, A. Mishchenko, A. S. Mayorov, C. R. Woods, J. R. Wallbank, M. Mucha-Kruczynski, B. A. Piot, M. Potemski, I. V. Grigorieva, K. S. Novoselov, F. Guinea, V. I. Fal'ko, and A. K. Geim, Cloning of Dirac fermions in graphene superlattices, Nature (London) **497**, 594 (2013).

[13] M. Aidelsburger, M. Lohse, C. Schweizer, M. Atala, J. T. Barreiro, S. Nascimbene, N. Cooper, I. Bloch, and N. Goldman, Measuring the Chern number of Hofstadter bands with ultracold bosonic atoms, Nat. Phys. **11**, 162 (2015).

[14] Z. Wang, Y. Chong, J. D. Joannopoulos, and M. Soljačić, Observation of unidirectional backscattering-immune topological electromagnetic states, Nature (London) **461**, 772 (2009).

[15] M. Hafezi, S. Mittal, J. Fan, A. Migdall, and J. Taylor, Imaging topological edge states in silicon photonics, Nat. Photonics **7**, 1001 (2013).

[16] M. C. Rechtsman, J. M. Zeuner, Y. Plotnik, Y. Lumer, D. Podolsky, F. Dreisow, S. Nolte, M. Segev, and A. Szameit, Photonic Floquet topological insulators, Nature (London) **496**, 196 (2013).

[17] A. Celi, P. Massignan, J. Ruseckas, N. Goldman, I. B. Spielman, G. Juzeliūnas, and M. Lewenstein, Synthetic Gauge Fields in Synthetic Dimensions, Phys. Rev. Lett. **112**, 043001 (2014).

[18] M. Mancini, G. Pagano, G. Cappellini, L. Livi, M. Rider, J. Catani, C. Sias, P. Zoller, M. Inguscio, M. Dalmonte, and L. Fallani, Observation of chiral edge states with neutral fermions in synthetic Hall ribbons, Science **349**, 1510 (2015).

[19] B. K. Stuhl, H.-I. Lu, L. M. Aycock, D. Genkina, and I. B. Spielman, Visualizing edge states with an atomic Bose gas in the quantum Hall regime, Science **349**, 1514 (2015).

[20] J. H. Han, J. H. Kang, and Y. Shin, Band Gap Closing in a Synthetic Hall Tube of Neutral Fermions, Phys. Rev. Lett. **122**, 065303 (2019).

[21] C.-H. Li, Y. Yan, S. Choudhury, D. B. Blasing, Q. Zhou, and Y. P. Chen, A Bose-Einstein condensate on a synthetic Hall cylinder, PRX Quantum **3**, 010316 (2022).

[22] Q.-Y. Liang, D. Trypogeorgos, A. Valdés-Curiel, J. Tao, M. Zhao, and I. B. Spielman, Coherence and decoherence in the Harper-Hofstadter model, Phys. Rev. Research **3**, 023058 (2021).

[23] T. Chalopin, T. Satoor, A. Evrard, V. Makhalov, J. Dalibard, R. Lopes, and S. Nascimbene, Probing chiral edge dynamics and bulk topology of a synthetic Hall system, Nat. Phys. **16**, 1017 (2020).

[24] A. Fabre, J.-B. Bouhiron, T. Satoor, R. Lopes, and S. Nascimbene, Simulating two-dimensional dynamics within a large-size atomic spin, Phys. Rev. A **105**, 013301 (2022).

[25] J. Dalibard, F. Gerbier, G. Juzeliūnas, and P. Öhberg, Colloquium: Artificial gauge potentials for neutral atoms, Rev. Mod. Phys. **83**, 1523 (2011).

[26] See Supplemental Material at http://link.aps.org/supplemental/10.1103/PhysRevLett.128.173202 for details on the experimental protocol, additional information on the derivation of the three-state model and on the link between adiabatic pumps and band topology, a study of the pump adiabaticity and measurements of low-energy excitations, which includes Refs. [27–29].

[27] C. Cohen-Tannoudji and J. Dupont-Roc, Experimental study of Zeeman light shifts in weak magnetic fields, Phys. Rev. A **5**, 968 (1972).

[28] F. T. Arecchi, E. Courtens, R. Gilmore, and H. Thomas, Atomic coherent states in quantum optics, Phys. Rev. A **6**, 2211 (1972).

[29] X.-W. Luo, J. Zhang, and C. Zhang, Tunable flux through a synthetic Hall tube of neutral fermions, Phys. Rev. A **102**, 063327 (2020).

[30] Y. Yan, S.-L. Zhang, S. Choudhury, and Q. Zhou, Emergent Periodic and Quasiperiodic Lattices on Surfaces of Synthetic Hall Tori and Synthetic Hall Cylinders, Phys. Rev. Lett. **123**, 260405 (2019).

[31] R. P. Anderson, D. Trypogeorgos, A. Valdés-Curiel, Q.-Y. Liang, J. Tao, M. Zhao, T. Andrijauskas, G. Juzeliūnas, and I. B. Spielman, Realization of a deeply subwavelength adiabatic optical lattice, Phys. Rev. Research **2**, 013149 (2020).

[32] M. Taherinejad, K. F. Garrity, and D. Vanderbilt, Wannier center sheets in topological insulators, Phys. Rev. B **89**, 115102 (2014).

[33] R. Lynch, The quantum phase problem: A critical review, Phys. Rep. **256**, 367 (1995).

[34] H.-I. Lu, M. Schemmer, L. M. Aycock, D. Genkina, S. Sugawa, and I. B. Spielman, Geometrical Pumping with a Bose-Einstein Condensate, Phys. Rev. Lett. **116**, 200402 (2016).

[35] D. R. Hofstadter, Energy levels and wave functions of Bloch electrons in rational and irrational magnetic fields, Phys. Rev. B **14**, 2239 (1976).

[36] F. D. M. Haldane, Model for a Quantum Hall Effect without Landau Levels: Condensed-Matter Realization of the "Parity Anomaly", Phys. Rev. Lett. **61**, 2015 (1988).

[37] R. Tao and D. J. Thouless, Fractional quantization of Hall conductance, Phys. Rev. B **28**, 1142 (1983).

[38] R. B. Laughlin, Nobel lecture: Fractional quantization, Rev. Mod. Phys. **71**, 863 (1999).

A.4 REALIZATION OF AN ATOMIC QUANTUM HALL SYSTEM IN FOUR DIMENSIONS

The following pages contain the main text of the preprint [378], which was mentioned in section 5.7.

Realization of an atomic quantum Hall system in four dimensions
J.-B. Bouhiron, A. Fabre, Q. Liu, Q. Redon, N. Mittal, T. Satoor, R. Lopes, S. Nascimbene
arXiv:2210.06322 (2022)

arXiv:2210.06322v1 [cond-mat.quant-gas] 12 Oct 2022

Realization of an atomic quantum Hall system in four dimensions

Jean-Baptiste Bouhiron, Aurélien Fabre, Qi Liu, Quentin Redon, Nehal Mittal, Tanish Satoor, Raphael Lopes, and Sylvain Nascimbene*
Laboratoire Kastler Brossel, Collège de France, CNRS, ENS-PSL University, Sorbonne Université, 11 Place Marcelin Berthelot, 75005 Paris, France
(Dated: October 13, 2022)

Topological states of matter lie at the heart of our modern understanding of condensed matter systems. In two-dimensional (2D) quantum Hall insulators, the non-trivial topology, defined by the first Chern number, manifests as a quantized Hall conductance [1, 2] and protected ballistic edge modes [3]. Besides topological insulators [4] and Weyl semi-metals [5, 6] experimentally realized in 3D materials, a large variety of topological systems, theoretically predicted in dimensions $D > 3$, remains unexplored [7] – among them a generalization of the quantum Hall effect in 4D [8, 9]. So far, topological properties linked with the 4D Hall effect have been revealed via geometrical charge pump experiments in 2D systems [10, 11]. A truly 4D Hall system has also been realized using electronic circuits – however, no direct evidence of topological quantization has been reported [12]. Here, we engineer an atomic quantum Hall system evolving in 4D, by coupling with light fields two spatial dimensions and two synthetic ones encoded in the electronic spin $J = 8$ of dysprosium atoms [13–15]. We measure the characteristic properties of a 4D quantum Hall system, namely the quantization of its electromagnetic non-linear response by a second Chern number, and the special nature of its 3D hyperedge modes, which combine ballistic motion along one orientation and insulating behaviour in the two remaining directions. We also probe low-lying excitations, revealing non-planar cyclotron orbits in contrast with their circular equivalents in $D \leq 3$. Our findings pave the way to the exploration of interacting quantum Hall systems in 4D, from the investigation of strongly-correlated liquids [9, 16] to the simulation of high-energy models in link with quantum gravity [9] and Yang-Mills field theory [17, 18].

Dimensionality plays a prominent role in the classification of topological physical systems [7]. While different topological classes have been explored in condensed matter systems [19] – effectively described in one, two or three dimensions – higher dimensional systems can potentially be accessed with engineered materials, based on the concept of synthetic dimensions [13, 20]. In particular, different protocols have been proposed to realize a generalization of a quantum Hall insulator to 4D [21–23], both for time-reversal invariant systems (classes AI and AII, as realized with electronic circuits [12]) and in the absence of discrete symmetry (class A). In 4D, a non-trivial topology leads to specific behaviour, such as the quantization of the non-linear response to both electric and magnetic perturbations, characterized by the second Chern number $\mathcal{C}_2$ [9, 22, 24] – a topological invariant also relevant for tensor monopoles in high dimensions [25–28]. The topology of a 4D quantum Hall insulator (class A) also gives rise to anisotropic motion at the edge of the system, ballistic along a given orientation, and still prohibited along the two remaining directions of the 3D hyperedge [29].

In this article, we realize an effectively 4D quantum Hall system using an ultracold sample of dysprosium

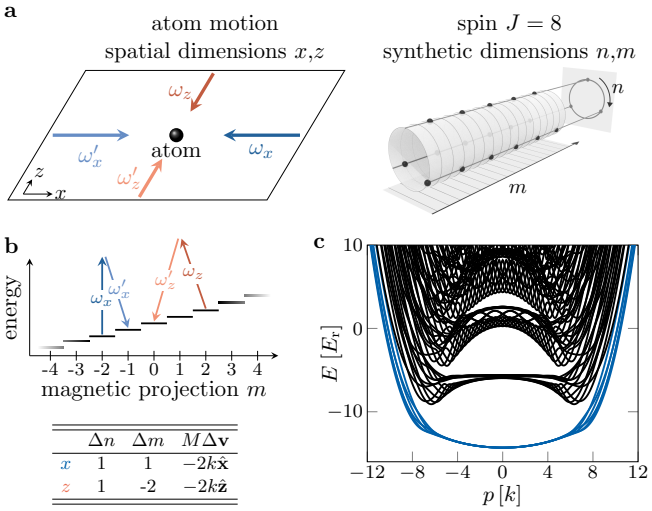

	Δn	Δm	$M\Delta \mathbf{v}$
x	1	1	$-2k\hat{\mathbf{x}}$
z	1	-2	$-2k\hat{\mathbf{z}}$

FIG. 1. **Scheme of the 4D atomic system. a.** The atomic motion in the xz plane is coupled to the internal spin $J = 8$ using two-photon optical transitions along x and z (blue and red arrows, respectively). The spin encodes two synthetic dimensions given by the magnetic projection m and its remainder $n = m$ (mod 3) of its Euclidian division by 3, leading to a synthetic space of cylindrical geometry [30]. **b.** Scheme of the light-induced spin transitions, of first- and second-order along x and z, respectively. They induce correlated spin-orbit dynamics, with distinct hopping along n and m according to the rules given in the table. **c.** Dispersion relation plotted as a function of the momentum p, for 6 values of the quasi-momentum q uniformly spanning the Brillouin zone. The ground band is pictured as blue lines.

* sylvain.nascimbene@lkb.ens.fr

atoms, whose motion along two spatial dimensions x and z is coupled to two synthetic dimensions encoded in the electronic spin $J = 8$ (Fig. 1a). The spin-orbit coupling is generated by two-photon optical transitions [31] (Fig. 1b), such that it produces an effective magnetic field leading to the band structure of a class A Hall insulator in 4D. We reveal the quantization of the non-linear response to both electric and magnetic perturbations, except on the system edges where we observe anisotropic dispersion. We also probe cyclotron excitations of the center of mass, whose non-planar trajectories contrast with cyclotron motion in dimensions $D \leq 3$.

The coupling between motion and spin degrees of freedom is generated by a pair of lasers counter-propagating along x (resp. z) and resonantly driving spin transitions $m \to m+1$ (resp. $m \to m-2$), while imparting a momentum kick $-2k\hat{\mathbf{x}}$ (resp. $-2k\hat{\mathbf{z}}$). Here, m is the spin projection along z ($-J \leq m \leq J$, m integer), $k = 2\pi/\lambda$ is the light momentum for a wavelength $\lambda = 626.1\,\mathrm{nm}$, and we assume a unit reduced Planck constant $\hbar = 1$. The atom dynamics is described by the Hamiltonian

$$H = \frac{Mv^2}{2} - \left(t_x \mathrm{e}^{\mathrm{i}\phi_x} \frac{J_+}{J} + t_z \mathrm{e}^{\mathrm{i}\phi_z} \frac{J_-^2}{J^2} + \mathrm{hc} \right) + \beta \frac{J_z^2}{J^2}, \quad (1)$$

where $\mathbf{v}$ is the atom velocity and $\phi_\alpha = -2k\alpha$ is the relative phase of the two laser beams involved in each Raman process $\alpha = x, z$. The laser intensities and polarisations control the amplitudes t_α and the quadratic Zeeman shift $\beta = -2t_z$ (see Methods).

The laser-induced spin transitions can be interpreted as hopping processes in a two-dimensional synthetic space (m, n) involving the spin projection m and the remainder $n = m \pmod 3$ of its Euclidian division by 3 (with $n = 0, 1, 2$) [30]. While the first-order spin coupling J_+ acts on these two dimensions in a similar manner (hopping $\Delta n^{(x)} = \Delta m^{(x)} = 1$), the second-order coupling J_-^2 induces hoppings $\Delta n^{(z)} = 1$ and $\Delta m^{(z)} = -2$ leading to differential dynamics along m and n. The complex phases ϕ_α (with $\alpha = x, z$) can be interpreted as Peierls phases upon the hopping of a charged particle on a lattice subjected to a magnetic field. Assuming unit charge, we write $\phi_\alpha = \int A_\beta \mathrm{d}r^\beta = A_n \Delta n^{(\alpha)} + A_m \Delta m^{(\alpha)}$, leading to the explicit expression for the vector potential

$$\mathbf{A} = \frac{1}{3}(0, 0, 2\phi_x + \phi_z, \phi_x - \phi_z)_{x,z,n,m}. \quad (2)$$

The magnetic field is then defined by the anti-symmetric tensor $B_{\alpha\beta} = \partial_\alpha A_\beta - \partial_\beta A_\alpha$, as

$$\mathbf{B} = \frac{2k}{3} \begin{pmatrix} 0 & 0 & -2 & -1 \\ 0 & 0 & -1 & 1 \\ 2 & 1 & 0 & 0 \\ 1 & -1 & 0 & 0 \end{pmatrix}. \quad (3)$$

Similarly to the 2D quantum Hall effect, this magnetic field gives rise to an energy separation between quasi-flat magnetic Bloch bands. Within each band, motion becomes effectively two-dimensional, with the guiding center coordinate along n canonically conjugated to the position along $\hat{\boldsymbol{\nu}} = (2\hat{\mathbf{x}} + \hat{\mathbf{z}})/\sqrt{5}$, while m is conjugated to the projection on $\hat{\boldsymbol{\mu}} = (\hat{\mathbf{x}} - \hat{\mathbf{z}})/\sqrt{2}$. The energy levels are indexed by the canonical momentum $\mathbf{p} = M\mathbf{v} + 2km\hat{\mathbf{x}} \pmod{\mathbf{K}}$, which is conserved in the absence of external force. Here, the reciprocal lattice vector $\mathbf{K} = 2k(2\hat{\mathbf{x}} + \hat{\mathbf{z}}) \parallel \hat{\boldsymbol{\nu}}$ corresponds to the momentum kick imparted on a non-trivial cycle $m \xrightarrow{z} m+2 \xrightarrow{x} m+1 \xrightarrow{x} m$ involving one transition along z and two along x. In the following, we decompose the momentum as $\mathbf{p} = p\hat{\boldsymbol{\xi}} + q\hat{\boldsymbol{\nu}}$, with $\hat{\boldsymbol{\xi}} = (\hat{\mathbf{x}} - 2\hat{\mathbf{z}})/\sqrt{5} \perp \hat{\boldsymbol{\nu}}$, such that the first Brillouin zone is defined for $|q| < K/2$ and arbitrary p. The energy levels of the Hamiltonian (1) organize in Bloch bands shown in Fig. 1d. We focus here on the ground band, which is quasi-flat in the bulk mode region $|p| \lesssim 7k$ (see Methods).

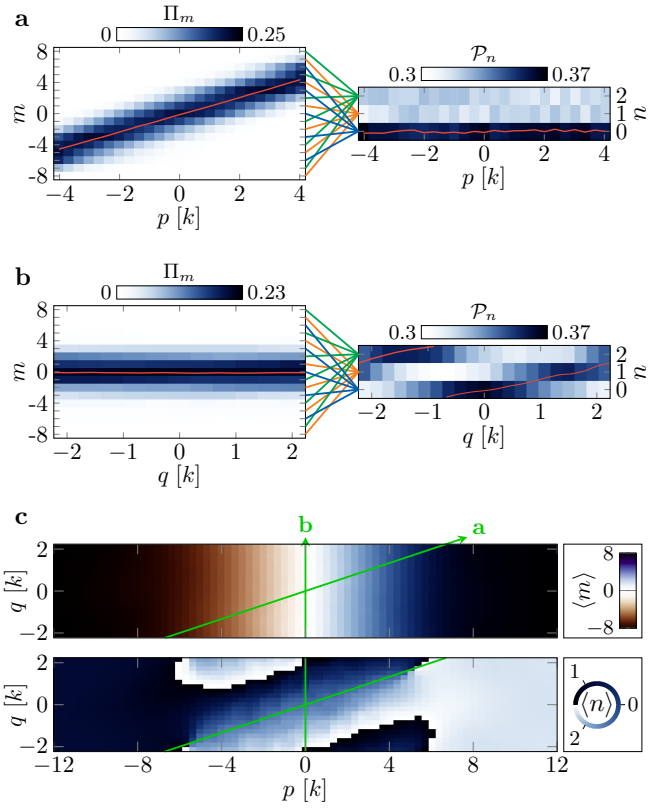

FIG. 2. **Hall drift along the synthetic dimensions.** **a.** Evolution of the measured spin projections Π_m and $\mathcal{P}_n$ as a function of p upon adiabatic driving along $\hat{\boldsymbol{\mu}}$ – the spatial direction conjugated with m. The mean values $\langle m \rangle$ and $\langle n \rangle$ (computed as $\frac{3}{2\pi} \arg\langle \mathrm{e}^{\mathrm{i}2\pi m/3} \rangle$) are shown as red lines. **b.** Same quantities plotted for a driving along $\hat{\boldsymbol{\nu}}$ – the spatial direction conjugated with n. **c.** Measurements of the mean values $\langle m \rangle$ and $\langle n \rangle$ in the Brillouin zone. The green arrows represent the driving directions considered in **a** and **b**.

Our experiments use ultracold dilute samples of $\simeq 3.0(3) \times 10^4$ atoms of ^{162}Dy, prepared in an optical dipole trap at a temperature $T = 260(10)\,\mathrm{nK}$. The atoms are subjected to a magnetic field $B = 221(1)\,\mathrm{mG}$

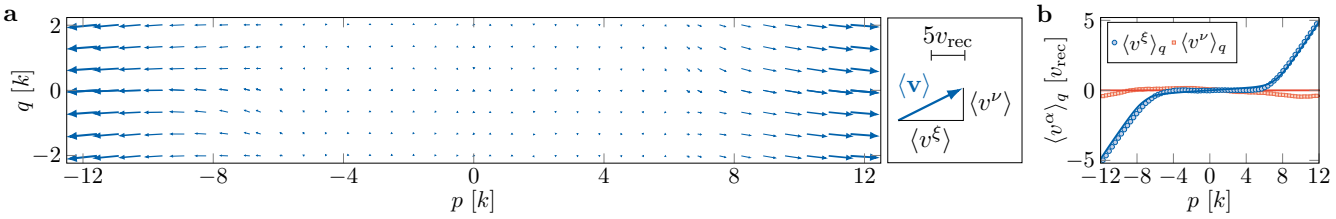

FIG. 3. **Frustration of motion in the bulk and anisotropic ballistic edge modes. a.** Evolution of the mean velocity $\langle \mathbf{v} \rangle$ versus momentum. The arrow is scaled according the mean velocity modulus. **b.** Measurements of the q-average velocity components versus p. The solid lines are the expected variations for the ground band of the Hamiltonian (1).

along z, and initially spin-polarized in the magnetic sublevel $m = -J$. We adiabatically ramp up the laser intensities to generate the spin couplings described in (1) with $t_x = 5.69(6)\, E_{\rm rec}$ and $t_z = 5.1(1)\, E_{\rm rec}$, where $E_{\rm rec} = k^2/(2M)$ is the recoil energy. Starting in the $m = -J$ edge mode region with $p < 7k$, we prepare arbitrary momentum states of the ground energy band by applying a weak force on a typical 1 ms timescale (see Methods). At the end of the experiments, we probe the velocity distribution by imaging the atomic sample after free expansion in the presence of a magnetic field gradient, such that the different m states are spatially separated.

We first investigate the anomalous Hall drift in spin space upon the application of a weak force in the xz plane. For a force oriented along $\hat{\boldsymbol{\mu}}$ (spatial direction conjugated to m), the spin projection probabilities Π_m reveal a drift of the mean spin projection $\langle m \rangle$, while the mean remainder $\langle n \rangle$ remain approximately constant (Fig. 2a). An opposite behavior is observed when applying a force along $\hat{\boldsymbol{\nu}}$ (direction conjugated to n), with a quasi-linear variation of $\langle n \rangle$ while $\langle m \rangle$ remains constant (Fig. 2b). More generally, in the bulk of the system, where the band dispersion can be neglected, the variation with momentum of the mean values $\langle n \rangle$ and $\langle m \rangle$ can be expressed as an anomalous Hall drift governed by the antisymmetric Berry curvature tensor $\boldsymbol{\Omega}_{\rm bulk}$, as

$$\mathrm{d}\langle r^\alpha \rangle = \Omega^{\alpha\beta}_{\rm bulk} \mathrm{d}p_\beta, \tag{4}$$

$$\boldsymbol{\Omega}_{\rm bulk} = \mathbf{B}^{-1} = \frac{1}{2k} \begin{pmatrix} 0 & 0 & 1 & 1 \\ 0 & 0 & 1 & -2 \\ -1 & -1 & 0 & 0 \\ -1 & 2 & 0 & 0 \end{pmatrix}, \tag{5}$$

where $\mathbf{r}$ is the position vector and $\mathrm{d}\mathbf{p}$ is the momentum variation due to the external force. We confront this prediction to our measurements of the mean positions $\langle m \rangle$ and $\langle n \rangle$ as a function of $\mathbf{p}$ (Fig. 2c). In the center of the Brillouin zone $|p| \leq 4k$ (bulk mode region), we fit the measured Hall drift with the linear function (4), yielding $\{\Omega^{nx}, \Omega^{nz}, \Omega^{mx}, \Omega^{mz}\} = \{-1.00(2), -0.98(2), -0.98(2), 1.96(2)\}/(2k)$, consistent with (5). We do not measure any significant spatial drift upon the application of a force in the xz plane, consistent with $\Omega^{xz} = 0$. Similarly, no Hall current along n is measured when applying a force along m (corresponding to a perturbative Zeeman field), compatible with $\Omega^{nm} = 0$ (see Methods).

Further insight on the ground band properties is provided by the mean velocity $\langle \mathbf{v} \rangle$ (Fig. 3), which reveals distinct behaviours between bulk and the edge modes.

In the bulk $|p| \lesssim 7k$, the mean velocity remains much smaller than the recoil velocity $v_{\rm rec} = k/M$ (Fig. 3b). Since $\langle \mathbf{v} \rangle = \nabla_{\mathbf{p}} E_0$, it confirms that the ground band energy E_0 is quasi-flat in the bulk (Fig. 1d). This measurement illustrates the frustration of motion induced by the magnetic field, similarly to flat Landau levels in 2D electron gases.

For $p \gtrsim 7k$, the atoms mostly occupy the edge $\mathbf{r}^{\rm edge} = J\hat{\mathbf{m}}$ of the synthetic dimension m. We measure a non-zero mean velocity, whose ξ component increases with p, while the ν projection remains small (Fig. 3b). This observation is characteristic of an anisotropic edge mode of a 4D quantum Hall system, which corresponds to a collection of 1D conduction channels oriented along the direction $\mathbf{w}_{\rm motion}$, with $w^\alpha_{\rm motion} \propto \Omega^{\alpha\beta}_{\rm bulk} r^{\rm edge}_\beta$, here corresponding to the direction $\hat{\boldsymbol{\xi}}$ [29]. Within the edge, the motion in the plane orthogonal to $\mathbf{w}_{\rm motion}$ remains inhibited, in agreement with the measured ν velocity. A similar behaviour is found on the edge $-J\hat{\mathbf{m}}$, albeit with opposite orientation of velocity.

A hallmark of 4D quantum Hall physics is the peculiar nature of excitations above the ground band, which can be linked to classical cyclotron trajectories. While cyclotron motion in 2D and 3D always corresponds to planar circular orbits, we expect more complex trajectories in 4D, involving two planar rotations occurring at different rates. In our system, each of these two elementary excitations is generated by the Raman coupling along x or z, of corresponding frequencies ω_x and ω_z independently set by the amplitudes t_x and t_z. We excite the atoms by applying a diabatic velocity kick, and measure the subsequent time evolution of the center of mass. We show in Fig. 4a the orbit measured for $\omega_z/\omega_x \simeq 2$, revealing a non-planar trajectory. For this integer frequency ratio, the orbit is almost closed, and is reminiscent of a Lissajous orbit (Fig. 4b). We also studied the case of degenerate frequencies $\omega_z \simeq \omega_x$, which correspond to the coupling amplitudes used for our study of the ground band. In this 'isoclinic' case, we recover a planar cyclotron motion akin to lower-dimensional cyclotron orbits (Fig. 4c,d).

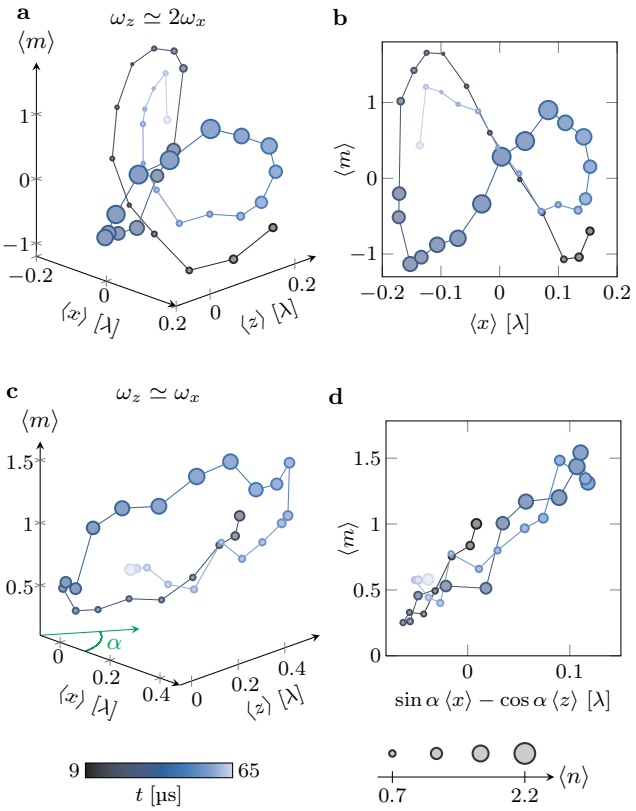

FIG. 4. **Cyclotron dynamics. a**. Evolution of the center-of-mass position following a velocity kick, for $\omega_z \simeq 2\omega_x$. The cartesian coordinates correspond to (x, z, m), while n is given by the mark size. The mark color indicates the evolution time subsequent to the kick. **b**. Projection in the xm plane corresponding to a quasi-closed Lissajouss curve. **c**. Cyclotron orbit measured for $\omega_z \simeq \omega_x$. The green arrow shows the viewpoint for the planar projection shown in **d**. **d**. Two-dimensional projection revealing the planar nature of the orbit viewed from the side.

The non-trivial topology of a quantum Hall system manifests in the quantization of its electromagnetic response. While involving the linear Hall conductance in 2D, it requires in 4D considering the non-linear response to both an electric force $\mathbf{f}$ and a magnetic field $\mathbf{b}$. These two perturbations induce a current

$$j^{\alpha}_{\text{non-linear}} = \frac{\mathcal{C}_2}{4\pi^2}\epsilon^{\alpha\beta\gamma\delta} f_\delta b_{\beta\gamma},$$

where $\epsilon^{\alpha\beta\gamma\delta}$ is the 4D Levi-Civita symbol and $\mathcal{C}_2$ is the integer second Chern number [22]. In other words, the magnetic field $b_{\beta\gamma}$ induces a Hall effect in the perpendicular plane.

We first demonstrate the quantization of the non-linear response by reconstructing the second Chern number in terms of a non-linear combination of Berry curvatures. For an infinite lattice system, it can be expressed as an integral over the Brillouin zone $\mathcal{C}_2 = \int \rho_2 \, \mathrm{d}^4q/(8\pi^2)$, where $\rho_2 = \frac{1}{8}\epsilon_{\alpha\beta\gamma\delta}\Omega^{\alpha\beta}\Omega^{\gamma\delta}$ is the second Chern character (see Fig. 5a and Methods). Since our system exhibits edges along m, the full band spectrum is gapless (Fig. 1d), preventing a truly topological character for the system as a whole. To recover quantization, we compute from our data the local second Chern marker, which quantifies the non-linear response resolved in m, as (see Methods)

$$C_2(m) = \frac{1}{3}\int_{|p|<p^\star} \rho_2(p,q)\Pi_m(p,q)\mathrm{d}p\,\mathrm{d}q,$$

where $p^\star = 7k$ is a momentum cutoff delimiting the bulk mode region (Fig. 5b). In the central region $-5 \leq m \leq 5$, we measure an almost constant marker $C_2(m) = 0.97(6)$, compatible with the second Chern number $\mathcal{C}_2 = 1$, demonstrating topological quantization.

In order to directly probe the non-linear response, we implement a magnetic perturbation b_{nm}, expecting the appearance of a Hall effect in the xz plane. For this, we modified the polarization of the laser beam propagating along x, such that the spin transition amplitude becomes (see Methods)

$$J_+ \to J_+ + \mathrm{i}\epsilon\frac{\{J_+, J_z\}}{2},$$

with $\epsilon \simeq 0.1$, leading to a complex phase amplitude $\phi'_x \simeq \epsilon m$. According to (2), this phase corresponds to an additional vector potential $\mathbf{A}' = (0, 0, 2\epsilon m, \epsilon m)/3$, hence the magnetic field component $b_{nm} = -\partial_m A_n = -2\epsilon/3$. We investigate its effect on the xz dynamics subsequent to a kick along x, using laser couplings such that $\omega_x \simeq \omega_z \equiv \omega$ in the absence of magnetic perturbation. The xz dynamics shown in Fig. 5c,d,e are reminiscent of those of a Foucault pendulum, namely a harmonic oscillation at ω, with a slower precession governed by the b_{nm} field. We show in Methods that, in the bulk, the precession rate

$$\omega_{\mathrm{p}} = \frac{1}{2}M\omega^2\rho_2^{\text{bulk}}b_{nm} \tag{6}$$

gives access to the second Chern character ρ_2^{bulk}. Our measurements yield $\rho_2^{\text{bulk}} \simeq 0.65(2)/k^2$, close to the theoretical expectation $\rho_2^{\text{bulk}} = \frac{1}{8}\epsilon_{\alpha\beta\gamma\delta}\Omega^{\alpha\beta}_{\text{bulk}}\Omega^{\gamma\delta}_{\text{bulk}} = 3/(4k^2)$ and to the value $0.75(7)/k^2$ computed from the Berry curvature measurements.

In conclusion, we realized a 4D quantum Hall system, and revealed its non-trivial topological character. Other specific properties of the 4D quantum Hall effect could be addressed in future work, such as the complex edge mode trajectories expected for compact boundaries [32]. Our protocol could also be generalized to engineer other classes of topological systems, such as 5D Weyl semimetals [33] and 6D quantum Hall systems [34, 35]. Furthermore, our work opens a door towards the study of interacting quantum many-body physics in high-dimensional topological structures, where one expects generalized fractional quantum Hall states [9, 16, 36]. Interacting quantum Hall states in high dimensions could also be used to simulate high-energy physics models, such as quantum gravity [9] and Yang-Mills field theory [17, 18].

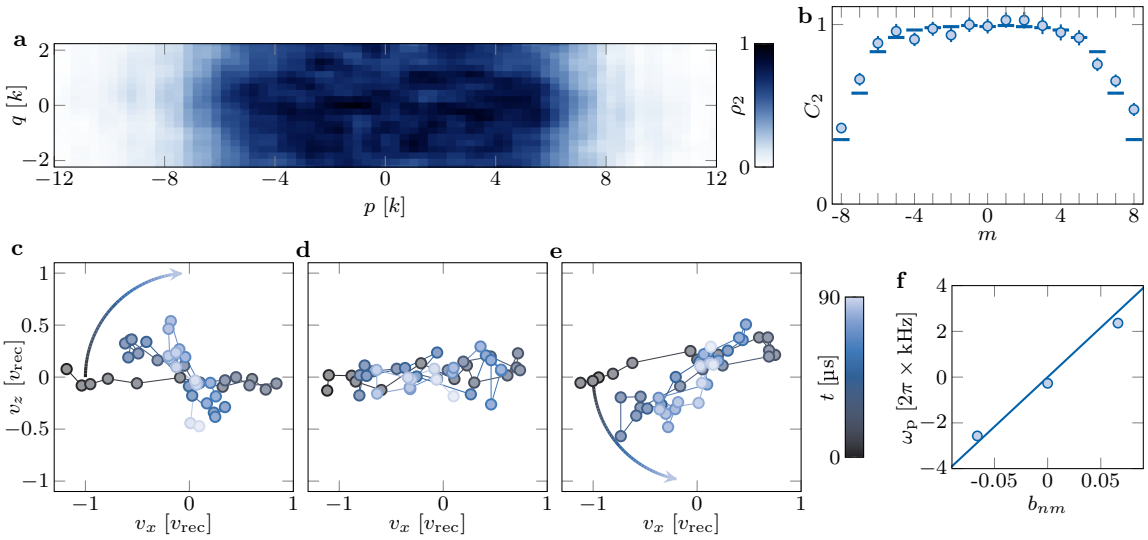

FIG. 5. **Topological structure of the ground band.** **a**. Second Chern character ρ_2 computed from the product of measured Berry curvatures. **b**. Local second Chern marker inferred from **a**. **c**, **d**, **e.** Velocity dynamics in the xz plane for three different values of the magnetic perturbation $b_{nm} = -0.066, 0, 0.066$, respectively. **f.** Precession rate $\omega_{\rm p}$ as a function of the b_{nm} field. The solid line is the prediction of (6) for the bulk second Chern character $\rho_2^{\rm bulk} = 3/(4k^2)$.

[1] K. v. Klitzing, G. Dorda, and M. Pepper, New Method for High-Accuracy Determination of the Fine-Structure Constant Based on Quantized Hall Resistance, Phys. Rev. Lett. **45**, 494 (1980).

[2] D. J. Thouless, M. Kohmoto, M. P. Nightingale, and M. den Nijs, Quantized Hall Conductance in a Two-Dimensional Periodic Potential, Phys. Rev. Lett. **49**, 405 (1982).

[3] B. I. Halperin, Quantized Hall conductance, current-carrying edge states, and the existence of extended states in a two-dimensional disordered potential, Phys. Rev. B **25**, 2185 (1982).

[4] D. Hsieh, D. Qian, L. Wray, Y. Xia, Y. S. Hor, R. J. Cava, and M. Z. Hasan, A topological Dirac insulator in a quantum spin Hall phase, Nature **452**, 970 (2008).

[5] L. Lu, Z. Wang, D. Ye, L. Ran, L. Fu, J. D. Joannopoulos, and M. Soljačić, Experimental observation of Weyl points, Science **349**, 622 (2015).

[6] S.-Y. Xu, I. Belopolski, N. Alidoust, M. Neupane, G. Bian, C. Zhang, R. Sankar, G. Chang, Z. Yuan, C.-C. Lee, S.-M. Huang, H. Zheng, J. Ma, D. S. Sanchez, B. Wang, A. Bansil, F. Chou, P. P. Shibayev, H. Lin, S. Jia, and M. Z. Hasan, Discovery of a Weyl fermion semimetal and topological Fermi arcs, Science **349**, 613 (2015).

[7] S. Ryu, A. P. Schnyder, A. Furusaki, and A. W. W. Ludwig, Topological insulators and superconductors: Tenfold way and dimensional hierarchy, New J. Phys. **12**, 065010 (2010).

[8] J. Fröhlich and B. Pedrini, New applications of the chiral anomaly, in *Mathematical Physics 2000* (World Scientific, 2000) pp. 9–47.

[9] S.-C. Zhang and J. Hu, A Four-Dimensional Generalization of the Quantum Hall Effect, Science **294**, 823 (2001).

[10] M. Lohse, C. Schweizer, H. M. Price, O. Zilberberg, and I. Bloch, Exploring 4D quantum Hall physics with a 2D topological charge pump, Nature **553**, 55 (2018).

[11] O. Zilberberg, S. Huang, J. Guglielmon, M. Wang, K. P. Chen, Y. E. Kraus, and M. C. Rechtsman, Photonic topological boundary pumping as a probe of 4D quantum Hall physics, Nature **553**, 59 (2018).

[12] Y. Wang, H. M. Price, B. Zhang, and Y. D. Chong, Circuit implementation of a four-dimensional topological insulator, Nat Commun **11**, 2356 (2020).

[13] A. Celi, P. Massignan, J. Ruseckas, N. Goldman, I. B. Spielman, G. Juzeliūnas, and M. Lewenstein, Synthetic Gauge Fields in Synthetic Dimensions, Phys. Rev. Lett. **112** (2014).

[14] M. Mancini, G. Pagano, G. Cappellini, L. Livi, M. Rider, J. Catani, C. Sias, P. Zoller, M. Inguscio, M. Dalmonte, and L. Fallani, Observation of chiral edge states with neutral fermions in synthetic Hall ribbons, Science **349**, 1510 (2015).

[15] B. K. Stuhl, H.-I. Lu, L. M. Aycock, D. Genkina, and I. B. Spielman, Visualizing edge states with an atomic Bose gas in the quantum Hall regime, Science **349**, 1514 (2015).

[16] B. A. Bernevig, C.-H. Chern, J.-P. Hu, N. Toumbas, and S.-C. Zhang, Effective Field Theory Description of the Higher Dimensional Quantum Hall Liquid, Annals of Physics **300**, 185 (2002).

[17] C. N. Yang and R. L. Mills, Conservation of Isotopic Spin and Isotopic Gauge Invariance, Phys. Rev. **96**, 191 (1954).

[18] A. Barns-Graham, N. Dorey, N. Lohitsiri, D. Tong, and C. Turner, ADHM and the 4d quantum Hall effect, J. High Energ. Phys. **2018**, 40.

[19] A. Bansil, H. Lin, and T. Das, *Colloquium* : Topological

band theory, Rev. Mod. Phys. **88** (2016).
[20] T. Ozawa and H. M. Price, Topological quantum matter in synthetic dimensions, Nat. Rev. Phys. **1**, 349 (2019).
[21] Y. E. Kraus, Z. Ringel, and O. Zilberberg, Four-Dimensional Quantum Hall Effect in a Two-Dimensional Quasicrystal, Phys. Rev. Lett. **111**, 226401 (2013).
[22] H. M. Price, O. Zilberberg, T. Ozawa, I. Carusotto, and N. Goldman, Four-Dimensional Quantum Hall Effect with Ultracold Atoms, Phys. Rev. Lett. **115**, 195303 (2015).
[23] T. Ozawa, H. M. Price, N. Goldman, O. Zilberberg, and I. Carusotto, Synthetic dimensions in integrated photonics: From optical isolation to four-dimensional quantum Hall physics, Phys. Rev. A **93**, 043827 (2016).
[24] X.-L. Qi, T. L. Hughes, and S.-C. Zhang, Topological field theory of time-reversal invariant insulators, Phys. Rev. B **78**, 195424 (2008).
[25] C. N. Yang, Generalization of Dirac's monopole to SU2 gauge fields, J. Math. Phys. **19**, 320 (1978).
[26] S. Sugawa, F. Salces-Carcoba, A. R. Perry, Y. Yue, and I. B. Spielman, Second Chern number of a quantum-simulated non-Abelian Yang monopole, Science **360**, 1429 (2018).
[27] X. Tan, D.-W. Zhang, W. Zheng, X. Yang, S. Song, Z. Han, Y. Dong, Z. Wang, D. Lan, H. Yan, S.-L. Zhu, and Y. Yu, Experimental Observation of Tensor Monopoles with a Superconducting Qudit, Phys. Rev. Lett. **126**, 017702 (2021).
[28] M. Chen, C. Li, G. Palumbo, Y.-Q. Zhu, N. Goldman, and P. Cappellaro, A synthetic monopole source of Kalb-Ramond field in diamond, Science **375**, 1017 (2022).
[29] H. Elvang and J. Polchinski, The quantum Hall effect on R4, Comptes Rendus Physique **4**, 405 (2003).
[30] A. Fabre, J.-B. Bouhiron, T. Satoor, R. Lopes, and S. Nascimbene, Simulating two-dimensional dynamics within a large-size atomic spin, Phys. Rev. A **105**, 013301 (2022).
[31] Y.-J. Lin, R. L. Compton, K. Jiménez-García, J. V. Porto, and I. B. Spielman, Synthetic magnetic fields for ultracold neutral atoms, Nature **462**, 628 (2009).
[32] B. Estienne, B. Oblak, and J.-M. Stéphan, Ergodic edge modes in the 4D quantum Hall effect, SciPost Phys. **11**, 016 (2021).
[33] B. Lian and S.-C. Zhang, Five-dimensional generalization of the topological Weyl semimetal, Phys. Rev. B **94**, 041105 (2016).
[34] C. H. Lee, Y. Wang, Y. Chen, and X. Zhang, Electromagnetic response of quantum Hall systems in dimensions five and six and beyond, Phys. Rev. B **98**, 094434 (2018).
[35] I. Petrides, H. M. Price, and O. Zilberberg, Six-dimensional quantum Hall effect and three-dimensional topological pumps, Phys. Rev. B **98**, 125431 (2018).
[36] C. Nayak, S. H. Simon, A. Stern, M. Freedman, and S. Das Sarma, Non-Abelian anyons and topological quantum computation, Rev. Mod. Phys. **80**, 1083 (2008).
[37] R. Lynch, The quantum phase problem: A critical review, Physics Reports **256**, 367 (1995).
[38] R. Bianco and R. Resta, Mapping topological order in coordinate space, Phys. Rev. B **84**, 241106 (2011).
[39] J. Sykes and R. Barnett, Local topological markers in odd dimensions, Phys. Rev. B **103**, 155134 (2021).
[40] T. Chalopin, T. Satoor, A. Evrard, V. Makhalov, J. Dalibard, R. Lopes, and S. Nascimbene, Probing chiral edge dynamics and bulk topology of a synthetic Hall system, Nat. Phys. **16**, 1017 (2020).

B

RÉSUMÉ ÉTENDU EN FRANÇAIS

Production de gaz ultrafroids de dysprosium

Au XXe siècle, les systèmes de matière condensée, tels que les matériaux magnétiques, les supraconducteurs et l'hélium liquide, ont été à l'avant-garde des développements de la physique quantique. Au cours des dernières décennies, les expériences sur les atomes ultrafroids (et leurs cousins dans le domaine plus large de la physique atomique, moléculaire et optique) ont apporté de nouvelles possibilités passionnantes pour sonder les fondements de la mécanique quantique, comprendre les effets de nombreux corps par simulation quantique et concevoir des systèmes entièrement nouveaux sans équivalent traditionnel en matière condensée. Cela est rendu possible par un contrôle exquis des paramètres physiques, notamment des potentiels spatiaux, des interactions, de la dimensionnalité et du couplage à l'environnement, le tout combiné à des protocoles de détection précis et microscopiques.

Les principes de la manipulation du mouvement et des états internes des atomes à l'aide de la lumière étaient déjà présents dans les premiers travaux d'Einstein [13] et de Kastler [14]. Les techniques modernes de refroidissement par laser se sont rapidement développées à partir du milieu des années 1970, suite à la généralisation des sources laser accordables avec précision. On peut en trouver un résumé dans les conférences Nobel 1998 de Chu, Cohen-Tannoudji et Phillips [15-17]. Ces développements ont abouti à la création de gaz ultrafroids dilués et dégénérés, où la taille du paquet d'ondes quantiques associé à un seul atome, c'est-à-dire la longueur d'onde de de Broglie thermique, est comparable à l'espacement entre les atomes. Selon les statistiques quantiques des atomes impliqués, de tels échantillons forment des condensats de Bose-Einstein (BEC) [18, 19] ou des gaz de Fermi dégénérés [20]. Ce fut la naissance du domaine des atomes ultrafroids dans sa forme actuelle, et plusieurs résultats marquants ont été obtenus au cours des années suivantes. Il s'agit notamment de l'observation de la transition de phase de l'isolant Mott au superfluide [21], de la transition Berezinskii-Kosterlitz-Thouless [22] et le passage du BEC moléculaire au superfluide Bardeen-Cooper-Schrieffer [23-26] (voir réf. [27, 28] pour des revues plus complètes).

Les travaux ci-dessus ont été réalisés avec des éléments dont les interactions interatomiques sont données par des forces de van der Waals à courte portée. De nouvelles

possibilités sont créées avec des interactions dipôle-dipôle magnétiques à longue portée, comme cela a été illustré pour la première fois avec les BECs de chrome avec l'observation d'un comportement ferrofluide [29]. L'étude des gaz ultrafroids dipolaires s'est accélérée au cours de la dernière décennie, suite au refroidissement des éléments lanthanides dysprosium [30, 31] et erbium [32] jusqu'à la dégénérescence quantique. Ici, le contrôle des interactions fortes à longue portée et leur interaction subtile avec les interactions à courte portée ont conduit à l'observation de nouvelles phases de gouttelettes [33] et de supersolides [34-36] (voir réf. [37] pour une revue).

Dans le chapitre 2, nous décrirons notre dispositif expérimental pour la production de gaz de dysprosium ultrafroid. Plutôt que des interactions à longue portée, le travail présenté dans cette thèse exploite une autre caractéristique unique du dysprosium : son grand moment angulaire d'état fondamental $J = 8$. Nous expliquons comment nous utilisons les décalages lumineux dépendant du spin associés aux transitions à ligne étroite pour créer des hamiltoniens de spin non linéaires, avec des effets de chauffage minimaux. En combinant cette capacité avec le grand nombre d'états internes $2J + 1 = 17$, dont nous pouvons détecter les probabilités de projection individuellement, nous discutons de la façon dont notre expérience comme une plateforme flexible pour réaliser les études décrites ci-dessous.

Comportement critique et rupture de symétrie dans le modèle Lipkin-Meshkov-Glick

Les transitions de phase sont omniprésentes dans la nature, dans des systèmes à toutes les échelles d'énergie et de longueur, du plasma quark-gluon dans l'univers primitif à l'hélium liquide dans les cryostats de laboratoire. Notre compréhension des transitions de phase a historiquement reposé sur le comportement non analytique des quantités thermodynamiques, la rupture spontanée de la symétrie et les fluctuations du paramètre d'ordre. Ces concepts jouent toujours un rôle clé dans la description moderne des transitions de phase, qui est sous-tendue par le groupe de renormalisation [38], développé par Fisher, Wilson et Kadanoff dans les années 1970. Cette théorie permet une description commune et élégante de classes entières de systèmes proches d'une transition en termes de quelques paramètres universels, indépendants des détails microscopiques des systèmes particuliers [4]. Dans les systèmes quantiques, le changement de comportement observé lorsqu'on fait varier un paramètre de contrôle est compris en termes de véritable transition de phase se produisant à un point critique quantique - défini à température zéro dans un système infini. Aux températures finies, une interaction complexe de fluctuations thermiques et quantiques conduit à la criticité quantique, où les excitations ne peuvent être réduites à une théorie effective avec des interactions faibles [39]. Dans les systèmes finis, le point critique quantique apparaît également dans le régime de croisement, décrit quantitativement par des paramètres universels issus de la théorie de l'échelle de taille finie [40].

Les propriétés distinctes attendues à proximité d'un point critique quantique peuvent parfois être sondées par des observables macroscopiques, comme le ralentissement des temps de relaxation. Cependant, la révélation de propriétés spécifiquement quantiques, comme l'intrication quantique entre plusieurs corps, reste un défi. Le développement récent de systèmes quantiques hautement contrôlés de taille mésoscopique, tels que les cristaux ioniques [42], les systèmes de réseaux optiques [43], les réseaux d'atomes de Rydberg [44], ou les photons en interaction [45], permet une caractérisation microscopique des propriétés quantiques collectives [46] telles que la matrice de densité complète [45], l'entropie d'intrication [47] ou l'ordre non local des cordes [48]. Ce degré de contrôle pourrait être utilisé pour étudier des aspects fondamentaux des transitions de phase quantiques, comme le lien entre la rupture d'une symétrie sous-jacente et l'apparition d'un paramètre d'ordre non nul [3]. Ce lien ne peut être testé dans les systèmes macroscopiques, où les superpositions quantiques de grande taille ne peuvent pratiquement pas exister et où la rupture spontanée de symétrie est inévitable [49].

Dans le chapitre 3, nous présentons une étude expérimentale du modèle Lipkin-Meshkov-Glick (LMGm), qui décrit des spin-1/2s quantiques avec des interactions Ising de portée infinie dans un champ transversal. Dans la limite thermodynamique, le LMGm présente une transition de phase ferromagnétique, caractérisée par la rupture spontanée d'une symétrie $\mathbb{Z}_2$. Ce modèle a été proposé à l'origine pour les systèmes nucléaires : [50-52], mais il a trouvé une utilisation généralisée. Par exemple, le LMGm décrit des systèmes subissant la transition de superradiance de Dicke [53] (dans la limite de température zéro), et des BECs bimodes avec un effet tunnel de type Josephson [54, 55]. D'un point de vue théorique, le LMGm a été largement étudié en raison de sa tractabilité mathématique et de son lien étroit, via la théorie du champ moyen et l'échelle de taille finie, avec le modèle d'Ising à champ transversal à courte portée [56].

Notre réalisation du LMGm est basée sur l'équivalence entre le spin électronique $J = 8$ de l'atome de dysprosium et un ensemble de $N = 2J$ spins-1/2s dans un état symétrique d'échange. Nous simulons les interactions ferromagnétiques d'Ising avec un décalage de lumière quadratique. Étant donné ce codage de qubits, les moments du spin total-J donnent accès aux valeurs des corrélateurs à quelques qubits. Nous mesurons le passage entre les comportements para- et ferromagnétiques en utilisant les propriétés thermodynamiques et la réponse dynamique. Nous révélons un régime de comportement critique quantique et une dynamique ralentie autour du point de transition. Un atout spécifique de notre installation est l'accès direct à l'observable de parité correspondant à la symétrie $\mathbb{Z}_2$, rendu possible par la résolution d'un seul sous-niveau magnétique – ceci n'est pas possible dans les systèmes macroscopiques. Nous étudions le lien fondamental entre la rupture de symétrie et l'apparition d'un paramètre d'ordre fini. La taille mésoscopique du système nous offre un degré de contrôle qui nous permet de sonder spécifiquement la rupture de symétrie due à une perturbation appliquée manuellement (par exemple, pour mesurer la susceptibilité), ainsi que d'observer la rupture de symétrie spontanée due à des fluctuations environnementales aléatoires.

Partitionnement du spin électronique du dysprosium pour révéler l'intrication

L'intrication a toujours été la forme d'étrangeté associée aux systèmes quantiques. Schrödinger a appelé l'intrication "le trait caractéristique de la mécanique quantique, celui qui l'éloigne entièrement de la pensée classique" [57]. En bref, l'intrication permet des situations où la meilleure connaissance possible d'un tout (système quantique) n'inclut pas la meilleure connaissance possible de ses parties (sous-systèmes). Les premières discussions sur l'intrication se sont concentrées sur sa pertinence pour les interprétations à variables cachées de la mécanique quantique [5, 6]. Aujourd'hui, elle est également reconnue comme une ressource dans le contexte des technologies quantiques, pour des tâches telles que le calcul algorithmique, la communication, la cryptographie et la téléportation [58].

L'intrication joue également un rôle fondamental dans la conduite des transitions de phase quantiques [4, 41], sous la forme de la propagation des corrélations à travers de grandes échelles de longueur. En effet, si l'étude du modèle LMG décrit ci-dessus était réalisée sur un système avec des qubits individuellement distinguables, l'écrasement observé d'une quadrature de spin globale dans la région de croisement impliquerait une intrication entre les qubits [59]. Il est alors naturel de se demander si une signification physique peut être attribuée à l'"intrication des qubits codés" et dans quelle mesure elle est accessible en tant que ressource. C'est la ligne d'investigation qui anime notre deuxième étude expérimentale, présentée dans le chapitre 4, où nous effectuons une partition de cet ensemble à l'aide de transitions optiques, donnant accès aux propriétés d'intrication.

Précisons tout d'abord que l'intrication fait partie de la catégorie plus générale des comportements non-classiques. La non-classicalité peut être identifiée même dans les cas où les sous-systèmes ne peuvent être identifiés, par exemple les états de Fock en optique quantique. Les corrélations non classiques au sein de systèmes indivisibles peuvent être fondamentalement incompatibles avec une description classique, comme le démontre la violation des inégalités de type Bell [60]. Dans le spin de l'état fondamental du dysprosium, si l'ensemble des qubits codés ne peut pas être partitionné, nous devons nous limiter à affirmer que nous pouvons avoir un comportement non classique au niveau du spin total, correspondant aux corrélations quantiques de ses degrés de liberté internes.

Avant de décrire nos travaux, il est également utile de discuter les types de systèmes utilisés pour créer et détecter l'intrication. Les systèmes minimaux intriqués de paires de qubits, tels que réalisés avec des paires de photons corrélés, jouent un rôle central dans la vérification des fondements de la mécanique quantique [7, 61], par la violation des inégalités de Bell [6]. L'intrication peut également être conçue dans des systèmes à plusieurs particules [62], tels qu'un ensemble d'atomes en interaction [63]. Dans ce cas, les atomes ne sont pas adressables individuellement, et les corrélations quantiques sont indirectement révélées par la mesure de propriétés globales, telles qu'une quadrature de

projection de spin comprimée [64-67] ou via l'amélioration quantique de la sensibilité métrologique [68-70]. Des expériences de pointe avec des systèmes photoniques [71], des qubits supraconducteurs [72], des ions piégés [73] et des réseaux d'atomes de Rydberg [74] peuvent maintenant produire des états hautement intriqués de dizaines de qubits identifiables individuellement, où l'intrication est plus facilement observable.

Dans notre travail, nous accédons d'abord aux propriétés d'intrication en partitionnant le spin à l'aide d'un couplage optique à un état excité $J' = J - 1$. Cela supprime une paire de qubits dans un état défini par la polarisation de la lumière. En partant des états W et comprimés bien connus, nous extrayons la concurrence des paires de qubits, qui quantifie leur caractère non classique. Nous démontrons aussi directement l'intrication entre les sous-systèmes à 14 et 2 qubits par une augmentation de l'entropie lors de la partition. Dans une deuxième série de mesures, nous sondons la décohérence d'un état préparé dans le niveau excité $J' = J + 1$ et interprétons l'émission spontanée comme une perte d'une paire de qubits dans un état aléatoire. Cela nous permet de contraster la robustesse des corrélations non classiques par paire de l'état W avec la fragilité de la cohérence impliquée dans un état chat de Schr'odinger [75]. Ces observations sont liées à l'information *which path* portée par la polarisation du photon émis. Nos résultats peuvent être considérés dans le cadre du récent débat sur la non-classicalité et l'intrication dans les systèmes de constituants indiscernables [76]. Nous discutons également d'expériences futures impliquant des atomes intriqués dans des configurations spatialement séparées, et plus généralement de la physique de spin à plusieurs corps avec le dysprosium.

Topologie et spectre d'intrication d'un système de Hall synthétique

Nous nous éloignons maintenant de l'idée de qubits encodés dans le spin de l'état fondamental électronique. Pour la réalisation de systèmes topologiques, nous utilisons les sous-niveaux magnétiques de $2J + 1$ pour représenter une 'position' discrète dans une dimension synthétique, comme cela a été proposé à l'origine dans l'article [77]. Le mouvement le long de points voisins dans la dimension synthétique est permis par des transitions laser à deux photons, qui créent des facteurs de phase de saut complexes (cf. la phase Aharanov-Bohm) et un lien bien défini avec le mouvement de l'atome le long de l'axe de recul du photon. Cela motive une analogie avec une particule chargée se déplaçant en deux dimensions en présence d'un champ magnétique perpendiculaire. Ainsi, nous réalisons un système de Hall dans une géométrie en ruban ; ici, une dimension est le long d'un axe dans l'espace réel, tandis que l'autre est une dimension synthétique finie encodée dans le spin.

Les systèmes de Hall quantique sont célèbres pour la quantification extrêmement robuste de leur conductance transversale. Dans les systèmes traditionnels de matière condensée, les impuretés et le désordre conduisent à des bandes conductrices entourant des domaines isolants d'électrons localisés, ce qui rend les comparaisons avec des

modèles simples difficiles [78, 79]. La conductance de Hall quantifiée résulte de la structuration topologique non triviale des états quantiques d'une bande d'électrons [10]. Pour un système infini, cette structure est décrite par le nombre de Chern, un invariant topologique prenant des valeurs entières, qui est robuste jusqu'à un certain degré de désordre [10]. Dans un système réel de taille finie, la topologie non triviale conduit à des modes de bord sans vide, caractérisés par un mouvement unidirectionnel protégé de la rétrodiffusion [79]. Ces modes de bord chiraux, ainsi que leur généralisation aux isolants topologiques, aux supraconducteurs topologiques ou aux états de Hall quantiques fractionnaires [80, 81], sont au cœur d'applications possibles en spintronique [82] ou en informatique quantique [83].

Les premiers travaux utilisant des dimensions synthétiques de taille limitée ont permis de mesurer des courants de bord chiraux [84, 85]. Cependant, la pertinence des propriétés topologiques nécessite la notion de bulk. Dans BLAH, nous décrivons la réalisation d'un système de Hall synthétique avec des propriétés de bulk et de bord distinctes. Dans la bande la plus basse, nous caractérisons les modes de masse sans dispersion, où le mouvement est inhibé en raison d'une bande d'énergie aplatie, et les états de bord chiraux, où les particules sont libres de se déplacer dans une seule direction. Nous étudions également les excitations élémentaires du système vers des bandes supérieures, qui prennent la forme d'orbites cyclotron dans le volume et d'orbites à saut le long des bords. Enfin, nous mesurons la dérive de Hall induite par une tension externe, et caractérisons la réponse de Hall locale de la bande en utilisant le marqueur de Chern local, qui quantifie l'ordre topologique dans l'espace réel [86]. Nos expériences montrent que la dimension synthétique est suffisamment grande pour permettre un bulk significatif avec des propriétés topologiques robustes.

Les propriétés d'intrication des états à plusieurs corps contiennent des informations clés sur les propriétés topologiques. En particulier, la structure des valeurs propres de la matrice de densité d'un sous-système donné, connue sous le nom de spectre d'intrication, donne le spectre d'excitation à plusieurs corps des modes de bord chiraux du système global [87]. Nous réinterprétons nos résultats expérimentaux de ce point de vue, révélant une signature du spectre d'intrication au niveau de la particule unique. Nous discutons ensuite de la façon dont les propriétés d'intrication pourraient être sondées directement dans notre système avec de futures expériences, inspirées par une proposition récente non encore réalisée [88]. Nous concluons par une perspective sur la réalisation d'états topologiques à corps multiples avec le dysprosium.

BIBLIOGRAPHY

[1] T. S. Kuhn, *The Structure of Scientific Revolutions: 50th Anniversary Edition*, edited by I. Hacking (University of Chicago Press, Chicago, IL, Apr. 2012), 264 pp. (cited on page 11).

[2] P. W. Anderson, 'More Is Different', Science **177**, 393–396 (1972) (cited on page 11).

[3] L. D. Landau, 'On the theory of phase transitions', Journal of Experimental and Theoretical Physics **7**, 19–32 (1937) (cited on pages 11, 14, 65, 202).

[4] S. Sachdev, *Quantum Phase Transitions*, 2nd ed. (Cambridge University Press, Cambridge, 2011) (cited on pages 11, 13, 15, 48, 52, 67, 71, 201, 203).

[5] A. Einstein, B. Podolsky and N. Rosen, 'Can Quantum-Mechanical Description of Physical Reality Be Considered Complete?', Physical Review **47**, 777–780 (1935) (cited on pages 11, 15, 203).

[6] J. S. Bell, 'On the Einstein Podolsky Rosen paradox', Physics Physique Fizika **1**, 195–200 (1964) (cited on pages 11, 15, 90, 203).

[7] A. Aspect, J. Dalibard and G. Roger, 'Experimental Test of Bell's Inequalities Using Time-Varying Analyzers', Physical Review Letters **49**, 1804–1807 (1982) (cited on pages 11, 15, 203).

[8] A. Aspect, P. Grangier and G. Roger, 'Experimental Realization of Einstein-Podolsky-Rosen-Bohm Gedankenexperiment: A New Violation of Bell's Inequalities', Physical Review Letters **49**, 91–94 (1982) (cited on page 11).

[9] K. v. Klitzing, G. Dorda and M. Pepper, 'New Method for High-Accuracy Determination of the Fine-Structure Constant Based on Quantized Hall Resistance', Physical Review Letters **45**, 494–497 (1980) (cited on pages 11, 127, 139).

[10] D. J. Thouless, M. Kohmoto, M. P. Nightingale and M. den Nijs, 'Quantized Hall Conductance in a Two-Dimensional Periodic Potential', Physical Review Letters **49**, 405–408 (1982) (cited on pages 11, 17, 131, 205).

[11] C. Nayak, S. H. Simon, A. Stern, M. Freedman and S. Das Sarma, 'Non-Abelian anyons and topological quantum computation', Reviews of Modern Physics **80**, 1083–1159 (2008) (cited on page 12).

[12] R. B. Laughlin, 'Anomalous Quantum Hall Effect: An Incompressible Quantum Fluid with Fractionally Charged Excitations', Physical Review Letters **50**, 1395–1398 (1983) (cited on page 12).

[13] A. Einstein, 'Zur Quantentheorie der Strahlung', Phys. Z. **18**, 121–128 (1917) (cited on pages 12, 200).

[14] A. Kastler, 'Quelques suggestions concernant la production optique et la détection optique d'une inégalité de population des niveaux de quantifigation spatiale des atomes. Application à l'expérience de Stern et Gerlach et à la résonance magnétique', Journal de Physique et le Radium **11**, 255–265 (1950) (cited on pages 12, 200).

[15] S. Chu, 'Nobel Lecture: The manipulation of neutral particles', Reviews of Modern Physics **70**, 685–706 (1998) (cited on pages 12, 200).

[16] C. N. Cohen-Tannoudji, 'Nobel Lecture: Manipulating atoms with photons', Reviews of Modern Physics **70**, 707–719 (1998) (cited on pages 12, 200).

[17] W. D. Phillips, 'Nobel Lecture: Laser cooling and trapping of neutral atoms', Reviews of Modern Physics **70**, 721–741 (1998) (cited on pages 12, 200).

[18] M. H. Anderson, J. R. Ensher, M. R. Matthews, C. E. Wieman and E. A. Cornell, 'Observation of Bose-Einstein Condensation in a Dilute Atomic Vapor', Science **269**, 198–201 (1995) (cited on pages 12, 200).

[19] K. B. Davis, M.-O. Mewes, M. R. Andrews, N. J. van Druten, D. S. Durfee, D. M. Kurn and W. Ketterle, 'Bose-Einstein Condensation in a Gas of Sodium Atoms', Physical Review Letters **75**, 3969–3973 (1995) (cited on pages 12, 200).

[20] B. DeMarco and D. S. Jin, 'Onset of Fermi Degeneracy in a Trapped Atomic Gas', Science **285**, 1703–1706 (1999) (cited on pages 12, 200).

[21] M. Greiner, O. Mandel, T. Esslinger, T. W. Hänsch and I. Bloch, 'Quantum phase transition from a superfluid to a Mott insulator in a gas of ultracold atoms', Nature **415**, 39–44 (2002) (cited on pages 12, 200).

[22] Z. Hadzibabic, P. Krüger, M. Cheneau, B. Battelier and J. Dalibard, 'Berezinskii-Kosterlitz-Thouless crossover in a trapped atomic gas', Nature **441**, 1118–1121 (2006) (cited on pages 13, 200).

[23] M. Bartenstein, A. Altmeyer, S. Riedl, S. Jochim, C. Chin, J. H. Denschlag and R. Grimm, 'Collective Excitations of a Degenerate Gas at the BEC-BCS Crossover', Physical Review Letters **92**, 203201 (2004) (cited on pages 13, 200).

[24] T. Bourdel, L. Khaykovich, J. Cubizolles, J. Zhang, F. Chevy, M. Teichmann, L. Tarruell, S. J. J. M. F. Kokkelmans and C. Salomon, 'Experimental Study of the BEC-BCS Crossover Region in Lithium 6', Physical Review Letters **93**, 050401 (2004) (cited on pages 13, 200).

[25] C. A. Regal, M. Greiner and D. S. Jin, 'Observation of Resonance Condensation of Fermionic Atom Pairs', Physical Review Letters **92**, 040403 (2004) (cited on pages 13, 200).

[26] M. W. Zwierlein, C. A. Stan, C. H. Schunck, S. M. F. Raupach, A. J. Kerman and W. Ketterle, 'Condensation of Pairs of Fermionic Atoms near a Feshbach Resonance', Physical Review Letters **92**, 120403 (2004) (cited on pages 13, 200).

[27] I. Bloch, J. Dalibard and W. Zwerger, 'Many-body physics with ultracold gases', Reviews of Modern Physics **80**, 885–964 (2008) (cited on pages 13, 200).

[28] I. Bloch, J. Dalibard and S. Nascimbène, 'Quantum simulations with ultracold quantum gases', Nature Physics **8**, 267–276 (2012) (cited on pages 13, 200).

[29] T. Lahaye, T. Koch, B. Fröhlich, M. Fattori, J. Metz, A. Griesmaier, S. Giovanazzi and T. Pfau, 'Strong dipolar effects in a quantum ferrofluid', Nature **448**, 672–675 (2007) (cited on pages 13, 201).

[30] M. Lu, N. Q. Burdick, S. H. Youn and B. L. Lev, 'Strongly Dipolar Bose-Einstein Condensate of Dysprosium', Physical Review Letters **107**, 190401 (2011) (cited on pages 13, 21, 40, 201).

[31] M. Lu, N. Q. Burdick and B. L. Lev, 'Quantum Degenerate Dipolar Fermi Gas', Physical Review Letters **108**, 215301 (2012) (cited on pages 13, 201).

[32] K. Aikawa, A. Frisch, M. Mark, S. Baier, A. Rietzler, R. Grimm and F. Ferlaino, 'Bose-Einstein Condensation of Erbium', Physical Review Letters **108**, 210401 (2012) (cited on pages 13, 21, 201).

[33] I. Ferrier-Barbut, H. Kadau, M. Schmitt, M. Wenzel and T. Pfau, 'Observation of Quantum Droplets in a Strongly Dipolar Bose Gas', Physical Review Letters **116**, 215301 (2016) (cited on pages 13, 201).

[34] L. Chomaz et al., 'Long-Lived and Transient Supersolid Behaviors in Dipolar Quantum Gases', Physical Review X **9**, 021012 (2019) (cited on pages 13, 201).

[35] L. Tanzi, E. Lucioni, F. Famà, J. Catani, A. Fioretti, C. Gabbanini, R. N. Bisset, L. Santos and G. Modugno, 'Observation of a Dipolar Quantum Gas with Metastable Supersolid Properties', Physical Review Letters **122**, 130405 (2019) (cited on pages 13, 201).

[36] F. Böttcher, J.-N. Schmidt, M. Wenzel, J. Hertkorn, M. Guo, T. Langen and T. Pfau, 'Transient Supersolid Properties in an Array of Dipolar Quantum Droplets', Physical Review X **9**, 011051 (2019) (cited on pages 13, 201).

[37] L. Chomaz, I. Ferrier-Barbut, F. Ferlaino, B. Laburthe-Tolra, B. L. Lev and T. Pfau, 'Dipolar physics: A review of experiments with magnetic quantum gases', 7th Jan. 2022, arXiv:2201.02672 [cond-mat, physics:physics, physics:quant-ph] (cited on pages 13, 21, 122, 201).

[38] M. E. Fisher, 'The renormalization group in the theory of critical behavior', Reviews of Modern Physics **46**, 597–616 (1974) (cited on pages 13, 201).

[39] P. Coleman and A. J. Schofield, 'Quantum criticality', Nature **433**, 226–229 (2005) (cited on pages 13, 52, 201).

[40] M. E. Fisher and M. N. Barber, 'Scaling Theory for Finite-Size Effects in the Critical Region', Physical Review Letters **28**, 1516–1519 (1972) (cited on pages 13, 53, 201).

[41] A. Osterloh, L. Amico, G. Falci and R. Fazio, 'Scaling of entanglement close to a quantum phase transition', Nature **416**, 608–610 (2002) (cited on pages 13, 15, 67, 203).

[42] R. Blatt and C. F. Roos, 'Quantum simulations with trapped ions', Nature Physics **8**, 277–284 (2012) (cited on pages 14, 202).

[43] C. Gross and I. Bloch, 'Quantum simulations with ultracold atoms in optical lattices', Science **357**, 995–1001 (2017) (cited on pages 14, 202).

[44] M. Saffman, 'Quantum computing with atomic qubits and Rydberg interactions: progress and challenges', Journal of Physics B: Atomic, Molecular and Optical Physics **49**, 202001 (2016) (cited on pages 14, 202).

[45] X.-s. Ma, B. Dakic, W. Naylor, A. Zeilinger and P. Walther, 'Quantum simulation of the wavefunction to probe frustrated Heisenberg spin systems', Nature Physics **7**, 399–405 (2011) (cited on pages 14, 202).

[46] I. M. Georgescu, S. Ashhab and F. Nori, 'Quantum simulation', Reviews of Modern Physics **86**, 153–185 (2014) (cited on pages 14, 202).

[47] R. Islam, R. Ma, P. M. Preiss, M. Eric Tai, A. Lukin, M. Rispoli and M. Greiner, 'Measuring entanglement entropy in a quantum many-body system', Nature **528**, 77–83 (2015) (cited on pages 14, 89, 202).

[48] T. A. Hilker, G. Salomon, F. Grusdt, A. Omran, M. Boll, E. Demler, I. Bloch and C. Gross, 'Revealing hidden antiferromagnetic correlations in doped Hubbard chains via string correlators', Science **357**, 484–487 (2017) (cited on pages 14, 202).

[49] P. W. Anderson, *Basic notions of condensed matter physics* (Benjamin-Cummings, 1984), 578 pp. (cited on pages 14, 49, 202).

[50] H. J. Lipkin, N. Meshkov and A. J. Glick, 'Validity of many-body approximation methods for a solvable model: (I). Exact solutions and perturbation theory', Nuclear Physics **62**, 188–198 (1965) (cited on pages 14, 50, 202).

[51] N. Meshkov, A. J. Glick and H. J. Lipkin, 'Validity of many-body approximation methods for a solvable model: (II). Linearization procedures', Nuclear Physics **62**, 199–210 (1965) (cited on pages 14, 50, 202).

[52] A. J. Glick, H. J. Lipkin and N. Meshkov, 'Validity of many-body approximation methods for a solvable model: (III). Diagram summations', Nuclear Physics **62**, 211–224 (1965) (cited on pages 14, 50, 202).

[53] J. Reslen, L. Quiroga and N. F. Johnson, 'Direct equivalence between quantum phase transition phenomena in radiation-matter and magnetic systems: Scaling of entanglement', Europhysics Letters **69**, 8 (2004) (cited on pages 14, 51, 67, 202).

[54] M. Albiez, R. Gati, J. Fölling, S. Hunsmann, M. Cristiani and M. K. Oberthaler, 'Direct Observation of Tunneling and Nonlinear Self-Trapping in a Single Bosonic Josephson Junction', Physical Review Letters **95**, 010402 (2005) (cited on pages 14, 51, 202).

[55] S. Levy, E. Lahoud, I. Shomroni and J. Steinhauer, 'The a.c. and d.c. Josephson effects in a Bose–Einstein condensate', Nature **449**, 579–583 (2007) (cited on pages 14, 51, 202).

[56] R. Botet, R. Jullien and P. Pfeuty, 'Size Scaling for Infinitely Coordinated Systems', Physical Review Letters **49**, 478–481 (1982) (cited on pages 14, 53, 60, 61, 74, 82, 202).

[57] E. Schrödinger, 'Discussion of Probability Relations between Separated Systems', Mathematical Proceedings of the Cambridge Philosophical Society **31**, 555–563 (1935) (cited on pages 15, 203).

[58] R. Horodecki, P. Horodecki, M. Horodecki and K. Horodecki, 'Quantum entanglement', Reviews of Modern Physics **81**, 865–942 (2009) (cited on pages 15, 87, 203).

[59] X. Wang and B. C. Sanders, 'Spin squeezing and pairwise entanglement for symmetric multiqubit states', Physical Review A **68**, 012101 (2003) (cited on pages 15, 108, 203).

[60] R. Lapkiewicz, P. Li, C. Schaeff, N. K. Langford, S. Ramelow, M. Wieśniak and A. Zeilinger, 'Experimental non-classicality of an indivisible quantum system', Nature **474**, 490–493 (2011) (cited on pages 15, 93, 203).

[61] S. J. Freedman and J. F. Clauser, 'Experimental Test of Local Hidden-Variable Theories', Physical Review Letters **28**, 938–941 (1972) (cited on pages 15, 203).

[62] L. Amico, R. Fazio, A. Osterloh and V. Vedral, 'Entanglement in many-body systems', Reviews of Modern Physics **80**, 517–576 (2008) (cited on pages 15, 203).

[63] L. Pezzè, A. Smerzi, M. K. Oberthaler, R. Schmied and P. Treutlein, 'Quantum metrology with nonclassical states of atomic ensembles', Rev. Mod. Phys. **90**, 035005 (2018) (cited on pages 15, 93, 121, 203).

[64] A. Sørensen, L.-M. Duan, J. I. Cirac and P. Zoller, 'Many-particle entanglement with Bose–Einstein condensates', Nature **409**, 63–66 (2001) (cited on pages 16, 204).

[65] A. S. Sørensen and K. Mølmer, 'Entanglement and Extreme Spin Squeezing', Physical Review Letters **86**, 4431–4434 (2001) (cited on pages 16, 204).

[66] J. Estève, C. Gross, A. Weller, S. Giovanazzi and M. K. Oberthaler, 'Squeezing and entanglement in a Bose–Einstein condensate', Nature **455**, 1216–1219 (2008) (cited on pages 16, 204).

[67] M. F. Riedel, P. Böhi, Y. Li, T. W. Hänsch, A. Sinatra and P. Treutlein, 'Atom-chip-based generation of entanglement for quantum metrology', Nature **464**, 1170–1173 (2010) (cited on pages 16, 84, 94, 204).

[68] C. Gross, T. Zibold, E. Nicklas, J. Estève and M. K. Oberthaler, 'Nonlinear atom interferometer surpasses classical precision limit', Nature **464**, 1165–1169 (2010) (cited on pages 16, 84, 94, 204).

[69] P. Hyllus, W. Laskowski, R. Krischek, C. Schwemmer, W. Wieczorek, H. Weinfurter, L. Pezzé and A. Smerzi, 'Fisher information and multiparticle entanglement', Physical Review A **85**, 022321 (2012) (cited on pages 16, 204).

[70] G. Tóth, 'Multipartite entanglement and high-precision metrology', Physical Review A **85**, 022322 (2012) (cited on pages 16, 204).

[71] J.-W. Pan, Z.-B. Chen, C.-Y. Lu, H. Weinfurter, A. Zeilinger and M. Żukowski, 'Multiphoton entanglement and interferometry', Reviews of Modern Physics **84**, 777–838 (2012) (cited on pages 16, 204).

[72] G. Wendin, 'Quantum information processing with superconducting circuits: a review', Reports on Progress in Physics **80**, 106001 (2017) (cited on pages 16, 204).

[73] R. Blatt and D. Wineland, 'Entangled states of trapped atomic ions', Nature **453**, 1008–1015 (2008) (cited on pages 16, 204).

[74] M. Saffman, T. G. Walker and K. Mølmer, 'Quantum information with Rydberg atoms', Reviews of Modern Physics **82**, 2313–2363 (2010) (cited on pages 16, 204).

[75] W. Dür, G. Vidal and J. I. Cirac, 'Three qubits can be entangled in two inequivalent ways', Physical Review A **62**, 062314 (2000) (cited on pages 16, 91, 117, 204).

[76] F. Benatti, R. Floreanini, F. Franchini and U. Marzolino, 'Entanglement in indistinguishable particle systems', Physics Reports **878**, 1–27 (2020) (cited on pages 16, 121, 204).

[77] A. Celi, P. Massignan, J. Ruseckas, N. Goldman, I. B. Spielman, G. Juzeliūnas and M. Lewenstein, 'Synthetic Gauge Fields in Synthetic Dimensions', Physical Review Letters **112**, 043001 (2014) (cited on pages 17, 131, 204).

[78] R. B. Laughlin, 'Quantized Hall conductivity in two dimensions', Physical Review B **23**, 5632–5633 (1981) (cited on pages 17, 139, 205).

[79] B. I. Halperin, 'Quantized Hall conductance, current-carrying edge states, and the existence of extended states in a two-dimensional disordered potential', Physical Review B **25**, 2185–2190 (1982) (cited on pages 17, 135, 205).

[80] H. L. Stormer, D. C. Tsui and A. C. Gossard, 'The fractional quantum Hall effect', Reviews of Modern Physics **71**, S298–S305 (1999) (cited on pages 17, 205).

[81] M. Z. Hasan and C. L. Kane, 'Colloquium: Topological insulators', Reviews of Modern Physics **82**, 3045–3067 (2010) (cited on pages 17, 131, 205).

[82] D. Pesin and A. H. MacDonald, 'Spintronics and pseudospintronics in graphene and topological insulators', Nature Materials **11**, 409–416 (2012) (cited on pages 17, 205).

[83] A. Y. Kitaev, 'Fault-tolerant quantum computation by anyons', Annals of Physics **303**, 2–30 (2003) (cited on pages 17, 205).

[84] M. Mancini et al., 'Observation of chiral edge states with neutral fermions in synthetic Hall ribbons', Science **349**, 1510–1513 (2015) (cited on pages 17, 133, 205).

[85] B. K. Stuhl, H. I. Lu, L. M. Aycock, D. Genkina and I. B. Spielman, 'Visualizing edge states with an atomic Bose gas in the quantum Hall regime', Science **349**, 1514–1518 (2015) (cited on pages 17, 133, 205).

[86] R. Bianco and R. Resta, 'Mapping topological order in coordinate space', Physical Review B **84**, 241106 (2011) (cited on pages 18, 133, 139, 205).

[87] H. Li and F. D. M. Haldane, 'Entanglement Spectrum as a Generalization of Entanglement Entropy: Identification of Topological Order in Non-Abelian Fractional Quantum Hall Effect States', Physical Review Letters **101**, 010504 (2008) (cited on pages 18, 140, 142, 148, 205).

[88] M. Dalmonte, B. Vermersch and P. Zoller, 'Quantum simulation and spectroscopy of entanglement Hamiltonians', Nature Physics **14**, 827–831 (2018) (cited on pages 18, 141, 151, 205).

[89] D. Dreon, 'Designing and building an ultracold Dysprosium experiment : a new framework for light-spin interaction', PhD thesis (ENS-PSL Research University, Paris, 12th July 2017) (cited on pages 20, 24, 33).

[90] C. Bouazza, 'Ultracold dysprosium gas in optical dipole traps : control of interactions between highly magnetic atoms', PhD thesis (ENS-PSL Research University, Paris, 4th May 2018) (cited on pages 20, 24, 25).

[91] T. Chalopin, 'Quantum-enhanced sensing and synthetic Landau levels with ultracold dysprosium atoms', PhD thesis (Sorbonne Université, 12th Dec. 2019) (cited on pages 20, 28, 33, 126).

[92] A. Evrard, 'Non-Gaussian spin states of ultracold dysprosium atoms', PhD thesis (ENS-PSL Research University, Paris, 29th Sept. 2020) (cited on pages 20, 25).

[93] D. Dreon, L. A. Sidorenkov, C. Bouazza, W. Maineult, J. Dalibard and S. Nascimbene, 'Optical cooling and trapping of highly magnetic atoms: the benefits of a spontaneous spin polarization', Journal of Physics B: Atomic, Molecular and Optical Physics **50**, 065005 (2017) (cited on pages 20, 25).

[94] T. Chalopin et al., 'Anisotropic light shift and magic polarization of the intercombination line of dysprosium atoms in a far-detuned dipole trap', Physical Review A **98**, 040502 (2018) (cited on pages 20, 25).

[95] N. Q. Burdick, Y. Tang and B. L. Lev, 'Long-Lived Spin-Orbit-Coupled Degenerate Dipolar Fermi Gas', Physical Review X **6**, 031022 (2016) (cited on page 21).

[96] A. Griesmaier, J. Werner, S. Hensler, J. Stuhler and T. Pfau, 'Bose-Einstein Condensation of Chromium', Physical Review Letters **94**, 160401 (2005) (cited on page 21).

[97] E. T. Davletov, V. V. Tsyganok, V. A. Khlebnikov, D. A. Pershin, D. V. Shaykin and A. V. Akimov, 'Machine learning for achieving Bose-Einstein condensation of thulium atoms', Physical Review A **102**, 011302 (2020) (cited on page 21).

[98] C. J. Foot, *Atomic Physics*, Oxford Master Series in Physics (Oxford University Press, Oxford, 25th Nov. 2004), 344 pp. (cited on page 21).

[99] M. Lu, S. H. Youn and B. L. Lev, 'Spectroscopy of a narrow-line laser-cooling transition in atomic dysprosium', Physical Review A **83**, 012510 (2011) (cited on pages 22, 40).

[100] K. Baumann, N. Q. Burdick, M. Lu and B. L. Lev, 'Observation of low-field Fano-Feshbach resonances in ultracold gases of dysprosium', Physical Review A **89**, 020701 (2014) (cited on page 22).

[101] C. J. Pethick and H. Smith, *Bose–Einstein Condensation in Dilute Gases*, 2nd ed. (Cambridge University Press, Cambridge, 2008) (cited on page 26).

[102] K. M. O'Hara, M. E. Gehm, S. R. Granade and J. E. Thomas, 'Scaling laws for evaporative cooling in time-dependent optical traps', Physical Review A **64**, 051403 (2001) (cited on page 28).

[103] J.-F. Clément, J.-P. Brantut, M. Robert-de-Saint-Vincent, R. A. Nyman, A. Aspect, T. Bourdel and P. Bouyer, 'All-optical runaway evaporation to Bose-Einstein condensation', Physical Review A **79**, 061406 (2009) (cited on page 28).

[104] N. Gross and L. Khaykovich, 'All-optical production of ^{7}Li Bose-Einstein condensation using Feshbach resonances', Physical Review A **77**, 023604 (2008) (cited on page 28).

[105] L. Luo, B. Clancy, J. Joseph, J. Kinast, A. Turlapov and J. E. Thomas, 'Evaporative cooling of unitary Fermi gas mixtures in optical traps', New Journal of Physics **8**, 213–213 (2006) (cited on page 28).

[106] F. Le Kien, P. Schneeweiss and A. Rauschenbeutel, 'Dynamical polarizability of atoms in arbitrary light fields: general theory and application to cesium', The European Physical Journal D **67**, 92 (2013) (cited on page 35).

[107] I. H. Deutsch and P. S. Jessen, 'Quantum control and measurement of atomic spins in polarization spectroscopy', Optics Communications, Quo Vadis Quantum Optics? **283**, 681–694 (2010) (cited on page 35).

[108] C. Ravensbergen, V. Corre, E. Soave, M. Kreyer, S. Tzanova, E. Kirilov and R. Grimm, 'Accurate Determination of the Dynamical Polarizability of Dysprosium', Physical Review Letters **120**, 223001 (2018) (cited on page 36).

[109] V. A. Dzuba, V. V. Flambaum and B. L. Lev, 'Dynamic polarizabilities and magic wavelengths for dysprosium', Physical Review A **83**, 032502 (2011) (cited on pages 36, 104).

[110] H. Li, J.-F. Wyart, O. Dulieu, S. Nascimbène and M. Lepers, 'Optical trapping of ultracold dysprosium atoms: transition probabilities, dynamic dipole polarizabilities and van der Waals C_6 coefficients', Journal of Physics B: Atomic, Molecular and Optical Physics **50**, 014005 (2016) (cited on pages 36, 81).

[111] A. Kramida, Y. Ralchenko and J. Reader, *NIST Atomic Spectra Database (version 5.9)* (National Institute of Standards and Technology, 2021) (cited on page 37).

[112] J. Dalibard, 'A Brief History of Cold Atoms: From the Doppler Mechanism to Quantum Gases', in Lecture Series of the Atoms and Radiation Chair, Collège de France (2015) (cited on page 40).

[113] M. Fleischhauer, A. Imamoglu and J. P. Marangos, 'Electromagnetically induced transparency: Optics in coherent media', Reviews of Modern Physics **77**, 633–673 (2005) (cited on page 40).

[114] P. Král, I. Thanopulos and M. Shapiro, 'Colloquium: Coherently controlled adiabatic passage', Reviews of Modern Physics **79**, 53–77 (2007) (cited on page 40).

[115] J. Dalibard, F. Gerbier, G. Juzeliūnas and P. Öhberg, 'Colloquium: Artificial gauge potentials for neutral atoms', Reviews of Modern Physics **83**, 1523–1543 (2011) (cited on pages 40, 155).

[116] X. Cui, B. Lian, T.-L. Ho, B. L. Lev and H. Zhai, 'Synthetic gauge field with highly magnetic lanthanide atoms', Physical Review A **88**, 011601 (2013) (cited on pages 40, 133).

[117] N. R. Cooper, J. Dalibard and I. B. Spielman, 'Topological bands for ultracold atoms', Reviews of Modern Physics **91**, 015005 (2019) (cited on page 40).

[118] N. Petersen, M. Trümper and P. Windpassinger, 'Spectroscopy of the 1001-nm transition in atomic dysprosium', Physical Review A **101**, 042502 (2020) (cited on page 40).

[119] V. Makhalov, T. Satoor, A. Evrard, T. Chalopin, R. Lopes and S. Nascimbene, 'Probing Quantum Criticality and Symmetry Breaking at the Microscopic Level', Physical Review Letters **123**, 120601 (2019) (cited on page 47).

[120] A. Dutta, G. Aeppli, B. K. Chakrabarti, U. Divakaran, T. F. Rosenbaum and D. Sen, *Quantum Phase Transitions in Transverse Field Spin Models: From Statistical Physics to Quantum Information* (Cambridge University Press, Cambridge, 2015) (cited on page 48).

[121] H. E. Stanley, 'Scaling, universality, and renormalization: Three pillars of modern critical phenomena', Reviews of Modern Physics **71**, S358–S366 (1999) (cited on page 50).

[122] P. Pfeuty, 'The one-dimensional Ising model with a transverse field', Annals of Physics **57**, 79–90 (1970) (cited on page 50).

[123] R. H. Dicke, 'Coherence in Spontaneous Radiation Processes', Physical Review **93**, 99–110 (1954) (cited on page 50).

[124] K. Baumann, C. Guerlin, F. Brennecke and T. Esslinger, 'Dicke quantum phase transition with a superfluid gas in an optical cavity', Nature **464**, 1301–1306 (2010) (cited on page 51).

[125] T. Zibold, E. Nicklas, C. Gross and M. K. Oberthaler, 'Classical Bifurcation at the Transition from Rabi to Josephson Dynamics', Physical Review Letters **105**, 204101 (2010) (cited on pages 51, 55).

[126] R. Islam et al., 'Onset of a quantum phase transition with a trapped ion quantum simulator', Nature Communications **2**, 377 (2011) (cited on page 51).

[127] I. D. Leroux, M. H. Schleier-Smith and V. Vuletić, 'Implementation of Cavity Squeezing of a Collective Atomic Spin', Physical Review Letters **104**, 073602 (2010) (cited on page 51).

[128] D. Gatteschi and R. Sessoli, 'Quantum Tunneling of Magnetization and Related Phenomena in Molecular Materials', Angewandte Chemie International Edition **42**, 268–297 (2003) (cited on pages 51, 75, 93).

[129] G. J. Milburn, J. Corney, E. M. Wright and D. F. Walls, 'Quantum dynamics of an atomic Bose-Einstein condensate in a double-well potential', Physical Review A **55**, 4318–4324 (1997) (cited on page 51).

[130] A. Smerzi, S. Fantoni, S. Giovanazzi and S. R. Shenoy, 'Quantum Coherent Atomic Tunneling between Two Trapped Bose-Einstein Condensates', Physical Review Letters **79**, 4950–4953 (1997) (cited on page 51).

[131] J. I. Cirac, M. Lewenstein, K. Mølmer and P. Zoller, 'Quantum superposition states of Bose-Einstein condensates', Physical Review A **57**, 1208–1218 (1998) (cited on page 51).

[132] A. Facon, E.-K. Dietsche, D. Grosso, S. Haroche, J.-M. Raimond, M. Brune and S. Gleyzes, 'A sensitive electrometer based on a Rydberg atom in a Schrödinger-cat state', Nature **535**, 262–265 (2016) (cited on pages 52, 91, 93).

[133] G. Ortiz, R. Somma, J. Dukelsky and S. Rombouts, 'Exactly-solvable models derived from a generalized Gaudin algebra', Nuclear Physics B **707**, 421–457 (2005) (cited on pages 52, 81).

[134] F. Pan and J. P. Draayer, 'Analytical solutions for the LMG model', Physics Letters B **451**, 1–10 (1999) (cited on pages 52, 81).

[135] S. Sachdev and B. Keimer, 'Quantum criticality', Physics Today **64**, 29–35 (2011) (cited on page 52).

[136] R. Botet and R. Jullien, 'Large-size critical behavior of infinitely coordinated systems', Physical Review B **28**, 3955–3967 (1983) (cited on pages 53, 62, 74).

[137] S. Dusuel and J. Vidal, 'Finite-Size Scaling Exponents of the Lipkin-Meshkov-Glick Model', Physical Review Letters **93**, 237204 (2004) (cited on pages 53, 74).

[138] S. Dusuel and J. Vidal, 'Continuous unitary transformations and finite-size scaling exponents in the Lipkin-Meshkov-Glick model', Physical Review B **71**, 224420 (2005) (cited on pages 53, 65, 67).

[139] N. Debergh and F. Stancu, 'On the exact solutions of the Lipkin-Meshkov-Glick model', Journal of Physics A: Mathematical and General **34**, 3265–3276 (2001) (cited on page 54).

[140] L. D. Landau and E. M. Lifshitz, 'Fluctuations of the order parameter', in *Statistical Physics, Third Edition, Part 1: Volume 5*, 3rd edition (Butterworth-Heinemann, Amsterdam Heidelberg, 15th Jan. 1980), pp. 471–478 (cited on page 60).

[141] P. Cejnar, P. Stránský, M. Macek and M. Kloc, 'Excited-state quantum phase transitions', Journal of Physics A: Mathematical and Theoretical **54**, 133001 (2021) (cited on pages 64, 71, 83).

[142] T. Holstein and H. Primakoff, 'Field Dependence of the Intrinsic Domain Magnetization of a Ferromagnet', Physical Review **58**, 1098–1113 (1940) (cited on page 65).

[143] V. V. Ulyanov and O. B. Zaslavskii, 'New methods in the theory of quantum spin systems', Physics Reports **216**, 179–251 (1992) (cited on page 66).

[144] A. V. Turbiner, 'Quasi-exactly-solvable problems and SL(2) algebra', Communications in Mathematical Physics **118**, 467–474 (1988) (cited on page 66).

[145] E. Majorana, 'Atomi orientati in campo magnetico variabile', Il Nuovo Cimento (1924-1942) **9**, 43–50 (1932) (cited on pages 66, 122).

[146] P. Ribeiro, J. Vidal and R. Mosseri, 'Thermodynamical Limit of the Lipkin-Meshkov-Glick Model', Physical Review Letters **99**, 050402 (2007) (cited on pages 66, 83).

[147] D. Ulam-Orgikh and M. Kitagawa, 'Spin squeezing and decoherence limit in Ramsey spectroscopy', Physical Review A **64**, 052106 (2001) (cited on page 67).

[148] J. Vidal, 'Concurrence in collective models', Physical Review A **73**, 062318 (2006) (cited on pages 67, 103).

[149] R. Orús, S. Dusuel and J. Vidal, 'Equivalence of Critical Scaling Laws for Many-Body Entanglement in the Lipkin-Meshkov-Glick Model', Physical Review Letters **101**, 025701 (2008) (cited on page 67).

[150] L.-A. Wu, M. S. Sarandy and D. A. Lidar, 'Quantum Phase Transitions and Bipartite Entanglement', Physical Review Letters **93**, 250404 (2004) (cited on page 67).

[151] J. Vidal, G. Palacios and R. Mosseri, 'Entanglement in a second-order quantum phase transition', Physical Review A **69**, 022107 (2004) (cited on page 67).

[152] J. I. Latorre, R. Orús, E. Rico and J. Vidal, 'Entanglement entropy in the Lipkin-Meshkov-Glick model', Physical Review A **71**, 064101 (2005) (cited on page 67).

[153] J. Vidal, G. Palacios and C. Aslangul, 'Entanglement dynamics in the Lipkin-Meshkov-Glick model', Physical Review A **70**, 062304 (2004) (cited on page 67).

[154] J. Wilms, J. Vidal, F. Verstraete and S. Dusuel, 'Finite-temperature mutual information in a simple phase transition', Journal of Statistical Mechanics: Theory and Experiment **2012**, P01023 (2012) (cited on page 67).

[155] M. Filippone, S. Dusuel and J. Vidal, 'Quantum phase transitions in fully connected spin models: An entanglement perspective', Physical Review A **83**, 022327 (2011) (cited on page 67).

[156] J. Werschnik and E. K. U. Gross, 'Quantum optimal control theory', Journal of Physics B: Atomic, Molecular and Optical Physics **40**, R175–R211 (2007) (cited on page 69).

[157] R. Kaubruegger, D. V. Vasilyev, M. Schulte, K. Hammerer and P. Zoller, 'Quantum Variational Optimization of Ramsey Interferometry and Atomic Clocks', Physical Review X **11**, 041045 (2021) (cited on page 69).

[158] C. D. Marciniak, T. Feldker, I. Pogorelov, R. Kaubruegger, D. V. Vasilyev, R. van Bijnen, P. Schindler, P. Zoller, R. Blatt and T. Monz, 'Optimal metrology with programmable quantum sensors', Nature **603**, 604–609 (2022) (cited on page 69).

[159] F. T. Hioe, D. Macmillen and E. W. Montroll, 'Quantum theory of anharmonic oscillators: Energy levels of a single and a pair of coupled oscillators with quartic coupling', Physics Reports **43**, 305–335 (1978) (cited on page 71).

[160] F. Leyvraz and W. D. Heiss, 'Large-N Scaling Behavior of the Lipkin-Meshkov-Glick Model', Physical Review Letters **95**, 050402 (2005) (cited on page 71).

[161] A. Sartori, J. Marino, S. Stringari and A. Recati, 'Spin-dipole oscillation and relaxation of coherently coupled Bose–Einstein condensates', New Journal of Physics **17**, 093036 (2015) (cited on page 74).

[162] G. Valtolina, F. Scazza, A. Amico, A. Burchianti, A. Recati, T. Enss, M. Inguscio, M. Zaccanti and G. Roati, 'Exploring the ferromagnetic behaviour of a repulsive Fermi gas through spin dynamics', Nature Physics **13**, 704–709 (2017) (cited on page 74).

[163] C. M. Newman and L. S. Schulman, 'Metastability and the analytic continuation of eigenvalues', Journal of Mathematical Physics **18**, 23 (1977) (cited on page 74).

[164] J. R. Friedman, M. P. Sarachik, J. Tejada and R. Ziolo, 'Macroscopic Measurement of Resonant Magnetization Tunneling in High-Spin Molecules', Physical Review Letters **76**, 3830–3833 (1996) (cited on page 75).

[165] L. Thomas, F. Lionti, R. Ballou, D. Gatteschi, R. Sessoli and B. Barbara, 'Macroscopic quantum tunnelling of magnetization in a single crystal of nanomagnets', Nature **383**, 145 (1996) (cited on page 75).

[166] S. A. Owerre and M. B. Paranjape, 'Macroscopic quantum tunneling and quantum–classical phase transitions of the escape rate in large spin systems', Physics Reports **546**, 1–60 (2015) (cited on page 75).

[167] J. R. Friedman, V. Patel, W. Chen, S. K. Tolpygo and J. E. Lukens, 'Quantum superposition of distinct macroscopic states', Nature **406**, 43–46 (2000) (cited on pages 75, 91).

[168] C. H. van der Wal, A. C. J. ter Haar, F. K. Wilhelm, R. N. Schouten, C. J. P. M. Harmans, T. P. Orlando, S. Lloyd and J. E. Mooij, 'Quantum Superposition of Macroscopic Persistent-Current States', Science **290**, 773–777 (2000) (cited on page 75).

[169] Y. Makhlin, G. Schön and A. Shnirman, 'Quantum-state engineering with Josephson-junction devices', Reviews of Modern Physics **73**, 357–400 (2001) (cited on page 75).

[170] J. L. Van Hemmen and A. Sütö, 'Tunneling of quantum spins', Physica B+C **141**, 37–75 (1986) (cited on page 76).

[171] G. Scharf, W. F. Wreszinski, van and J. L. Hemmen, 'Tunnelling of a large spin: mapping onto a particle problem', Journal of Physics A: Mathematical and General **20**, 4309–4319 (1987) (cited on page 76).

[172] M. Enz and R. Schilling, 'Spin tunnelling in the semiclassical limit', Journal of Physics C: Solid State Physics **19**, 1765–1770 (1986) (cited on page 76).

[173] E. M. Chudnovsky and L. Gunther, 'Quantum Tunneling of Magnetization in Small Ferromagnetic Particles', Physical Review Letters **60**, 661–664 (1988) (cited on page 76).

[174] O. B. Zaslavskii, 'Spin tunneling and the effective potential method', Physics Letters A **145**, 471–475 (1990) (cited on page 76).

[175] H. Bernien et al., 'Probing many-body dynamics on a 51-atom quantum simulator', Nature **551**, 579–584 (2017) (cited on page 78).

[176] Y. Tang, A. Sykes, N. Q. Burdick, J. L. Bohn and B. L. Lev, '*s*-wave scattering lengths of the strongly dipolar bosons ^{162}Dy and ^{164}Dy', Physical Review A **92**, 022703 (2015) (cited on page 80).

[177] G. F. Gribakin and V. V. Flambaum, 'Calculation of the scattering length in atomic collisions using the semiclassical approximation', Physical Review A **48**, 546–553 (1993) (cited on page 81).

[178] J. C. Louw, J. N. Kriel and M. Kastner, 'Thermalization of a Lipkin-Meshkov-Glick model coupled to a bosonic bath', Physical Review A **100**, 022115 (2019) (cited on page 81).

[179] J. R. Webster and M. Kastner, 'Subexponentially Growing Hilbert Space and Nonconcentrating Distributions in a Constrained Spin Model', Journal of Statistical Physics **171**, 449–461 (2018) (cited on page 81).

[180] O. Castaños, R. López-Peña, J. G. Hirsch and E. López-Moreno, 'Classical and quantum phase transitions in the Lipkin-Meshkov-Glick model', Physical Review B **74**, 104118 (2006) (cited on page 82).

[181] O. L. Acevedo, L. Quiroga, F. J. Rodríguez and N. F. Johnson, 'New Dynamical Scaling Universality for Quantum Networks Across Adiabatic Quantum Phase Transitions', Physical Review Letters **112**, 030403 (2014) (cited on page 83).

[182] T. Caneva, R. Fazio and G. E. Santoro, 'Adiabatic quantum dynamics of the Lipkin-Meshkov-Glick model', Physical Review B **78**, 104426 (2008) (cited on page 83).

[183] N. Defenu, T. Enss, M. Kastner and G. Morigi, 'Dynamical Critical Scaling of Long-Range Interacting Quantum Magnets', Physical Review Letters **121**, 240403 (2018) (cited on page 83).

[184] M.-J. Hwang, R. Puebla and M. B. Plenio, 'Quantum Phase Transition and Universal Dynamics in the Rabi Model', Physical Review Letters **115**, 180404 (2015) (cited on page 83).

[185] P. Solinas, P. Ribeiro and R. Mosseri, 'Dynamical properties across a quantum phase transition in the Lipkin-Meshkov-Glick model', Physical Review A **78**, 052329 (2008) (cited on page 83).

[186] C. Monroe et al., 'Programmable quantum simulations of spin systems with trapped ions', Reviews of Modern Physics **93**, 025001 (2021) (cited on page 83).

[187] A. Das and B. K. Chakrabarti, 'Colloquium: Quantum annealing and analog quantum computation', Reviews of Modern Physics **80**, 1061–1081 (2008) (cited on page 83).

[188] V. Bapst and G. Semerjian, 'On quantum mean-field models and their quantum annealing', Journal of Statistical Mechanics: Theory and Experiment **2012**, P06007 (2012) (cited on page 83).

[189] M. Heyl, 'Dynamical quantum phase transitions: a review', Reports on Progress in Physics **81**, 054001 (2018) (cited on page 83).

[190] J. C. Halimeh and V. Zauner-Stauber, 'Dynamical phase diagram of quantum spin chains with long-range interactions', Physical Review B **96**, 134427 (2017) (cited on page 83).

[191] I. Homrighausen, N. O. Abeling, V. Zauner-Stauber and J. C. Halimeh, 'Anomalous dynamical phase in quantum spin chains with long-range interactions', Physical Review B **96**, 104436 (2017) (cited on page 83).

[192] B. Žunkovič, A. Silva and M. Fabrizio, 'Dynamical phase transitions and Loschmidt echo in the infinite-range XY model', Philosophical Transactions of the Royal Society A: Mathematical, Physical and Engineering Sciences **374**, 20150160 (2016) (cited on page 83).

[193] G. Salvatori, A. Mandarino and M. G. A. Paris, 'Quantum metrology in Lipkin-Meshkov-Glick critical systems', Physical Review A **90**, 022111 (2014) (cited on page 83).

[194] M. Kitagawa and M. Ueda, 'Squeezed spin states', Physical Review A **47**, 5138–5143 (1993) (cited on pages 83, 94, 95).

[195] J. G. Bohnet, B. C. Sawyer, J. W. Britton, M. L. Wall, A. M. Rey, M. Foss-Feig and J. J. Bollinger, 'Quantum spin dynamics and entanglement generation with hundreds of trapped ions', Science **352**, 1297–1301 (2016) (cited on page 84).

[196] T. Chalopin, C. Bouazza, A. Evrard, V. Makhalov, D. Dreon, J. Dalibard, L. A. Sidorenkov and S. Nascimbene, 'Quantum-enhanced sensing using non-classical spin states of a highly magnetic atom', Nature Communications **9**, 4955 (2018) (cited on pages 84, 91, 93, 94, 112).

[197] A. Evrard, V. Makhalov, T. Chalopin, L. A. Sidorenkov, J. Dalibard, R. Lopes and S. Nascimbene, 'Enhanced Magnetic Sensitivity with Non-Gaussian Quantum Fluctuations', Physical Review Letters **122**, 173601 (2019) (cited on page 84).

[198] X.-Y. Luo, Y.-Q. Zou, L.-N. Wu, Q. Liu, M.-F. Han, M. K. Tey and L. You, 'Deterministic entanglement generation from driving through quantum phase transitions', Science **355**, 620–623 (2017) (cited on page 84).

[199] D. J. Wineland, J. J. Bollinger, W. M. Itano, F. L. Moore and D. J. Heinzen, 'Spin squeezing and reduced quantum noise in spectroscopy', Physical Review A **46**, R6797–R6800 (1992) (cited on page 84).

[200] I. Frérot and T. Roscilde, 'Quantum Critical Metrology', Physical Review Letters **121**, 020402 (2018) (cited on page 84).

[201] J. Ma and X. Wang, 'Fisher information and spin squeezing in the Lipkin-Meshkov-Glick model', Physical Review A **80**, 012318 (2009) (cited on page 84).

[202] T. Satoor, A. Fabre, J.-B. Bouhiron, A. Evrard, R. Lopes and S. Nascimbene, 'Partitioning dysprosium's electronic spin to reveal entanglement in nonclassical states', Physical Review Research **3**, 043001 (2021) (cited on pages 86, 122).

[203] E. Schrödinger, 'Die gegenwärtige Situation in der Quantenmechanik', Naturwissenschaften **23**, 807–812 (1935) (cited on page 87).

[204] O. Gühne and G. Tóth, 'Entanglement detection', Physics Reports **474**, 1–75 (2009) (cited on pages 87, 88).

[205] M. A. Nielsen and I. L. Chuang, *Quantum Computation and Quantum Information: 10th Anniversary Edition* (Cambridge University Press, 2010) (cited on pages 87, 90).

[206] W. Wootters, 'Entanglement of formation and concurrence', Quantum Inf. Comput. (2001) (cited on page 87).

[207] E. Schmidt, 'Zur Theorie der linearen und nichtlinearen Integralgleichungen', Mathematische Annalen **63**, 433–476 (1907) (cited on page 87).

[208] C. H. Bennett, D. P. DiVincenzo, J. A. Smolin and W. K. Wootters, 'Mixed-state entanglement and quantum error correction', Physical Review A **54**, 3824–3851 (1996) (cited on page 88).

[209] S. Hill and W. K. Wootters, 'Entanglement of a Pair of Quantum Bits', Physical Review Letters **78**, 5022–5025 (1997) (cited on pages 88, 89).

[210] A. K. Ekert, C. M. Alves, D. K. L. Oi, M. Horodecki, P. Horodecki and L. C. Kwek, 'Direct Estimations of Linear and Nonlinear Functionals of a Quantum State', Physical Review Letters **88**, 217901 (2002) (cited on page 89).

[211] N. J. Cerf and C. Adami, 'Negative Entropy and Information in Quantum Mechanics', Physical Review Letters **79**, 5194–5197 (1997) (cited on page 90).

[212] R. Horodecki and M. Horodecki, 'Information-theoretic aspects of inseparability of mixed states', Physical Review A **54**, 1838–1843 (1996) (cited on page 90).

[213] A. Rényi, 'On Measures of Entropy and Information', Proceedings of the Fourth Berkeley Symposium on Mathematical Statistics and Probability, Volume 1: Contributions to the Theory of Statistics **4.1**, 547–562 (1961) (cited on page 90).

[214] R. Konig, R. Renner and C. Schaffner, 'The Operational Meaning of Min- and Max-Entropy', IEEE Transactions on Information Theory **55**, 4337–4347 (2009) (cited on page 90).

[215] K. S. Choi, A. Goban, S. B. Papp, S. J. van Enk and H. J. Kimble, 'Entanglement of spin waves among four quantum memories', Nature **468**, 412–416 (2010) (cited on page 91).

[216] F. Haas, J. Volz, R. Gehr, J. Reichel and J. Estève, 'Entangled States of More Than 40 Atoms in an Optical Fiber Cavity', Science **344**, 180–183 (2014) (cited on page 91).

[217] R. McConnell, H. Zhang, J. Hu, S. Ćuk and V. Vuletić, 'Entanglement with negative Wigner function of almost 3,000 atoms heralded by one photon', Nature **519**, 439–442 (2015) (cited on page 91).

[218] M. Ebert, M. Kwon, T. G. Walker and M. Saffman, 'Coherence and Rydberg Blockade of Atomic Ensemble Qubits', Physical Review Letters **115**, 093601 (2015) (cited on page 91).

[219] J. Zeiher, P. Schauß, S. Hild, T. Macrì, I. Bloch and C. Gross, 'Microscopic Characterization of Scalable Coherent Rydberg Superatoms', Physical Review X **5**, 031015 (2015) (cited on page 91).

[220] H. Häffner et al., 'Scalable multiparticle entanglement of trapped ions', Nature **438**, 643–646 (2005) (cited on page 91).

[221] F. Fröwis, P. C. Strassmann, A. Tiranov, C. Gut, J. Lavoie, N. Brunner, F. Bussières, M. Afzelius and N. Gisin, 'Experimental certification of millions of genuinely entangled atoms in a solid', Nature Communications **8**, 907 (2017) (cited on page 91).

[222] Y. Pu, Y. Wu, N. Jiang, W. Chang, C. Li, S. Zhang and L. Duan, 'Experimental entanglement of 25 individually accessible atomic quantum interfaces', Science Advances **4**, eaar3931 (2018) (cited on page 91).

[223] C. Monroe, D. M. Meekhof, B. E. King and D. J. Wineland, 'A "Schrödinger Cat" Superposition State of an Atom', Science **272**, 1131–1136 (1996) (cited on page 91).

[224] X.-C. Yao, T.-X. Wang, P. Xu, H. Lu, G.-S. Pan, X.-H. Bao, C.-Z. Peng, C.-Y. Lu, Y.-A. Chen and J.-W. Pan, 'Observation of eight-photon entanglement', Nature Photonics **6**, 225–228 (2012) (cited on pages 91, 112).

[225] G. Kirchmair, B. Vlastakis, Z. Leghtas, S. E. Nigg, H. Paik, E. Ginossar, M. Mirrahimi, L. Frunzio, S. M. Girvin and R. J. Schoelkopf, 'Observation of quantum state collapse and revival due to the single-photon Kerr effect', Nature **495**, 205–209 (2013) (cited on page 91).

[226] C. L. Degen, F. Reinhard and P. Cappellaro, 'Quantum sensing', Reviews of Modern Physics **89**, 035002 (2017) (cited on page 91).

[227] X.-L. Wang et al., '18-Qubit Entanglement with Six Photons' Three Degrees of Freedom', Physical Review Letters **120**, 260502 (2018) (cited on page 91).

[228] E. K. Dietsche, A. Larrouy, S. Haroche, J. M. Raimond, M. Brune and S. Gleyzes, 'High-sensitivity magnetometry with a single atom in a superposition of two circular Rydberg states', Nature Physics **15**, 326–329 (2019) (cited on page 91).

[229] C. Song et al., 'Generation of multicomponent atomic Schrödinger cat states of up to 20 qubits', Science **365**, 574–577 (2019) (cited on pages 91, 112).

[230] A. Omran et al., 'Generation and manipulation of Schrödinger cat states in Rydberg atom arrays', Science **365**, 570–574 (2019) (cited on pages 91, 112).

[231] K. X. Wei, I. Lauer, S. Srinivasan, N. Sundaresan, D. T. McClure, D. Toyli, D. C. McKay, J. M. Gambetta and S. Sheldon, 'Verifying multipartite entangled Greenberger-Horne-Zeilinger states via multiple quantum coherences', Physical Review A **101**, 032343 (2020) (cited on pages 91, 112).

[232] M. Brune, E. Hagley, J. Dreyer, X. Maître, A. Maali, C. Wunderlich, J. M. Raimond and S. Haroche, 'Observing the Progressive Decoherence of the "Meter" in a Quantum Measurement', Physical Review Letters **77**, 4887–4890 (1996) (cited on page 91).

[233] C. A. Sackett et al., 'Experimental entanglement of four particles', Nature **404**, 256–259 (2000) (cited on pages 91, 112).

[234] D. Leibfried et al., 'Creation of a six-atom 'Schrödinger cat' state', Nature **438**, 639–642 (2005) (cited on pages 91, 112).

[235] A. Ourjoumtsev, R. Tualle-Brouri, J. Laurat and P. Grangier, 'Generating Optical Schrödinger Kittens for Quantum Information Processing', Science **312**, 83–86 (2006) (cited on page 91).

[236] J. S. Neergaard-Nielsen, B. M. Nielsen, C. Hettich, K. Mølmer and E. S. Polzik, 'Generation of a Superposition of Odd Photon Number States for Quantum Information Networks', Physical Review Letters **97**, 083604 (2006) (cited on page 91).

[237] S. Deléglise, I. Dotsenko, C. Sayrin, J. Bernu, M. Brune, J.-M. Raimond and S. Haroche, 'Reconstruction of non-classical cavity field states with snapshots of their decoherence', Nature **455**, 510–514 (2008) (cited on pages 91, 93).

[238] T. Monz, P. Schindler, J. T. Barreiro, M. Chwalla, D. Nigg, W. A. Coish, M. Harlander, W. Hänsel, M. Hennrich and R. Blatt, '14-Qubit Entanglement: Creation and Coherence', Physical Review Letters **106**, 130506 (2011) (cited on pages 91, 112).

[239] M. Bourennane, M. Eibl, C. Kurtsiefer, S. Gaertner, H. Weinfurter, O. Gühne, P. Hyllus, D. Bruß, M. Lewenstein and A. Sanpera, 'Experimental Detection of Multipartite Entanglement using Witness Operators', Physical Review Letters **92**, 087902 (2004) (cited on page 92).

[240] A. Acín, D. Bruß, M. Lewenstein and A. Sanpera, 'Classification of Mixed Three-Qubit States', Physical Review Letters **87**, 040401 (2001) (cited on page 92).

[241] G. Tóth and O. Gühne, 'Detecting Genuine Multipartite Entanglement with Two Local Measurements', Physical Review Letters **94**, 060501 (2005) (cited on page 92).

[242] G. Grynberg, A. Aspect and C. Fabre, *Introduction to Quantum Optics: From the Semiclassical Approach to Quantized Light* (Cambridge University Press, Cambridge, 2010) (cited on page 92).

[243] E. C. G. Sudarshan, 'Equivalence of Semiclassical and Quantum Mechanical Descriptions of Statistical Light Beams', Physical Review Letters **10**, 277–279 (1963) (cited on page 92).

[244] R. J. Glauber, 'Coherent and Incoherent States of the Radiation Field', Physical Review **131**, 2766–2788 (1963) (cited on page 92).

[245] E. Wigner, 'On the Quantum Correction For Thermodynamic Equilibrium', Physical Review **40**, 749–759 (1932) (cited on page 93).

[246] S. Haroche and J.-M. Raimond, *Exploring the Quantum: Atoms, Cavities, and Photons*, Oxford Graduate Texts (Oxford University Press, Oxford, 2006), 616 pp. (cited on page 93).

[247] O. Giraud, P. Braun and D. Braun, 'Classicality of spin states', Physical Review A **78**, 042112 (2008) (cited on pages 93, 102).

[248] S. Chaudhury, S. Merkel, T. Herr, A. Silberfarb, I. H. Deutsch and P. S. Jessen, 'Quantum Control of the Hyperfine Spin of a Cs Atom Ensemble', Physical Review Letters **99**, 163002 (2007) (cited on page 93).

[249] T. Fernholz, H. Krauter, K. Jensen, J. F. Sherson, A. S. Sørensen and E. S. Polzik, 'Spin Squeezing of Atomic Ensembles via Nuclear-Electronic Spin Entanglement', Physical Review Letters **101**, 073601 (2008) (cited on page 93).

[250] 'Antenna Elements and Arrays', in *The Electrical Engineering Handbook*, edited by W.-K. Chen, in collab. with N. K. Das (Academic Press, Burlington, 1st Jan. 2005), pp. 569–583 (cited on page 96).

[251] S. Nascimbene, 'Quantum-enhanced sensing and topological matter with ultracold dysprosium atoms', HDR thesis (Ecole Normale Supérieure, Paris, 2020) (cited on page 99).

[252] G. Tóth and O. Gühne, 'Entanglement and Permutational Symmetry', Physical Review Letters **102**, 170503 (2009) (cited on page 102).

[253] J. K. Korbicz, J. I. Cirac and M. Lewenstein, 'Spin Squeezing Inequalities and Entanglement of N Qubit States', Physical Review Letters **95**, 120502 (2005) (cited on page 103).

[254] M. Hillery, 'Nonclassical distance in quantum optics', Physical Review A **35**, 725–732 (1987) (cited on page 103).

[255] M. Koashi, V. Bužek and N. Imoto, 'Entangled webs: Tight bound for symmetric sharing of entanglement', Physical Review A **62**, 050302 (2000) (cited on page 107).

[256] V. I. Man'ko and O. V. Man'ko, 'Spin state tomography', Journal of Experimental and Theoretical Physics **85**, 430–434 (1997) (cited on page 110).

[257] J. J. . Bollinger, W. M. Itano, D. J. Wineland and D. J. Heinzen, 'Optimal frequency measurements with maximally correlated states', Physical Review A **54**, R4649–R4652 (1996) (cited on page 112).

[258] E. Davis, G. Bentsen and M. Schleier-Smith, 'Approaching the Heisenberg Limit without Single-Particle Detection', Physical Review Letters **116**, 053601 (2016) (cited on page 112).

[259] D. Linnemann, H. Strobel, W. Muessel, J. Schulz, R. J. Lewis-Swan, K. V. Kheruntsyan and M. K. Oberthaler, 'Quantum-Enhanced Sensing Based on Time Reversal of Nonlinear Dynamics', Physical Review Letters **117**, 013001 (2016) (cited on page 112).

[260] F. Fröwis, P. Sekatski and W. Dür, 'Detecting Large Quantum Fisher Information with Finite Measurement Precision', Physical Review Letters **116**, 090801 (2016) (cited on page 112).

[261] T. Macrì, A. Smerzi and L. Pezzè, 'Loschmidt echo for quantum metrology', Physical Review A **94**, 010102 (2016) (cited on page 112).

[262] M. Gustavsson, H. Lundberg, L. Nilsson and S. Svanberg, 'Lifetime measurements for excited states of rare-earth atoms using pulse modulation of a cw dye-laser beam', JOSA **69**, 984–992 (1979) (cited on page 116).

[263] C.-W. Lee and H. Jeong, 'Quantification of Macroscopic Quantum Superpositions within Phase Space', Physical Review Letters **106**, 220401 (2011) (cited on page 117).

[264] W. K. Wootters and W. H. Zurek, 'Complementarity in the double-slit experiment: Quantum nonseparability and a quantitative statement of Bohr's principle', Physical Review D **19**, 473–484 (1979) (cited on page 119).

[265] B.-G. Englert, 'Fringe Visibility and Which-Way Information: An Inequality', Physical Review Letters **77**, 2154–2157 (1996) (cited on page 119).

[266] C. Cabrillo, J. I. Cirac, P. García-Fernández and P. Zoller, 'Creation of entangled states of distant atoms by interference', Physical Review A **59**, 1025–1033 (1999) (cited on pages 120, 121).

[267] X.-L. Feng, Z.-M. Zhang, X.-D. Li, S.-Q. Gong and Z.-Z. Xu, 'Entangling Distant Atoms by Interference of Polarized Photons', Physical Review Letters **90**, 217902 (2003) (cited on pages 120, 121).

[268] C. Simon and W. T. M. Irvine, 'Robust Long-Distance Entanglement and a Loophole-Free Bell Test with Ions and Photons', Physical Review Letters **91**, 110405 (2003) (cited on page 120).

[269] T. E. Northup and R. Blatt, 'Quantum information transfer using photons', Nature Photonics **8**, 356–363 (2014) (cited on page 120).

[270] B. B. Blinov, D. L. Moehring, L.-M. Duan and C. Monroe, 'Observation of entanglement between a single trapped atom and a single photon', Nature **428**, 153–157 (2004) (cited on pages 120, 121).

[271] J. Volz, M. Weber, D. Schlenk, W. Rosenfeld, J. Vrana, K. Saucke, C. Kurtsiefer and H. Weinfurter, 'Observation of Entanglement of a Single Photon with a Trapped Atom', Physical Review Letters **96**, 030404 (2006) (cited on pages 120, 121).

[272] T. Wilk, S. C. Webster, A. Kuhn and G. Rempe, 'Single-Atom Single-Photon Quantum Interface', Science **317**, 488–490 (2007) (cited on pages 120, 121).

[273] E. Togan et al., 'Quantum entanglement between an optical photon and a solid-state spin qubit', Nature **466**, 730–734 (2010) (cited on pages 120, 121).

[274] D. L. Moehring, P. Maunz, S. Olmschenk, K. C. Younge, D. N. Matsukevich, L.-M. Duan and C. Monroe, 'Entanglement of single-atom quantum bits at a distance', Nature **449**, 68–71 (2007) (cited on pages 120, 121).

[275] J. Hofmann, M. Krug, N. Ortegel, L. Gérard, M. Weber, W. Rosenfeld and H. Weinfurter, 'Heralded Entanglement Between Widely Separated Atoms', Science **337**, 72–75 (2012) (cited on pages 120, 121).

[276] N. Sangouard, C. Simon, H. de Riedmatten and N. Gisin, 'Quantum repeaters based on atomic ensembles and linear optics', Reviews of Modern Physics **83**, 33–80 (2011) (cited on page 120).

[277] D. Cozzolino, B. Da Lio, D. Bacco and L. K. Oxenløwe, 'High-Dimensional Quantum Communication: Benefits, Progress, and Future Challenges', Advanced Quantum Technologies **2**, 1900038 (2019) (cited on page 120).

[278] A. Grimm, N. E. Frattini, S. Puri, S. O. Mundhada, S. Touzard, M. Mirrahimi, S. M. Girvin, S. Shankar and M. H. Devoret, 'Stabilization and operation of a Kerr-cat qubit', Nature **584**, 205–209 (2020) (cited on page 120).

[279] R. Lescanne, M. Villiers, T. Peronnin, A. Sarlette, M. Delbecq, B. Huard, T. Kontos, M. Mirrahimi and Z. Leghtas, 'Exponential suppression of bit-flips in a qubit encoded in an oscillator', Nature Physics **16**, 509–513 (2020) (cited on page 120).

[280] K. Eckert, J. Schliemann, D. Bruß and M. Lewenstein, 'Quantum Correlations in Systems of Indistinguishable Particles', Annals of Physics **299**, 88–127 (2002) (cited on page 121).

[281] H. M. Wiseman and J. A. Vaccaro, 'Entanglement of Indistinguishable Particles Shared between Two Parties', Physical Review Letters **91**, 097902 (2003) (cited on page 121).

[282] G. Ghirardi and L. Marinatto, 'General criterion for the entanglement of two indistinguishable particles', Physical Review A **70**, 012109 (2004) (cited on page 121).

[283] A. P. Balachandran, T. R. Govindarajan, A. R. de Queiroz and A. F. Reyes-Lega, 'Entanglement and Particle Identity: A Unifying Approach', Physical Review Letters **110**, 080503 (2013) (cited on page 121).

[284] Y. S. Li, B. Zeng, X. S. Liu and G. L. Long, 'Entanglement in a two-identical-particle system', Physical Review A **64**, 054302 (2001) (cited on page 121).

[285] F. Benatti, R. Floreanini, F. Franchini and U. Marzolino, 'Remarks on Entanglement and Identical Particles', Open Systems & Information Dynamics **24**, 1740004 (2017) (cited on page 121).

[286] N. Killoran, M. Cramer and M. B. Plenio, 'Extracting Entanglement from Identical Particles', Physical Review Letters **112**, 150501 (2014) (cited on page 121).

[287] R. Lo Franco and G. Compagno, 'Quantum entanglement of identical particles by standard information-theoretic notions', Scientific Reports **6**, 20603 (2016) (cited on page 121).

[288] R. Lo Franco and G. Compagno, 'Indistinguishability of Elementary Systems as a Resource for Quantum Information Processing', Physical Review Letters **120**, 240403 (2018) (cited on page 121).

[289] B. Morris, B. Yadin, M. Fadel, T. Zibold, P. Treutlein and G. Adesso, 'Entanglement between Identical Particles Is a Useful and Consistent Resource', Physical Review X **10**, 041012 (2020) (cited on page 121).

[290] M. Fadel, T. Zibold, B. Décamps and P. Treutlein, 'Spatial entanglement patterns and Einstein-Podolsky-Rosen steering in Bose-Einstein condensates', Science **360**, 409–413 (2018) (cited on page 121).

[291] P. Kunkel, M. Prüfer, H. Strobel, D. Linnemann, A. Frölian, T. Gasenzer, M. Gärttner and M. K. Oberthaler, 'Spatially distributed multipartite entanglement enables EPR steering of atomic clouds', Science **360**, 413–416 (2018) (cited on page 121).

[292] K. Lange, J. Peise, B. Lücke, I. Kruse, G. Vitagliano, I. Apellaniz, M. Kleinmann, G. Tóth and C. Klempt, 'Entanglement between two spatially separated atomic modes', Science **360**, 416–418 (2018) (cited on page 121).

[293] J. H. Becher, E. Sindici, R. Klemt, S. Jochim, A. J. Daley and P. M. Preiss, 'Measurement of Identical Particle Entanglement and the Influence of Antisymmetrization', Physical Review Letters **125**, 180402 (2020) (cited on page 121).

[294] L.-M. Duan, M. D. Lukin, J. I. Cirac and P. Zoller, 'Long-distance quantum communication with atomic ensembles and linear optics', Nature **414**, 413–418 (2001) (cited on page 121).

[295] N. Killoran, F. E. S. Steinhoff and M. B. Plenio, 'Converting Nonclassicality into Entanglement', Physical Review Letters **116**, 080402 (2016) (cited on page 121).

[296] D. M. Stamper-Kurn and M. Ueda, 'Spinor Bose gases: Symmetries, magnetism, and quantum dynamics', Reviews of Modern Physics **85**, 1191–1244 (2013) (cited on page 122).

[297] Y. Kawaguchi and M. Ueda, 'Spinor Bose–Einstein condensates', Physics Reports **520**, 253–381 (2012) (cited on page 122).

[298] R. Barnett, A. Turner and E. Demler, 'Classifying Novel Phases of Spinor Atoms', Physical Review Letters **97**, 180412 (2006) (cited on page 122).

[299] S. Uchino, M. Kobayashi and M. Ueda, 'Bogoliubov theory and Lee-Huang-Yang corrections in spin-1 and spin-2 Bose-Einstein condensates in the presence of the quadratic Zeeman effect', Physical Review A **81**, 063632 (2010) (cited on page 122).

[300] B. Pasquiou, E. Maréchal, G. Bismut, P. Pedri, L. Vernac, O. Gorceix and B. Laburthe-Tolra, 'Spontaneous Demagnetization of a Dipolar Spinor Bose Gas in an Ultralow Magnetic Field', Physical Review Letters **106**, 255303 (2011) (cited on page 122).

[301] B. Pasquiou, E. Maréchal, L. Vernac, O. Gorceix and B. Laburthe-Tolra, 'Thermodynamics of a Bose-Einstein Condensate with Free Magnetization', Physical Review Letters **108**, 045307 (2012) (cited on page 122).

[302] M. Vengalattore, S. R. Leslie, J. Guzman and D. M. Stamper-Kurn, 'Spontaneously Modulated Spin Textures in a Dipolar Spinor Bose-Einstein Condensate', Physical Review Letters **100**, 170403 (2008) (cited on page 122).

[303] B. Lian, T.-L. Ho and H. Zhai, 'Searching for non-Abelian phases in the Bose-Einstein condensate of dysprosium', Physical Review A **85**, 051606 (2012) (cited on page 123).

[304] R. Hardin, N. Sloane and W. Smith, *Minimal Energy Arrangements of Points on a Sphere*, 1994 (cited on page 123).

[305] A. R. U. Devi, Sudha and A. K. Rajagopal, 'Majorana representation of symmetric multiqubit states', Quantum Information Processing **11**, 685–710 (2012) (cited on page 122).

[306] N. D. Mermin, 'The topological theory of defects in ordered media', Reviews of Modern Physics **51**, 591–648 (1979) (cited on page 123).

[307] P. Bruno, 'Quantum Geometric Phase in Majorana's Stellar Representation: Mapping onto a Many-Body Aharonov-Bohm Phase', Physical Review Letters **108**, 240402 (2012) (cited on page 123).

[308] X.-F. Zhou, C. Wu, G.-C. Guo, R. Wang, H. Pu and Z.-W. Zhou, 'Synthetic Landau Levels and Spinor Vortex Matter on a Haldane Spherical Surface with a Magnetic Monopole', Physical Review Letters **120**, 130402 (2018) (cited on page 124).

[309] F. D. M. Haldane, 'Fractional Quantization of the Hall Effect: A Hierarchy of Incompressible Quantum Fluid States', Physical Review Letters **51**, 605–608 (1983) (cited on page 124).

[310] B. Lian and S. Zhang, 'Singlet Mott state simulating the bosonic Laughlin wave function', Physical Review B **89**, 041110 (2014) (cited on page 124).

[311] T. Chalopin, T. Satoor, A. Evrard, V. Makhalov, J. Dalibard, R. Lopes and S. Nascimbene, 'Probing chiral edge dynamics and bulk topology of a synthetic Hall system', Nature Physics **16**, 1017–1021 (2020) (cited on pages 126, 133, 158).

[312] D. C. Tsui, H. L. Stormer and A. C. Gossard, 'Two-Dimensional Magnetotransport in the Extreme Quantum Limit', Physical Review Letters **48**, 1559–1562 (1982) (cited on page 127).

[313] S. M. Girvin, 'The Quantum Hall Effect: Novel Excitations And Broken Symmetries', in *Aspects topologiques de la physique en basse dimension. Topological aspects of low dimensional systems*, edited by A. Comtet, T. Jolicœur, S. Ouvry and F. David, Les Houches - Ecole d'Ete de Physique Theorique (Springer, Berlin, Heidelberg, 1999), pp. 53–175 (cited on page 127).

[314] F. D. M. Haldane, 'Nobel Lecture: Topological quantum matter', Reviews of Modern Physics **89**, 040502 (2017) (cited on page 127).

[315] K. von Klitzing, '25 Years of Quantum Hall Effect (QHE) A Personal View on the Discovery, Physics and Applications of this Quantum Effect', in *The Quantum Hall Effect: Poincaré Seminar 2004*, edited by B. Douçot, V. Pasquier, B. Duplantier and V. Rivasseau, Progress in Mathematical Physics (Birkhäuser, Basel, 2005), pp. 1–21 (cited on page 127).

[316] M. V. Berry, 'Quantal phase factors accompanying adiabatic changes', Proceedings of the Royal Society of London. A. Mathematical and Physical Sciences **392**, 45–57 (1984) (cited on page 130).

[317] B. Simon, 'Holonomy, the Quantum Adiabatic Theorem, and Berry's Phase', Physical Review Letters **51**, 2167–2170 (1983) (cited on page 131).

[318] F. A. An, E. J. Meier and B. Gadway, 'Direct observation of chiral currents and magnetic reflection in atomic flux lattices', Science Advances **3**, e1602685 (2017) (cited on page 133).

[319] Y.-J. Lin, R. L. Compton, K. Jiménez-García, J. V. Porto and I. B. Spielman, 'Synthetic magnetic fields for ultracold neutral atoms', Nature **462**, 628–632 (2009) (cited on pages 133, 154).

[320] Y.-J. Lin, K. Jiménez-García and I. B. Spielman, 'Spin–orbit-coupled Bose–Einstein condensates', Nature **471**, 83–86 (2011) (cited on page 133).

[321] L. F. Livi et al., 'Synthetic Dimensions and Spin-Orbit Coupling with an Optical Clock Transition', Physical Review Letters **117**, 220401 (2016) (cited on page 133).

[322] S. Kolkowitz, S. L. Bromley, T. Bothwell, M. L. Wall, G. E. Marti, A. P. Koller, X. Zhang, A. M. Rey and J. Ye, 'Spin–orbit-coupled fermions in an optical lattice clock', Nature **542**, 66–70 (2017) (cited on page 133).

[323] N. Goldman, G. Juzeliūnas, P. Öhberg and I. B. Spielman, 'Light-induced gauge fields for ultracold atoms', Reports on Progress in Physics **77**, 126401 (2014) (cited on page 133).

[324] M. Aidelsburger, M. Atala, M. Lohse, J. T. Barreiro, B. Paredes and I. Bloch, 'Realization of the Hofstadter Hamiltonian with Ultracold Atoms in Optical Lattices', Physical Review Letters **111**, 185301 (2013) (cited on page 133).

[325] H. Miyake, G. A. Siviloglou, C. J. Kennedy, W. C. Burton and W. Ketterle, 'Realizing the Harper Hamiltonian with Laser-Assisted Tunneling in Optical Lattices', Physical Review Letters **111**, 185302 (2013) (cited on page 133).

[326] G. Jotzu, M. Messer, R. Desbuquois, M. Lebrat, T. Uehlinger, D. Greif and T. Esslinger, 'Experimental realization of the topological Haldane model with ultracold fermions', Nature **515**, 237–240 (2014) (cited on pages 133, 154).

[327] N. Goldman, J. C. Budich and P. Zoller, 'Topological quantum matter with ultracold gases in optical lattices', Nature Physics **12**, 639–645 (2016) (cited on page 133).

[328] O. Zilberberg, S. Huang, J. Guglielmon, M. Wang, K. P. Chen, Y. E. Kraus and M. C. Rechtsman, 'Photonic topological boundary pumping as a probe of 4D quantum Hall physics', Nature **553**, 59–62 (2018) (cited on page 133).

[329] M. Lohse, C. Schweizer, H. M. Price, O. Zilberberg and I. Bloch, 'Exploring 4D quantum Hall physics with a 2D topological charge pump', Nature **553**, 55–58 (2018) (cited on page 133).

[330] A. Kitaev, 'Anyons in an exactly solved model and beyond', Annals of Physics, January Special Issue **321**, 2–111 (2006) (cited on page 139).

[331] A. Fabre, J.-B. Bouhiron, T. Satoor, R. Lopes and S. Nascimbene, 'Simulating two-dimensional dynamics within a large-size atomic spin', Physical Review A **105**, 013301 (2022) (cited on pages 139, 178).

[332] A. Fabre, J.-B. Bouhiron, T. Satoor, R. Lopes and S. Nascimbene, 'Laughlin's Topological Charge Pump in an Atomic Hall Cylinder', Physical Review Letters **128**, 173202 (2022) (cited on pages 139, 187).

[333] N. Laflorencie, 'Quantum entanglement in condensed matter systems', Physics Reports **646**, 1–59 (2016) (cited on page 140).

[334] N. Regnault, 'Entanglement spectroscopy and its application to the quantum Hall effects', in *Topological Aspects of Condensed Matter Physics*, École de Physique Des Houches, Session CIII, 4-29 August 2014 (Oxford University Press, Oxford, 2017) (cited on pages 141, 142).

[335] J. Eisert, M. Cramer and M. B. Plenio, 'Colloquium: Area laws for the entanglement entropy', Reviews of Modern Physics **82**, 277–306 (2010) (cited on page 141).

[336] M. M. Wolf, F. Verstraete, M. B. Hastings and J. I. Cirac, 'Area Laws in Quantum Systems: Mutual Information and Correlations', Physical Review Letters **100**, 070502 (2008) (cited on page 141).

[337] M. Levin and X.-G. Wen, 'Detecting Topological Order in a Ground State Wave Function', Physical Review Letters **96**, 110405 (2006) (cited on page 141).

[338] A. Kitaev and J. Preskill, 'Topological Entanglement Entropy', Physical Review Letters **96**, 110404 (2006) (cited on page 141).

[339] M. Haque, O. Zozulya and K. Schoutens, 'Entanglement Entropy in Fermionic Laughlin States', Physical Review Letters **98**, 060401 (2007) (cited on page 141).

[340] A. M. Läuchli, E. J. Bergholtz and M. Haque, 'Entanglement scaling of fractional quantum Hall states through geometric deformations', New Journal of Physics **12**, 075004 (2010) (cited on page 141).

[341] T. V. Zache, C. Kokail, B. Sundar and P. Zoller, 'Entanglement Spectroscopy and probing the Li-Haldane Conjecture in Topological Quantum Matter', Quantum **6**, 702 (2022) (cited on pages 146, 152).

[342] J. Dubail, N. Read and E. H. Rezayi, 'Real-space entanglement spectrum of quantum Hall systems', Physical Review B **85**, 115321 (2012) (cited on pages 146, 148).

[343] L. Fidkowski, 'Entanglement Spectrum of Topological Insulators and Superconductors', Physical Review Letters **104**, 130502 (2010) (cited on pages 146, 148).

[344] I. D. Rodríguez and G. Sierra, 'Entanglement entropy of integer quantum Hall states', Physical Review B **80**, 153303 (2009) (cited on page 146).

[345] E. Prodan, T. L. Hughes and B. A. Bernevig, 'Entanglement Spectrum of a Disordered Topological Chern Insulator', Physical Review Letters **105**, 115501 (2010) (cited on page 148).

[346] A. Sterdyniak, C. Repellin, B. A. Bernevig and N. Regnault, 'Series of Abelian and non-Abelian states in $C > 1$ fractional Chern insulators', Physical Review B **87**, 205137 (2013) (cited on page 148).

[347] Y.-L. Wu, N. Regnault and B. A. Bernevig, 'Bloch Model Wave Functions and Pseudopotentials for All Fractional Chern Insulators', Physical Review Letters **110**, 106802 (2013) (cited on page 148).

[348] B. M. Garjani, B. Estienne and E. Ardonne, 'On the particle entanglement spectrum of the Laughlin states', Journal of Physics A: Mathematical and Theoretical **48**, 285205 (2015) (cited on page 148).

[349] R. Thomale, D. P. Arovas and B. A. Bernevig, 'Nonlocal Order in Gapless Systems: Entanglement Spectrum in Spin Chains', Physical Review Letters **105**, 116805 (2010) (cited on page 148).

[350] A. M. Läuchli, E. J. Bergholtz, J. Suorsa and M. Haque, 'Disentangling Entanglement Spectra of Fractional Quantum Hall States on Torus Geometries', Physical Review Letters **104**, 156404 (2010) (cited on page 148).

[351] M. P. Zaletel and R. S. K. Mong, 'Exact matrix product states for quantum Hall wave functions', Physical Review B **86**, 245305 (2012) (cited on page 148).

[352] B. Swingle and T. Senthil, 'Geometric proof of the equality between entanglement and edge spectra', Physical Review B **86**, 045117 (2012) (cited on page 148).

[353] J. I. Cirac, D. Poilblanc, N. Schuch and F. Verstraete, 'Entanglement spectrum and boundary theories with projected entangled-pair states', Physical Review B **83**, 245134 (2011) (cited on page 148).

[354] G. De Chiara, L. Lepori, M. Lewenstein and A. Sanpera, 'Entanglement Spectrum, Critical Exponents, and Order Parameters in Quantum Spin Chains', Physical Review Letters **109**, 237208 (2012) (cited on page 148).

[355] Z. Gong and M. Ueda, 'Topological Entanglement-Spectrum Crossing in Quench Dynamics', Physical Review Letters **121**, 250601 (2018) (cited on page 148).

[356] J. Surace, L. Tagliacozzo and E. Tonni, 'Operator content of entanglement spectra in the transverse field Ising chain after global quenches', Physical Review B **101**, 241107 (2020) (cited on page 148).

[357] A. Chandran, M. Hermanns, N. Regnault and B. A. Bernevig, 'Bulk-edge correspondence in entanglement spectra', Physical Review B **84**, 205136 (2011) (cited on page 148).

[358] A. Sterdyniak, N. Regnault and B. A. Bernevig, 'Extracting Excitations from Model State Entanglement', Physical Review Letters **106**, 100405 (2011) (cited on page 148).

[359] M. Hermanns, A. Chandran, N. Regnault and B. A. Bernevig, 'Haldane statistics in the finite-size entanglement spectra of $1/m$ fractional quantum Hall states', Physical Review B **84**, 121309 (2011) (cited on page 148).

[360] Z. Papić, B. A. Bernevig and N. Regnault, 'Topological Entanglement in Abelian and Non-Abelian Excitation Eigenstates', Physical Review Letters **106**, 056801 (2011) (cited on page 148).

[361] J. J. Bisognano and E. H. Wichmann, 'On the duality condition for quantum fields', Journal of Mathematical Physics **17**, 303–321 (1976) (cited on page 151).

[362] J. J. Bisognano and E. H. Wichmann, 'On the duality condition for a Hermitian scalar field', Journal of Mathematical Physics **16**, 985–1007 (1975) (cited on page 151).

[363] C. Kokail, R. van Bijnen, A. Elben, B. Vermersch and P. Zoller, 'Entanglement Hamiltonian tomography in quantum simulation', Nature Physics **17**, 936–942 (2021) (cited on page 152).

[364] C. Kokail, B. Sundar, T. V. Zache, A. Elben, B. Vermersch, M. Dalmonte, R. van Bijnen and P. Zoller, 'Quantum Variational Learning of the Entanglement Hamiltonian', Physical Review Letters **127**, 170501 (2021) (cited on page 152).

[365] M. Dalmonte, V. Eisler, M. Falconi and B. Vermersch, *Entanglement Hamiltonians: from field theory, to lattice models and experiments*, 10th Feb. 2022, arXiv:2202.05045 [cond-mat, physics:hep-th, physics:math-ph, physics:quant-ph] (cited on page 152).

[366] B. I. Halperin, 'Statistics of Quasiparticles and the Hierarchy of Fractional Quantized Hall States', Physical Review Letters **52**, 1583–1586 (1984) (cited on page 154).

[367] V. J. Goldman, B. Su and J. K. Jain, 'Detection of composite fermions by magnetic focusing', Physical Review Letters **72**, 2065–2068 (1994) (cited on page 154).

[368] T.-S. Zeng, C. Wang and H. Zhai, 'Charge Pumping of Interacting Fermion Atoms in the Synthetic Dimension', Physical Review Letters **115**, 095302 (2015) (cited on page 154).

[369] L. Taddia, E. Cornfeld, D. Rossini, L. Mazza, E. Sela and R. Fazio, 'Topological Fractional Pumping with Alkaline-Earth-Like Atoms in Synthetic Lattices', Physical Review Letters **118**, 230402 (2017) (cited on page 154).

[370] A. A. Abrikosov, 'The magnetic properties of superconducting alloys', Journal of Physics and Chemistry of Solids **2**, 199–208 (1957) (cited on page 154).

[371] V. Bretin, S. Stock, Y. Seurin and J. Dalibard, 'Fast Rotation of a Bose-Einstein Condensate', Physical Review Letters **92**, 050403 (2004) (cited on page 154).

[372] V. Schweikhard, I. Coddington, P. Engels, V. P. Mogendorff and E. A. Cornell, 'Rapidly Rotating Bose-Einstein Condensates in and near the Lowest Landau Level', Physical Review Letters **92**, 040404 (2004) (cited on page 154).

[373] M. Aidelsburger, M. Atala, S. Nascimbène, S. Trotzky, Y.-A. Chen and I. Bloch, 'Experimental Realization of Strong Effective Magnetic Fields in an Optical Lattice', Physical Review Letters **107**, 255301 (2011) (cited on page 154).

[374] M. Aidelsburger, M. Lohse, C. Schweizer, M. Atala, J. T. Barreiro, S. Nascimbène, N. R. Cooper, I. Bloch and N. Goldman, 'Measuring the Chern number of Hofstadter bands with ultracold bosonic atoms', Nature Physics **11**, 162–166 (2015) (cited on page 154).

[375] S. Barbarino, L. Taddia, D. Rossini, L. Mazza and R. Fazio, 'Magnetic crystals and helical liquids in alkaline-earth fermionic gases', Nature Communications **6**, 8134 (2015) (cited on page 154).

[376] G. Juzeliūnas, J. Ruseckas, P. Öhberg and M. Fleischhauer, 'Light-induced effective magnetic fields for ultracold atoms in planar geometries', Physical Review A **73**, 025602 (2006) (cited on page 155).

[377] R. Dum and M. Olshanii, 'Gauge Structures in Atom-Laser Interaction: Bloch Oscillations in a Dark Lattice', Physical Review Letters **76**, 1788–1791 (1996) (cited on page 155).

[378] J.-B. Bouhiron, A. Fabre, Q. Liu, Q. Redon, N. Mittal, T. Satoor, R. Lopes and S. Nascimbene, *Realization of an atomic quantum Hall system in four dimensions*, arXiv:2210.06322 (arXiv, 12th Oct. 2022), p. 2210.06322, arXiv:2210.06322 [cond-mat, physics:quant-ph] (cited on page 193).

RÉSUMÉ

Cette thèse porte sur trois études utilisant des gaz ultrafroids d'atomes de dysprosium bosoniques. Nous encodons des états quantiques d'intérêt dans le grand spin électronique J=8 de l'état fondamental de chaque atome. Des transitions optiques étroites sont utilisées pour manipuler ces états en créant de forts décalages lumineux tensoriels dépendant du spin avec un chauffage négligeable. Notre schéma de détection utilise des rotations de spin arbitraires suivies d'une mesure des probabilités de projection de chaque état interne.

Premièrement, nous étudions un modèle d'Ising de spins 1/2 quantiques soumis à un champ transverse et interagissant à portée infinie. Ce modèle présente une transition de phase quantique du type paramagnétique-ferromagnétique dans la limite thermodynamique. Notre expérience repose sur l'équivalence formelle entre les états d'un spin J=8 et les états symétriques par échange de 2J=16 qubits dans le secteur de spin maximal. Nous sondons les propriétés thermodynamiques et dynamiques, révélant un comportement critique quantique de taille finie autour de la transition. Ensuite, nous testons directement le lien fondamental entre la brisure de symétrie et l'apparition d'un paramètre d'ordre fini. Ceci est rendu possible par l'accès à l'observable collectif qui définit la symétrie Z2 sous-jacente.

Deuxièmement, nous partitionnons le spin électronique pour révéler l'intrication dans les états non-classiques. En couplant optiquement le niveau de base à un état excité J'=J-1, nous extrayons une paire de qubits encodés dans un état défini par la polarisation de la lumière. Nous sondons la concomitance (*concurrence*) des paires de qubits extraites des états W et des états comprimés pour quantifier leur caractère non-classique. Nous démontrons directement l'intrication entre les sous-systèmes à 14 et 2 qubits par une augmentation de l'entropie lors de la partition. Dans un ensemble complémentaire d'expériences, nous sondons la décohérence d'un état préparé dans le niveau excité J'=J+1 et interprétons l'émission spontanée comme la perte d'une paire de qubits dans un état aléatoire. Cela nous permet de contraster la robustesse des corrélations non classiques par paire de l'état W avec la fragilité de la cohérence d'un état chat de Schrödinger.

Troisièmement, nous simulons un système de Hall quantique en exploitant le spin de l'état fondamental électronique comme une dimension synthétique discrète, et en le couplant optiquement au mouvement atomique le long d'une deuxième dimension réelle. Cela crée un champ magnétique artificiel, les deux dimensions couplées formant un ruban de Hall avec des bords nets le long de l'axe synthétique. Nous démontrons que le grand nombre de sous-niveaux magnétiques conduit à des comportements distincts dans le cœur et sur les bords du système, et à une réponse de Hall caractéristique d'une topologie non-triviale. Nous effectuons une étude préliminaire du spectre d'intrication associé à une partition au centre de la dimension synthétique, et nous expliquons comment de futures études pourraient directement implémenter le hamiltonien d'intrication correspondant. Nous concluons avec une feuille de route pour étendre les techniques présentées dans cette thèse afin de réaliser des états topologiques à N corps.

MOTS CLÉS

gaz quantiques, atomes ultrafroids, criticité quantique, intrication quantique, matière topologique

ABSTRACT

This thesis describes three studies using ultracold gases of bosonic dysprosium atoms. We encode quantum states of interest in the large electronic ground state spin J=8 of each atom. Narrow-line optical transitions are used to manipulate these states by creating strong spin-dependent tensor light shifts with negligible heating. Our detection scheme uses arbitrary spin rotations followed by measurement of projection probabilities with single magnetic sublevel resolution.

Firstly, we study a transverse-field Ising model of quantum spin-1/2's with infinite-range interactions. This model shows a paramagnetic to ferromagnetic quantum phase transition in the thermodynamic limit. Our experiment relies on the formal equivalence between the states of a spin J=8 and exchange-symmetric states of 2J=16 qubits in the sector of maximum total spin. We probe the thermodynamic and dynamical properties, revealing finite-size quantum critical behaviour around the transition point. We also directly test the fundamental link between symmetry breaking and the appearance of a finite order parameter. This is enabled by access to the collective observable defining the underlying Z2 symmetry.

Secondly, we partition the electronic spin to reveal entanglement in nonclassical states. By optically coupling the ground level to an excited state J' = J-1, we remove a pair of encoded qubits in a state defined by the light polarisation. We probe the concurrence of qubit pairs extracted from W and squeezed states to quantify their nonclassical character. We directly demonstrate entanglement between the 14- and 2-qubit subsystems via an increase in entropy upon partition. In a complementary set of experiments, we probe the decoherence of a state prepared in the excited level J' = J + 1 and interpret spontaneous emission as a loss of a qubit pair in a random state. This allows us to contrast the robustness of nonclassical pairwise correlations of the W state with the fragility of the coherence of a Schrödinger cat state.

Thirdly, we simulate a quantum Hall system by exploiting the electronic ground state spin as a discrete synthetic dimension, and optically coupling it to atomic motion along a second real dimension. This creates an artificial magnetic field, with the two coupled dimensions forming a Hall ribbon with sharp edges along the synthetic axis. We demonstrate that the large number of magnetic sublevels leads to distinct bulk and edge behaviours, and a Hall response characteristic of a non-trivial topology. We perform a preliminary investigation of the entanglement spectrum associated with a partition at the centre of the synthetic dimension, and we explain how future studies could directly implement the corresponding entanglement Hamiltonian. We conclude with a roadmap for extending the techniques presented in this thesis in order to realise many-body topological states.

KEYWORDS

quantum gases, ultracold atoms, quantum criticality, quantum entanglement, topological matter